UNIVERSITY OF BIRMINGHAM

APPLICATIONS OF PARTICLE PHYSICS TECHNIQUES FOR PROTON COMPUTED TOMOGRAPHY

by

MARC GRANADO-GONZÁLEZ

A thesis submitted to the University of Birmingham for the degree of
DOCTOR OF PHILOSOPHY

High Energy Physics - BILPA
School of Physics and Astronomy
College of Physics and Engineering
University of Birmingham
May 2023

UNIVERSITY OF
BIRMINGHAM

University of Birmingham Research Archive

e-theses repository

This unpublished thesis/dissertation is copyright of the author and/or third parties. The intellectual property rights of the author or third parties in respect of this work are as defined by The Copyright Designs and Patents Act 1988 or as modified by any successor legislation.

Any use made of information contained in this thesis/dissertation must be in accordance with that legislation and must be properly acknowledged. Further distribution or reproduction in any format is prohibited without the permission of the copyright holder.

© Copyright by MARC GRANADO-GONZÁLEZ, 2023
All Rights Reserved

Success is not measured by what you accomplish, but by the opposition you have encountered, and the courage with which you have maintained the struggle against overwhelming odds.
- ***Orison Swett Marden.***

ABSTRACT

Proton beam therapy can potentially offer improved treatment for head and neck cancers and paediatric patients. There has been a sharp uptake of proton beam therapy in recent years as improved delivery techniques and patient benefits are observed. However, treatments are currently planned using conventional X-ray CT images due to the absence of devices able to perform high-quality proton computed tomography (pCT) under realistic clinical conditions. The rise of new technologies such as the Depleted Monolithic Active Pixel Sensors (DMAPS), developed for the inner tracker upgrades at the High Luminosity Large Hadron Collider (HL-LHC) or the plastic scintillators detectors used at the Fine Grained Detector at the Tamioka to Kamio (T2K) experiment, could imply a big step forward in the field. This thesis aims to show the potential of both technologies by providing a proof of concept on the capabilities of these technologies. First, by building a tracker with two TJ-Monopix sensors and testing it at Birmingham's MC40 cyclotron and the proton minibeam radiotherapy centre at the Curie Institue under real clinical conditions, and second by simulating a full pCT system consisting in a DMAPS as proton trackers and a novel range telescope ASTRA (designed during the thesis). The simulation and consequent analysis aimed to obtain a pCT image of a phantom with 7 different materials. Using a set of classic algorithms and demonstrating later the enhancement obtained by using Convoluted Neural Networks (CNN). For the first part, the TJ-Monopix chip is used. The chip presents an excellent response up to a fluency of $\sim$ 1 M $\frac{particles}{s}$ with no area coverage dependence, allowing flux above $\sim$ 13.3 M $\frac{particles}{s*cm^2}$ with a fast detection rate of 40 MHz. Thus, the TJ-Monopix properties allow it also to be used as a beam monitoring device for micro-beam therapy and to improve the knowledge of the clinical beam's behaviour at low currents. ASTRA is the new plastic-scintillator-based range telescope concept designed to simulate a full proton CT system, it was first presented in the peer-reviewed paper [1] and it was used here to measure the proton's energy loss in a pCT system. Simulations conducted using GEANT4 yield an expected energy resolution of 0.7%. When calorimetric information is used in combination with Boosted Decision Trees (BDT) techniques the energy resolution could be further improved to about 0.5%. In addition, the ability of ASTRA to track multiple protons simultaneously is presented, first with classic algorithms that do not use the energy-deposited information and then with the use of this information combined with a Comboluted Neural Network of the type U-Net using a novel in-pixel Multi-Label analysis. Due to its fast components, ASTRA is expected to reach unprecedented data collection rates around 10^8 protons/s. The performance of ASTRA has also been tested by simulating the imaging of phantoms The results show excellent image contrast and relative stopping power reconstruction.

ACKNOWLEDGMENTS

The work performed in this thesis was performed between September 2019 and May 2023. During these almost four years of work, many things have shaped me and the way this thesis has evolved. It is for this that I want to acknowledge all the contributions from all the people and institutions that have allowed the personal growth and strength needed to finish this thesis.

First of all, I would like to thank the University of Birmingham and the school of Physics and Astronomy and the *STFC network + for advanced radiotherapy* for funding the project for this PhD. Secondly, I would like to thank Dr. Laura Gonnella and Dr. Tony Price for selecting me as their PhD candidate. I would also like to extend this thanks to Laura for being an excellent supervisor during the first year and offering her support even when her workload did not allow her to keep on supervising the project. Moreover, to thank Tony for his guidance and help during all this time, for his good insights on how to proceed, the methods, and the biggest influence on my thesis which was the "baby-steps" approach. However, I have to say I am the most thankful for his attitude towards the work and the un-numerous adversities that the project has faced due to Covid and other bureaucratic issues, as well as the concern for my wellbeing during the hardest times.

Second I would need to thank all the colleagues from the High Energy Physics department at the UoB, but with a bigger thanks to Drs. Alastair Winter and John Coterill; for their invaluable help during the begining of my PhD and for being the only people in the group who would understand what being a medical applications student among our CERN colleagues. I would like to thank Dr. Francesco Gonella for his help with the firmware and founding the southern musicians club. I would also like to thank my office colleagues in the basement; Daniel Briglin, Dan Lewis, Nandish Gorasia, Jack Lindon,

and Govind Virdee for their warm welcome in Birmingham city. I do not want to forget the colleagues from the corridor office who were a big help during the last year of the PhD when, after coming back from the CERN environment in April 2022, finding motivation was sometimes hard. On a more personal basis, I would need to thank Julia Silva for being the best UoB could have ever provided. For the coffee breaks before covid, for the hour-long coffee breaks at 7:30 am during covid times through Zoom, for the invaluable friendship that grew from there, and for being one of a kind. To Ben Franklin's suitcase which travelled back and forth Paris allowing us to carry all the equipment needed for the test beam at the Curie insitute.

Back from my hometown Sabadell I would like to thank my family for the support they gave me during the PhD application process, during the PhD and during the my whole life in general. Thanks for sponsoring my studies with a smile and for trying to understand when I shared why my work made me happy. Without all your help none of this could have been achieved. Within this "little" city, two groups of friends have always been a stronghold supporting every step and providing the breaks that would allow me to get back with much more strength. Thanks to the Girona group: Pol Berch, Jan Saura, Ferran Vidal, Joan Valls and Groka Plans. An extended thanks to Gorka who, a part from being a great friend, has also been a great designer and has drawn all the sketches used in this thesis defining with this the colour pallet of all the plots, bringing the aesthetics of this thesis to another level. Thanks also to the Pessigàvers group, for all the amazing times not only during these four years but during most of my life, and within this group, to the subgroup of "Som empos però..." for creating an environment in which being a scientist was something to be proud of, and sharing our research was always cheered and valued.

To my friends from University Autònoma de Barcelona, many thanks for Claudia Grimal i Bosch, Dr. Marcel Alageró-Casas and Dr. Sergi Julià-Farré for always being there, for the 5 years of uni and for the bond that has kept us together for the next six and many more to come. I forgot, to mention Dr. Cesar Jesus-Valls on purpose because

he needs a special mention. Cesar has been a key figure during this PhD. Out of a random discussion at 3:00 am through Zoom after a friends dinner, we came up with the idea for ASTRA which has latter become a structural part of this thesis. Not only for that but after this, Cesar was like the Postdoc the UoB group was missing, helping me on every step of the way with the simulations and analysis. The month we spent working together in Geneva with you and Claudia was by far best part of my PhD.

I could not go without thanking the people who have turned the city of Birmingham into the perfect environment for this work. Thanks to Alex and Mau for their warm welcome to the city and their friendship during all these years; to Sara for being a great company during one of the hardest parts of the thesis; to Zaen for being a friend I could always count on for having a good time and forget about the work; and to Argyró for turning the writing months of the thesis into an adventure.

Contents

1 Introduction **1**

2 Radiotherapy and computed tomography **7**

2.1 Main oncology treatments 7

2.2 Principles of Radiotherapy 8

2.2.1 The protons' beam range 11

2.2.2 Stopping power and Linear Energy Transfer 12

2.2.3 The Bragg peak 14

2.2.4 Therapeutic window 17

2.2.5 Proton Mini-Beam radiotherapy 19

2.2.6 FLASH radiotherapy 22

2.3 Proton Computed Tomography 23

2.3.1 State-of-the-art systems 25

3 Particle Physics Techniques **33**

3.1 Electromagnetic radiation and matter interaction 33

3.1.1 Photons interactions 34

3.2 Particle-matter interaction 36

3.2.1 Main proton interactions 38

3.2.2 Multiple Coulomb scattering 41

3.3 Particle physics detectors 42

3.3.1 The P-N junction 44

3.3.2 Detection principles . . . 46
3.3.3 CMOS . . . 47
3.3.4 Silicon photo-multipliers . . . 54
3.3.5 Scintillation Detectors . . . 55
3.4 Machine Learning and Deep Learning . . . 57
3.4.1 Convolutional Neural Networks . . . 57
3.4.2 Learning Rate, optimizers, and ADAM . . . 57
3.4.3 Different kinds of problems to solve with CNN: . . . 59
3.4.4 Signal Segmentation . . . 59
3.4.5 Multi-labeling . . . 59
3.4.6 Regression . . . 60
3.5 Geant4 a toolkit for physics simulations . . . 60
3.5.1 Stepping Action . . . 61
3.5.2 Position Tracking . . . 61
3.5.3 Sensitive detectors . . . 62

4 Characterisation of the TJ-Monopix 63

4.1 TJ-Monopix . . . 63
4.2 Comissioning of the TJ-Monopix . . . 65
4.2.1 Setup for the TJ-Monopix . . . 66
4.2.2 Threshold scans . . . 69
4.2.3 Tunning of the front end parameters . . . 69
4.3 Source scans . . . 73
4.4 Test beam with low energy protons . . . 77
4.5 Clustering algorithms . . . 77
4.5.1 Cluster size and charge reconstruction . . . 79
4.6 Chapter summary . . . 82

5 TJ-Monopix for beam monitoring at the MC40 Cyclotron 83

5.1 The MC40 cyclotron . . . 84

5.2 Flux studies . . . 85

5.2.1 Methodology . . . 85

5.2.2 Results . . . 88

5.2.3 Impact of the cluster size . . . 94

5.3 Study of the opening of the Faraday Cup . . . 96

5.3.1 Methodology . . . 98

5.3.2 Results . . . 100

5.4 Chapter summary . . . 102

6 Tracking MC40 protons with the TJ-Monopix 103

6.1 Methodology . . . 103

6.1.1 Telescope mechanics and alignment . . . 104

6.1.2 Event matching . . . 107

6.1.3 Effect of MCS when tracking with two planes . . . 111

6.2 Tracking results at MC40 Cyclotron . . . 113

6.2.1 Beam's angular dispersion . . . 115

6.3 Chapter summary . . . 117

7 Test beam and simulations of the Curie institute pMBRT line 119

7.1 Expected number of protons at the Curie Institute . . . 121

7.2 Test beam and single sensor analysis . . . 123

7.2.1 Methodology . . . 123

7.2.2 Results . . . 125

7.3 Simulation . . . 130

7.3.1 Methodology . . . 130

7.4 Results . . . 131

7.5 Chapter summary . . . 135

8 Simulation of a full pCT system **137**

8.1 Introduction . . . 137

8.2 The simulated setup . . . 137

8.2.1 The design of ASTRA . . . 139

8.3 Geant4 simulations . . . 141

8.3.1 Full system analysis with ROOT and classic algoritms . . . 142

8.3.2 Fully simulated pCT with DMAPS and ASTRA . . . 150

8.4 CNN analysis decoupling multi-proton events . . . 160

8.4.1 Methodology . . . 161

8.4.2 Results of the CNN analysis . . . 164

8.4.3 Comparing with classic algorithms . . . 168

8.5 Energy measurement with DNN for inelastically scattered protons . . . 170

8.5.1 Methodology . . . 170

8.5.2 Results . . . 172

8.6 Summary of the chapter . . . 175

9 Conclusions **177**

List of Figures

1.1 Relative dose deposition X-Ray vs protons as a function of depth 2

1.2 Sketch of a proton Computed Tomography (pCT) setup with two layer trackers in front and after the imaged body and a range telescope to measure the residual energy downstream. 5

2.1 Schematic of the types of DNA damage. 10

2.2 Relative fraction of the fluence ϕ in a broad beam of protons remaining as a function of depth z in water. 12

2.3 Mass stopping power (S) as a function of proton energy. 13

2.4 Therapeutic window sketch. 18

2.5 Sketch of the dose deposition of a standard proton beam (right) and a proton MiniBeam Radiotherapy (pMBRT) beam [33]. 20

2.6 Sketch defining the combination of Proton Arch Therapy (top left), proton Mini Beam Radiotherapy (bottom left) leading to proton Mini Beam Arch Therapy [38]. 21

2.7 Sketch of the back-projection method using three different projections of a body with a circle of a different density. 24

2.8 Sketch of the proton path within a body. 24

2.9 Image of the phase II prototype scanner. 26

2.10 Sketch of the ProtonVDA system depicting the tracking planes with a human head between planes and the Photomultipler Tubes (PMT) based calorimeter. 28
2.11 The PRaVDA pCT system showing upstream and downstream trackers, phantom holder, RT and beam nozzle at the iThemba LABS proton facility, South Africa [12]. 29
2.12 Schematic drawing of the Bergen pCT calorimeter 30

3.1 Sketch of the three main photon interactions; Compton scattering (left), photoelectric effect (middle), and pair production (right). 34
3.2 Plot of the mass attenuation coefficient of iron for an X-ray beam as a function 36
3.3 Stopping power for positive muons in copper as a function of $\beta\gamma$ from 10^{-3} to 10^{6}. The vertical lines show the different ranges for different equations. The middle range, with $\beta\gamma$ from 0.1 to 1000 show the Bethe-Bloch regime. Figure obtained from [52] 39
3.4 Sketch of the three different proton interactions, inelastic and elastic Compton scattering (left) and (middle) respectively, and inelastic nuclear interactions (right). 40
3.5 Sketch of the definition of the dispersion angles ω and ρ between two planes. 43
3.6 Sketch of the transverse cut of a p-n junction. 45
3.7 Sketch of the transverse section of a hybrid (left) and a monolighic (right) pixel detctors with a ionising particle passing through. 47
3.8 Diagram of a CMOS inverter 48
3.9 Sketch of the charge sharing effect. 49
3.10 Cross section of a MAPS chip 51
3.11 Cross section of a Depleted Monolithic Active Pixel Sensor (DMAPS) chip. 52
3.12 Block diagram of the typical analog front-end circuit in a pixel. 53
3.13 Sketch of the signals observed at the points (a), (b) and (c) in Figure 3.12. 53

3.14 Layout of the 50R-Silicon Photo Multiplier (SiPM) with 16 × 16 SPADs and quenching resistors and implified structure of a generic SiPM. 55
3.15 Example of the effect of a too low (left), just right (middle) and too high (right) learning rate when optimising a parameter. 58

4.1 Pixel cross-sections for the Removed Deep P-Well (RDPW) (above) and Full Deep P-Well (FDPW) (below) layouts in TJ-Monopix. 64
4.2 Top view of the FDPW and RDPW flavours dividing the TJ-Monopix chip 65
4.3 Schematics of the architecture of the TJ-Monopix electronics [62]. 66
4.4 Setup of the TJ-Monopix commissioned in the BILPA ISO7 clean room in Birmingham. 67
4.5 Picture of the connections of the MIO3 and FPGA, the GPAC board, and the PCB with the TJ-Monopix sensor. 67
4.6 Close up of the TJ-Monopix chip wire-bonded to the PCB designed in Si-Lab 68
4.7 Sketch of the carrier board of the TJ-Monopix showing the different flavours. 68
4.8 Histogram of the threshold distribution of the FDPW and RDPW for the default FE parameters. 70
4.9 Histogram of the threshold distribution of the FDPW and RDPW for the CP FE parameters. 72
4.10 Histogram of the Equivalent Noise Charge (ENC) for the FDPW (left) and RDPW (right) for the Front End (FE) parameters optimised for Clinical Protons (CP). 72
4.11 Spectrum of radiation of the isotope ^{55}Fe obtained by C. Fiorini, *et al.*[83] 74
4.12 Charge collection dispersion of the TJ-Monopix with default FE prameters 74
4.13 Charge collection dispersion of the TJ-Monopix with FE prameters optimised for CP. 75
4.14 Hit occupancy map ^{55}Fe with the default and optimised for CP sets of FE parameters. 76
4.15 2D hit map before and after clustering. 79

4.16 Cluster size distribution for the test beam with 36 MeV protons and a flat 1 cm^2 beam. 79
4.17 Reconstructed charge at a test beam with 36 MeV protons and a flat 1 cm^2 beam. 80
4.18 Histogram of the charge collection distributions separated by cluster size. . 81

5.1 Sketch of the MC40 cyclotron with the control and the main room. The beam line used is the one in the supervised with lower beam intensities. . . 85
5.2 Image of a full TJ-Monopix system close to the beam nozzle of the MC40 cyclotron at the test beam performed in March 2020. 86
5.3 Picture of the slits collimator. The collimator consists on a 2 mm plate of Tantalum with 15 slits with 100 μm width, 8 mm length separated by 400 μm. 87
5.4 Picture of the holes collimator placed in the aluminium support. 87
5.5 Plot of the total number of measured hits as a function of time for a current with the normal behaviour of the readout system at a flux of 5 M p/cm^2/s (black) and an example of saturation of the bus with 7 M p/cm^2/s (red). . 89
5.6 Cluster hit map of a scan with the squared collimator with 36 MeV protons. 89
5.7 Plot of the clusters per second as a function of the proton flux using a 1 cm^2 collimator. 90
5.8 Histogram of the time difference between two consecutive events for two different data sets taken with an equivalent current of 0.03 Mp/s (yellow) and 0.35 Mp/s (blue). 91
5.9 Cluster hit map of a scan with the 8×0.1 mm^2 slits collimator with 36 MeV protons. 92
5.10 Plot of the clusters per second as a function of the proton flux using the slits collimator. 92
5.11 Plot of the hits per second as a function of proton flux (black) and clusters per second as a function of proton flux for nine slits. 93

5.12 Cluster hit map of a scan with the six 0.75 mm diameter holes collimator with 36 MeV protons. 94

5.13 Plot of the clusters per second as a function of the proton flux using the six holes collimator. The data obtained on test beams (black crosses) has been fitted (dashed black) to obtain the sensitive area covered by the beam. The yellow and green areas show the expected number of protons ±5% and ±10% respectively. 95

5.14 Plot of the hits per second as a function of proton flux (black) and clusters per second as a function of proton flux for six holes with a total area of 0.023 cm^2. 95

5.15 Opening area of the beam as a function of the percentage of the FC opening fitted and error of the fit. 97

5.16 Number of hits observed as a function of time from the opening of the FC and vertical dashed black lines show the time in which the FC is fully open. 100

5.17 2D cluster map of the TJ-Monopix for intervals while the FC is opening. . 101

6.1 Image of the mechanical telescope built at the MC40 Birmingham's beamline. 105

6.2 Image of the XY micrometer used for the mechanical system of the TJ-Monopix telescope. 105

6.3 X and Y position dispersion for the first and second sensors before and after the fine alignment. 106

6.4 Event number as a function of the scanning time for the front (blue) and back (orange) sensors on a On-Off beam scan and delay between the front and back sensors as a function of scanning time measured through On-Off points and event by event after matching. 108

6.5 Normalised histogram of the time between events. The data measured on a test beam scan is presented in blue, a black dashed line shows the exponential fit and the red line shows the simulation obtained afterward. . 110

6.6 Efficiency dispersion of the efficiency of running the matching algorithm for 1000 different data sets of 100000 events each. The mean of the distribution is at 85.9 % 111

6.7 2D histograms of the proton positions at the first (left) and 2nd (right) sensors, 5 cm apart, with a proton beam energy of 28 MeV. 112

6.8 Top visualisation of the effect of Multiple Coulomb Scattering (MCS) defining the initial distance between protons (D_0) and the dispersion distance (D_{MCS}) due to the MCS. 113

6.9 Histogram of the distribution of the proton displacement due to MCS (D_{MCS}) in yellow and the initial distance between two consecutive protons (D_0). 114

6.10 2D hit map of the first (middle) and second (right) sensors and the back projection to the collimator position, of the proton track using a 2 mm circular collimator. 114

6.11 Position variation dispersion (left) and angular dispersions for the angles defined in Figure 3.5 middle and right for measured 28 MeV protons from the MC40 cyclotron. 115

6.12 Position variation dispersion (left) and angular dispersions for the angles defined in Figure 3.5 middle and right for the simulated 28 MeV protons. . 116

7.1 Expected number of protons per second at the TJ-Monopix sensitive area for different positions of the Curie pencil beam relative to the center of a single mini beam slit. 122

7.2 Setup for the test beam at the Curie mini beamline with two TJ-Monopix detectors. 124

7.3 Hit occupancy maps of the measurements used for the alignment of the beam with the TJ-Monopix using the slit in a horizontal position and vertical position. 124

7.4 Sketch representing the displacement $\Delta(\mu_x, \mu_y)$ between the centre of the slit and the centre of the pencil beam. 125

7.5 Hit occupancy scans at 55 and 145 mm from the vertical slit collimator and the X position distribution fitted with a Gaussian to obtain the σ of the distribution. 126

7.6 Projection of the hits in the Y direction of a scan using the vertical slit at the pMBRT line at the Curie Institute. 127

7.7 Profile of the Curie slit beam opening as a function of distance to the collimator. The blue dots represent the sigma of a Gaussian fitted to the horizontal position dispersion of the protons measured by the TJ-Monopix at the test beam and the dashed red line is the linear fit. 128

7.8 Distribution of the cluster size for the FDPW and the RDPW from a test beam taken with the 100 MeV protons using the mini-beam line at the Curie institute. 128

7.9 Reconstructed charge using a vertical slit at the Curie Institute with 100 MeV protons separated for different cluster sizes. 129

7.10 From left to right, distributions of the displacement in x (olive) and y (blue) directions, ω and θ dispersion angles 131

7.11 Hit occupancy scan of the full 10 M simulated protons and 5 consecutive events in both sensors and back projection. 133

7.12 Variation in position r between the first and second layer of the pixel tracker for all particles (blue) and secondary particles (olive). 134

7.13 Normalised histograms of the charge collected by protons (blue) and secondary particles (olive) at the pixel sensors. 134

7.14 Position resolution in X (olive) and Y (blue) of the back projection of the simulated protons with the TJ-Monopix-like sensor with the mini-beam slit. 135

8.1 3D visualisation of the pCT system with four DMAPS layers, a spherical phantom with 6 cylindrical inserts in place, and the ASTRA system. . . . 138

8.2 FGD and ASTRA concepts. 140

8.3 Sketch of the tracking algorithm showing the performance with two tracks see from above. 144

8.4 Purity×efficiency of the DMAPS tracker as a function of the number of protons per event for different thicknesses of the phantom in place. 145

8.5 Fit of the simulated data of the water tank thickness as a function of the energy loss by a monochromatic proton beam of 180 MeV. 146

8.6 Fit of 2D plane of the true energy as a function of the reconstructed range. 147

8.7 Examples of two of the distributions for bars of 3 mm used in Figure 8.8. The left (right) plot corresponds to a resolution of 1.02% (0.70%) 148

8.8 Energy resolution of the ASTRA range telescope using range-only information for three different squared-shaped bar sizes. 149

8.9 Purity×efficiency of reconstructed tracks in the pCT system (DMAPS+ASTRA). 149

8.10 Sketch of two protons going through different paths leaving the phantom with different energies E_1 and E_2. 151

8.11 Fraction of protons good for imaging as a function of the proton true kinetic energy using a different number of simultaneous protons for a Gaussian beam ($\sigma = 10$ mm) and for a flat 75×75 mm^2 beam. 152

8.12 Energy resolution for different number of simultaneous protons as a function of the proton initial kinetic energy. 153

8.13 Reconstructed protons light yield as a function of the distance to the layer with maximum recorded light yield using the 3 mm bar configuration and two different ranges of values. The initial protons energy is uniform in the range of 40 to 240 MeV. 154

8.14 Energy resolution for single proton events with and without using calorimetric information. 155

8.15 Proton radiography of the squared phantom using 1 and 3 protons. 157

8.16 Sketch of the PRaVDA phantom used for the pCT measurements seen from above (left) and front (middle) and picture of the real phantom in the lab. 158
8.17 Slices of a proton computed tomography using single proton events showing the contrast in Relative Stopping Power (RSP) for the six inserts. 158
8.18 Projection of the RSP along the line highlighted in Figure 8.17. 159
8.19 Sketch of the U-Net input and output images. 162
8.20 Efficiency as a function of the cut in the energy range resolution for a single proton Convolutet Neural Network (CNN) analysis. 165
8.21 2D histogram of the true energy as a function of the reconstructed range for one proton events with CNN tracking. 166
8.22 Dispersion of the reconstructed energy error for different energies with the range reconstruction done using CNN. 166
8.23 Display, from left to right, energy deposited of the track used as input, the true values and the outputs of the U-Net for track ID 1 and track ID 2. . . 167
8.24 Efficiency as a function of the energy range resolution for two proton events with CNN analysis. 168
8.25 2D histogram of the true energy as a function of the reconstructed range for two proton events with CNN tracking. 168
8.26 Dispersion of the reconstructed energy error on the range between 80 to 180 MeV with multi-proton events and with range reconstruction using U-Net. 169
8.27 Mean absolute error as a function of the epoch for different batch sizes of 8, 16 173
8.28 Mean absolute error as a function of the epoch for first training with batch size equal to 16 and for the pre-trained test with batch size equal to 16 and an added extra activation layer of tanh 173
8.29 Dispersion of the relative error of the energy reconstructed by the CNN. . . 174

List of Tables

4.1 Table of the front end parameters, default and the optimised for clinical protons and their corresponding mean threshold associated. 71

5.1 Mean of the position distribution in the X and Y axis for the different intervals between $t = 0$ and $t = 20$ ms. 101

8.1 Density values of the simulated materials used for imaging. 150

8.2 Relative Stopping Power (RSP) values for seven different materials extracted from the pCT image of the spherical phantom. The labels *True* and *Reco* stand for the energy used to compute the RSP . To help to compare the values the rightmost column shows the relative difference between the columns on the left. 159

8.3 RSP values for the seven different materials of the spherical phantom reconstructed from three proton events compared withe true values and the values reconstructed from single proton events. 159

8.4 Comparison of the efficiencies between the classic algorithms and the U-Net based tracking for 1 and 2 proton events for within 1 % error in range reconstruction and protons good for imaging. 169

8.5 Comparison of the efficiencies between the classic algorithms and the U-Net based tracking for 1 and 2 proton events for within 1 % error in range reconstruction and protons good for imaging after using the DNN algorithm to reconstruct the energy of the inelastically scattered protons. 174

Chapter 1

Introduction

The aim of this chapter is to convey an introduction to the work performed for this thesis together with an outlook of its structure. The work presented here was fully performed by the author, with the exception of the first part of Chapter 8 that was performed in collaboration with Cesar Jesus-Valls working on the Tokay to Kamioka (T2K) experiment from the Institut de Física d'Altes Energies (IFAE) in Barcelona. The whole thesis revolves around the subject of particle physics technologies and data analysis techniques applied for proton imaging and clinical proton beam monitoring.

A demographic study performed by the University of Oxford in 2018 [2] stated that cancer is the second cause of death in the world after cardiovascular diseases. Among the now-rising oncology treatments, proton therapy is a technique that uses high energy protons ($\sim$ 200 MeV) instead of x-ray photons to target the tumour cells. The differences of the interactions with matter between photons and protons result in differences in the treatment plan and toxicity.

On the one hand, as seen in Figure 1.1, a photon beam deposits its energy following a distribution with its maximum close to the body's surface and then presents an exponential decay due to the attenuation of the beam. For a further explanation see Section 3.1. This results in tissue damage along the whole path of the beam before and after traversing the tumour.

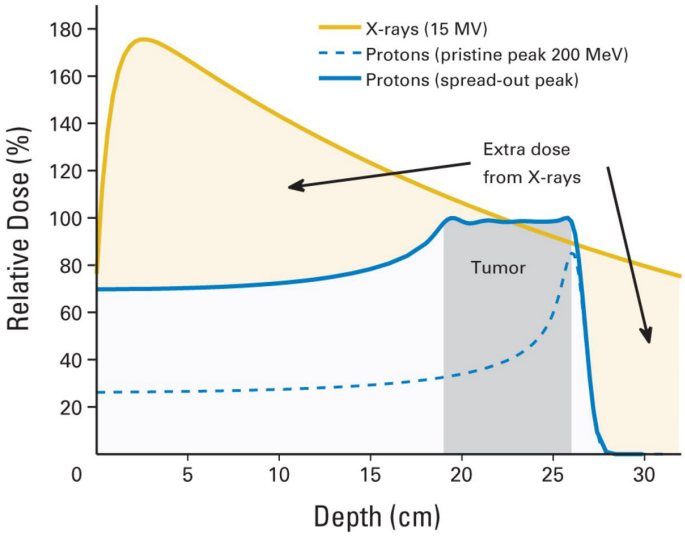

Figure 1.1: Relative dose deposition, normalised to the dose deposited at the tumour, for photons (yellow) and a pristine (dashed blue) and spread-out energy proton Bragg peak (blue) as a function of depth for the treatment of a tumour (grey shadowed). Image taken from [3].

On the other hand, as seen with the dashed blue line of Figure 1.1, the dose profile of a mono-energetic proton beam presents a low energy deposition along its path and a well-defined peak with a steep rise and fall-off before the protons' stopping point. This distribution is called the Bragg peak (BP). The stopping point is dependent on the initial energy of the proton and the Proton Stopping Power (PSP) of the materials the beam is traversing. Thus, the location of the BP can be easily modified by changing the initial energy of the proton. This allows the optimisation of the dose delivered to the tumour on a case-by-case basis implying that, with a good measurement of the PSP of the tissues encountered by the beam before the tumour, a proton-based treatment has the potential to deposit an equivalent dose to the tumor as x-ray radiotherapy, while minimizing harm to healthy tissue [4], [5].

There are currently over 89 proton therapy sites operational worldwide with 41 more planned. In the UK, there are two proton therapy centres in Manchester and London. By the end of 2021, over 170,000 patients had received proton radiotherapy worldwide and with the new facilities and treatment planning techniques, more patients will be able to

benefit from proton radiotherapy.

When treating with proton therapy, in order to obtain a treatment plan, the state-of-the-art technique is to perform a Computed Tomography (CT) scan of the target using x-rays and map the CT Hounsfield image into PSP [6].

However, this approach has associated uncertainties on the reconstructed values of PSP. These uncertainties do not go below 1.6 % for Single-Energy CT (SECT) [7], [8], and this can result in sub-optimal treatment plans; while Dual-Energy CT (DECT), a novel and improved technique, has been shown to yield better PSP uncertainties of 0.7% [7], [8]. Other comparisons between values obtained from x-ray CT scans using clinical scanner-specific Hounsfield Unit (HU) to RSP [1] calibrations and values obtained directly from pCT indicated agreements within 1 % to 2 % for most types of soft tissues, with discrepancies of up to 7 % for compact bone [9]. More importantly, shows that cavitated areas with mixed air, soft tissue, and bone contents, such as sinus cavities or tympanic bullae, revealed the highest disparities, up to 40 %.

In order to reduce these uncertainties, a direct measurement of the PSP could be obtained with the use of pCT. The use of proton CT has the potential to provide low-dose imaging with smaller margins, as shown in the images and results from [9] with a clinically relevant pCT scanner. Moreover, x-ray imaging methods result in a much higher dose compared to proton imaging (with a difference of a factor of around 50 in benefit of the pCT [9]). Thus, pCT could not only improve the accuracy of treatment planning by reducing uncertainties, but also lower the radiation dose during imaging, enable daily pre-treatment range verification, and provide convenience and repeatability conditions for treatment planning.

Proton imaging systems could also work in parallel with x-ray CT to improve the treatment plan. Recent studies from the Ludwig-Maximilians-Universität München study the possibility of combining a set of proton radiographies and a common x-ray CT scan in order to reduce the uncertainty of the conversion from HU to RSP [10]. The reduction

[1] Relative Stopping Power is defined as the Proton Stopping Power relative to water.

in systematic uncertainties, and the reduction of imaging dose could allow daily pre-treatment verifications, which are crucial to provide optimised treatments, and thus, the need for a system capable of performing a direct measurement of the PSP and with pCT or proton radiography arises.

Despite its exceptional potential, no commercial devices able to perform a pCT under clinical conditions are yet available. The requirements for a pCT system are a position tracker, able to reconstruct the proton trajectory within the body and an energy tagger, able to reconstruct the proton energy.

Figure 1.2 shows the sketch of a pCT system proposed for this thesis, equivalent to the setup proposed in Chapter 8. The setup includes four layers of silicon pixel sensors divided into two-layer tracker modules before, and after the imaged body in order to know the incident and exit direction of the protons, and a plastic scintillator bars-based range telescope to measure the residual energy of the protons after they left the body.

Thus, the key limitation when developing a pCT system that could work at a clinical facility is to deal with the high proton currents provided at the clinical beamlines. Treatment facilities use pencil beams of about a few millimeters with proton currents of the order of 10^8 protons per second. While the aim is to reduce the proton flux for imaging there are technical constraints and the knowledge of the behaviour of the beam at lower currents is limited. The work performed in [11] presents a good effort in achieving pCT images at a clinical facility with a plastic scintillator-based tracker using a reduced current of 1 to 2 million protons per second within a pencil beam with a 2D Gaussian distribution with a width corresponding to a sigma between 4 to 8 mm at the isocenter.

In May 2023, when this thesis was written, different proton CT scanners had already been built, and some even commercialised. A research prototype based on strip modules built by PRaVDA showed promising results in 2018 [12]; A Fast Experimental Scanner for Proton CT presents the technical performance on the imaging of a phantom[2] Scans [13] with their first results shown in [14]; or the commercial scanner built by ProtonVDA,

[2]In research experiments, artificially manufactured objects with materials that have tissue-like properties such as density are used. These objects are called phantoms.

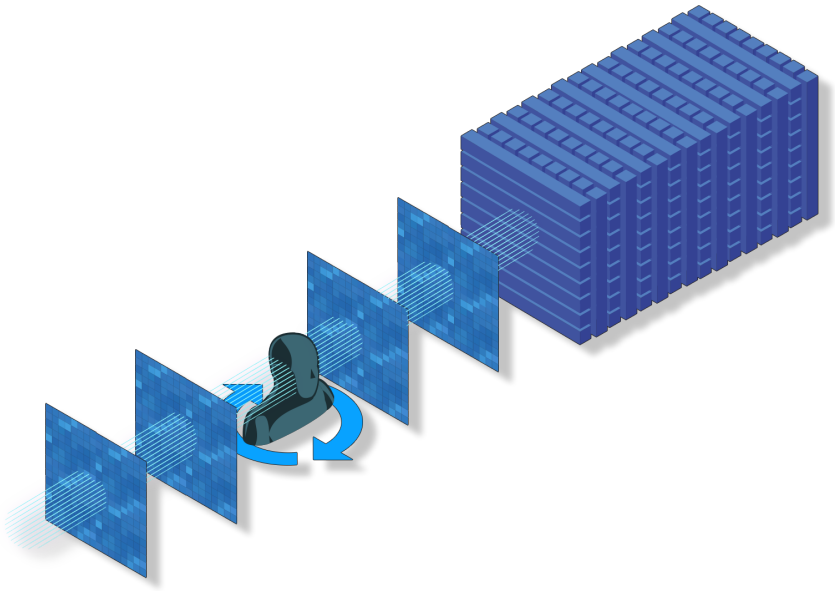

Figure 1.2: Sketch of a pCT setup with two layer trackers in front and after the imaged body and a range telescope to measure the residual energy downstream.

used as a benchmark for [9]. However, the beam conditions needed for these scanners are far from those found at clinical beams in terms of proton flux. A continuation the PRaVDA research is now under development by the OPTIma collaboration with an effort to reach clinical currents [15]. Nonetheless, a tracker based on strip modules needs many layers of sensors that contribute to the MCS, see Section 3.2, and suffers from ambiguities when more than one track is found in the same event. As shown in this thesis, the use of pixel detectors simplifies the tracking system by solving the problem of ambiguities and reducing the material budget at the same time. In addition, this thesis shows how fast-tracking pixel technologies could also be a key factor in providing feedback to the beam operators; operating the beam at lower currents on one side; and providing a better understanding of the dose distribution as a function of time of FLASH and mini-beam radiotherapies.

This thesis enhances the field by providing a proof of concept of how the new technologies and techniques used in High Energy Physics (HEP) experiments can be adapted to solve the problems that the state-of-the-art techniques suffer from for pCT. For the experimental work presented here a set of two DMAPS chips initially designed for the

inner tracker at the new High-Luminosity Large Hadron Collider (HL-LHC), the TJ-Monopix [16], were used for beam monitoring purposes, and proton tracking at the MC40 cyclotron and at the pMBRT at the Curie Institute in Paris; complemented with the simulation of a full pCT system using 10×10 cm^2 pixel sensors together with a plastic scintillator range telescope, designed as part of the work performed for the thesis.

The structure of the thesis is divided into nine different Chapters: The first is this introduction, and the second and third provide a theoretical framework with information about the state-of-the-art oncology treatments and imaging techniques first; and the particle-matter interactions, the silicon and plastic scintillator detector technologies, the Geant4 toolkit, and machine learning techniques later. The fourth is a chapter based on the characterization of the TJ-Monopix with the studies performed to understand the sensor characteristics and the modifications of the front end parameters needed in order to use the chip under clinical conditions. Fifth, the use of the TJ-Monopix for beam monitoring at the MC40 cyclotron including flux studies and a study of the opening of the cyclotron's Faraday Cup (FC). Sixth; the work done to achieve proton tracking at the MC40 cyclotron with the TJ-Monopix using two sensors and an off-line custom-built event-matching algorithm. Seventh, the analysis of a single sensor test beam at the Curie Institute and the simulation of the Curie beam line with the mini-slit collimator, to define the geometrical efficiencies and constraints for proton tracking with fluencies up to $7.5 \cdot 10^9$ p/cm^2/s. Eighth, the simulation of a full pCT system imaging two different phantoms with up to seven different materials performing two analysis; one using classic algorithms; and the study of the implementation of Deep Neural Networks. The ninth and final chapter aims to summarise all the work presented and provide a conclusion for the thesis.

Chapter 2

Radiotherapy and computed tomography

This Chapter provides a medical background in oncology focused on proton radiotherapy and proton computed tomography, offering insight and motivation for the research.

Despite the fact that there is not cure for cancer, many treatments have been developed during the last decades to treat and cure oncology patients. The principal cancer treatments are surgery, chemotherapy, and radiotherapy. None of them are exclusive and they are usually combined in order to improve the final result. A brief discussion is given below.

2.1 Main oncology treatments

In a study presented by the UK government statistics in 2020 [17] it was shown that, in England, around 66 % of the patients diagnosed with cancer between 2013 and 2016 were treated with one of these main treatments; 28 % were treated with chemotherapy, 27 % with radiotherapy and 45 % with surgery, with some cancers receiving a combination.

Surgery, the most used treatment, is a physical technique used in localised solid tumors. The aim of this treatment is to fully remove the cancerous tumor when possible. If removing it as a whole can damage organs or other body parts, the tumor can also be

debulked and the surgery could be combined with other treatment techniques.

Chemotherapy is a drug-based treatment that aims to kill fast-growing cells. The drugs, however, damage both cancerous and healthy cells resulting in a high-toxicity treatment. Nonetheless, while the treatment is usually fatal for cancer cells their healthy counterparts have a better chance of repairing themselves. Due to the aggressivity of this treatment, it is usually combined with others to reduce its toxicity. Chemotherapy is used to cure completely the patient, lessen the chance it will return, or stop or slow its growth.

Complementary, radiotherapy is a cancer treatment modality that uses ionising radiation; either electromagnetic radiation, such as x-rays, or heavy charged particles such as protons; to kill cancer cells or inhibit their growth and proliferation. This ionising radiation causes damage to the cells, causing oxidative stress by chemically modifying the DNA molecules of exposed tumour tissue. When the DNA in a cell is sufficiently damaged, it can no longer replicate and the cell dies. This process is known as cell death or apoptosis. However, radiation can also damage healthy tissue and this is why a good treatment plan is important.

There are two main divisions regarding radiotherapy. The first is based on the type of particle/radiation used resulting in proton radiotherapy or x-ray radiotherapy, and the second one is on regard to the source and position of the radiation; internal and external. Internal, also known as brachytherapy, involves the insertion of a small, short-lived radioactive source into or near the tumor, while external radiotherapy uses a machine to deliver a beam of radiation to the tumor from outside the body.

2.2 Principles of Radiotherapy

Human cells are constantly exposed to oxidative stress, with as many as 50 000 lesions of DNA modifications induced by Reactive Oxygen Species (ROS) [18]. ROS are highly reactive molecules that contain oxygen and have an unpaired electron in their outer orbital, making them highly unstable. This ROS can be generated within cells during

normal cellular metabolism or can be induced by external factors such as ionizing radiation, ultraviolet (UV) light, and various chemicals. Examples of ROS include superoxide, hydrogen peroxide, and hydroxyl radicals. While ROS play important roles in normal cellular signaling pathways, high levels of ROS can cause oxidative stress and damage to cell structures such as DNA, proteins, and lipids. Cells have a well-developed process to fix the damage caused by oxidative stress, as it is vital that the cellular responses are able to maintain genome integrity and stability to minimise the onset of potential tumorigenesis and the aging process. Antioxidant enzymes and molecules help to neutralize ROS and prevent their harmful effects.

As aforementioned, different types of radiation interact differently, and deposit energy through different mechanisms resulting in different dose deposition distributions as a function of the depth, the mechanisms of interaction with matter for photons and protons are explained in Sections 3.1 and 3.2 respectively. Figure 1.1 shows the dose deposition as a function of depth for a proton beam and x-rays. Another quantity that is commonly used in the medical environment is the Linear Energy Transfer (Linear Energy Transfer (LET), which is defined as the average of the energy transferred per unit length, *i.e.* the average of energy that is locally absorbed by the medium. Due to their interaction mechanisms, photons have a low LET while massive particles such as protons or heavy ions have a much higher LET. High LET particles result in a much higher density of interactions; the density of these interactions defines the distribution of the cell damage as shown in Figure 1.1. There are several ways in which radiation can damage DNA, including the direct transfer of energy from the radiation to the DNA molecule, the generation of free radicals that react with DNA, and the production of ROS that can damage DNA and other cellular components. The extent to which radiation damages cells and tissues depends on the type and energy of the radiation, as well as the sensitivity of the cells to radiation. Some cells and tissues, such as the skin and the lining of the digestive tract, are more sensitive to radiation than others, such as the brain and spinal cord.

A therapeutic dose of 2 Gy/(fraction of sparsely ionising radiation) induces around

3000 DNA lesions [18]. Thus, to understand how a much-reduced number of lesions can result in a significant loss of the clonogenic survival of the tumour cells, it is key to consider the distribution of the damage. Isolated lesions, such as the ones induced by ROS, including Single and Clustered damage sites, are easily fixed by the cellular response; while complex and dense lesions like Double Standard Breaks (DSB) reduce the recovery potential of the cell, leading to cell death [19]. Both damage structures are presented in the left and right diagrams in Figure 2.1.

The choice of the particles used for radiotherapy has deep implications: With low LET radiation, like photons, about 70% of the energy deposited induces isolated lesions and about 30% of the energy deposited induces clustered damage sites of varying structural and chemical complexity [20], [21]; however, massive particles, with a higher LET, interact generating clustered damage including DSB in 90% of the interactions [22]. The left and middle diagrams of Figure 2.1 show the different damage densities observed with particles with low and high LET.

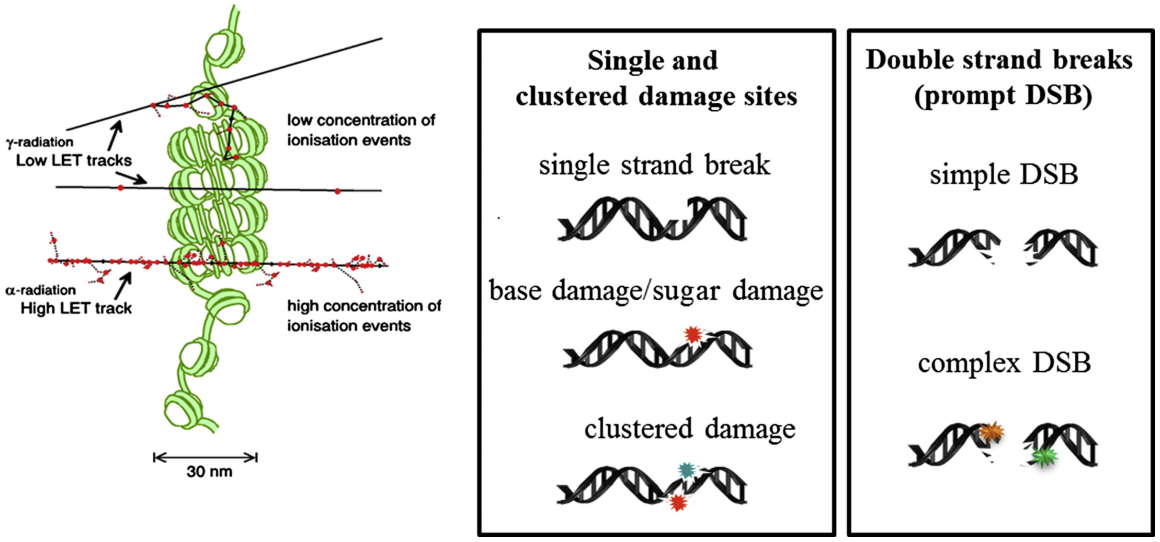

Figure 2.1: Schematic of the types of DNA damage, ranging from single and clustered damage sites through to simple and complex DSB, formed by passage of a single radiation track. Low linear energy transfer radiation induces lower concentrations of ionisation events and consequently less complex DNA damage sites than high linear energy transfer. The coloured stars represent base or sugar lesions [18].

Despite the effectiveness of radiotherapy in killing cancer cells, it can also damage

healthy cells and tissues, leading to side effects. It is important to carefully balance the benefits of radiotherapy with the potential risks and side effects, as the dose of radiation required to effectively treat the cancer may also cause significant harm to normal tissues. This is further explained in Section 2.2.4. Thus, despite the upgrades and evolution in radiotherapy techniques, protons are expected to show advantages over X-rays in a variety of tumours when they are placed close to vital organs. Thanks to the Bragg peak dose distribution and the higher LET close to the peak, protons can deliver a much higher dose rate in the tumor, and much more efficiently, while sparing the healthy tissue. Since the dose delivered into healthy tissue can result into future malignancies it is important to ensure this high ratio. Low toxicity is crucial for young patients since their cells are still under development and are more sensitive to radiation.

2.2.1 The protons' beam range

The range is a stochastic property of the proton beam rather than individual protons, it is defined as the depth at which half of the protons have stopped.

Nonetheless, in some cases, as shown in Figure 2.2 the flux is normalised to 1 after the nuclear losses and the range is expressed as the depth at which half of the protons arrive close to this endpoint instead, ignoring nuclear losses.

Figure 2.2 shows the fluence of a proton beam as a function of depth. The plot shows a close-to-linear descent in the fluence along the whole path, due to nuclear losses, but when the protons start to come to rest a steep fall, with an error function shape, is observed. This error function can be fitted and the derivative of this function results in a Gaussian from which the value of the dispersion of the beam range (σ) can be computed. The σ value is known as the range straggling, and it is the result of the differences in the protons' path within the absorber due to the stochastic nature of MCS. Most protons travel following a nearly straight line and the small deviations due to MCS account for a small increase in total length compared to the projection of the pathlength. The range straggling has been measured to be around 1.1 % of the total proton range *i.e.* a value

of 2.85 mm for a 200 MeV proton beam in a water equivalent material [23].

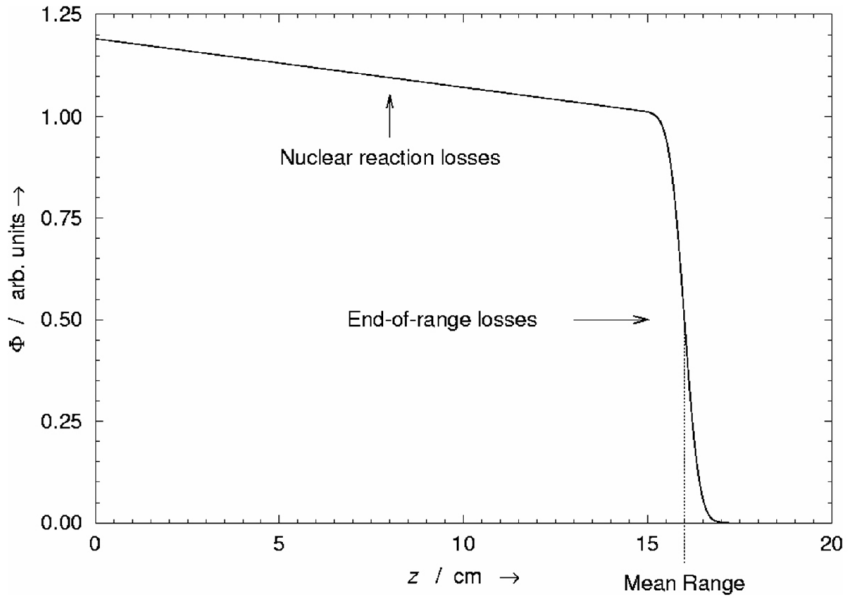

Figure 2.2: Relative fraction of the fluence ϕ in a broad beam of protons remaining as a function of depth z in water. The gradual depletion of protons from entrance to near the end of range is caused by removal of protons from nuclear reactions. The rapid falloff in the number of protons near the end of range is caused by ions running out of energy and being absorbed by the medium. The sigmoid shape of the distal falloff is caused by range straggling or by stochastic fluctuations in the energy loss of individual protons [24].

2.2.2 Stopping power and Linear Energy Transfer

The frequency of interactions with the atomic lattice is so high that the energy lost along the path could be considered continuous. The stopping power, S, of a material is defined as the total energy loss of a charged particle per unit distance traveled through the material. It is usually expressed in units of energy per unit distance MeV/cm or KeV/μm. The stopping power can be calculated using the Bethe-Bloch equation, further explained in Section 3.2:

$$S = -\left\langle \frac{dE}{dx} \right\rangle = -\frac{4\pi}{m_e c^2 n_e} \frac{Z_1^2 e^4}{\beta^2} \left[\ln \frac{2 m_e c^2 \beta^2 \gamma^2 T_{max}}{I^2} - \beta^2 - \frac{\delta}{2} \right] - K \tag{2.1}$$

Where δ is the Barkas term that, for low energy protons, can be better expressed in terms of the density effect correction as follows:

$$\delta = \frac{C}{Z} \ln\left(\frac{Z}{A}\frac{1}{\beta^2}\right) \tag{2.2}$$

where C and Z are the density and atomic number of the medium, respectively, and A is its atomic mass. Equation 2.1 takes into account all the energy lost by the beam including radiation losses. For clinical protons, most energy losses occur due to collisions. However, at higher energies, radiative losses, which are more dependent on the atomic number (Z), become increasingly significant.

In proton radiotherapy, the PSP is used to calculate the range of the protons in tissue which, as defined in 2.2.1, is the depth at which half of the protons have stopped, and can be computed as the depth at which protons have lost all their energy. Figure 2.3 plots proton stopping power as a function of proton energy in water calculated by using Equation 2.1 at high proton energies (above about 1 MeV) and other methods (not presented) at lower energies.

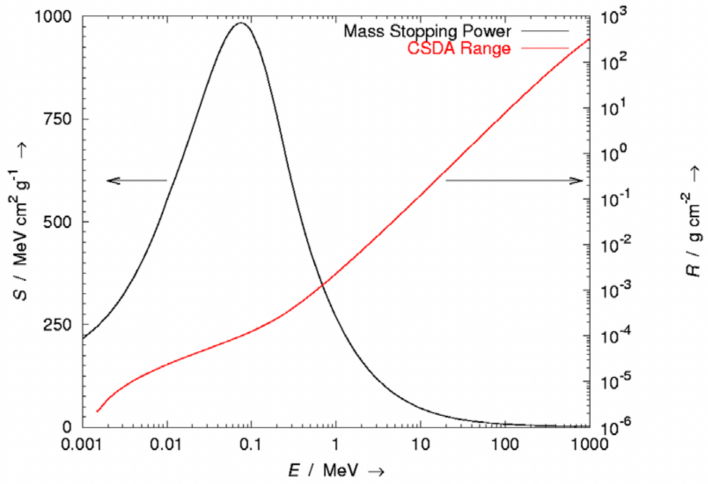

Figure 2.3: Plot of the mass stopping power S as a function of the proton energy in liquid water (black) and the corresponding range (R) calculated using S values on the assumption of CSDA (red) [25].

Another formulation independent of the mass density is the mass stopping power as the stopping power over density and that can be computed using the following approximation [25]:

$$\frac{S}{\rho} = \frac{dE}{\rho dx} \simeq -\frac{E^{1-p}}{\rho \alpha p} \tag{2.3}$$

where S is the stopping power defined in 2.1, ρ is the mass density of the material, α is a material-dependent constant, E is the energy of the proton beam, and p is a constant that takes into account the dependence of the proton's energy. The parameters α and p can be obtained by fitting ranges or stopping power from data measurements or theory [25].

The units of the mass stopping power are MeV/(g·cm^2). The value of mass stopping power does not change significantly from materials with a similar atomic composition.

The damage generated in the cells is dependent on the density of interactions that deposit energy locally and thus, at times it is convenient to express the energy loss rate or the LET instead of the PSP. LET is a measure of the amount of energy that is transferred from a charged particle to the material it is passing through per unit distance traveled. It is usually expressed in units of MeV/cm:

$$LET = \frac{dE_{abs}}{dx} \tag{2.4}$$

where E_{abs} is the energy absorbed by the material. LET is usually the term used to account for the biological effects of radiation. It is measured in units of keV/μm and is defined as the local rate of energy deposition along the particle track. It includes only the energy deposited along the track excluding radiative losses like bremsstrahlung, which are not relevant at clinical energies, and delta-rays.

2.2.3 The Bragg peak

The Bragg peak is a phenomenon that arises due to the characteristic energy loss of ionizing radiation, such as protons, or heavy ions, as they traverse through matter. This energy loss, described by Equation 3.2 and its corrections in Equation 3.4, results in a unique dose distribution for heavy charged particles, which is significantly different

from that of photons, as shown in Figure 1.1. The difference in the shape of these dose distributions is the reason for the various advantages that proton therapy offers.

The blue dashed line in Figure 1.1 shows the dose distribution as a function of depth due to the proton interaction mechanisms described in Section 3.2. The curve can be divided into two regions, before and after 25 cm depth, which have distinct dose characteristics. The region defined by a depth below 25 cm shows a low relative dose compared with photons, and the dose remains approximately constant along the proton's path until it approaches the end of its range. This is because the interactions between the proton and matter are relatively infrequent at high energies, and the energy loss is mainly due to inelastic Coulomb interactions as seen in Figure 3.3. As the proton slows down, the interactions become more frequent, leading to a fast increase in dose and the characteristic Bragg peak, well-defined by the rise of the region above 25 cm depth. There is no dose delivered beyond the peak of the dose distribution [24], at around 27 cm. As also seen in Figure 1.1, this is an important characteristic for proton radiotherapy; alternatively, x-rays continue to deliver dose beyond the peak of their dose distribution.

The Bragg peak has important implications for proton therapy. By adjusting the energy of the proton beam, the position of the Bragg peak can be precisely controlled, allowing for targeted delivery of radiation to the tumor while sparing healthy tissue. This is particularly advantageous for tumors located near critical organs or structures, where minimizing collateral damage is crucial.

Features of pristine and spread-out Bragg curves

The features of pristine and spread-out Bragg curves are fundamental to the use of charged particle radiotherapy as a treatment modality. As aforementioned, heavy charged particles deposit their energy following a Bragg peak curve resulting in a maximum deposition at the last few millimeters of their trajectory when their speed slows.

The depth of the Bragg peak depends on the initial energy (speed) of the charged particles. By adjusting the energy of the charged particles and the intensity of the beam, if

the RSP of the body is known, one can deliver prescribed doses anywhere in the patient's body with high precision. With this, proton and heavy ion radiotherapy can cover the tumor area in lateral dimensions and depth by using multiple small beams scanning the tumour with the so-called "pencil-beam scans" using only one angle, something impossible with photon beams. The biological effects of charged particle beams increase with absorbed radiation dose, and because charged particles interact with tissues differently than photons, the same amount of radiation can have a greater effect on cellular damage when delivered as charged particles. The Relative Biological Effectiveness (RBE) is the ratio of the dose required to produce a specific biological effect with Co-60 photons to the charged particle dose that is required to achieve the same biological effect. The RBE of protons is approximately 1.1, but heavier particles can have different RBE and dose distribution characteristics. For example, carbon ions have been reported to have an RBE around 3 in several tissues and experiments [26], [27].

The pristine Bragg peak is the fundamental feature of charged particle radiotherapy [28]. The precision of the location of the Bragg peak allows the tumor to be targeted with high precision, sparing healthy tissues from unnecessary radiation. The characteristics of the Bragg peak have been extensively studied using simulations and experiments [29], [30].

The spread-out Bragg peak (SOBP) is a broad and flattened distribution of energy deposition in particle therapy. It is achieved by combining multiple Bragg peaks of different energies along the path of the particle beam. The SOBP ensures a uniform dose distribution within the target volume, maximizing tumor control while minimizing damage to healthy tissues. By modulating the particle beam's energy at different depths, the SOBP delivers an effective dose to the entire tumor region. This technique improves treatment outcomes by providing a homogeneous dose distribution and allowing treatment from multiple angles.

The SOBP also plays a role in charged particle radiotherapy. The wider and shallower spread-out Bragg peak can be useful for treating tumors that are larger or irregularly

shaped. By using a broad beam of charged particles, the spread-out Bragg peak can be spread over the target volume, delivering a uniform dose to the tumor while sparing healthy tissues from unnecessary radiation. The spread-out Bragg peak has been studied in detail using simulations and experiments [31].

Ongoing research is exploring even more advanced methods to deliver charged particle beam radiotherapy, including intensity-modulated proton therapy (IMPT). IMPT uses a narrow proton beam that is "scanned" over the target volume by means of a magnetic field, while both the energy (speed) of the protons and the intensity of the beam are modulated. This allows for even more precise targeting of the tumor, sparing healthy tissues from unnecessary radiation. As of this writing, only the Paul Scherrer Institute in Switzerland has facilities that deliver IMPT [26].

In conclusion, the features of pristine and spread-out Bragg curves are fundamental to the use of charged particle radiotherapy as a treatment.

2.2.4 Therapeutic window

The goal of radiotherapy is to irradiate the tumour with a dosage that will cause it to die while sparing healthy tissue from radiation-induced morbidity. To minimize these side effects and maximize the benefits of radiotherapy, radiation oncologists aim to deliver a therapeutic dose of radiation to the cancerous tissue while minimizing exposure to the healthy tissue. This is known as the therapeutic window. Figure 2.4 shows two sigmoid curves, one for the tumour control probability (TCP) (curve A) and the other for the normal tissue complication probability (NTCP) (curve B).

The therapeutic window is the range of radiation doses that can effectively treat cancer while minimizing damage to healthy tissues. It is the balance between the desired TCP and the acceptable NTCP. The TCP is the likelihood that the radiation will control or eliminate the cancer, while the NTCP is the probability of radiation-induced side effects in normal tissues. The therapeutic window is therefore defined as the range of radiation doses that achieves a high TCP while maintaining an acceptable NTCP.

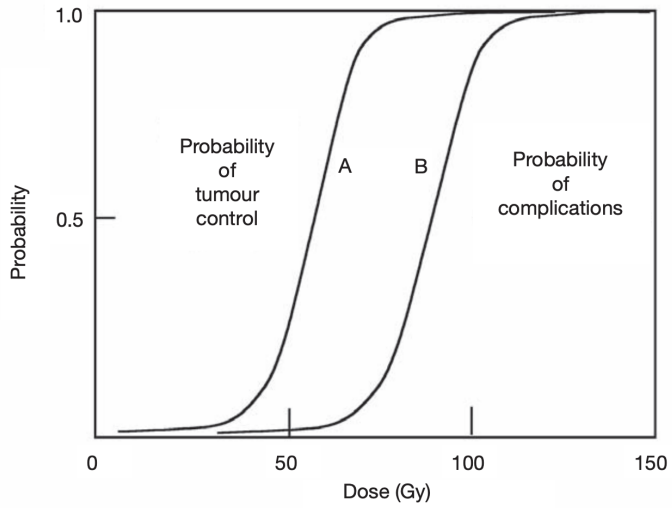

Figure 2.4: The principle of therapeutic ratio. Curve A represents the TCP, and curve B the probability of complications. The total clinical dose is usually delivered in 2 Gy fractions [32].

The therapeutic window is dependent on various factors, including the type of cancer, the location of the tumor, the patient's overall health, and the treatment method. For example, some cancers are more sensitive to radiation than others, and tumors near critical organs may have a smaller therapeutic window due to the potential to damage those organs. Additionally, patients with pre-existing medical conditions may have a lower tolerance for radiation, making it necessary to adjust the therapeutic window accordingly. Moreover, new techniques such as pMBRT and FLASH radiotherapy (both described below) have been shown to increase the therapeutic window of the treatment.

Recent preclinical studies using FLASH radiotherapy have shown promising results. A study conducted by the Sloan Kettering Cancer Center in New York demonstrated that FLASH radiotherapy can reduce the side effects of radiation therapy in mice by up to 50%. Another study conducted by the University of California, San Francisco, showed that FLASH radiotherapy can significantly reduce radiation-induced lung damage in mice.

Moreover, preclinical studies using pMBRT have shown that it can significantly reduce the damage to healthy tissue while maintaining the efficacy of radiation therapy. A study conducted by the Paul Scherrer Institute in Switzerland showed that pMBRT can reduce

damage to the spinal cord by a factor of 10 compared to conventional proton therapy.

Both FLASH radiotherapy and proton mini-beam radiotherapy have shown great promise in increasing the therapeutic window of radiation therapy. These techniques have the potential to reduce the damage to healthy tissue while maintaining or even improving the efficacy of radiation therapy. However, further preclinical and clinical studies are needed to confirm the safety and efficacy of these techniques in humans. If these studies are successful, these techniques could revolutionize the field of radiation therapy and provide a new standard of care for cancer patients.

To determine the optimal therapeutic window for a patient, radiation oncologists use a variety of tools and techniques. One such tool is treatment planning software, which allows oncologists to create a personalized treatment plan based on the patient's specific needs. Treatment planning software takes into account the location and size of the tumor, as well as the surrounding healthy tissues, to calculate the optimal radiation dose and delivery method.

Another technique used to determine the therapeutic window is dose-response modeling. This technique involves analyzing the relationship between radiation dose and the probability of tumor control and normal tissue complications. By using mathematical models to predict the outcomes of different radiation doses, oncologists can estimate the therapeutic window for a given patient and adjust the treatment plan accordingly.

2.2.5 Proton Mini-Beam radiotherapy

Proton Mini-Beam Radiotherapy is a technique proposed to overcome the limitations of conventional radiotherapy on delivering a curative radiative dose resulting in critical dose deposition on healthy tissues by using the angular straggle of the beam. pMBRT is a dose delivery method based on the spatial segmentation of the incident beam using slits with a width ranging between 400 to 700 μm. The method aims to use the well-known effect of the MCS, see Section 3.2.2, that broadens the beam as it travels through the body in order to merge initially separated beams resulting in a quasi-homogeneous dose

distribution within the volume of the tumour while a peak and valleys dose distribution is observed along the healthy tissue precedent to the tumour. The ratio between peak and valley doses is called Peak-to-Valley Ratio (PVDR) and plays a key role in biological response. Figure 2.5 shows dose distribution for a standard pencil beam with a 1 cm Full Width at Half Maximum (FWHM) (left) and a pMBRT with slits with a FWHM below 1 mm and separated from between 1 and 4 mm (right).

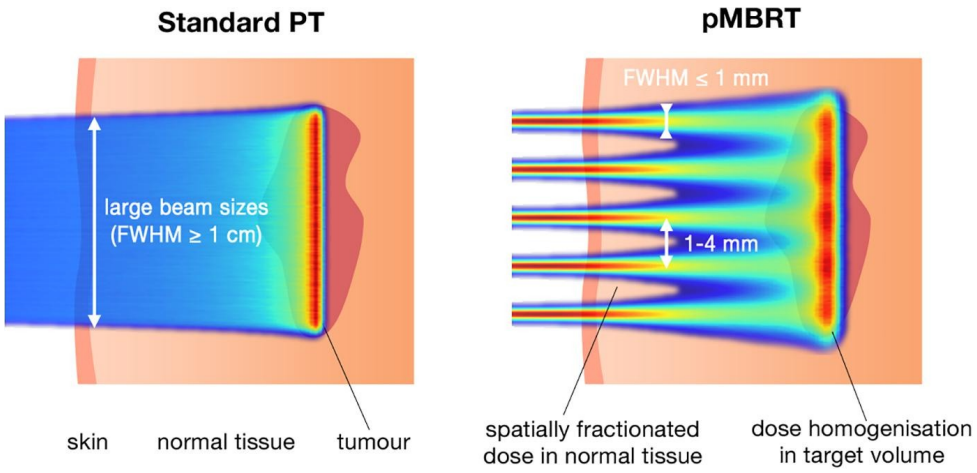

Figure 2.5: Sketch of the dose deposition of a standard proton beam (right) and a pMBRT beam [33].

Tissue repair is associated with repopulation and migrating healthy, proliferating cells from low dosed areas to the heavily irradiated ones. Hence, the high dose regions will recover although the cells that were originally present in the high dose region will not proliferate anymore with high probability. Characteristic migration lengths limit the size of damaged skin areas that are efficiently repaired. It has been observed that healthy cells from low dose areas migrate to the heavily irradiated ones leading to recovery in the tissue [34], [35].

The technique has been shown to have promising results on radioresistant tumours by reducing the side effects and providing more tumour control while experimenting on rats compared to common proton radiotherapy. The clinical potential of this technique has already been studied in [36]. When treating tumours near organs at risk and non-cancer diseases like epilepsy, the assessment of the penumbras demonstrates a definite advantage

over conventional radiosurgery. Some of the current implementations of pMBRT use mechanical collimators which result in a decrease in efficiency and the production of secondary neutrons that increase the toxicity of the treatment. However, an effort has been made to produce the mini-beam using techniques that modify the magnetic structure of the beam, leading to a reduction of the neutron yield maintaining a competitive PVDR [37] when compared with traditional techniques.

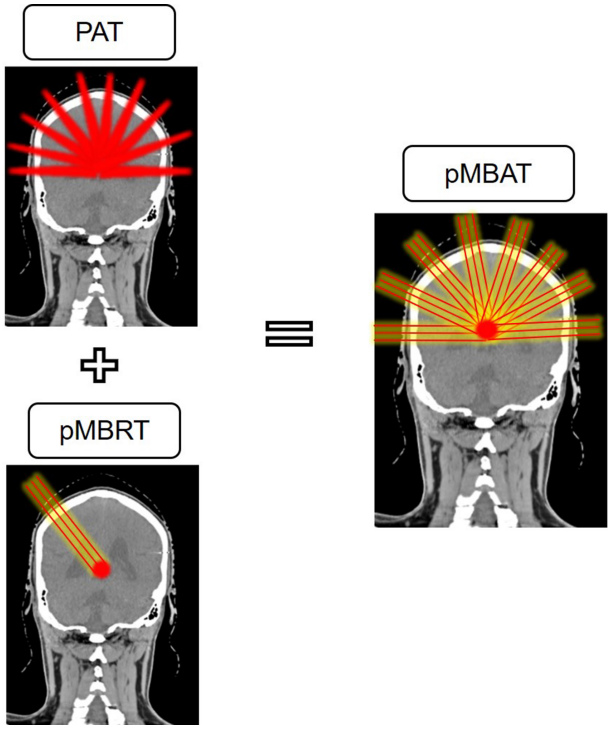

Figure 2.6: Sketch defining the combination of Proton Arch Therapy (top left), proton Mini Beam Radiotherapy (bottom left) leading to proton Mini Beam Arch Therapy [38].

The combination of pMBRT and Arch Therapy, See Figure 2.6 is a recent technique known as proton Mini Beam Arch Therapy (pMBAT). Using this technique, a quasi-homogeneous dose distribution is achieved in the tumor with a PVDR ranging from 1.06 ± 0.05 to 1.27 ± 0.06 [38]. PVDRs were computed as the ratio between peak and valley doses at the center of the lateral profiles.

2.2.6 FLASH radiotherapy

FLASH radiotherapy is a novel approach that has been shown to improve the therapeutic window of radiotherapy with both proton and x-ray beams. The main principle behind FLASH radiotherapy is the delivery of a high dose of radiation at an ultra-high dose rate, typically greater than 40 Gy/s, which is several orders of magnitude higher than conventional radiotherapy. This ultra-high dose rate has been shown to significantly reduce the toxicity of radiotherapy while maintaining its efficacy.

Proton FLASH radiotherapy has been extensively studied in preclinical models, and the results have been promising. In a study published in the International Journal of Radiation Oncology, Biology, and Physics, researchers investigated the effect of proton FLASH radiotherapy on tumor growth and normal tissue toxicity in mice. The study found that proton FLASH radiotherapy significantly reduced the toxicity of radiation in the lungs and the heart, two critical organs that are commonly affected by radiation therapy. Moreover, proton FLASH radiotherapy was found to be more effective in controlling tumor growth compared to conventional radiotherapy. These findings suggest that proton FLASH radiotherapy has the potential to significantly improve the therapeutic window of radiotherapy [39].

Similarly, x-ray FLASH radiotherapy has also shown promising results in preclinical studies. A study published in the journal Cancer Research investigated the effect of x-ray FLASH radiotherapy on normal tissue toxicity in mice. The study found that x-ray FLASH radiotherapy significantly reduced the toxicity of radiation in the skin and the gut, two organs that are commonly affected by radiation therapy. Moreover, x-ray FLASH radiotherapy was found to be more effective in controlling tumor growth compared to conventional radiotherapy [40]. These findings suggest that x-ray FLASH radiotherapy has the potential to significantly improve the therapeutic window of radiotherapy.

Despite the promising results of FLASH radiotherapy, there are still several challenges that need to be addressed before it can be widely adopted in clinical practice. One of the main challenges is the development of suitable flash delivery systems. The current

flash delivery systems are large, expensive, and require significant technical expertise to operate. Moreover, the safety of ultra-high dose rate radiation delivery needs to be carefully evaluated to ensure that it does not cause any long-term side effects.

2.3 Proton Computed Tomography

Computed Tomography is an imaging technique that uses the computational treatment of 2D images, obtained from different angles, to obtain a 3D cross-sectional image with voxelized information. Proton CT and x-ray CT differ not only in the measured values *i.e.* RSP for protons and HU for x-rays, but also in the image acquisition techniques.

X-rays travel on a straight line and the individual photons are absorbed, or not, according to the probability given by the cross-section of the interaction. When imaging with x-rays, the energies used are around tenths of keV in order to ensure that the photoelectric effect is the main interacting mode, see Section 3.1. The probability of an X-ray photon being absorbed or scattered is proportional to the number of atoms it encounters, and the number of atoms increases approximately exponentially with increasing depth into the material due to, among other factors the growth of the beam footprint. Thus, the probability of being absorbed depends on the electronic density (z) of the material and the transversed length.

When imaging with x-rays, a pixel sensor[1] placed after the imaged body and capable of counting the integrated number of photons over the scanning time is enough to obtain a radiography and combining different angular projections, as seen in Figure 2.7, a full CT scan.

In contrast, in order to obtain a pCT image, the proton path within the body and the energy lost along the path need to be measured. In proton and ion CT, the charged particles interact with the atomic nuclei of the imaged object, the interactions result in the loss of energy and deflection of the particles. The amount of energy loss and deflection

[1]Pixel sensors are explained in Section 3.3.3

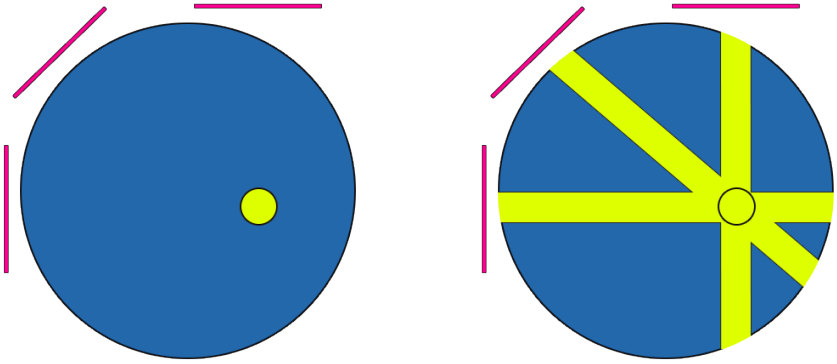

Figure 2.7: Sketch of the back-projection method using three different projections of a body with a circle of a different density.

depends on the energy of the proton and the PSP of the material. Thus, with a pCT a 3D scan of the PSP can be measured. However, due to MCS, and as seen in Figure 2.8, protons do not travel following a straight line and more complex methods need to be applied to reconstruct the proton's track.

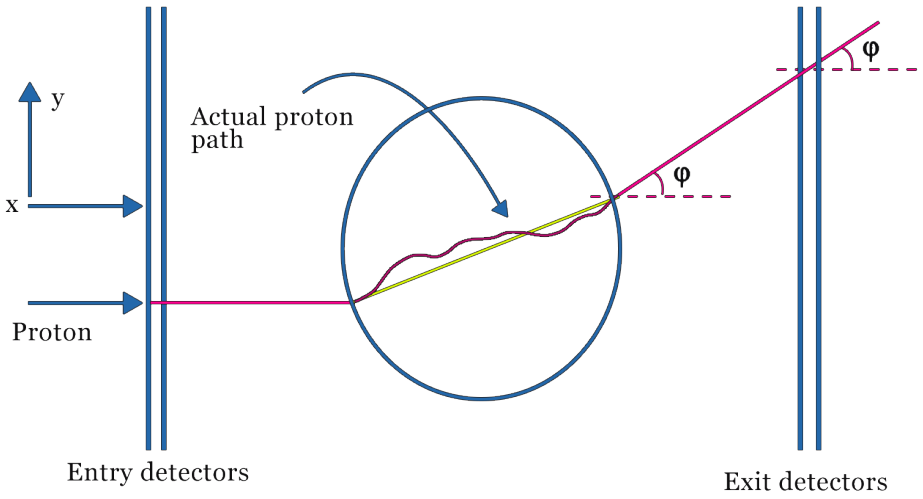

Figure 2.8: Sketch of the proton path within a body.

The proton position is usually measured with front and back tracker modules, frequently based on two modules of silicon detectors each as seen in Figure 1.2. Since protons follow a nonperfect straight-line path, using the projection of the entering and outgoing points and angles, also depicted in 2.8, their Most Likely Path (MLP) has to

be computed with statistical methods; examples of it would be the cubic spline fitted path [41], or a Bayesian maximum likelihood approach [42]. This computation gives rise to statistical uncertainties in the spatial resolution of the image. Due to this intrinsic limitation, other techniques use a single tracking module behind the phantom or imaging body, measuring only the exiting direction of the proton and assuming a parallel beam coming out of the collimator. Alternatively, an interesting study presenting the performances of other imaging methods based on the Richardson-Lucy algorithm is presented in [43]. The energy of the protons can then be measured with different devices including a Range Telescope (as later suggested in this thesis), a calorimeter [44], or a Time of Flight (ToF) detector [45]. Later, the proton's path and energy loss through the body are matched in an offline analysis.

To obtain the 3D image, the incident angle is rotated 360 degrees, either moving the imaged body or rotating the proton beam as in gantry mountings. The reconstruction of all tracks and their associated energy loss through all angles generates the 3D map of the proton stopping power of each voxel.

2.3.1 State-of-the-art systems

This section aims to provide an overview of the state-of-the-art pCT systems presenting their performances and limitations together with a brief discussion on what the system proposed here further the field.

Phase II prototype scanner

The phase II prototype scanner is a pCT system designed at Baylor University, Loma Linda University, and the University of California at Santa Cruz [13]. Figure 2.9 shows an image of the Phase II prototype scanner with a pediatric head phantom.

The tracker is based on four silicon-strip tracking-detector modules, two before and two after the imaging body; and an energy tagging system composed of five plastic scintillator stages. The system also includes a rotation stage for the phantom and a custom data

acquisition system.

The tracking system was capable of reconstructing tracks with a resolution of 66 μm and the performance of the energy tagging system was tested with 200 MeV protons and the resolution of the energy measurement was estimated to be of 1 %.

The limitation of this system is the five-stage calorimeter. The stages have no lateral segmentation and thus are limited to measuring one proton per readout frame, rejecting all multi-proton events. This limits the practical event rate to no more than 1 MHz and due to the nature of the proton bunches at the cyclotrons, results in a reduction of the efficiency that implies a higher dose to the patient. The finer segmentation of the strip trackers allows applying vetos for multi-proton events when more than one track is reconstructed in the trackers and there is an abnormal excess of energy deposited in the scintillator.

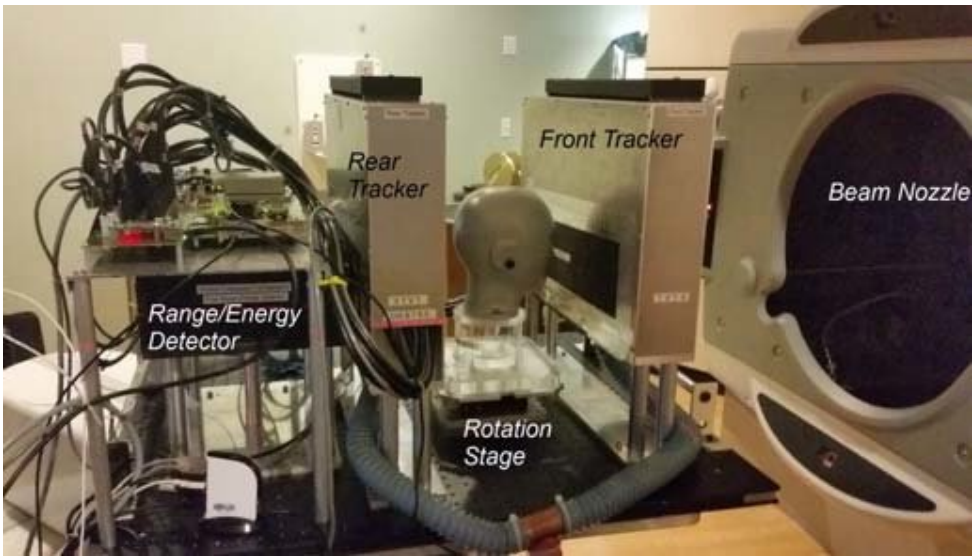

Figure 2.9: Image of the phase II prototype scanner located in a fixed-beam treatment room of the Northwestern Medicine Chicago Proton Center, with a pediatric head phantom (model 715-HN from CIRS Inc., Norfolk, VA) mounted on the rotation stage [46].

ProtonVDA

ProtonVDA LLC (Naperville, IL, USA) built a radiography system prototype based on a set of X-Y plastic scintillator fiber-based tracker planes before and after the imaging

object [47]. A sketch of the system with a human head phantom in place can be seen in Figure 2.10.

Each tracker consists of two layers of 1 mm^2 scintillating fibers with an offset of half of the fiber each. The fibers are paired, and 12 bunches of 32 fiber pairs laid side-by-side create an X or Y tracker plane creating a 38.4×38.4 cm^2 sensitive area.

The energy tagger consists of a compact 13 cm thick scintillator block with a 40×40 cm^2 cross-section and a 4×4 grid of 76 mm diameter vacuum PMTs tubes. Resulting in a sensitive thickness of 10 cm. The grid of PMTs is located at the back of the scintillator block, opposite the beam nozzle, and it is aimed to collect the scintillating photons coming from the energy deposited by the transversing protons. The amount of light collected by the PMTs is dependent on the position and thus a calibration needed to be performed using the position information coming from the trackers.

The system measured was calibrated and able to measure, using a 128 MeV proton beam a Water Equivalent Path Lenght (WEPL) for individual protons of 6.12 cm with a resolution of 0.26 cm and a Water Equivalent Thickness (WET) of 6.13 cm of 0.02 cm. The system is designed to operate at a proton rate of 10 MHz meaning that with a 20×20 cm^2 field size, 100 protons per 1 mm^2 pixel can be delivered in < 1 s.

Pravda

The PRaVDA collaboration presented a pCT system based on four modules of silicon-strip trackers and a silicon-strip detector-based range telescope [12].

PRaVDA, using silicon-strip detectors with a sensitive area of 93×96 mm^2 and a strip pitch of 90.8 μm, meant to go a bit further than the work from Phase II adding a third strip layer on each module. The strips are placed in three directions $x - u - v$ with a 60-degree rotation angle from one layer to another. This effort aims to reduce the ambiguities caused by multi-proton events and improve tracking performance and efficiency at high currents.

The energy tagger is based on 21 layers of silico-strip detectors with 2-mm thick

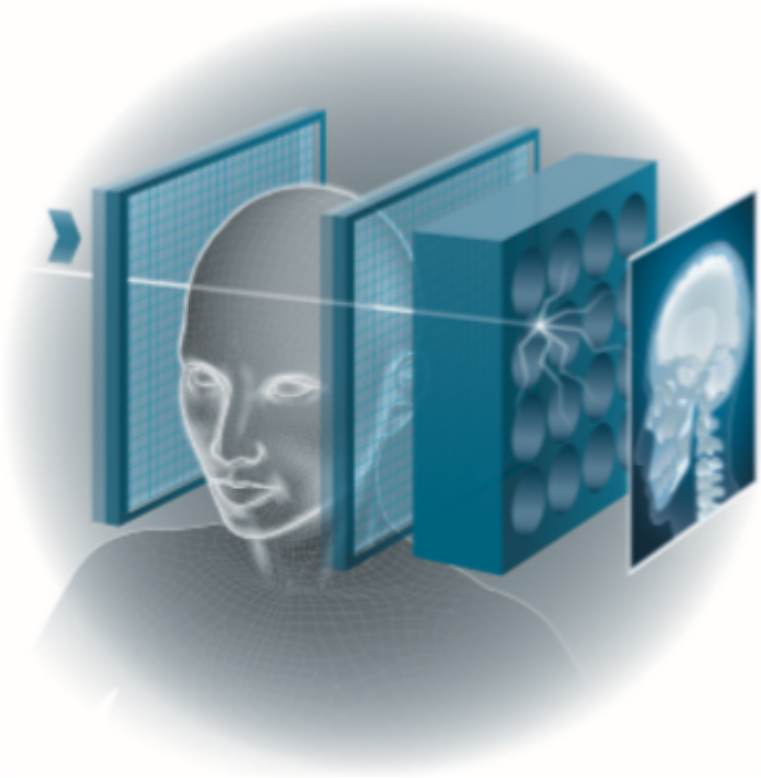

Figure 2.10: Sketch of the ProtonVDA system depicting the tracking planes with a human head between planes and the PMT based calorimeter.

PMMA absorbers resulting in a 55.4 mm of WEPL. The range telescope was designed to measure energies proton energies between 30 and 80 MeV being the expected after trespassing their 75 mm thick PMMA imaged phantom.

The system, exposed in Figure 2.11, used a 125 MeV beam with an 85 mm diameter and was able to perform a fast pCT with $2{\cdot}10^8$ protons/s with an RSP resolution below 1.6 % for several tissue-like materials.

A continuation of the PRaVDA collaboration followed up this work and added yet an extra layer on the tracker system improving the tracking performance at high proton fluxes.

The limitation of this system is the performance for higher fluxes with smaller areas that are common on the clinical pencil beams. Despite the effort to get rid of the ambiguities generated by the multi-proton events, the Si-strip tracker results are dependent on the area of the beam.

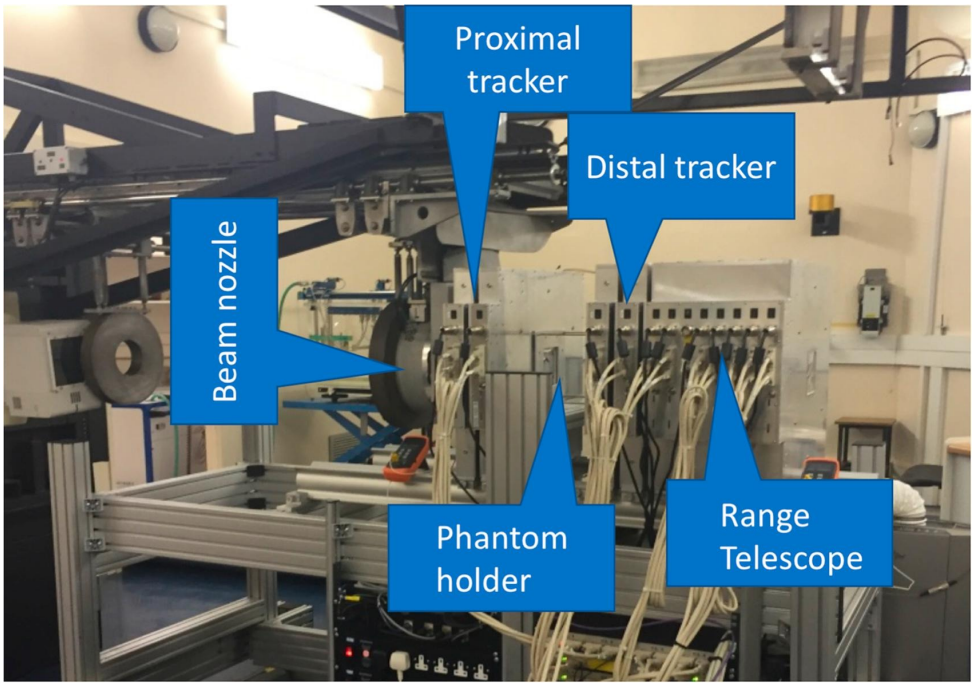

Figure 2.11: The PRaVDA pCT system showing upstream and downstream trackers, phantom holder, RT and beam nozzle at the iThemba LABS proton facility, South Africa [12].

The Bergen pCT System

The Bergen pCT system [48] is a state-of-the-art compact tracker and calorimeter based on the ALPIDE chip [49].

The prototype consists of 2 tracker layers and 41 calorimeter layers. A sketch of the calorimeter can be seen in Figure 2.12. Each layer contains 108 ALPIDE chip sensors, with a high granularity of 1024×512 pixels. The ALPIDE chip is capable of amplifying, discriminating, and shaping the incoming signal. Nine ALPIDE sensor chips are bonded to a flex cable known as a string, and three strings together form a slab. A complete layer is created by combining two half layers with alternating chip positioning.

For the calorimeter layers, 100 μm thick ALPIDE chips are mounted with 3.5 mm aluminum plates as absorber material between the layers. To minimize non-sensor material in the tracking layers, 50 μm thick ALPIDE chips are mounted on $\simeq$ 300μm thick carbon-epoxy sandwich sheets.

The final prototype of the Bergen pCT system will have a size of 27 × 16.6 cm^2,

sufficient to image a human head without any need of moving stages. The system's high granularity allows for the simultaneous tracking of multiple particles, making it well-suited for precise particle trajectory reconstruction and calorimetric measurements. The integration of ALPIDE chip sensors and custom readout electronics enhances the system's data acquisition and processing capabilities.

The main limitation of this system is the readout frequency of the ALPDE chip which has a maximum readout frequency of 100 KHz. This implies that at clinical fluxes one may find thousands of protons on the same frame within the small area of the pencil beam (2D Gaussian of $\sigma = 10$ mm) which complicates the tracking within the calorimeter.

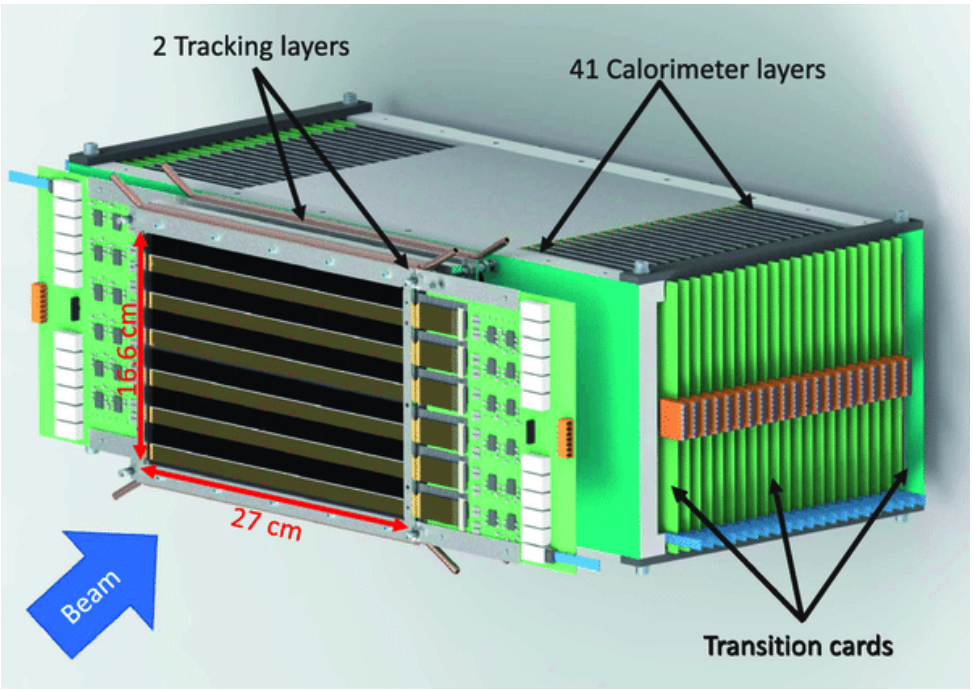

Figure 2.12: Schematic drawing of the Bergen pCT calorimeter [48].

Discussion

The system proposed in this thesis would imply a step forward by using a DMAPS-based tracker, thanks to its much simpler and more efficient tracking reconstruction at higher proton rates than the previously mentioned systems with a much smaller material budget. The TJ-Monopix, with non-dedicated readout electronics, is capable of coping with fluxes

up to 3.7×10^7 p/cm^2/s, see Section 7. Despite being about a factor of magnitude smaller than clinical currents, an upgrade including dedicated readout electronics, could allow to increase the maximum flux. Moreover, the ASTRA range telescope aims to improve the capabilities of multi-proton reconstruction at high proton rates of 100 MHz without compromising the energy reconstruction or the RSP measurements.

With all this, and acknowledging that clinical currents could be lowered for imaging purposes, the system proposed shows evidence of its capability to perform with currents of up to 10^7 p/cm^2/s with room for improvement with a dedicated DMAPS tracker.

Chapter 3

Particle Physics Techniques

This chapter covers topics such as the interactions between protons and photons, typically X-rays, with matter stating the most relevant differences; key concepts related to silicon and plastic scintillator detectors; an overview of the tools employed, including the Geant4 simulation package and machine learning, and imaging algorithms.

3.1 Electromagnetic radiation and matter interaction

Different types of radiation result in different interactions with matter. In the work performed for this thesis three types of radiation were observed. X-ray photons are widely used for medical applications from imaging purposes to treatment in radiotherapy. For this work x-rays obtained from an ^{55}Fe source, see Section 4.1), where an ^{55}Fe source is used in the lab experiments for the characterization of the TJ-Monopix; protons are the main particle of interest in the thesis, they have been used for the measurements at the MC40 cyclotron in Birmingham and at the pMBRT line at the Curie institute; and secondary electrons generated by the interaction of protons with the air and the surface of the chip or collimators are one of the main sources of noise in both the simulations and the test beams.

3.1.1 Photons interactions

Photons travel through matter without interacting until they ionize an atom when hitting, and/or being absorbed by, an electron. The probability of interaction grows exponentially with the transversed depth and thus a full photon beam would experience an exponential attenuation of its intensity. Photons interact with matter through the following three mechanisms presented in Figure 3.1.

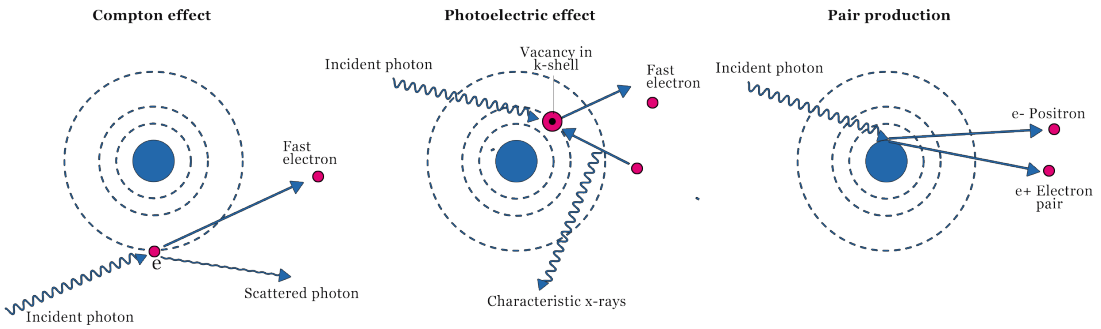

Figure 3.1: Sketch of the three main photon interactions; Compton scattering (left), photoelectric effect (middle), and pair production (right).

Compton scattering describes the interaction between an external shell electron, weakly bound to the atom, see the left sketch in Figure 3.1. The electron can be considered free within the context. The result of Compton scattering is a lower energy photon and a recoiled electron. This interaction rate depends linearly on Z. This results in a free electron with an energy and direction dependent on the energy of the photon and the amount of energy transferred, and a positively charged ion.

The photoelectric effect is the interaction between an inner electron strongly bound to the atom and a photon, typically x-ray, that has an energy close (always equal or slightly above) the bounding energy. The effect of this phenomenon can be seen in Figure 3.2; one can see that there is a sawtooth-like peak at 10^{-2} MeV that correlates to an electron's bonding energy. Any deviation would result in less cross-section until the photon energy reaches the energy of the next layer. As seen in 3.1 (middle) the photon is absorbed and thus it results in an immediate dose. Regarding the material transversed, the rate of this interaction depends on the atomic number as Z^{4-5}. The cross-section of the interaction

is also dependent on energy as $\frac{1}{E^3}$ as seen in Figure 3.2. This results in a free electron with the energy of the photon minus the binding energy and the positive ion, *i.e.*

$$E_e = E_\gamma - E_B \tag{3.1}$$

where E_e is the energy of the free electron, E_γ is the x-ray energy, and E_B is the binding energy of the electron.

In order for the pair production process to occur the photon has to be energetic enough to interact with the strong electromagnetic field generated by the atomic nucleus. As observed in 3.1 (right), through this interaction, an electron-positron pair is generated, and thus the energy of the photon has to be above 1.022 MeV ($2\ m_e c^2$). The positron will generate a photon through annihilation. In this case there is no ionisation and thus the result is an electron, a positron, and an unchanged atom.

The plot in Figure 3.2 shows the X-ray beam linear attenuation coefficient as a function of the energy of the photons. The different contributions to the total attenuation are shown separately: photoelectric effect (red), Compton scattering (green), and pair production due to the nuclear field (cian) and electronic field (purple). It can be seen how the photoelectric absorption falls for lower energies and the pick observed close to 10^{-2} MeV indicates the exact value of the bonding energy of a shell electron. It can also be seen how Compton scattering has a maximum at between 10^{-2} and 10^{-1} MeV and then falls smoothly. Last, it can be seen that the pair production due to the nuclear field is an order of magnitude higher than the one due to the electrons field and both reach a Plateau around 100 MeV.

The different contributions in attenuation at different energies are used in medical applications to optimise the treatment. The imaging and treatment plan is done with lower energy x-rays ($\sim$ 100 keV), as seen in Figure 3.2 these are more sensitive to photoelectric absorption and thus more dependent on the electonic density (Z^{4-5}). However, the treatment is performed with higher energy x-rays ($>$ 10 MeV), to ensure that the

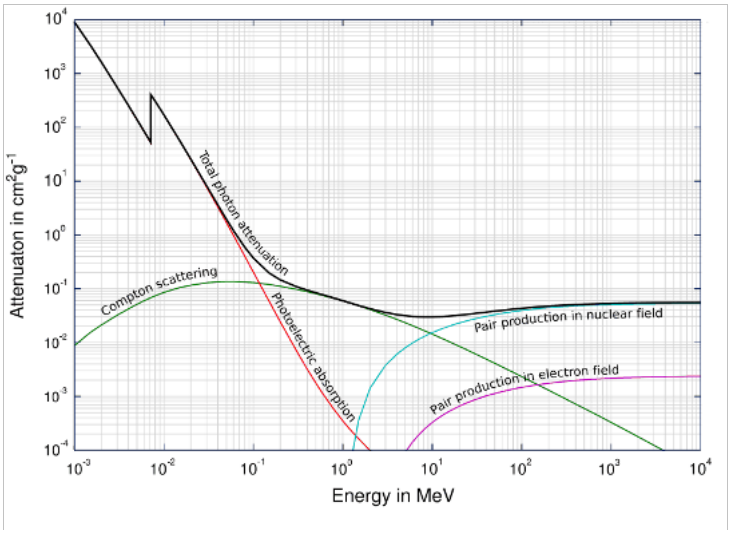

Figure 3.2: Plot of the mass attenuation coefficient of iron for an X-ray beam as a function of energy decoupling the different contributions from, photoelectric effect (red), Compton scattering (green), and pair production due to the nuclear field (cian) and electronic field (purple).[50]

dominant interaction is the pair production, which is less dependent in Z and can ensure a more homogeneous dose. In this thesis, the x-rays used were provided by a ^{55}Fe source with two peaks at 5.6 and 5.9 keV.

3.2 Particle-matter interaction

Protons have been used in the first measurements at Birmingham's MC40 cyclotron with the chip and in the simulations, and secondary electrons generated by the interaction of protons with the air and the surface of the chip or collimators are one of the main sources of noise in both the simulations and the test beams.

Heavy charged particles ($m \gg m_e$) traversing a material lose energy in electromagnetic interactions with the atomic lattice. For particles traveling with a speed $v = \beta c$ the energy loss E occurs in differential single collisions [51]. Typically, Coulomb scattering with atomic electrons is the dominant interaction due to the difference in mass and size between the atomic nuclei and the electronic cloud. Coulomb scattering results in ionisation or atomic or collective excitation.

The mean rate of energy loss for a moderately relativistic charged heavy particle in this regime is given by the *Bethe* equation 3.2. This function is a mathematical expression used to describe the energy loss of charged particles as they pass through matter at intermediate energies. The mass stopping power is defined as the energy loss per unit of the path's length and mass of the absorbing material. The function takes into account various factors such as the density and atomic number of the material, the energy and velocity of the particle, and the particle's mass and charge. Hence, the mean rate of energy loss for a moderately relativistic charged heavy particle in this regime is given by:

$$-\left\langle \frac{dE}{dx} \right\rangle = 4\pi N_A r_e^2 m_e c^2 z^2 \frac{Z}{A} \frac{1}{\beta^2} \left[\frac{1}{2} ln \frac{2m_e c^2 \beta^2 \gamma^2 T_{max}}{I^2} - \beta^2 \right] \tag{3.2}$$

where N_A is the Avogadro's number,Z is the atomic number of the absorber, A is the atomic mass of the absorber, I is the mean excitation potential of the material, $\gamma = \frac{1}{\sqrt{1-\beta^2}}$ is the Lorenz factor, $\delta(\beta\gamma)$ a density effect correction and again, T_{max} is the maximum energy transfer for single interaction defined here as:

$$T_{max} = \frac{2m_e c^2 \beta^2 \gamma^2}{1 + 2\gamma m_e/M + (m_e/M)^2} \tag{3.3}$$

A small correction taking into account the periodicity of the atomic lattice, which can cause the energy loss of the particle to deviate from the Bethe formula can be added to the brackets in Equation 3.2. The Bloch correction arises from the fact that the motion of a charged particle in a crystal lattice can be treated as a series of scattering events, where the particle is scattered by individual atoms in the lattice. The correction accounts for the modifications due to the periodic potential of the medium and can be approximated as a series of scattering centers. Each scattering event can cause a change in the energy and direction of the particle, leading to a modification of its energy loss in the medium. A term $f(\beta\gamma)$, the Bloch correction term, is added to the Bethe equation in order to obtain the Bethe-Bloch equation.

At energies around 100 MeV, the most significant correction to the Bethe equation

is the Bloch correction, or density correction term, δ. The density correction takes into account the fact that the electrons in the material are not uniformly distributed, but rather are more tightly packed together near the nuclei. This results in a higher Coulomb interaction between the incident particle and the electrons, leading to a higher energy loss. The density correction can be expressed as:

$$\delta(\beta\gamma) \simeq K \cdot \ln\left(\frac{2m_e c^2 \beta^2 \gamma^2}{I}\right) \tag{3.4}$$

The Bloch correction is applied to the Bethe equation to account for the average effect of multiple scattering on the energy loss of charged particles. It modifies the energy loss calculation by including an additional term that takes into account the scattering angle and the scattering power of the material. The correction factor accounts for the increased energy loss due to the random angular deviations caused by multiple scattering.

The radiative correction used for the last section of Figure 3.3, accounts for the fact that the incident particle may emit bremsstrahlung radiation as it interacts with the electrons in the material. However, it is not relevant at clinical energies since it becomes relevant above $\beta\gamma > 1000$.

The combination of all corrections has been used for the plot in Figure 3.3, the resulting equation is known as the *Bethe-Bloch* formula.

Figure 3.3 presents a minimum stopping power value between $\beta\gamma = 1$ and $\beta\gamma = 10$ labeled in red with Minimum ionization. Particles with this value of $\beta\gamma$ are known as Minimum Ionising Particles (MIP).

3.2.1 Main proton interactions

This section gives a deeper, insight on proton interactions framing them within the scope of clinical energies. Protons ionize and excite the atoms in the atomic lattice along their path mostly via Coulomb interactions. Due to their high mass, this scattering through the lattice results only in small deflections for the individual protons. The mean free path

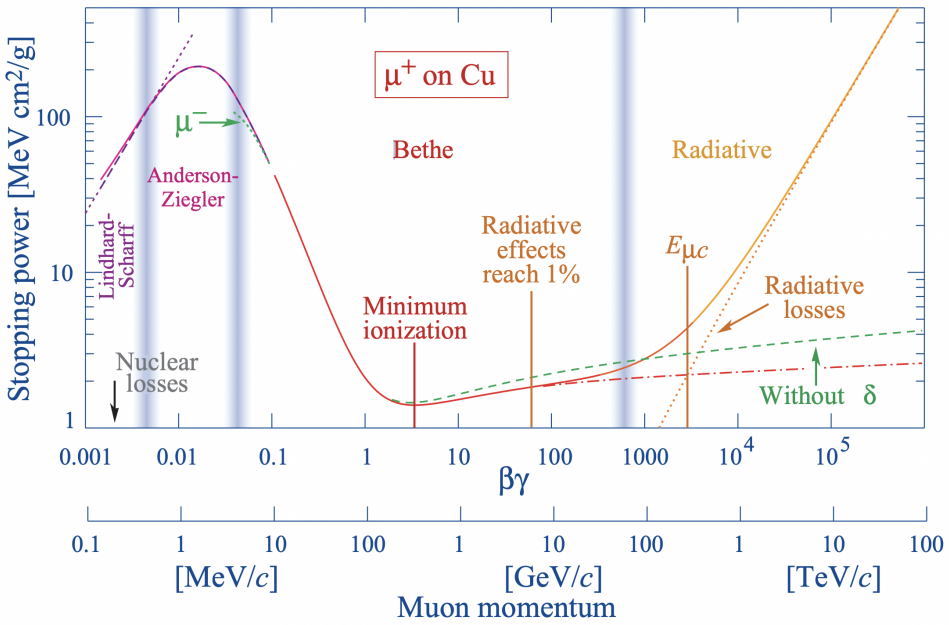

Figure 3.3: Stopping power for positive muons in copper as a function of $\beta\gamma$ from 10^{-3} to 10^{6}. The vertical lines show the different ranges for different equations. The middle range, with $\beta\gamma$ from 0.1 to 1000 show the Bethe-Bloch regime. Figure obtained from [52]

of a proton is energy dependent, the lower the energy the shorter the mean free path, and this results in a high number of interactions and a high peak of energy loss right before their stopping point. Clinical protons have a $\beta\gamma$ up to 0.55 and mainly interact in three ways with matter elastic and inelastic Coulomb scattering (explained by Equations 3.2 and 3.4) and nuclear interactions. Figure 3.4 shows a sketch of the three main modes of interaction described below. Notice, that clinical protons are not relativistic and thus, as seen in Figure 3.3, the radiative losses, due to *bremsstrahlung*, are negligible.

Inelastic Coulomb interactions

Inelastic Coulomb Interactions (ICI) are given when a proton ionizes an atom by hitting a shell electron. For a proton with initial energy K_{P0}, the result of this interaction is a free electron with a given kinetic energy K_e, an ionised atom, and a proton with final energy $K_{PF} = K_{P0} - (K_e + K_B)$ where K_B is the binding energy of the electron, see Figure 3.1 (left). At first order, ICI results in a continuous loss of energy due to the frequency of the interactions. The properties of ICI described by the *Bethe-Bloch* equation 3.2 and 3.4

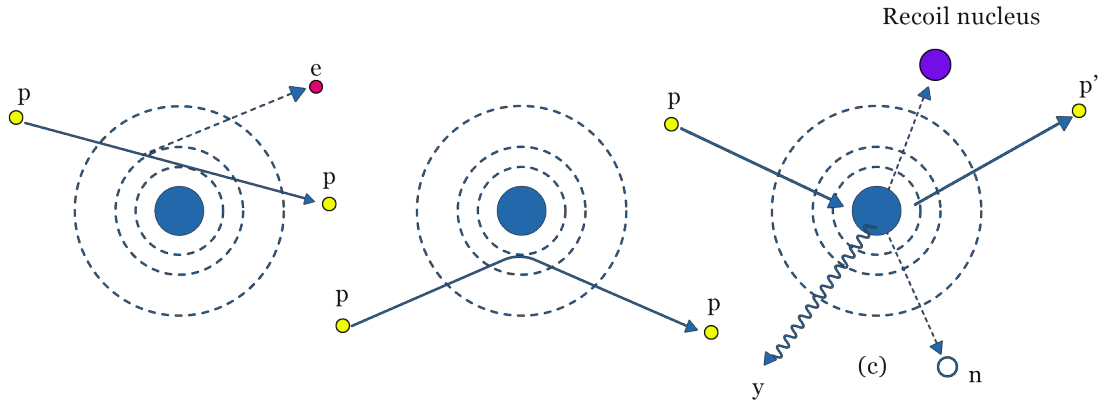

Figure 3.4: Sketch of the three different proton interactions, inelastic and elastic Compton scattering (left) and (middle) respectively, and inelastic nuclear interactions (right).

result in the main cause of the proton's energy deposition and energy and range straggling. The ICI is the dominant interaction and the most important in terms of cancer treatment. The dose deposition is localised due to the short range of the liberated electron ~ 1 mm. This ionisation is also the cause of the death of cancer cells, see Section 2.1.

Elastic Coulomb interaction

The Elastic Coulomb Interactions (ECI) are the electromagnetic interactions of the protons with the nuclei and are the so-called "multiple Coulomb scattering" (MCS), see Figure 3.1 (middle). These are rare in comparison with ICI due to the difference in size between the atomic shell and nucleus. However, as a consequence of the high mass of the nuclei these interactions result in a larger scattering angle for the outgoing proton and thus, are the main cause of the beam dispersion and angular straggling. After the interaction, the target nucleus is left in an excited state due to the transfer of kinetic energy from the incident proton to the recoiling nucleus. The excited state of the nucleus typically lasts for a very short time, on the order of 10^{-15} to 10^{-12} seconds, before it emits gamma radiation to transition to its ground state. This process is known as nuclear gamma de-excitation and may result in a non-localised dose deposition.

Nuclear interactions

Inelastic nuclear interactions are nuclear interactions between the incoming proton and the target nucleus. The nuclear reaction will lead to the emission of Γ-rays, secondary protons, neutrons, deuteron, triton or heavier ions, see Figure 3.1 (right).

Hence, these interactions do not deposit dose in the immediate interaction point. The massive particles will travel in random directions and deliver dose at unwanted parts of the body increasing the treatment's toxicity. Thus, nuclear interactions reduce the number of primary protons in the beam resulting in the main cause of beam attenuation before the Bragg peak. Due to the complexity of nuclear interaction models, an experimental approach is taken to determine an effective proton stopping power that takes into account the effect of these nuclear interactions on the shape of the Bragg peak.

In order to undergo nuclear interactions protons must have sufficient energy to overcome the Coulomb barrier of the nucleus to enter it. The total non-elastic cross-section for proton-induced nuclear reactions rises rapidly to a maximum at around 20 MeV and then declines asymptotically to about half the maximum value by about 100 MeV. Neutrons, which are produced in large quantities, pose a potential safety hazard and can increase the risk of radiogenic late effects. However, nuclear reactions inside the patient may be used to measure various beam and patient properties. To monitor this effect, several detection techniques, such as positron emission tomography cameras, Compton cameras, 1D detector arrays, and photon counting systems, are under development. Studies of the use of the prompt gamma profile for *in vivo* measurements of the Bragg peak show promising results with Geant4 simulations [53].

3.2.2 Multiple Coulomb scattering

MCS arises from the cumulative effect of elastic Coulomb interactions, leading to small random angle deflections of charged particles. Even for thin silicon sensors like the TJ-Monopix (∼100 μm) operating at low energies, such as the 36 MeV protons from the

MC40 cyclotron, the impact of MCS cannot be neglected. See the effect of MCS in Section 6.1.3.

In the context of proton radiotherapy and pCT, MCS plays a critical role as protons traverse through the human body, deviating from a straight path. The presence of MCS significantly affects the projection of particle tracks within the imaged phantom or body and impacts tracking efficiency. For experimental purposes, the widely used parametrization of the Highland formula, as described in [54], is employed:

$$\theta_0 = \frac{13.6\ MeV}{\beta cp} z \sqrt{x/X_0 \left[1 + 0.038 \ln(x/X_0)\right]} \tag{3.5}$$

where θ_0 is the RMS calculated from the central 98% of the scattering angle distribution, ρ is the momentum, βc the velocity, and z the charge number of the incident particle and x/X_0 is the material thickness in radiation lengths defined in [55].

The cumulative effect of MCS results in angular dispersion, the so-called angular straggling, when considering the entire proton beam. In mini-beam proton radiotherapy, the intentional dispersion of the beam is used to spare healthy tissues before reaching the tumor, as explained in Section 2.2.5. When tracking individual protons, the effects of MCS must be taken into account, considering that the proton's direction may undergo small changes between sensors. Furthermore, the generation of a Most Likely Path (MLP) within the imaged phantom, using the entering and exiting positions, is crucial for pCT, as discussed in Section 2.3. Figure 3.5 shows a sketch defining the dispersion angles (ω and ρ) in the context of MCS between two planes.

3.3 Particle physics detectors

In this section, a brief introduction to silicon detectors and their use in high-energy physics experiments and clinical purposes is given. Silicon is the most intensively studied semiconductor and its electrical properties are well known. All semiconductors have a forbidden region in the energy band structure called the band gap. The band gap is

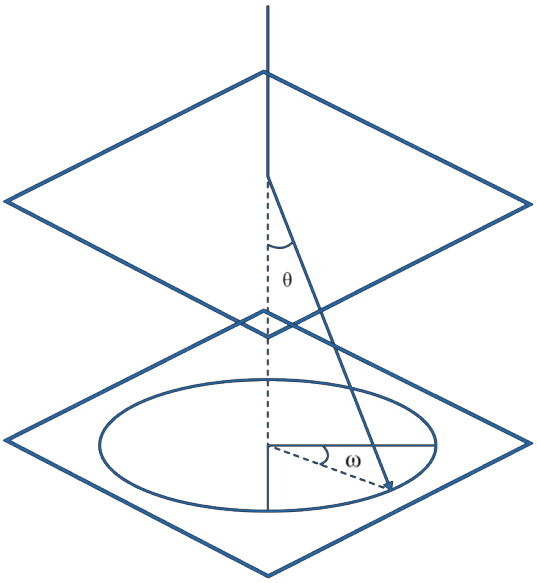

Figure 3.5: Sketch of the definition of the dispersion angles ω and ρ between two planes.

an energy barrier that separates the conduction band and the valence band. At low temperatures, the electrons are in the valence band and the two bands are well separated, however, at high temperatures the covalent bond may break creating free electron and leaving a hole in the valence band. It is usual to treat holes as pseudo-particles because we can associate charge and mass to these entities. Electrons and holes are fermions so they follow Fermi statistics. The probability to find an electron in a certain state with energy E is given by:

$$F(E) = \frac{1}{e^{\frac{E-E_f}{k_B T}} + 1} \tag{3.6}$$

Where k_B is the Boltzmann constant and E_f is the Fermi level defined as the energy where the probability to find a particle in each level is one half. As a function of the temperature, the number of charge carriers (electrons or holes) per unit volume is given by:

$$n_i = (N_c N_V)^{\frac{1}{2}} e^{\frac{E_g}{2k_B T}} \tag{3.7}$$

with,

$$N_{c,V} = 2\left(\frac{2\pi m \star_{n,p} k_B T}{h^2}\right)^{\frac{3}{2}} \tag{3.8}$$

where h is the Plank constant and $m\star_{n,p}$ are the effective masses of electrons and holes respectively. These effective masses are related to the charge carrier mobility inside the semiconductor lattice and are temperature dependent. Silicon has an indirect band gap, due to the absorption energy by lattice excitations, which means that in order to move an electron from the maximum of the valence band to the minimum of the conduction band it needs to increase both its energy and momentum. Thus, despite the band gap of 1.1 eV, on average 3.6 eV are needed to move an electron from the valence band to the conduction band. This low energy threshold allows a high production of electron-hole pairs even by low LET particles such as soft x-rays and a MIP[1]. This is an advantage in order to reduce the silicon bulk and thus, the material budget of the detectors.

3.3.1 The P-N junction

Depending on its purity level, semiconductors are classified in intrinsic and extrinsic. Intrinsic semiconductors are the idealized case of a semiconductor without any impurity. Adding impurities with 5 valence electrons, such as phosphorous, one electron of the external shell of the phosphorous atom remains free and is donated to the conduction band. Those impurities are called donors and their implantation turns intrinsic silicon into extrinsic n-type. If impurities come from the implantation of 3 valence electrons, such as Boron or Aluminium, there is a missing electron in the bonds and a free positive charge, a hole, will be created in the valence band. Those impurities are called acceptors and they make the original intrinsic silicon convert to an extrinsic p-type.

A p-n junction or diode is created when a p-type and a n-type semiconductors are adjoint [56], see Figure 3.6. In a p-n junction, due to the different concentrations of electrons

[1]Notice that the protons used in clinical facilities and in this work are not MIP and thus generate much more charge when traveling through the silicon

and holes between the two types, there will be a diffusion of the charges. Electrons from the n-side will diffuse towards the p-side, correspondingly holes from the p-side defuse towards the n-side[2]. The electrons and holes recombine around the junction will create a depleted region free of charge carriers.

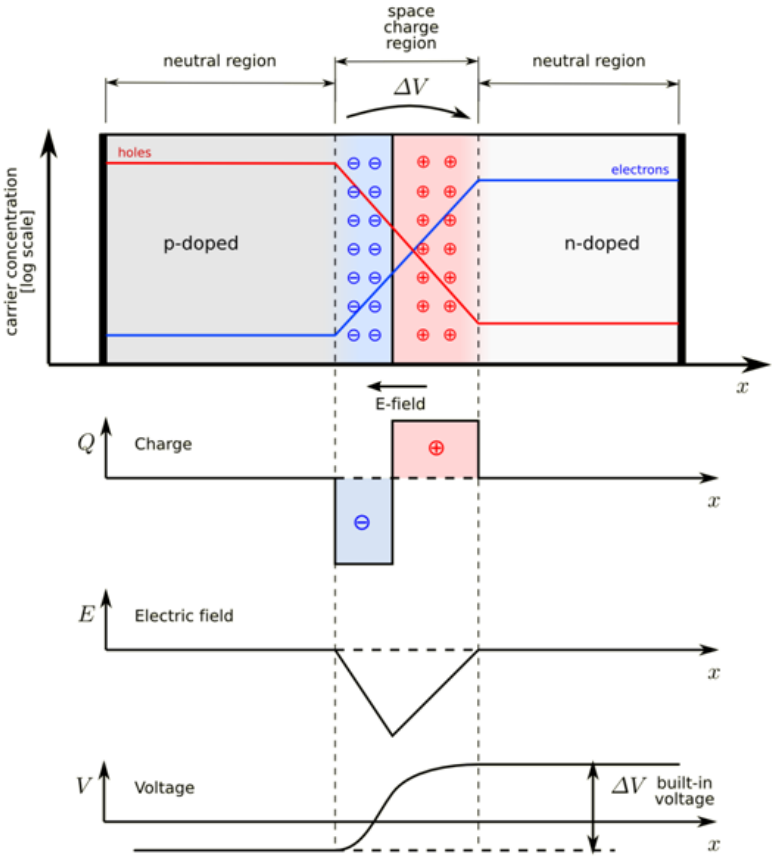

Figure 3.6: Sketch of the transverse cut of a p-n junction showing the carrier concentration (a), the charge (b), the electric field (c) and the voltage (d) all as function of the depth from the p-doped (left) to the n-doped side (right). Image from [57].

Thus, an electric field between the two sides is created opposing the diffusion. When this electric field builds up to the point where it cancels the diffusion the system reaches thermal equilibrium. The electric potential related to this field is called the built-in potential.

[2]In particle detectors, it is usual that the n or the p side is much more heavily doped than the other one. It is denoted by p^+-n if the p side is much more doped than the n side, and n^+-p *vice-versa*.

3.3.2 Detection principles

In this section a discussion about the detection principles for silicon trackers and SiPM will be given. Standard silicon sensors are fabricated by implanting a thin doped layer on top of the silicon substrate. Applying a reverse bias voltage on a p-n junction, a negative voltage to the p side and a positive on the n side, allows to extend the depleted region up to the whole silicon bulk. When the sensor is fully depleted, a uniform electric field is created within the bulk. If higher voltages are applied overdepletion is reached and then the depletion region remains constant while the electric field keeps growing with the external voltage. Thus, if a particle passes through the sensor ionising atoms along its path, generating a cloud of electron and hole pairs, the charge carriers would travel following the electric field toward the electrodes. The charge collected is then read out by the Front End (FE) electronics of the detector.

As seen in Figure 3.7, when the detector is functioning and an ionising particle travels through (or is absorbed in) the silicon, as seen before, the energy lost in the process generates electron-hole pairs. These charge carriers travel across the sensor, under the influence of the electric field, the nearest electrode inducing a current following the *Shockley–Ramo* theorem [58]. Then the current is registered, amplified, compared against a threshold, and recorded as an electrical signal in the FE electronics. The FE electronics can be integrated into the same substrate (monolithic sensors) or designed in a separate substrate and bump bonded to the sensor (hybrid detectors). Figure 3.7 shows a transverse section of both a hybrid (left) and a monolithic (right) pixel in a sensor with an ionising particle passing through.

Charge can also be created by a high energy photon being absorbed within the sensitive area of the silicon transferring it, typically, to a lattice electron which generates additional electron-hole pairs. The amount of charge generated is proportional to the energy of the photon, allowing the detector to measure the energy of the photon as well as its position. Some silicon detectors used for tracking such as SiPM 3.3.4 typically rely on the internal electric field of the detector to cause electron-hole pairs generated by the incident photons

to be multiplied through avalanche multiplication. This multiplication process increases the sensitivity and signal-to-noise ratio of the detector, allowing it to detect weak signals that would be difficult to detect otherwise.

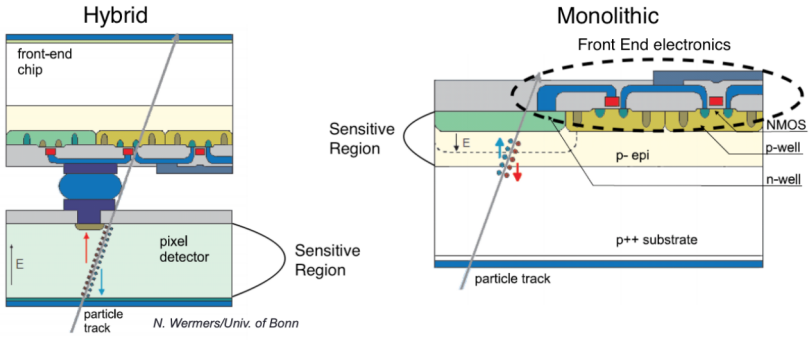

Figure 3.7: Sketch of the transverse section of a hybrid (left) and a monolighic (right) pixel detctors with a ionising particle passing through.

3.3.3 CMOS

Complementary Metal-Oxide-Semiconductor (CMOS) technology is a widely used technology in modern electronics due to its low power consumption, high integration density, and low manufacturing cost. In particle physics, CMOS technology is also being used for various applications such as particle detectors, readout electronics, and tracking detectors.

CMOS technology is a type of Metal-Oxide-Semiconductor (MOS) transistor that uses both n-type (nMOS) and p-type MOS (pMOS) transistors to form complementary pairs. The basic unit of a CMOS transistor is a gate, which is formed by a layer of polysilicon material on top of a thin oxide layer on top of a silicon substrate. The gate can be set to high or low voltage (with respect to the source or drain for the pMOS and nMOS transistors respectively) allowing it to control the flow of electrons through the transistor.

As seen in Figure 3.8, the most simple structure of a CMOS gate consists on the connection of the nMOS and the pMOS transistors' drains. This results in a low power consumption for the CMOS technology. When a low gate voltage is provided, a PMOS transistor's composition results in low resistance between its source and drain contacts,

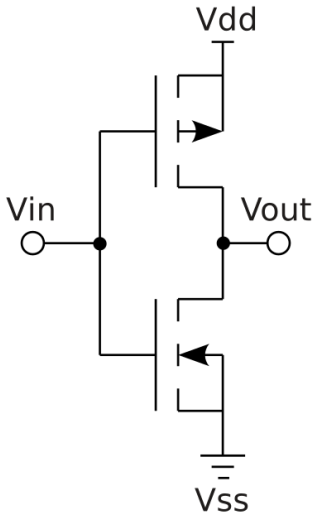

Figure 3.8: Diagram of a CMOS inverter (NOT gate) showing the pMOS on top, with the Vdd (Voltage source), and the nMOS at the bottom with the Vss (ground).

and high resistance when a high gate voltage is applied. But when a low gate voltage is used, an NMOS transistor's composition results in high resistance between the source and drain and low resistance when a high gate voltage is used. Every nMOSFET in CMOS is paired with a pMOSFET, and the gates and drains of each are connected to reduce current. The nMOSFET will conduct and the pMOSFET will not conduct when the gate voltage is high, and the opposite is true when the gate voltage is low. The low power consumption makes them ideal for HEP projects in which cooling is not trivial. Thanks to their high integration density, CMOS transistors can be made very small with feature sizes on the order of a few nanometers. This allows for the fabrication of complex circuits with millions or even billions of transistors on a single chip. CMOS transistors can be fabricated using standard semiconductor manufacturing processes, which are well-established and widely used. This means that the cost of producing CMOS chips is relatively low compared to other types of electronic devices, again an ideal feature for HEP detectors. Another characteristic of CMOS readout electronics is that they are able to collect data very quickly, making them ideal for high-energy physics experiments where large amounts of data are generated.

Pixel detectors

When a silicon sensor is built, the top and bottom implants that generate the pn junction may be further segmented in smaller sensitive regions that define the spatial resolution of the sensor such as pad detectors (with a large uniform implant), strips, or pixel geometries. Each segmentation works as an individual diode and thus needs FE readout electronics.

If the trajectory of a particle goes next to more than one collection electrode the charge is shared between them, see Figure 3.9. Consequently, this particle could generate a signal above the threshold in more than one neighboring pixel in a single event, the pixel with largest charge collected is known as the seed pixel. If the charge collected is not above the threshold, as seen in the rightmost pixel, the charge would be lost. For some pixels sensors, such as the TJ-Monopix, when this happens, the output obtained is a given number of adjacent pixels fired in a single event with a sum of Time over Threshold (ToT) values , defined in Section 3.3.3, that's proportional to the total charge deposited by the particle. Thist type of signals are known as clusters.

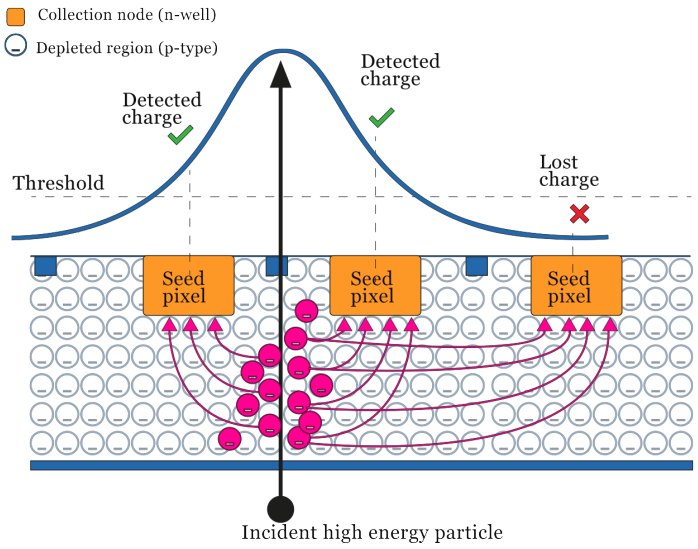

Figure 3.9: Sketch of the charge sharing effect when a particle passes close to two different charge collection electrodes. The top plot illustrates how the distribution of the charge in different pixels can result in charge losses due to the threshold values.

The charge carriers can either be collected by drift or diffusion depending on sensor being fully depleted or not respectively. In the first case the electric field is stronger and

this results in smaller charge clouds and faster charge collection. In the latest, the electric fields is weak and the charges move due to the charge carrier density gradient. This results in slow movement and long collecting times. The slower movement of the drifted charge carriers make them be trapped easier in impurities of the silicon that can be generated by radiation. Therefore, whilst full depletion of the bulk is not needed for most commercial devices, it is key for radiation hardness and fast readout. These are key requirements for HEP detectors and the fast readout is the key feature that motivates the use of such sensors on pCT performed in clinical environments.

MAPS and DMAPS

The Depleted Monolithic Active Pixel Sensors are a state-of-the-art upgrade of the well-known Monolithic Active Pixel Detectors (MAPS) [59] widely used for industrial purposes such as digital cameras. The MAPS present some advantages over the hybrid sensors, currently used in High Energy Physics. The devices contain both the sensor and the FE electronics in the same silicon crystal and this avoids the process of fine pitch bump-bonding. In addition, this process allows for a reduction in the material budget and expensive manufacturing. MAPS have already been successfully used in experiments with low radiation environments [60]. However, these sensors are not fully depleted, see Figure 3.10, and consequently, charges are collected by diffusion and not drift which makes their charge collection slower and their radiation tolerance limited. For this reason, new advantages in CMOS imaging technologies were exploited to achieve full depletion of the silicon substrate volume and the generation of high electric fields to ensure fast charge collection by drift and thus radiation hardness.

In Figure 3.11 one can see an example of these modifications, a planar low dose n-well (pink) that allows to grow the depleted region laterally so the full pixel area is depleted. The Figure shows a partially depleted sensor (a) on top for low reverse bias voltage and a fully depleted sensor (b) at higher bias voltage. There are two main classifications of the DMAPS chips depending on where are the in-pixel FE electronics are implemented,

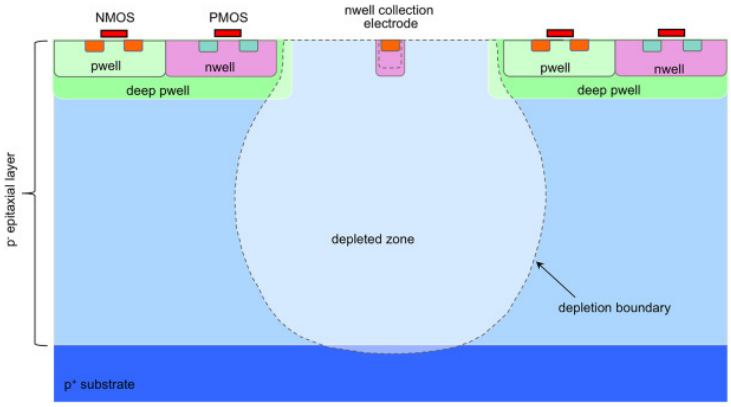

Figure 3.10: Cross section of a MAPS chip showing the depleted region (white shadow) growing from the n-well collection electrode through the p epitaxial layer. No lateral growth is observed leaving the areas along the electronics covered by the deep p-well undepleated. Image from [61].

inside or around the Charge Collection Electrode (CCE). This results in different sizes of the CCE and a difference in the performance and radiation hardness of the devices. The device under test for this thesis is a small electrode prototype called TJ-Monopix.

In the TJ-Monopix chip, a source follower readout circuit is used to read out the voltage from each pixel in the image. A diagram of the chip from the column to the pixel electronics is shown in Figure 4.3, it consists of an array of photodiodes, which are used to detect ionising particles and convert it into an electrical current. Each pixel in the array is connected to a source follower readout circuit, which amplifies the voltage produced by the photodiode. The amplified voltage is then digitalized, commonly as a ToT value (see Section 3.3.3

The source follower readout circuit in the TJ-Monopix chip consists of a field-effect transistor (FET) that is used as a voltage amplifier. The source of the FET is connected to the photodiode, and the drain is connected to a load resistor. The gate of the FET is connected to a voltage reference, which sets the operating point of the FET.

When an ionising particle deposits energy in the sensor, it generates current, this current is then converted into a voltage by the source follower readout circuit, which amplifies the voltage by a small amount. The amplified voltage is then used to digitize the charge collected by the pixel as a ToT value, which is then stored in a memory buffer.

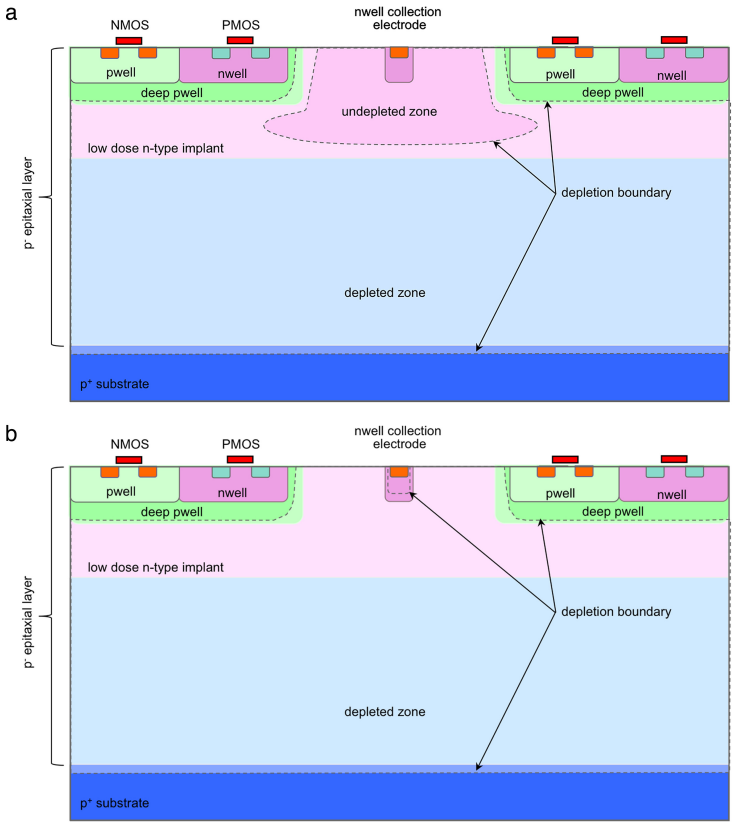

Figure 3.11: Cross section of a DMAPS chip showing the depleted region (white shadow marked with a dashed line) growing from the p-substrate through the p-epitaxial layer for low reversed bias voltage (a) presenting a partially depleted bulk and for higher reverse bias voltage (b) showing fully depletion of the sensor[61].

The advantage of using a source follower readout circuit in the TJ-Monopix chip is that it has a high input impedance, which means it does not draw much current from the sensor. This is important because the sensor is sensitive to light and can be easily damaged by high current levels. Using a source follower readout circuit allows the TJ-Monopix chip to read out the voltage from the sensor without drawing too much current, which helps to preserve the sensitivity of the sensor.

Figure 3.12 shows a common sketch of the readout in pixel FE analog electronics of a detector such as the TJ-Monopix. The charge is converted to a voltage using a Charge Sensitive Amplifier (CSA) and then compared to a threshold voltage. A discriminator converts the analog signal into a square digital one.

The difference in time between the Leading Edge and Tailing Edge defines the ToT

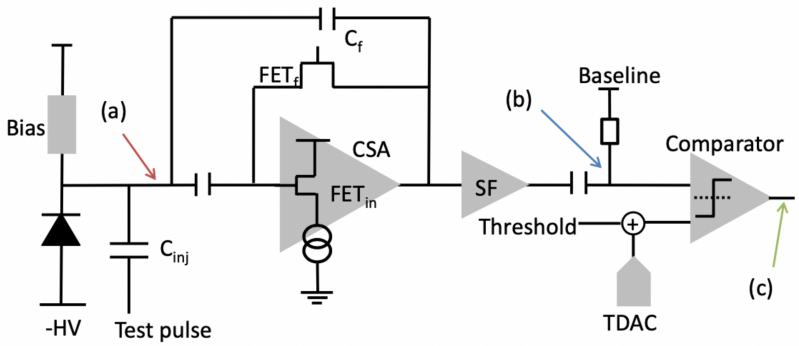

Figure 3.12: Block diagram of the typical analog front-end circuit in a pixel. The signal current is converted to voltage by the CSA and digitized by the discriminator.

as seen in Figure 3.13 is stored in the RAM memory of the pixel. The block diagram on Figure 3.12 also shows a capacitor labeled as C_{inj} that allows injecting an analog test pulse used to calibrate the FE electronics without the need for a signal in the sensor. The hits are propagated in priority through the column from top to bottom and from left to right for different columns. A review of a characterisation and evaluation of the TJ-Monopix before and after being irradiated up to 10^{15}neq/s can be seen in [62].

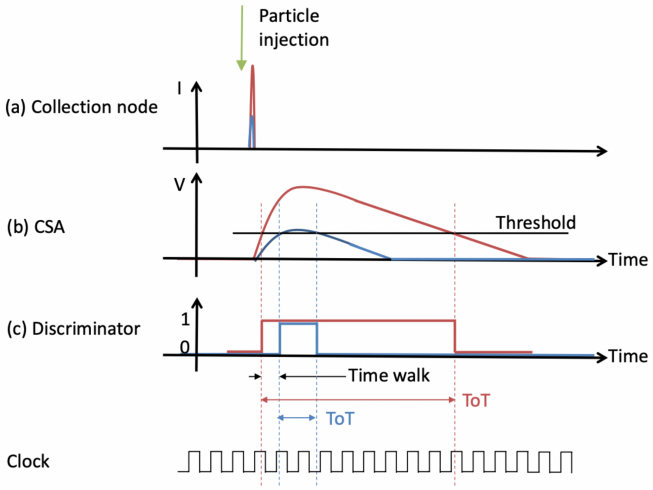

Figure 3.13: Sketch of the signals observed at the points (a), (b) and (c) in Figure 3.12. The red and blue lines represent a high and low signal recorded at the charge collection electrode.

3.3.4 Silicon photo-multipliers

SiPM [63], [64] are a type of segmented pixel sensor that is optimised for measuring small amounts of light (even single photons). The SiPM's substrate is divided in microcells, see Figure 3.14 (a), which aim to improve the detection efficiency and signal-to-noise ratio of the device. By dividing the sensitive area of the SiPM into a large number of small microcells, each of which can detect a single photon, the SiPM can achieve a higher level of detection efficiency than a single large pad. This is because the probability of a photon being absorbed by a microcell is higher than that of it being absorbed by a single large pad due to several factors including smaller surface area, higher detection efficiency, higher density of detector material. The charge creation process is the same as the one defined for other Si sensors; the energy of the photon is transferred to an electron in the silicon, which generates additional electron-hole pairs through a process called avalanche multiplication. The resulting electrical charge is detected by the microcells in the photomultiplier, and the total charge generated is proportional to the number of photons absorbed, allowing the SiPM to measure the intensity of light. The FE electronics consist of a single-photon avalanche diode (SPAD), which is a highly sensitive photodiode that is biased above its breakdown voltage, and a quenching resistor, which is used to limit the duration of the avalanche multiplication process. Figure 3.14 (b) shows the block diagram of the SPAD with the SiPM Cathode on top and Anode at the bottom.

The microcell structure is a key feature that allows for the efficient detection of individual photons and also increases its spatial and temporal resolutions. Since each microcell generates its own electrical signal, it is possible to analyze the signals from adjacent microcells and determine the position of the photon interaction within the SiPM with high precision. This is useful in applications that require high spatial resolution, such as positron emission tomography (PET)[66] and gamma-ray spectroscopy [67]. The different microcells are connected in parallel in order to sum all the energy deposited.

SiPMs are widely used in medical applications such as PET imaging [66] and many high energy experiments, from Cherenkov radiation astrophysics projects [67], to particle

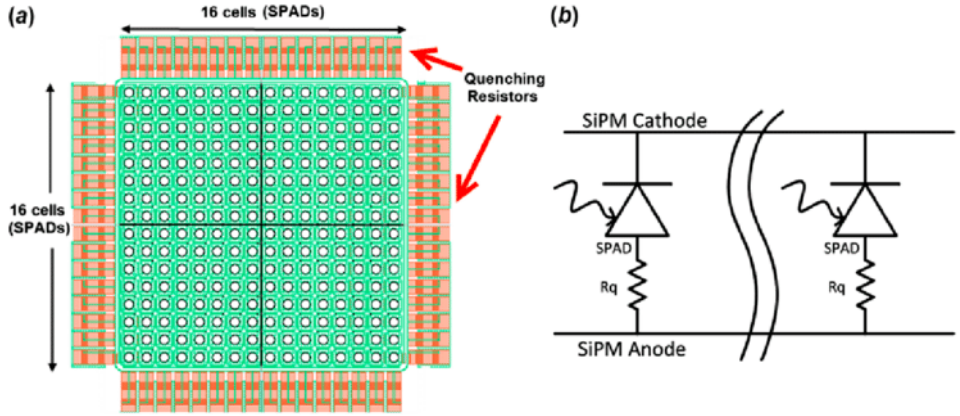

Figure 3.14: (a) Layout of the 50R-SiPM with 16 × 16 SPADs and quenching resistors; (b) simplified structure of a generic SiPM, with many microcells made by a SPAD and a quenching resistor each; the cathodes and the anode common pad are the only two SiPM electrodes [65].

physics projects such as the FGD in T2K [68].

3.3.5 Scintillation Detectors

Scintillation detectors are used to measure the light emitted during the de-excitation processes induced by charged tracks in matter. These detectors convert excitation energy to fluorescent light and should exhibit high efficiency and transparency to fluorescent radiation. The main classes of scintillators include noble gases, inorganic crystals (e.g., NaI or CsI), liquid organic scintillators, and plastics. Noble gases like Argon and Xenon are used in liquid form for detectors that measure both ionization and scintillation. Inorganic crystals, although costly, provide high light yield and are suitable for precision measurements and nuclear medicine. Plastics are widely used due to their overall good performance, cost-effectiveness, and mechanical stability. Organic liquid scintillators offer a similar scintillating performance as plastics. The de-excitation time of different materials is also considered, as it varies from nanoseconds for plastics to tens or hundreds of nanoseconds for some inorganic crystals [69].

Light Extraction in Plastic Scintillators

To detect scintillation light in plastic scintillators, light-sensitive devices like photomultipliers are used. The photons produced are reflected on the scintillator surfaces, and to transfer them to the photosensor, areas of the plastic surface are left free of optical insulation. Another approach involves using wavelength-shifting (WLS) fibers inserted in the plastic volume or located on one side. These fibers convert the light into a longer wavelength and guide it to the photosensor, improving light attenuation, response uniformity, and performance. The choice between the two solutions depends on the detector purpose and geometry.

Energy Reconstruction

Compared to gas detectors, liquid/solid detectors have higher stopping power due to increased density which results in a higher energy loss. This allows tracks to fully stop within the plastic scintillator volume, offering advantages for energy reconstruction. The range of a track can be measured, enabling reconstruction of the initial particle kinematics based on energy losses predicted by the Bethe-Bloch formula. If the track stops within the scintillator volume without any neutrals escaping, the total energy deposit corresponds to the initial particle energy. Hence, by measuring the total energy deposited in the detector, the particle energy can be reconstructed through calorimetry. Linearity between the light yield and energy deposit is crucial for accurate mapping. Although the relationship is mostly linear for high energy loss rates (dE/dx), the signal is quenched for highly ionizing tracks. The semi-empirical Birks model [70] is used to correct for the quenching effect. Equation 3.9 relates the light output per unit length (dL/dx) to the stopping power (dE/dx) using parameters such as the absolute scintillation efficiency (A) and the Birks constant (κ_B):

$$\frac{dL}{dx} = \frac{A\frac{dE}{dx}}{1 + \kappa_B \frac{dE}{dx}} \tag{3.9}$$

3.4 Machine Learning and Deep Learning

In recent years, machine learning techniques have revolutionized various fields, including signal processing and image analysis. Deep learning, a subfield of machine learning, has gained significant attention due to its ability to automatically learn hierarchical representations from raw data. CNN have emerged as a powerful class of deep learning models, particularly effective in tasks involving image analysis, such as signal segmentation, multi-labeling, and regression.

3.4.1 Convolutional Neural Networks

CNN have proven to be highly successful in image analysis tasks [71], [72]. Unlike traditional neural networks, CNN exploit the spatial structure of images by using convolutional layers that apply filters to local patches of input data. This architecture enables CNN to capture relevant features at multiple spatial scales, making them well-suited for tasks involving image segmentation and labeling.

U-Net Architecture

The U-Net architecture has gained popularity for its effectiveness in image segmentation tasks, particularly in biomedical image analysis [73], [74]. The U-Net architecture consists of a contracting path, which captures context and reduces spatial dimensions, and an expansive path, which enables precise localization. This architecture is characterized by skip connections that concatenate feature maps from the contracting path to the corresponding locations in the expansive path, allowing for the recovery of detailed spatial information.

3.4.2 Learning Rate, optimizers, and ADAM

The learning rate is a hyperparameter that determines the step size at each parameter update during training. It controls the balance between exploration (larger learning rate)

and exploitation (smaller learning rate). As shown in Figure 3.15 too high learning rate may lead to overshooting and unstable training, while a too low learning rate may result in slow convergence or getting stuck in local minima.

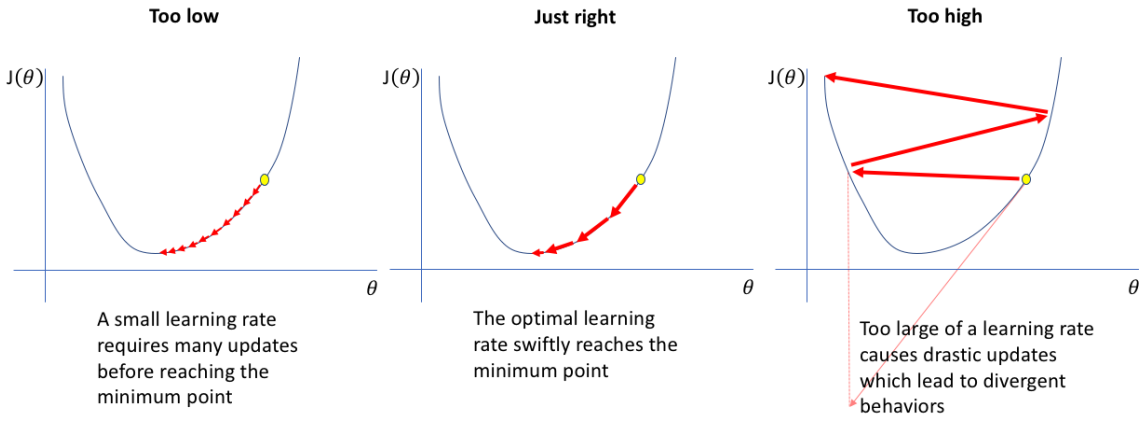

Figure 3.15: Example of the effect of a too low (left), just right (middle) and too high (right) learning rate when optimising a parameter.

Optimizers play a crucial role in training CNN by updating the model parameters to minimize the loss function. One commonly used optimizer is Adaptive Moment Estimation (ADAM) [75]. ADAM combines the advantages of two other popular optimizers: AdaGrad and RMSProp. It adapts the learning rate for each parameter based on past gradients and squared gradients, allowing for faster convergence and better handling of sparse gradients.

To train a CNN for signal segmentation, an appropriate learning rate is selected, and the ADAM optimizer is utilized. The training process involves feeding the input signals and corresponding labels to the CNN, computing the loss between the predicted segmentation maps and ground truth labels, and backpropagating the gradients to update the model parameters. The optimizer adjusts the parameters based on the computed gradients and the learning rate, gradually minimizing the loss function.

3.4.3 Different kinds of problems to solve with CNN:

CNN can be used to solve different kinds of problems and different architectures are optimised for specific problems. In this thesis, the use of CNN is focussed on two different problems. The first one is a combination of a Signal segmentation problem with multi-label at pixel level, the second one is a regression problem. A brief description of the mentioned problems is given below.

3.4.4 Signal Segmentation

Signal segmentation involves dividing a signal into distinct regions or segments based on specific criteria. CNNs, with their ability to capture spatial dependencies, have shown remarkable performance in signal segmentation tasks. The U-Net architecture, with its skip connections, further enhances the segmentation accuracy by preserving fine-grained details.

By training a CNN, specifically a U-Net, on a labeled dataset, the model can learn to automatically identify and segment relevant regions in signals. The training process involves defining an appropriate loss function, such as cross-entropy or Dice loss, and optimizing the model parameters through an iterative process known as training epochs. Each epoch involves feeding the input signals to the CNN, obtaining predicted segmentation maps, comparing them with the ground truth labels, and adjusting the model parameters using an optimizer.

3.4.5 Multi-labeling

Multi-labeling refers to the classification of instances into multiple classes simultaneously. CNNs can be extended to handle multi-labeling tasks by modifying the output layer to accommodate multiple classes. The U-Net architecture, with its ability to capture both local and global context, is well-suited for multi-labeling applications.

By training a U-Net CNN on a labeled dataset with multiple labels per instance, the

model can learn to associate different regions or features of the input signals with their corresponding labels. This enables the simultaneous identification of multiple classes within the signals, providing comprehensive and informative results.

3.4.6 Regression

Regression tasks involve predicting a continuous output variable based on input data. CNNs can be adapted for regression by modifying the output layer to produce continuous values instead of discrete class labels. The U-Net architecture, with its ability to capture spatial dependencies and preserve fine details, is also applicable to regression problems.

By training a U-Net CNN on a labeled dataset with corresponding continuous output values, the model can learn to predict accurate regression values for unseen input signals. This allows for precise estimation of continuous variables, facilitating various applications such as signal parameter estimation or prediction of signal properties.

In the context of regression tasks, the dataset is prepared with input signals and corresponding continuous output values. The U-Net CNN is trained using a suitable loss function, such as Mean Squared Error (MSE) or Mean Absolute Error (MAE), which quantifies the discrepancy between the predicted continuous values and the ground truth values. Similar to previous cases, the model parameters are optimized using the ADAM optimizer and training epochs. Through the iterative training process, the U-Net CNN learns to predict accurate regression values for unseen input signals, facilitating various applications such as signal parameter estimation or prediction of signal properties.

3.5 Geant4 a toolkit for physics simulations

Geant4 is a powerful simulation toolkit widely used for simulating the passage of particles through matter [76]. Based on Monte Carlo (MC), Geant4 uses an objected-orientated programming model, and provides a comprehensive set of tools and algorithms to accurately model particle interactions and track their trajectories. In this section, the Geant4's

tracking mechanism, based on the stepping action and position tracking is given.

3.5.1 Stepping Action

Stepping action is the core concept of Geant4 simulations. As particles propagate through matter, they traverse infinitesimally small steps, during which their state is updated. These steps are defined by a user-implemented stepping action, allowing for customization and fine-grained control over the simulation process. A new step is also defined when the particle encounters a material boundary.

The stepping action serves as a fundamental unit of simulation, providing access to the particle's properties, such as its position, momentum, energy, and time. Within the stepping action, various physics processes, such as electromagnetic interactions, hadronic interactions, and decay processes, are applied to the particle as it progresses through the material.

3.5.2 Position Tracking

Accurate position tracking is essential for capturing the intricate details of particle trajectories and their interactions with the material. Geant4 employs a precise position tracking algorithm that continuously updates the particle's position as it moves through the simulation geometry.

To ensure accurate position tracking, Geant4 utilizes a geometry model composed of various primitive shapes, such as boxes, spheres, and cylinders, to represent the physical components of the experimental setup or detector. This geometric model is constructed based on user-defined specifications or loaded from external CAD files [77], allowing for realistic and detailed simulations.

As particles traverse the simulation geometry, Geant4 determines their location by performing intersection tests with the geometrical boundaries. This process involves computing the intersection points of particle trajectories with the boundaries of the surrounding volumes. By accurately tracking the position at each step, Geant4 enables the simulation

to capture intricate geometrical features and complex particle paths.

3.5.3 Sensitive detectors

Sensitive detectors play a crucial role in Geant4 simulations as they are responsible for capturing and recording the interactions between particles and detector materials. These detectors act as virtual instruments, mimicking the behaviuor of real detectors and providing valuable information about the particle's energy deposition, track information, and other relevant quantities. Geant4 offers a variety of sensitive detectors that can be tailored to specific experimental setups or applications.

Geant4 provides a wide range of predefined sensitive detectors, including those for tracking detectors, calorimeters, dosimeters, and imaging devices. For example, the "G4MultiFunctionalDetector" can be used to combine different detector components, such as a tracker and a calorimeter, into a single detector, allowing for comprehensive analysis of particle interactions.

In addition to the predefined detectors, Geant4 allows users to define their own custom sensitive detectors, tailored to their specific requirements. This flexibility empowers researchers to simulate novel detector concepts or adapt existing detectors to new experimental conditions.

Chapter 4

Characterisation of the TJ-Monopix

4.1 TJ-Monopix

The TJ-Monopix is a DMAPS prototype fabricated in the TowerJazz 180 nm imaging process designed using a novel modification to enhance radiation tolerance [62], [78]. A cross section of the chip can be seen in Figure 4.1. The TJ-monopix uses a small n-well CCE, pictured in red in the middle of the cross section. The benefit of this small electrode geometry is a very low noise and fast signal timing with low power consumption. This is due to the small capacitance ($\simeq$ 3 fF) generated at the electrodes intermediate surface. The CCE is surrounded by its FE in pixel electronics presented on the top corners of each cross-section. The electronics are isolated from the depletable volume, marked with an orange dashed line, through deep p-type wells pictured in dark blue.

The sensitive volume of the sensor is a 25 μm thick high resistivity (> 1 k$\Omega \cdot cm$) p-type epitaxial layer that is grown on a low resistivity substrate. The modified process used for this chip consists in the implementation of a planar low dose n-type implant on the p epitaxial layer, see the salmon coloured region in Figure 4.1. With this new layer, the p-n junction is separated from the collection electrode and the depleted region grows from this new junction through all the pixel's area. Applying a reverse bias voltage the depleted region can grow up to the collection electrode. The low dose n implant that generates

the depleted region also isolates the substrate from the deep p-well in the pixel matrix allowing independent biases. Provided a sufficiently large potential barrier, it prevents the holes in the deep p-well from entering the epitaxial layer and hence avoids punch-through [78]. The TJ-Monopix is a test chip that has two different internal structures regarding the shape of the deep p-well. The first, labeled as FDPW, uses the original structure. The second structure enhances the electric field at the edge of the pixel by removing a fraction from the covered Deep P-Well (RDPW). Both cross sections, FDPW and RDPW, bottom and top respectively, can be seen in Figure 4.1. The RDPW structure aims to increase the radiation hardness of the sensor by improving the lateral electric field near the charge-collecting electrode and at the edge of the pixel [16], [78].

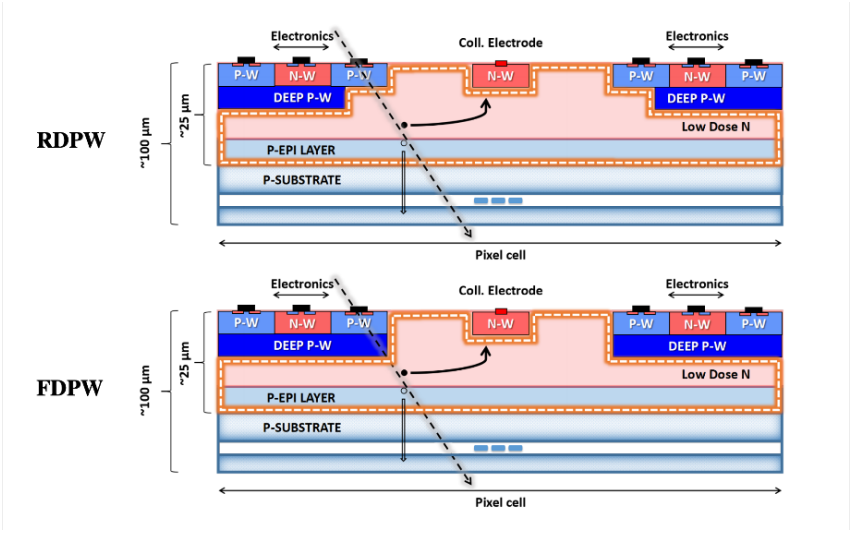

Figure 4.1: Pixel cross-sections for the RDPW (above) and FDPW (below) layouts in TJ-Monopix. The depletable volumes are delimited by white dashed lines [62].

The chip is segmented into four arrays of 224x112 pixels with a pixel pitch of 36x40 μm^2 using four different readout systems. The sensor is further divided using the two different deep p-well structures, FDPW and RDPW resulting in a total of 8, 112x112, matrix arrays. Figure 4.2 shows a layout of the matrix divisions and the different readout systems: a standard pixel variation that features PMOS input reset scheme, a novel leakage current compensation circuit, a structure that allows high voltage from the front side and a low power column bus readout variation.

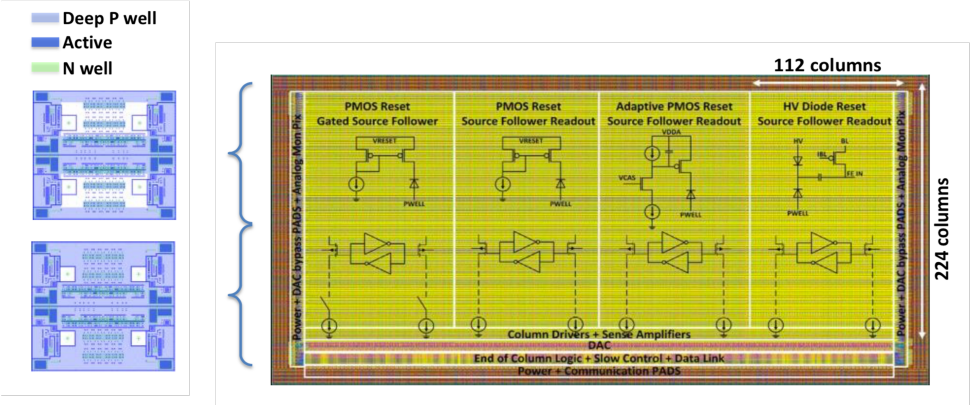

Figure 4.2: Top view of the FDPW and RDPW flavours dividing the TJ-Monopix chip by half bottom to top respectively (left) and the layout of the four different readout structures (right).

The TJ-Monopix readout system consists of a continuous readout Column-Drain Architecture that sends the hit data from a pixel to the end of the column logic derived from the FEI3 chip used in the ATLAS inner tracker [79], [80]. The architecture of the TJ-Monopix chip can be seen in Figure 4.3. The chip has a gray counter that distributes a 40 MHz (25ns) bunch crossing ID time stamp to the whole matrix. The data received from the charge-sensitive amplifiers at the end of each column are arbitrated by the end-of-column logic and sent to the DAQ system using a 160 Mbps serial link. A trigger memory has not been implemented in the current prototypes and hit data is sent out immediately.

4.2 Comissioning of the TJ-Monopix

In this section a brief explanation of the TJ-Monopix setup, the commissioning, and optimisation of the front-end parameters needed for the sensor to work with CP. Several tests were performed at the lab with the test pulses, an ^{55}Fe source and low energy protons at 28 and 36 MeV at the MC40 cyclotron. The setup and methodology for the studies performed at the MC40 cyclotron can be seen in Sections 5 6.

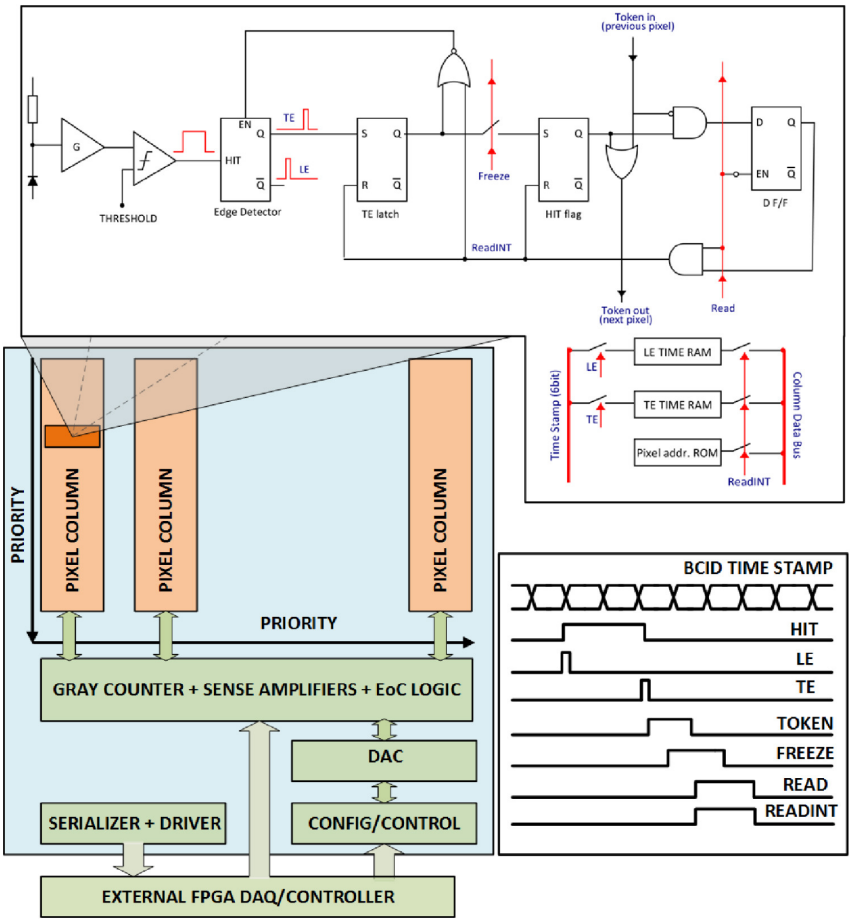

Figure 4.3: Schematics of the architecture of the TJ-Monopix electronics [62].

4.2.1 Setup for the TJ-Monopix

The chips were wire-bonded to dedicated single chip cards, which in turn were coupled to a General Purpose Analog Card (GPAC) and a Multiple Input/Output 3 (MIO3) card. The MIO3 is connected to a 5 V power supply and holds a programmable Kintex7 FPGA, and connectors for external triggers and it allows communication with a PC via Ethernet connection. A 6 V power supply is connected to the GPAC. The multiple functions of the GPAC include: providing an injection pulse generator, 12-bit DACs, ADCs, power sources for the TJ-Monopix chip, and the possibility to probe digital and analog signals. The TJ-Monopix is connected to a high precision power supply providing - 6 volts to the Substrate and the Deep P-Well to the chip, see Figure 4.4. Figure 4.5 shows the three different boards and connections described above while Figure 4.6 shows a closeup of the

PCB with the TJ-Monopix sensor.

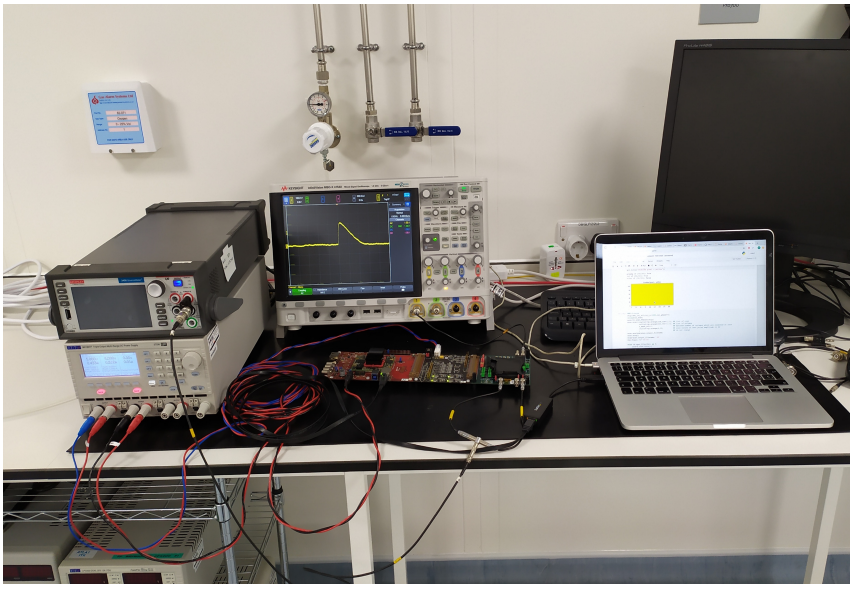

Figure 4.4: Setup of the TJ-Monopix commissioned in the BILPA ISO7 clean room in Birmingham.

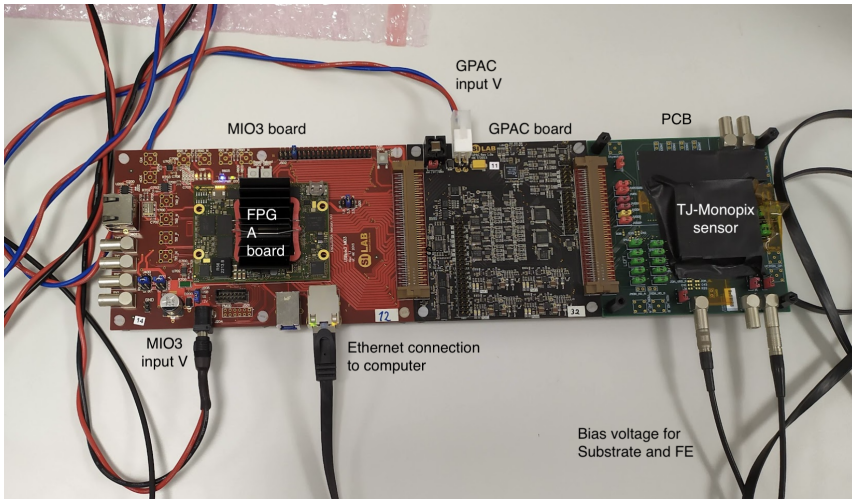

Figure 4.5: Picture of the connections of the MIO3 and FPGA (left), the GPAC board (middle), and the PCB with the TJ-Monopix sensor (right).

The firmware, together with a set of Python scripts with the basic set of scans that can be performed with the TJ-Monopix was provided by the Si-Lab from the University of Bonn that developed the chip and its readout system [81]. These scripts can be run by a Jupyter Notebook code that also allows to manual modification of the FE parameters of the chip's electronics and runs the electric tests needed to ensure proper functionality.

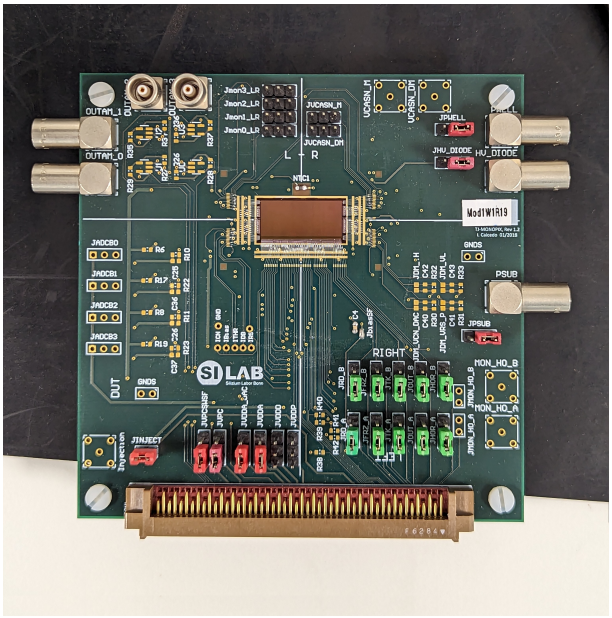

Figure 4.6: Close up of the TJ-Monopix chip wire-bonded to the PCB designed in Si-Lab

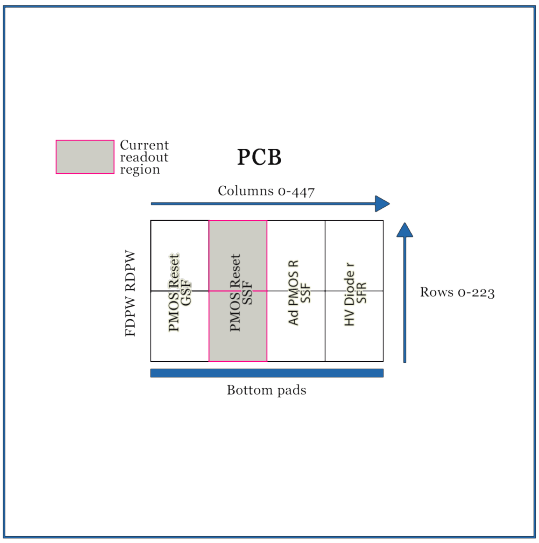

Figure 4.7: Sketch of the carrier board of the TJ-Monopix showing the different flavours. The PMOS Reset Source Follow Readout, the flavour used for this work, has been shadowed in grey.

Each flavour of the TJ-Monopix needs a different set of FE parameters and voltages and thus only one flavour at a time can be activated and read out.

Notice though, that both the FDPW (from row 0 to 111) and the RDPW (from row 112 to 223) structures from each flavour are readout together resulting in a sensitive array

of 224x112 pixels, equivalent to $\sim 0.9 \times 0.4$ mm. All the measurements shown in this work were performed with the PMOS Reset Source Follower readout flavour. Figure 4.7 shows a sketch of the PCB and the position of the TJ-Monopix chip, in grey shadowed area shows the flavour used for this work.

4.2.2 Threshold scans

The TJ-Monopix scripts allow to perform threshold scans. Threshold scans aim to understand the threshold distribution of the matrix for a given set of FE parameters. By design, the TJ-Monopix has low threshold dispersion and thus there is no need for in-pixel tuning logic.

The scan consists in a simple step-by-step procedure in which, on each step, a number (N) of equal analog current signals are injected on a given pixel. The signal current is increased by an amount ΔI at every step and registers the number of times the pixel is fired (n). The number of injections N, as well as the increase of signal ΔI (in DAC units) can be modified through the code. The number of times a pixel fired as a function of the DAC units injected at each step follows an error function (sigmoid) from which one can take the derivative and obtain a Gaussian with a mean value μ corresponding to the threshold of the pixel and the variance that corresponds to the ENC.

A pixel-by-pixel scan can be performed to get information on the whole matrix. However, in order to save time, a scan of all the pixels in one of every ten columns is usually performed giving enough statistics. Notice that since there is no in-pixel tuning the mean and variance of the threshold dispersion are enough to understand the full matrix behaviour. Figure 4.8 shows the threshold dispersion for the default parameters of the FDPW (left) and RDPW (right) structures.

4.2.3 Tunning of the front end parameters

The FE parameters, shown in the leftmost column of Table 4.1 affect the amplitude and length of the analog signal and the threshold voltage of the comparator as seen, which

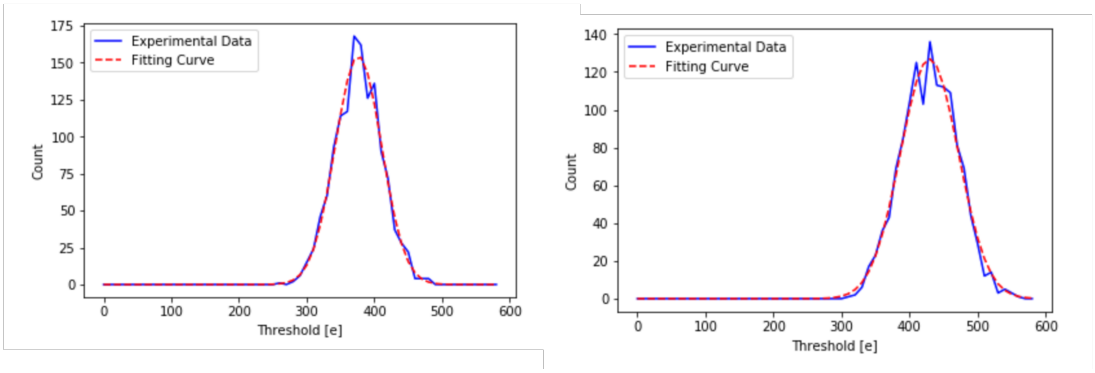

Figure 4.8: Histogram of the threshold distribution of the FDPW (left) and RDPW (right) for the default FE parameters (blue), fitted with a Gaussian to obtain the mean and the dispersion of the distribution (red).

has a direct effect on the digital readout as seen in Figure 3.13. The digital readout is defined as the ToT, *i.e.* the number of clock cycles (at 40 MHz for the TJ-Monopix) the signal is over threshold, and thus it is defined by the energy deposited (charge creation) and the FE parameters.

Since modifying the FE parameters determine the threshold of the whole matrix, a mask and enable scan is needed after each modification in order to mask the noisy pixels, *i.e.* the pixels that fire randomly above threshold, for a given set of FE parameters. Not doing so could result in noisy pixels not being masked or in masking pixels that would have a random noise that would remain below the new threshold reducing the sensor's efficiency. The mask and enable scan consists in enabling the readout of the pixels, column by column, waiting for a determined time (t_s). After this time, if a pixel has been fired more than N times it is tagged as a noisy pixel and masked. The configuration of t_s and N values can be modified by changing the Python scripts in order to lose or tighten the masking constraints. The default values of t_s and N provided by the Si-Lab, and used in this thesis, were $t_s = 0.2$ and $N = 2$.

A noise occupancy scan can be performed to cross-check that there are no unmasked noisy pixels to ensure the noise occupancy is in agreement with the value required. In the case of the TJ-Monopix from Bonn, the noise occupancy value obtained with the default FE parameters was $\frac{4 \cdot 10^{-8}}{25\ ns}$ [82].

Front end parameters for high energy deposition

The TJ-Monopix chip was designed to be part of HEP experiments such as the ATLAS ITk. For such sub-detectors, placed very close to the beam pipe, the particles measured are commonly MIPs. However, clinical protons have much lower energies, and as seen in Section 3.2, the energy deposited by a heavy charged particle on a medium depends on the BB Function 3.2. Following this, one can see that the proton energies used for this project (between 28 MeV and 150 MeV) deposit much more energy than a MIP. The Most Provable Value (MPV) of electron-hole pairs generated by a MIP is 2000 e^- whereas for 36 MeV protons it rumps up to 21000 e^-. With this, the FE parameters used on the chip for detecting MIPs, with high efficiency, in a very clean environment are not the same ones needed to deal with the low energy of clinical protons and the relatively high radioactive environment of clinical facilities.

FE parameters	Default	Optimisation for CP
Input baseline	35	20
Output baseline	0	0
Input reset rate	2	4
Output reset rate	15	45
Biasing Discriminator	20	75
DC current of amp.	5	5
Threshold FDPW $[\mu, \sigma]$	[375 e, 36 e]	[786 e, 76 e]
Threshold RDPW $[\mu, \sigma]$	[429 e, 42 e]	[963 e, 87 e]

Table 4.1: Table of the front end parameters, default and the optimised for clinical protons and their corresponding mean threshold associated.

Table 4.1 shows two different sets of values for the FE modifiable parameters and the resulting mean threshold values of the full matrix distribution. These values were obtained from the fits seen in Figures 4.8 and 4.9. The FE parameters have been optimised to reduce the analog signal length and amplitude by raising the input bias line, the bias of the discriminator, and the DC current of the amplifier. This modification improves the performance under the test beam conditions with 28 and 36 MeV protons at the MC40 cyclotron and clinical protons. The ToT counter of the TJ-Monopix has only 8-bits which results in 64 counts for the ToT before the overflow. As aforementioned, the

nonrelativistic protons sourced from the MC40 Birmingham's cyclotron deposit a large amount of charge in the silicon ($\sim$ 21 ke^-) which is more than ten times the charge deposited by a MIP. Therefore, the modifications aim to obtain a faster signal and to raise the threshold to reduce the ToT cycles for nonrelativistic protons. This also results in higher noise resistance and fewer pixels need to be masked.

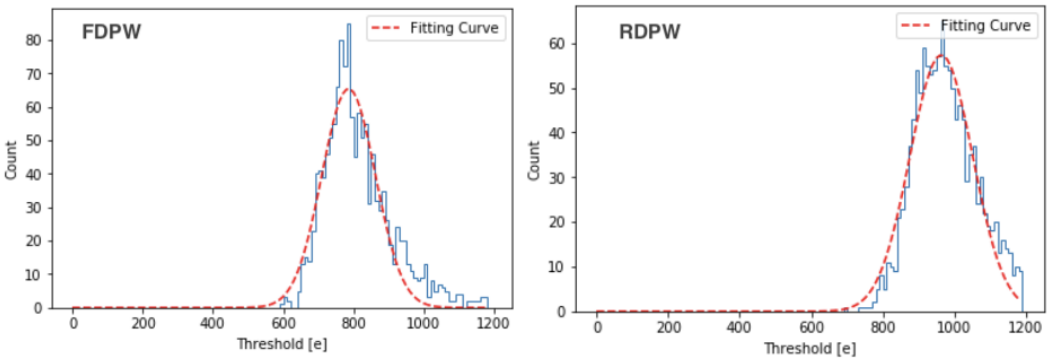

Figure 4.9: Histogram of the threshold distribution of the FDPW (left) and RDPW (right) for the FE parameters optimised for CP (blue), fitted with a Gaussian to obtain the mean and the dispersion of the distribution (red).

The associated values of ENC are also plotted in Figure 4.10, it can be seen that the mean of the threshold dispersion is more than five sigmas away from the ENC.

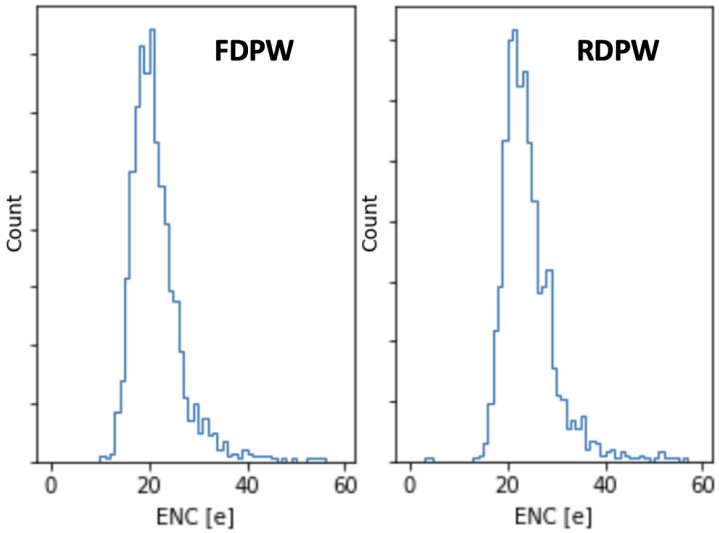

Figure 4.10: Histogram of the ENC for the FDPW (left) and RDPW (right) for the FE parameters optimised for CP.

Thus, the FE parameters optimised for clinical protons shown in Table 4.1 resulted

in no need for any pixel masking. Scans of up to 60 s in the clean room show no noisy pixels.

The value of noise frequency obtained with a noise occupancy scan in a clean environment with the FE parameters optimised for clinical protons was $\frac{2}{1min} < \frac{4^{-11}}{25ns}$ which is three orders of magnitude lower than the one accepted by Bonn.

These FE parameters have shown high efficiency and detection performances for particles ranging between the x-rays sourced by the K_α peak of the ^{55}Fe and the 36 MeV protons, including the measurement of 100 MeV protons at the Curie Institute. Clinical protons will deliver an energy close to the 100 MeV protons and always within this range. Thus, it is expected for these FE parameters to perform well in clinical environments.

4.3 Source scans

The scripts provided by Si-Lab allow to perform source scans in which the unmasked pixels of the chip are enabled for a selected period of time. The data is stored in three different HDF5[1] files and can be read and analysed using a Python script developed within this project's framework. The three different files are: a scan file with raw data, a file after converting the raw data into a hit list and a file after the hits have been aligned in events. The latest is the one used in this project and it contains the following hit information: Event number, time stamp (converted to 640MHz clock frequency), frame, row, column, ToT.

For the first source scans performed with the TJ-Monopix an ^{55}Fe radioactive source was used under clean room conditions. Iron-55 is a radioactive isotope of iron, its half-life time is 2,737 years and it is widely used as a source of x-rays in physics labs. The ^{55}Fe decays into ^{55}Mn through electron capture and then the Mn emits the x-ray photons used as a signal. Figure 4.11 shows the energy spectrum of the x-rays emitted by a ^{55}Fe source. Two peaks can be seen with different amplitudes (probabilities). The first and

[1]The Hierarchical Data Format version 5 (HDF5), is an open source file format that supports large, complex, heterogeneous data.

most probable is known as the K_α peak and the lower peak is known as K_β. Both peaks have energies of few keV, $K_\alpha = 5.9$ keV and $K_\beta = 6.4$ keV, and a branching ratio of about 28 % and 2.9 % respectively.

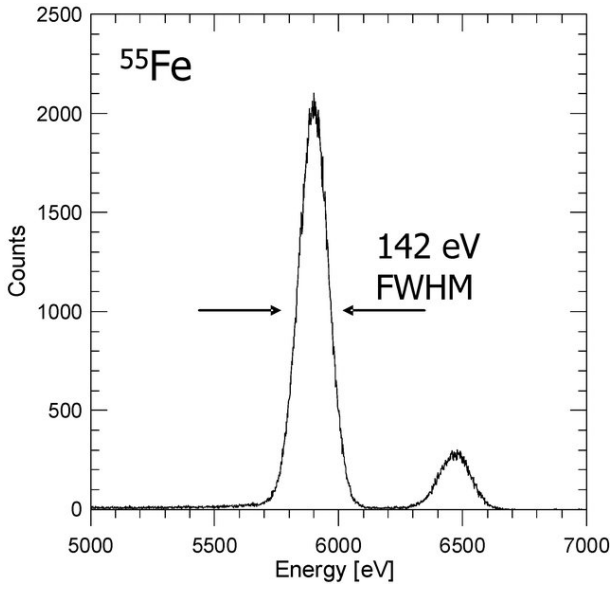

Figure 4.11: Spectrum of radiation of the isotope ^{55}Fe obtained by C. Fiorini, *et al.*[83]

The histogram, seen in Figure 4.12, shows the charge collected distribution of a single pixel obtained with a source scan using a ^{55}Fe source during 30 minutes.

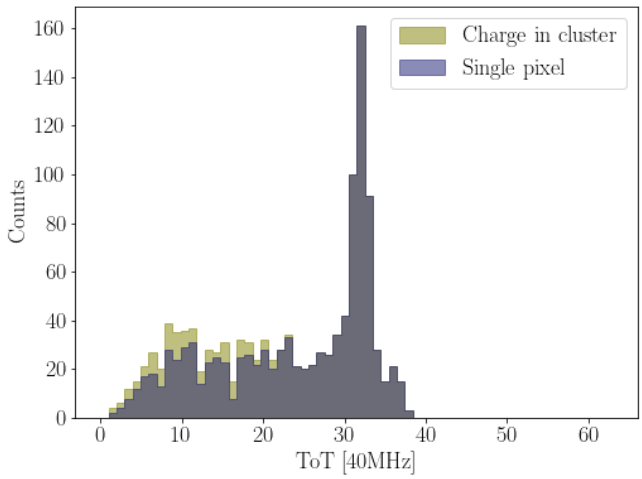

Figure 4.12: Charge collection dispersion of a single pixel before (blue) and after (olive) adding the entries of the neighboring pixels within the registered clusters for the default FE parameters.

The excess observed in the charge from clusters (olive) shows evidence of charge sharing for MIP-like particles such as the K_α peak of the ^{55}Fe. Notice that in this plot, the entries for the clusters are added to the pool but the value of ToT has not been summed. Both, K_α and K_β, peaks can be seen using single-pixel analysis for the default FE parameters. The position of the peak, in terms of ToT cycles, depends on the threshold value of each single pixel. Thus, the lack of in-pixel tuning and the consequent dispersion of the threshold values results also in a dispersion of the charge measurements. This, despite not being an issue for HEP experiments that measure MIPs, is large enough to smear the K_β out when showing the charge collection of the whole matrix as seen in Figure 4.13.

Figure 4.13 shows the charge collection distribution for the whole matrix. The tests were performed using both sets of FE parameters seen in Table 4.1, the default (left) and the optimised for clinical protons (right). The charge collected by each structure is presented separately, FDPW (olive) and RDPW (blue). It can be seen that the position of the K_α peak is different for the different FE parameters and for each structure. This is due to the different threshold values seen in the distributions of Figures 4.8 and 4.9 and Table 4.1. As discussed, the K_β peak is not visible in these plots.

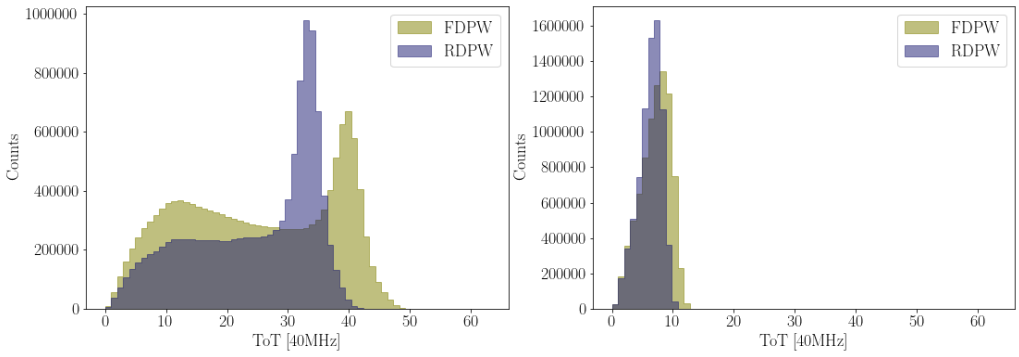

Figure 4.13: Charge collection distribution of the FDPW (olive) and the RDPW (blue) flavours after a 30-minute ^{55}Fe source scan using the default FE parameters (left) and the optimised from clinical protons (right).

The charge distribution of the lower threshold scan (default FE parameters) shows a clear K_α peak and a shoulder at lower ToT values due to charge sharing and losses at the edges of the pixels. Furthermore, it can also be seen that the FDPW distribution shows a

small bump at low energies that is not observed in the RDPW distribution. This effect is due to the charge sharing allowed by its lower threshold, see Figure 3.13, and the bigger charge cloud due to the weaker electric field at the edges of the pixel, see Figure 4.1.

However, when using the set of FE parameters optimised for clinical conditions, the charge distributions present a single wider peak. This shape is also expected due to the increment in threshold mean, the higher threshold results in a signal a factor of ~ 4 shorter, which results in a lower resolution on the energy deposited; and the dispersion observed when using the set of FE parameters optimised for CP. The ToT values of the positions of the K_α peak have been reduced from 34 to 7 ToT in the RDPW and from 40 to 7 ToT in the FDPW.

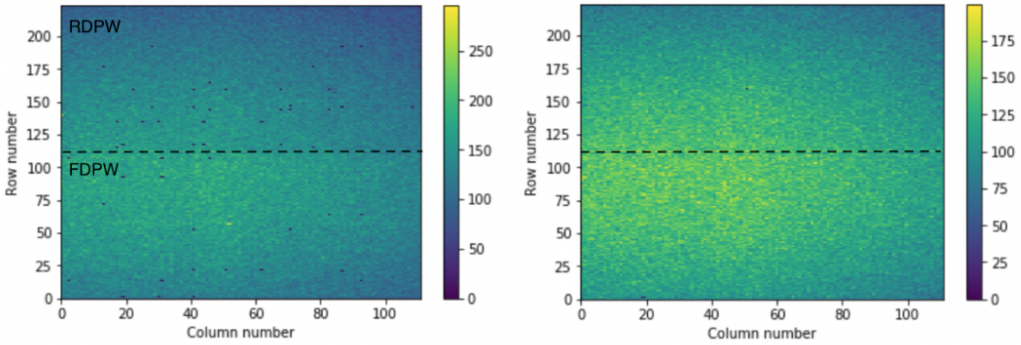

Figure 4.14: Hit occupancy maps of 600s source scans of an ^{55}Fe source under clean room conditions using the default (left) and optimised for clinical protons (right) FE parameters seen in Table 4.1.

Figure 4.14 shows two hit occupancy maps, before clustering, obtained from a ^{55}Fe source scan during 600 s, with the two different sets of FE values. Again, the values of the FE parameters used for these scans are the ones seen in Table 4.1, default (left), and the optimised for clinical protons (right). The plot on the left shows 51 masked pixels and an apparent non uniform response for the different structures. The difference in threshold between the FDPW and the RDPW results in more pixels being fired due to charge sharing. This issue is exposed when, as here, the hit map is computed before clustering. As seen in Section 4.5.1, the expected uniformity is recovered after clustering. The clinically optimised FE parameters result in no noisy pixels and a more uniform

response across the two sectors. The higher thresholds limit the charge sharing in both structures and this results in a uniform hit map for the K_α x-rays even before clustering.

4.4 Test beam with low energy protons

The MC40 Birmingham's cyclotron, described in 5.1, was used to target the TJ-Monopix with a 28 and 36 MeV proton beam in order to perform a source scan. The results and methodology of these experiments are presented in Sections 5 and 6.

Different collimators with different shapes and sizes were used for these scans. Notice that, protons at these energies are nonrelativistic ($\beta\gamma < 1$) and, as seen in Section 3.2 will deposit a large amount of charge of about 21 ke when passing through the detector. Thus, the high threshold distributions presented in 4.2.3 cannot compromise the efficiency of the sensors. The charge-sharing effect in the number of hits observed was seen in the previous section with the different performances of the FDPW and the RDPW. In the test beams, this effect is enhanced by the large amount of charge deposited by the non-relativistic protons. In order to reconstruct a track, the precise point is needed and therefore, in order to get this information and to properly analyse the data of these source scans the following clustering algorithm was developed.

4.5 Clustering algorithms

A specific Python script running the Density-Based Spatial Clustering of Applications with Noise (DBSCAN) [84] *sklearn* package was written to analyse the output data of the TJ-Monopix scans and merge the adjacent hits of a single event into a single cluster. DBSCAN, is a widely used clustering algorithm, it excels in analyzing complex datasets with irregular shapes and varying densities. The algorithm key parameters are ε, the maximum distance between a hit and the cluster for it to be added; and the number of minimum points (N_{Min}), DBSCAN identifies dense clusters and effectively detects outliers and noise. The algorithm then expands the cluster iteratively by examining the neighbors

of identified points. Points within ε distance but failing to meet N_{Min} become border ε are labeled as noise.

The clustering algorithm runs through all the events and takes all the pixels that are over threshold and runs a DBSCAN fit with the following parameters:

- $\varepsilon = \sqrt{2}$
- $N_{Min} = 1$
- Euclidean metric
- Default ('auto') algorithm

Where ε is set as $\sqrt{2}$ to include the adjacent pixels in the diagonal direction and N_{Min} here 1 is used in order to include single hits in the output. Since there are no correlations between axis the metric was set as Euclidean and the algorithm to be used by the NearestNeighbors module to compute pointwise distances and find nearest neighbors. With this "auto" selection, the algorithm will attempt to decide the most appropriate algorithm; between BallTree, KDTree and brute (brut force); based on the values passed to fit method. If a cluster contains hits in more than one pixel, the algorithm records the position of the particle by computing the centre of mass (charge) of all the fired pixels and adds all the charge values at that point.

Figure 4.15 shows a hit occupancy scan before (left) and after (right) applying the clustering algorithm for a test beam using a 2 mm colliator. As expected, the difference in the threshold dispersions for the FDPW and the RDPW structures, and different electric fields at the edge of the pixels; a uniform proton flux results in different hit occupancy densities between these structures due to charge sharing, see Figure 4.15 (left) Figure 4.15 (right), flavour uniformity is again recovered after clustering.

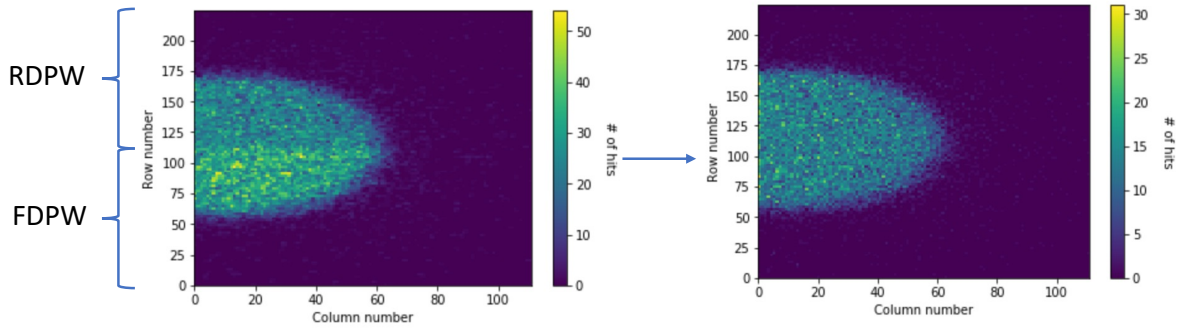

Figure 4.15: 2D hit map before (left) and after clustering (right). Before clustering, the difference in the mean threshold can be observed in the number of hits observed in both FDPW (below) and RDPW (above) through the higher number of hits observed before clustering; a lower threshold allows for larger charge sharing.

4.5.1 Cluster size and charge reconstruction

Once the hits have been clustered the results were analysed again to see if the algorithm worked as expected. In terms of grouping hits within the same event, the algorithm seems to perform as expected by grouping all adjacent hits and not creating artificial clusters nor mislabeling any hits as noise. However, the cluster size distribution, seen in Figure 4.16 did not follow the expected decaying trend. Moreover, the distribution for the FDPW and the RDPW demonstrated clear differences in shape and mean value.

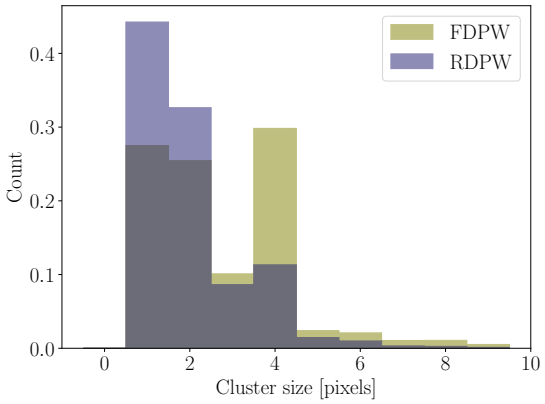

Figure 4.16: Cluster size distribution for the test beam with 36 MeV protons and a flat 1 cm^2 beam. The FDPW distribution is shown in olive while the RDPW is shown in blue.

With the results being far from expected, the cluster size was studied by comparing the performances with measurements done with the Default FE parameters and with the

measurements presented here, performed with the FE parameters optimised for clinical protons. The default parameters did provide an expected decaying distribution. Thus, the algorithm seemed to be working well regardless of the cluster size distribution observed with the high thresholds. This could be explained by the increase of dispersion in the threshold distribution seen in Figure 4.8.

Further tests were performed to deepen the understanding of this issue. First, the analysis of the distribution of the reconstructed charge. Figure 4.17 shows the reconstructed charge for the FDPW and RDPW clusters. The plots show histograms with the total reconstructed charge (yellow) and the charge separated for different cluster sizes: one (khaki), two (olive), three (royal blue), and four (navy blue).

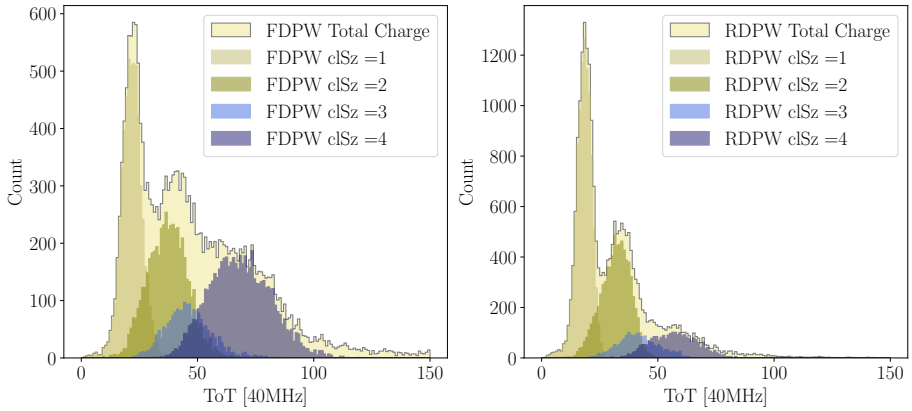

Figure 4.17: Histogram of the reconstructed charge at a test beam with 36 MeV protons and a flat 1 cm^2 beam. The histogram shows the summed charge of all clusters (yellow) and the charge separated for different cluster sizes: one (khaki), two (olive), three (royal blue), four (navy blue) for the FDPW (left) and the RDPW (right).

This shows an unexpected behaviour with well-defined, close-to-Gaussian, peaks that are equidistantly distributed. The first peak corresponding to cluster size one is found at a ToT of 15 cycles; then for cluster size two at 30 cycles, for three at 45 cycles, and for four at 60 cycles. The height of the peaks corresponds to the same observed in the cluster size distribution. This suggests that each hit has a ToT of around 15 cycles regardless of being part of a cluster or not. Thus, to test this, a histogram of the pixel charge collection was plotted with all hits, see Figure 4.18, separating the ones that are part of a cluster and

those that are not. As suggested by Figure 4.17, the distribution of the charge collected by all hits follows a distribution centered at 15 ToT cycles regardless of the size of the cluster.

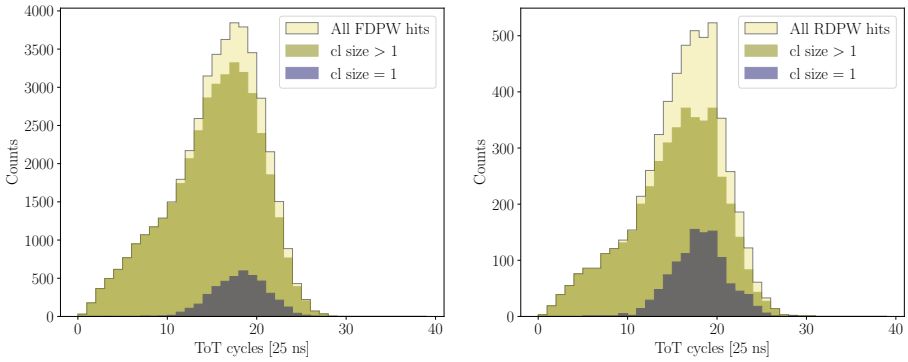

Figure 4.18: Histogram of the charge collection in all pixels (yellow) and separated by pixels within a cluster (olive) and single hits (blue) for the FDPW (left) and RDPW (right).

The unexpected cluster and reconstructed charge distributions suggest that the center of charge approach for the position of the hit might not be as accurate as expected. A simple mean position, not weighted by the charge deposited, of each pixel in the cluster could be a better approach until this issue is further understood. Nonetheless, regardless of the unexpected cluster distributions, the number of protons reconstructed seems to agree with the expected values, see Section 5.2 and thus, it does not affect the following work.

It is important to notice that, when using the MC40 cyclotron protons, the charge deposited in the sensor is around twenty times higher than the MIPs for which the sensor was optimised. Thus, to further understand the issue, a deeper understanding of the electric fields within the sensor and its response to high charge depositions would be needed. However, the TCAD[2] simulations were not available for this project and the analysis stopped here.

[2]TCAD stands for Technology Computer Aided Design and it is a simulation toolkit that allows studying the electric field within solid-state materials wildly used to design and simulate silicon sensors.

4.6 Chapter summary

A TJ-Monopix chip has been characterized and tested. With this characterisation the need of an optimised set of FE parameters for the clinical protons was obvious. A second TJ-Monopix set was characterised later with equivalent results in all sectors.

A new set of FE parameters was defined with the aim of increasing the threshold, reducing the analog signal length and finding a compromise with the threshold dispersion.

The TJ-Monopix chips were tested in the labs with a ^{55}Fe source with a K_α decay of 5.9 KeV and with 36 MeV protons at the MC40 cyclotron. The ^{55}Fe source scans were effective to get key insights of the TJ-Monopix. The test beams helped to understand the need for an optimised set of FE parameters to avoid the overflow of the ToT counter and confirmed the good performance of the TJ-Monopix measuring non-relativistic protons.

A DBSCAN based algorithm was written specifically for this project showing excellent performance. The cluster size distribution with the optimised set of FE parameters is yet to be understood. Several tests have been performed to ensure that given this issue we understand the signal with satisfactory results. TCAD simulations would be key to further understanding this issue.

With this, the TJ-Monopix can be used for medical applications with the question, answered in Section 5, if the electronics would be able to cope with high enough currents.

Chapter 5

TJ-Monopix for beam monitoring at the MC40 Cyclotron

pCT is a complex medical imaging technique that uses protons, rather than X-rays, to produce detailed images of the body. The technical challenges associated with pCT include the fact that clinical cyclotrons were designed primarily for proton therapy, rather than imaging. As a result, the operating currents used for proton therapy are much higher than those needed for pCT. To address this issue, techniques have been developed to reduce the beam current, however, the use of these techniques can limit the ability to monitor the beam for operators.

The TJ-Monopix has the potential to be used as a tool for beam monitoring in a clinical environment. This is due to its fast response, small pixel size, and low material budget. The device could provide feedback to the beam operators regarding the beams' behavior at low currents for individual protons for each bunch (if the frequency is below 40 MHz as in the MC40 cyclotron) or every few bunches for higher frequencies such as the 72 MHz frequency of the Christie beamline [85]. Thus, the TJ-Monopix could offer an online verification of the beam response when the current has been lowered. However, a limitation of this approach is the maximum flux of protons that the chip can read out without reaching saturation, see Section 5.2.

Additionally, a test was performed to evaluate the instantaneous capabilities of the TJ-Monopix by studying the opening time of the Faraday cup of the MC40 cyclotron and an external shutter. This serves both as a study of the MC40 cyclotron and as proof of the capabilities of the TJ-Monopix for beam monitoring.

5.1 The MC40 cyclotron

For this work, protons were sourced by the Scanditronix MC40 cyclotron that was brought to the University of Birmingham in 2002, see Figure 5.1.

The cyclotron, used mostly for irradiation purposes and nuclear and medical physics research, has a twelve-way switching magnet to split the beam at different lines. Line 4 is a research line used for detector testing and high irradiations.

For the purpose of this project only the research line, placed in the supervised area seen in yellow on the left of Figure 5.1, was used. This line can provide protons at energies between 11 to 40 MeV with a bunch frequency controlled by the Radio Frequency (RF) systems. The RF can be tuned over a range between 14.2 to 27.4 MHz. A frequency of 24 MHz, corresponding to 28 MeV, and proton currents ranging from pA to μA were used for this project.

The beamline consists of a set of modules divided into three different rooms. The MC40 cyclotron has a single diffusion pump whose exhaust is passed through a cold zeolite filter and then returned to the ion source in order to provide the vacuum. The cyclotron is then followed by a steering magnet, a quadrupole (for beam focusing), and the FC, labeled as FC1 in Figure 5.1, that blocks the beam when it is not needed in any of the target rooms. At the end of the cyclotron vault, a 12-way switching magnet is used to deliver the beam to the different lines.

Beamline 4 goes into the magnet room. The research line has a FC, labeled as FC2, placed at the beginning of the room, which is not used to control the beam delivery but only for security purposes. When a flat beam is needed, a Tantalum (Ta) foil is placed

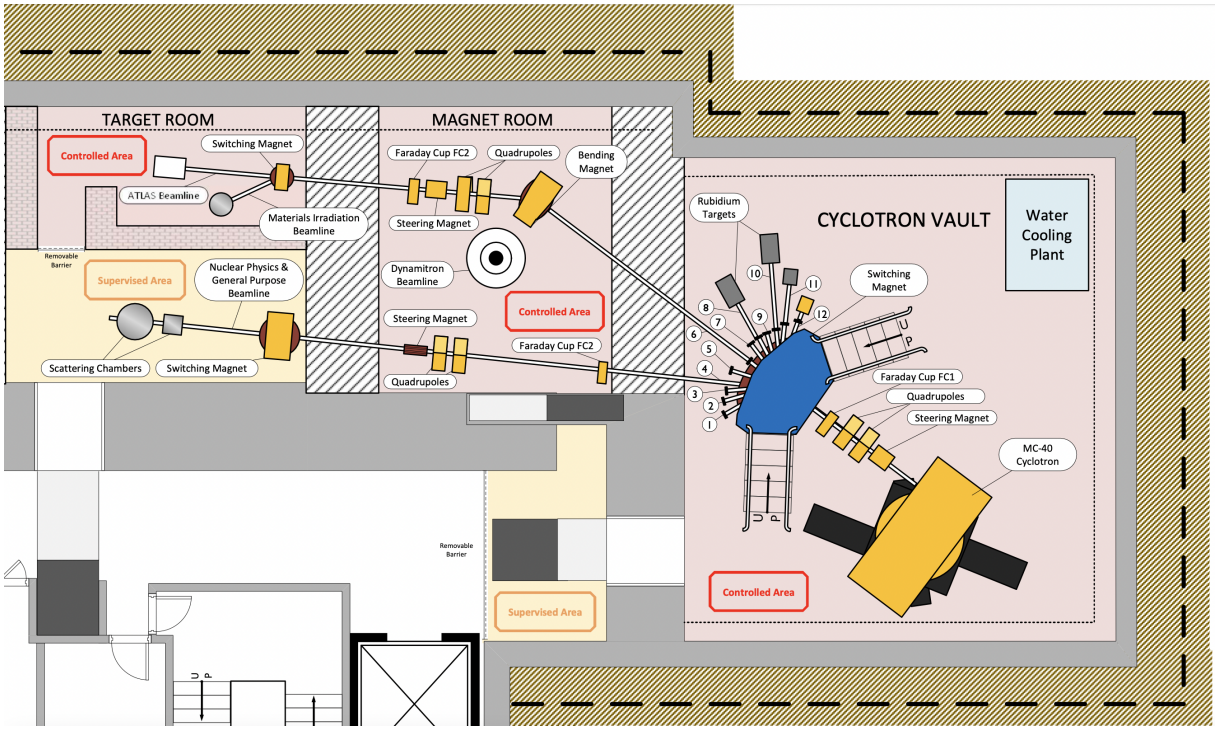

Figure 5.1: Sketch of the MC40 cyclotron with the control and the main room. The beam line used is the one in the supervised with lower beam intensities.

right after the FC2 in order to achieve an isotropic distribution thanks to the MCS. The quadrupoles in this room have also beam focusing purposes while the steering magnet aims to tune the beam down the beam pipe. In the target room the beam pipe has different extensions that can be used for each research purpose. The scattering chambers are not used for this work. After the switching magnet, an Ionisation Chamber (IC) is used to monitor the beam currents. The beam nozzle is placed right after the IC and a set of concrete blocks is used to stop the beam after the sensors.

5.2 Flux studies

5.2.1 Methodology

A single TJ-Monopix chip was used for this study at the MC40 cyclotron with a flat beam profile of 36 MeV protons, see Figure 5.2. To further reduce the size of the proton beam at the end of the beam nozzle, a set of collimators with different shapes and sizes was

used to study the saturation point as a function of the number of protons per second and flux. The first and second test beams were performed in September 2020 and April 2021 with a 1 cm thick aluminum collimator with a square-shaped 1 cm sided opening. The third set of test beams for this study was done in June 2022 with two smaller, 2 mm thick, Tantalum collimators: One counting 15 slits with 100 μm width and separated 400 μm, see Figure 5.3 and another with 6 holes with a 700 μm radius distributed in three rows separated 3 mm from row to row and 1.5, 2.5 and 3.5 mm, see Figure 5.4. The holes collimator is formed by four layers of 1 mm thick Ta shits. From now on, for clarity, the collimators will be referred to as squared, slits, and holes respectively.

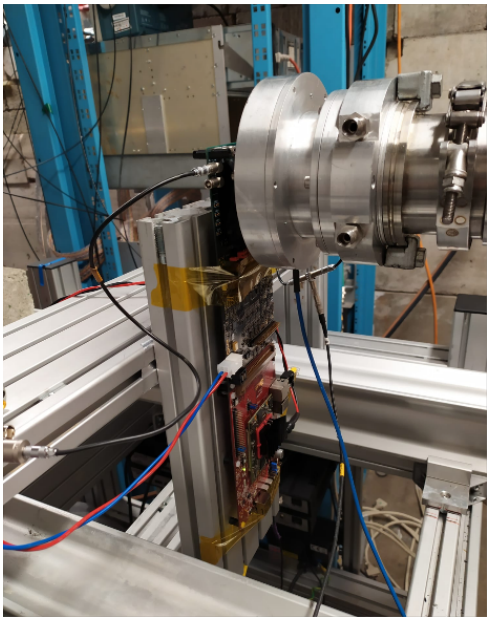

Figure 5.2: Image of a full TJ-Monopix system close to the beam nozzle of the MC40 cyclotron at the test beam performed in March 2020.

The number of protons measured as a function of time was compared with the expected values for each collimator. The expected number of protons was computed by integrating the beam profile over the slit size for the different opening areas.

For each collimator, several scans were taken at different beam currents measured at the IC. The currents used ranged between a few pico Amperes to one nano Ampere. These current values translate into a proton flux from 10^4 to 10^7 protons per second per cm^2 going through the IC. For each IC current (C_{IC}) the proton flux (ϕ), in units of

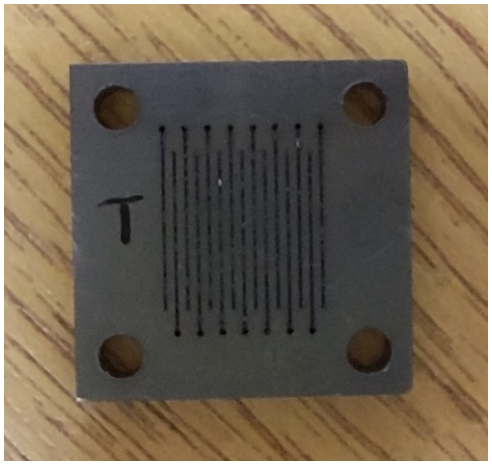

Figure 5.3: Picture of the slits collimator. The collimator consists on a 2 mm plate of Tantalum with 15 slits with 100 μm width, 8 mm length separated by 400 μm.

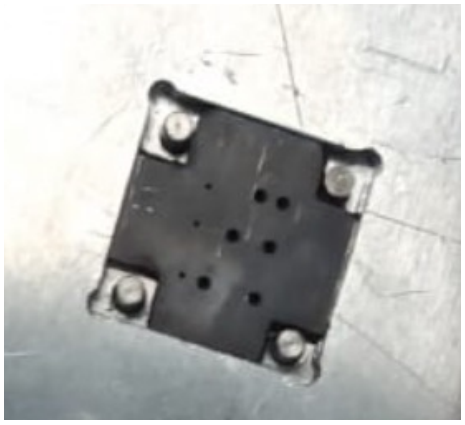

Figure 5.4: Picture of the holes collimator placed in the aluminium support. This collimator consists of four layers of 1 mm Ta shits. The three smaller holes were not used due to misalignment during the drilling process.

$\left[\frac{p}{cm^2 \times s}\right]$ can be computed as:

$$\phi = \frac{C_{IC} \times 6.28 \times 10^{18}}{160 \pi R_{Beam}^2} \tag{5.1}$$

Where 160 is the constant that correlates the number of electrons generated in the IC for each proton passing through and 6.28×10^{18} is the conversion from Coulomb to e for the charge. Notice that different collimator sizes will result in a different number of protons per second at a given IC current. Assuming a flat beam[1], for a given collimator with a total area A_C the number of expected protons as a function of time for a given

[1]Assumption valid when the scattering foil is in place.

time t is the result of the integral over time of $A_C \times \phi$:

$$N_{exp}(t) = \int_0^t A_C \times \phi \times dt' = A_C \times \phi \times t \tag{5.2}$$

For the squared and slits collimators, the current read at the IC was increased until reaching the breaking point in which the TJ-Monopix buffer was saturated. The saturation point is found when the number of events as a function of time does not react linearly over time and it behaves in a step ladder-like function. The plot on Figure 5.5 shows a normal time evolution for the number of clusters over time at a flux of 5 Mp/cm^2/s with an area of 0.072 cm^2 (black) and the time evolution for a saturating scenario with a flux of 7 Mp/cm^2/s over the same area (red). As expected, the gradient of the red line is steeper due to the higher current. However, a step pattern due to the saturation of the chip's readout electronics is observed. When this happens the breakdown point has been reached.

Different sizes of collimators were used to test different fluxes and fluences in order to test if the breakdown point was area dependent or not. It is noticeable that the evolution of clusters over time has a cyclic pattern that flattens the curve presenting a small Plateau every 10 ms. This is a consistent issue observed in all scans with currents above 0.1 Mp/s that needs to be further studied.

5.2.2 Results

The results of the test beam performed with each collimator are presented in this section.

Squared collimator

The test beams performed with the 1 cm^2 collimator present a good agreement between the expected and the measured clusters over time. Figure 5.6 shows the cluster hit map of the sensor presenting a flat distribution of clusters over the whole sensitive area of the sensor.

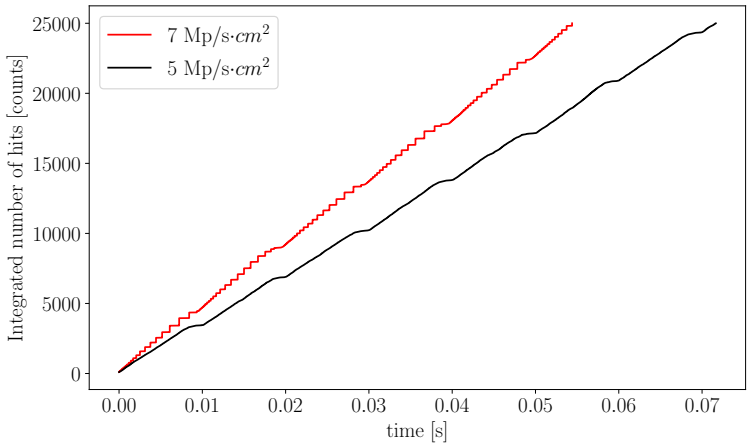

Figure 5.5: Plot of the total number of measured hits as a function of time for a current with the normal behaviour of the readout system at a flux of 5 M p/cm^2/s (black) and an example of saturation of the bus with 7 M p/cm^2/s (red).

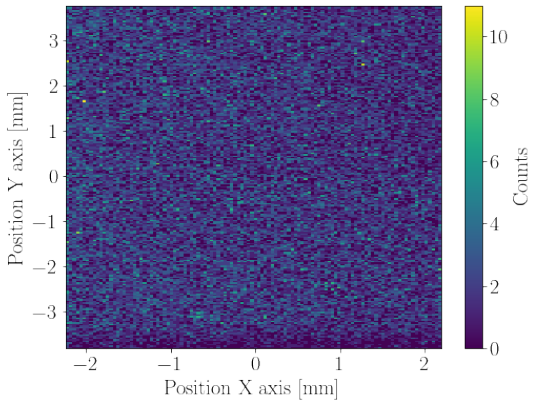

Figure 5.6: Cluster hit map of a scan with the squared collimator with 36 MeV protons.

Notice, that for this collimator, the number of protons is not limited by the size of the collimator but rather by the size of the sensor itself. The collimator is 1 cm^2 while the sensor is just 0.36 cm^2 and thus, this same fraction of the protons is going to be detected by the TJ-Monopix. Figure 5.7 shows the number of clusters per second as a function of the proton flux for the square collimator. The data shown was taken in September 2020 (red dots) and April 2021 (black crosses). Both data sets were then combined in order to obtain the fit shown by the black dashed line. The fitted gradient corresponds to A_C as seen in equation 5.2, the errors values associated with the fits were found to be one or

two orders of magnitude smaller than the precision of the known collimators' areas and thus, are presented. The expected number of protons, computed using Eq. 5.2, is shown with regions including ±5% and ±10% shown in the yellow and green areas respectively. These regions have been included as an estimate for the uncertainties of the calculation due to the different uncertainties of the parameters such as the pixel size, the current in the IC (C_{IC}), and the experimental conversion constant (160).

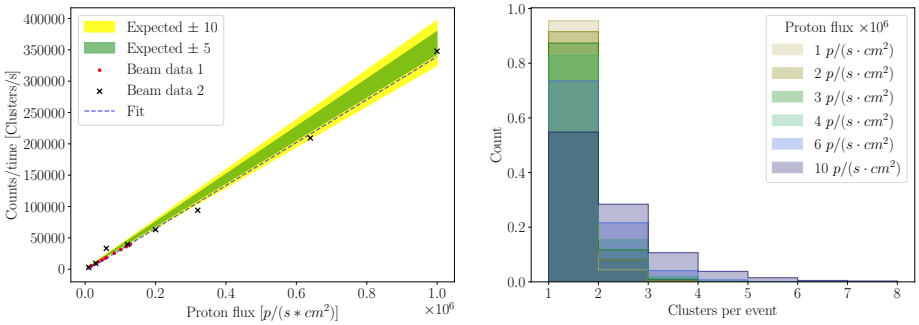

Figure 5.7: Plot of the clusters per second as a function of the proton flux using a 1 cm^2 collimator (left). The data obtained on test beams on in September 2020 (red dots) and April 2021 (black crosses) has been fitted (dashed black) to obtain the sensitive area covered by the beam. The yellow and green areas show the expected number of protons ±5% and ±10% respectively. Plot of the cluster size distribution for the different proton fluxes (right).

The area computed by the gradient $A'_C = 0.34$ cm^2, which corresponds to 5.6 % relative error compared to the value of $A_C = 0.36$ cm^2. This small discrepancy could be explained either by the loss of protons due to the beam's angular dispersion or an error in one of the multiple terms contributing to the computation of the expected number of protons such as the IC calibration or the pixel size (used to compute the sensor area) or more unlikely a drop in the efficiency of the TJ-Monopix.

The breakdown point was reached at about 0.4 M clusters per second at a flux of 1 $Mp/cm^2/s$.

The right plot from Figure 5.7 shows the distribution of the number of clusters per event for the different proton fluxes used. One can see how, as expected, the higher the proton flux the higher the number of clusters per event. However, the increase is not

linear. This suggests that at these low operating currents, the current increases due to more pulses being filled with protons rather than a proportional increase of the protons per bunch. Figure 5.8 shows, a histogram of the difference in time between two consecutive events for two different datasets; the first (yellow) with a current equivalent to 0.03 Mp/s and the second one with a current equivalent to 0.35 Mp/s (blue). The mean of both distributions is ∼0.007 ms and ∼0.036 ms. This way, the fast readout of the TJ-Monopix, allows to prove that the number of bunches increases when increasing the current at the order of a few pico Amperes read at the IC. Moreover, during these scans, the TJ-Monopix successfully measured up to 14 protons in a single event.

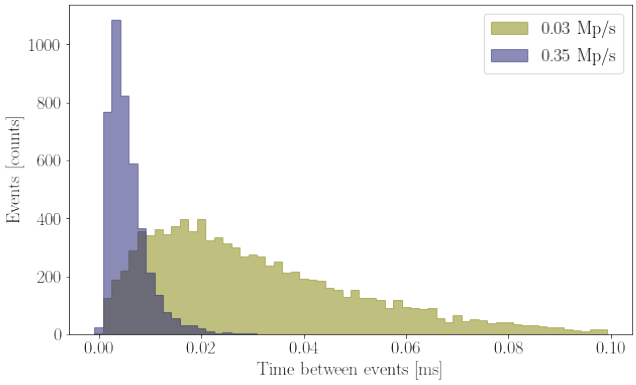

Figure 5.8: Histogram of the time difference between two consecutive events for two different data sets taken with an equivalent current of 0.03 Mp/s (yellow) and 0.35 Mp/s (blue).

Slits collimators

The slits collimator's data is presented in Figures 5.9, 5.10 and 5.11 for different scans with currents ranging between 0.2 to 7 Mp/cm^2/s. Figure 5.9 shows the cluster map for a scan using the slits collimator centered with the sensor using 36 MeV protons.

Similarly to the previous section, the expected number of clusters per second is plotted, as a function of the proton flux, with a ±5% and ±10% shown in yellow and green respectively together with the data points (black dots) and the fit of the data (dashed black).

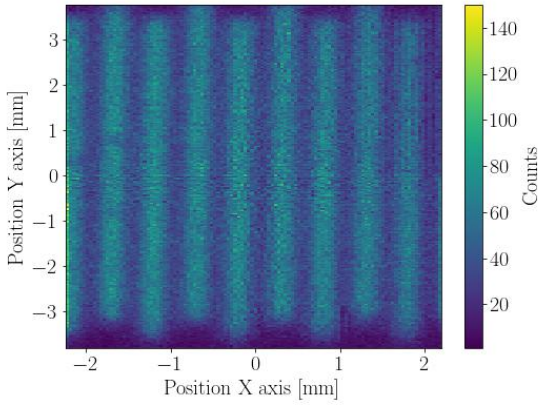

Figure 5.9: Cluster hit map of a scan with the 8×0.1 mm^2 slits collimator with 36 MeV protons.

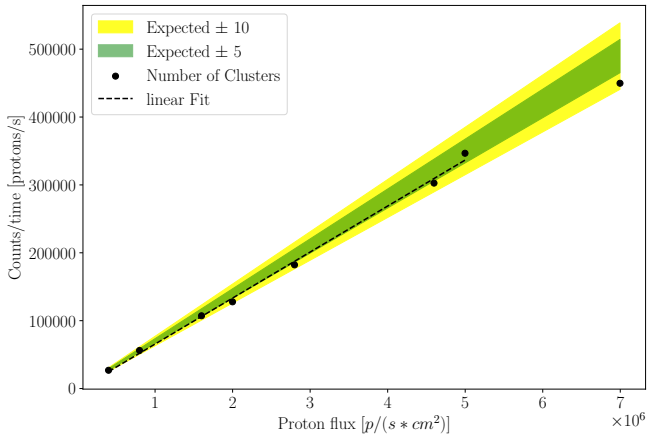

Figure 5.10: Plot of the clusters per second as a function of the proton flux using the slits collimator. The data obtained on test beams (black crosses) has been fitted (dashed black) to obtain the sensitive area covered by the beam. The yellow and green areas show the expected number of protons ±5% and ±10% respectively.

Notice that data was fitted up to 5 Mp/cm^2/s because the 7 Mp/cm^2/s dataset showed saturation effects and the breakdown point had been reached. The area measured using the gradient of the fit gives $A'_C = 0.068$ cm^2 compared with the expected $A_C = 0.07$ cm^2. The agreement between the expected and the measured gradient is again within a 5 % relative error. In this case, however, a further approximation needed to be done since there are slits that are partially integrated within the sensitive area of the sensor.

Figure 5.11 shows the number of clusters per second and the number of hits per second,

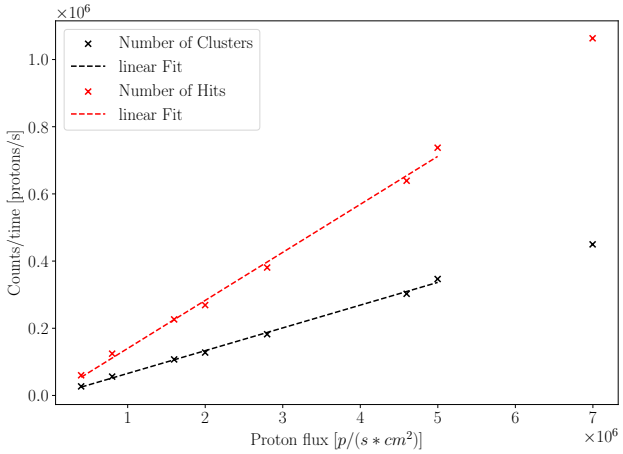

Figure 5.11: Plot of the hits per second as a function of proton flux (black) and clusters per second as a function of proton flux for nine slits with a total area of 0.072 cm^2. The data is fitted up to 5 p/cm^2/s avoiding fitting a value after reaching the breakdown point.

plotted here as a function of the beam's flux. It is important to notice that the breakdown point is reached again at about 1 M Hits/s regardless of the much smaller area. Hence, the idea to show these two different fits is to present the best and worst case scenario of flux reading that could be performed by the chip at a clinical beam with protons with energies above 100 MeV such as the pMBRT beamline at the Curie Institute. Chapter 7 shows the methodology and results of a test beam performed at this beamline. Due to the increased stopping power at 36 MeV compared to 100 MeV we expect the number of hits per cluster to be different. The best case scenario assumes that all hits would translate into actual protons *i.e.* the cluster size would be equal to one. The worst-case scenario assumes that the higher energy of the protons does not affect the cluster size regardless of the lower energy deposition.

Holes collimator

Figure 5.12 shows the cluster map for a scan using the holes collimator using 36 MeV protons.

The holes collimator has a much smaller area $A_C = 0.023$ cm^2. This allows the flux to go much higher without reaching the breakdown point. In Figure 5.13 one can see

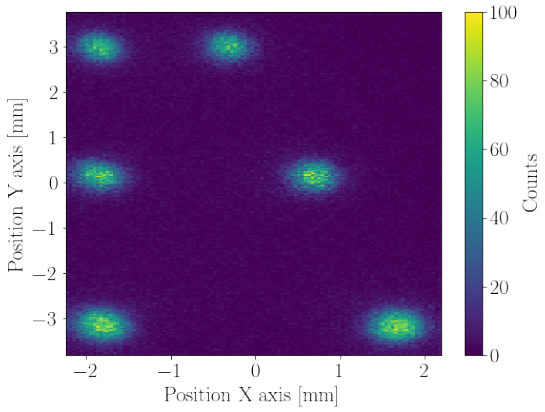

Figure 5.12: Cluster hit map of a scan with the six 0.75 mm diameter holes collimator with 36 MeV protons.

the data points taken for the different scans with currents up to 10 Mp/cm^2/s (black dots). In this case, the fit (black dashed line) includes all points since no saturation is observed. This was expected since, the number of hits per second is always below 0.5 M. Again, the regions within a ±5% and ±10% error in the gradient are shown in yellow and green respectively. The area measured by the gradient is $A'_C = 0.021$ cm^2, a 10% smaller than expected, again possibly due to a misalignment of the four Ta layers. This bigger discrepancy could be related to a misalignment of the Tantalum collimator layers resulting in a reduction of the effective area. Figure 5.14 shows the counts in hits and clusters per second as a function of the proton flux for the holes collimator. The proportion of the gradient between the hits and the clusters is smaller than the one observed in the slits collimator. This is due to the fact that most of the hits are in the RDPW section of the sensor (positive Y axis) and thus the cluster size is smaller. This effect is further explained in the next section.

5.2.3 Impact of the cluster size

As aforementioned, the key point for saturation is the total number of hits per second regardless of the area. Thus the cluster size can play a key role in the maximum flux that can be measured by the TJ-Monopix. As seen in Section 4.5.1, the cluster size distribution

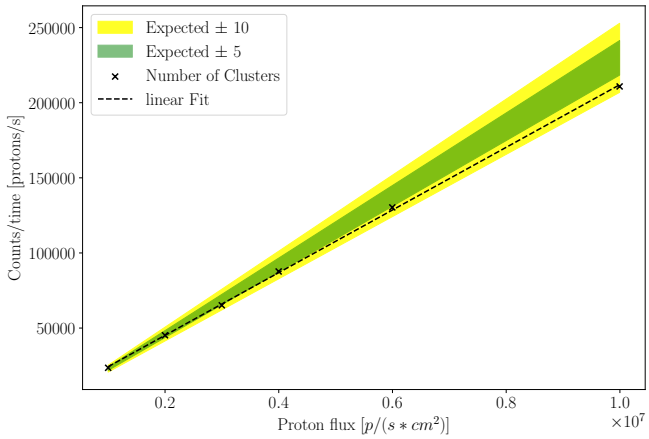

Figure 5.13: Plot of the clusters per second as a function of the proton flux using the six holes collimator. The data obtained on test beams (black crosses) has been fitted (dashed black) to obtain the sensitive area covered by the beam. The yellow and green areas show the expected number of protons ±5% and ±10% respectively.

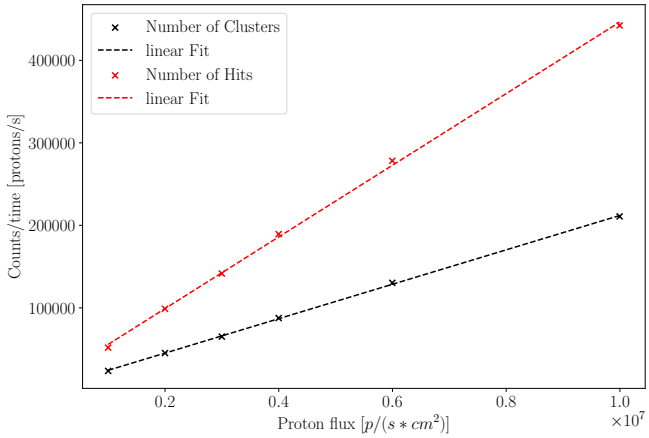

Figure 5.14: Plot of the hits per second as a function of proton flux (black) and clusters per second as a function of proton flux for six holes with a total area of 0.023 cm^2.

is different for each flavour. This means that for the same number of particles, the FDPW structure has a larger data flow due to a larger number of hits. It is important to know the mean cluster size of each matrix section.

- Mean cluster size (Cl_{Size}) for the different structures:

  Full Matrix: $Cl_{Size} = 2.1$

  FDPW: $Cl_{Size} = 2.4$

RDPW: $Cl_{Size} = 1.8$

Hence, measuring with only the RDPW structure one could hold 16% more clusters than with both of them and 33% more than with only the FDPW.

All these results suggest that the TJ-Monopix could be used to measure protons at with clinical beams containing high fluxes if the beam size is small enough, as it could be the case for pMBRT.

5.3 Study of the opening of the Faraday Cup

As previously mentioned, the MC40 cyclotron delivers the proton beam to the 12-way switching magnet by the opening of a FC that blocks the beam. In this section, a study of the time it takes for the FC1 to fully open the beam is performed by analysing the first milliseconds of the incidence of the beam in the sensor. As seen before, once the FC has fully opened the beam, the number of protons per second expected at the sensor grows as Equation 5.2 where A_C and ϕ are constant, and thus both can be extracted from the integral when integrating the hits over time. However, while the FC is opening the expected number of protons per second grows in time because the area of the opening of the FC is also time-dependent. Notice that, since the FC1 is placed before the Ta foil this affects the flux itself rather than the area of the collimator covered by the beam.

The expected number of hits over a time t grows following a parabolic behaviour while the FC is opening, after a time t_{FCO} at which the FC has opened the whole beam, the growth in the expected number of hits will be linear as shown by the following integrals:

$$N_{exp}(t) = \int_0^{t_{FCO}} A_C \times \phi(t') \times dt' + \int_{t_{FCO}}^{t} A_C \times \phi \times dt' \tag{5.3}$$

For the first integral, while the FC is opening ($t < t_{FCO}$) the flux would be a function of time that will depend on the velocity of the FC and the shape of the beam. However, for the purpose of this experiment, one can assume a Taylor expansion up to the third degree, see Figure 5.16, and thus the flux would be defined as:

$$\phi(t) = K_{v1} \times t + K_{v2} \times t^2 + K_{v3} \times t^3 \tag{5.4}$$

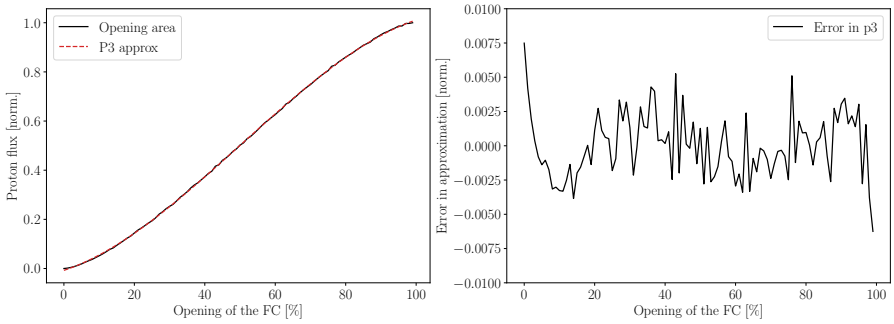

Figure 5.15: The plot on the left shows, the opening area of the beam as a function of the percentage of the FC opening (black) together with a third degree polynomial fit (dashed red). The plot on the right shows the error at each point for fit always below 0.8%.

Figure 5.15 shows the growth in the opening area of the beam as a function of the percentage of the FC opening using a circular collimator, together with fit of the expansion up to a third degree polynomial.

Using this definition the expected number of protons after a certain time $t \leq t_{FCO}$ would be:

$$N_{exp}(t) = \int_0^t A_C \times \phi(t') \times dt' \simeq \int_0^t A_C \times K_v \times P(t'^3) dt' \tag{5.5}$$

Where $P(t'^3)$ is the third degree polynomial resulting from the fit of the percentage of the opening area of the FC. This results in a fourth degree parabolic growth. Since A_C and K_v are constants, they can be extracted from the integral, and thus the expected number of protons after a time $t < t_{FCO}$ would be represented as:

$$N_{exp}(t) = A_C \times K_v \times P(t^4) \tag{5.6}$$

Where $P(t^4)$ is the fourth degree polynomial that represents the integral of $P(t^3)$.

This demonstration was used in this section as the basis to study the time that it takes for the FC to open the beam fully (t_{FCO}) following two different methods. One method aims to analyse the number of hits as a function of time and determine when the

parabolic behaviour ends and the linear growth starts while the second method studies when the time between events becomes constant.

The aim of this study is to understand if the MC40 cyclotron is capable of performing FLASH irradiations using the FC or if an external shutter is needed. Flash therapy aims to provide the full dose in a few hundred mili-seconds while ensuring that the beam distribution is uniform. The state-of-the-art FLASH treatments are performed within a time below 300 ms [39], [86]. Thus, showing that the MC40 cyclotron's FC could open and close faster than this time would imply an improvement in the dose rate and it would show that the TJ-Monopix is capable of monitoring such beam conditions. Further studies may show how fast one could go by using an external shutter.

5.3.1 Methodology

For these studies, the beam profile was flat (Ta foil in place), the circular 5 cm radius collimator was placed before the IC, and the squared 1 cm^2 collimator was used at the beam nozzle with 28 MeV protons. For the data acquisition, a single TJ-Monopix chip was placed 1 cm away from the beam nozzle and used to analyse the counts as a function of time for different scans.

In order to perform the scans, with the beam off, the sensor was turned on and started recording. The beam was turned on for a couple of seconds to ensure there was enough data to properly fit the linear behaviour of the number of protons as a function of time. The aim of this test was to observe the expected parabolic behaviour of equation 5.3 before the FC is fully open and compute the opening time t_{FCO}. The high threshold used on the TJ-Monopix for medical applications reduces the noise down to less than 20 hits every second in potentially noisy areas such as the cyclotron beam line. The noisy hits were removed by defining $t = 0$ at the time stamp when more than two events are found within 200 μs. Thus, the first hits coming from the proton beam were observed and analysed. For the purpose of this study, the time between events was analysed and averaged every five events.

The data was analysed through two different methods that were later on combined. First, the number of hits as function of the time; the expected response for this variable is to grow as following a parabola while the FC is opening (from $t = 0$ to $t = t_1$) and then a linear regime is reached.

For this method, a linear fit was provided between two points clearly beyond t_{FCO}. Starting at $t = 0$, the data points were compared with the linear fit defining a Δ_i for each data point until reaching the condition: $\Delta_i < \delta$ where δ was defined as two times the standard deviation of the distance between the data points and the linear fit within the selected fitting area.

The second, the time between events as a function of time, this variable decays until the FC is fully open and then it remains constant[2]. Similarly to the previous method, a stable region beyond t_{FCO} was selected to compute the mean distance between events. Then, starting from $t = 0$, the values of the distance between events were compared with the mean and t_{FCO} was selected when the distance between the data and the mean was smaller than two times the standard deviation of the points used to compute the mean.

The measure was repeated with 8 different datasets with currents ranging between 100 and 500 pA. The values obtained for the different measures were averaged and the error associated is the dispersion of the distribution. The measured t_{FCO} is then the mean of the results obtained with both methods.

Finally to test that the beam is, as expected, evenly distributed while the FC is still opening the 2D cluster maps, with data from 0 to 20 ms at intervals of 5 ms, were analised. The cluster maps shown are not accumulative and thus the clusters accepted are just within these 5 ms.

[2]Notice that here the spikes due to the beam behaviour are not taken into account and the mean time between events is computed between two peaks.

5.3.2 Results

Figure 5.16 shows the two plots presenting the data used in order to measure the opening time of the FC. The plot on the left shows the number of hits at the TJ-Monopix as a function of time from the beam opening (blue) and the constant evolution fitted (dashed blue) after the FC is fully open showing the contrast between the parabolic and linear behaviour.

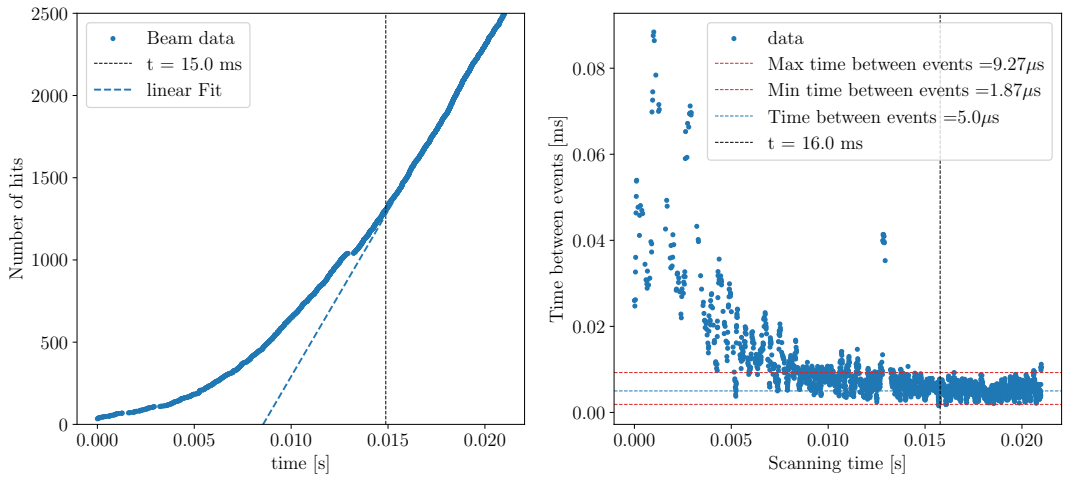

Figure 5.16: Left plot: Number of hits observed as a function of time from the opening of the FC (blue) and the constant evolution fitted (dashed blue) showing the contrast between the opening and fully open. Right plot: The vertical dashed black lines show the time in which the FC is fully open. The time between events as a function of time (blue) and the constant behaviour once the FC has fully opened the beam (dashed blue). The minimum and maximum times between events are shown in dashed red lines. The peaks observed are the result of the known small Plateau observed every 10 ms and shown in Figure 5.5. The dashed black line shows the time in which the FC is fully open.

The method checking the beginning of the linear response results in $t_{FCO_L} = 14 \pm 2$ms, while the method studying the time between events results in $t_{FCO_T} = 15 \pm 5$ ms. The combined result of the opening time is $t_{FCO} = 14.5 \pm 3$ ms.

Figure 5.17 shows the cluster maps of the intervals from 0 to 20 ms in steps of 5 ms. All distributions show clusters across the whole sensor area due to the flattening caused by the Ta foil as expected even during the opening time of the FC. The position distribution

in X and Y is shown in 5.1 with low deviations from the expected 0 mean besides the low statistics with a maximum of 0.12 mm deviation.

Interval [ms]	Mean position in X [mm]	Mean position in Y [mm]
[0,5)	0.07	0.11
[5,10)	0.12	-0.05
[10,15)	0.03	0.11
[15,20)	-0.07	0.01

Table 5.1: Mean of the position distribution in the X and Y axis for the different intervals between $t = 0$ and $t = 20$ ms.

This knowledge encourages the use of a shutter if used before the Ta foil since the shutter could still provide a flat beam during the moving time of the shutter at least for areas of 1 cm^2.

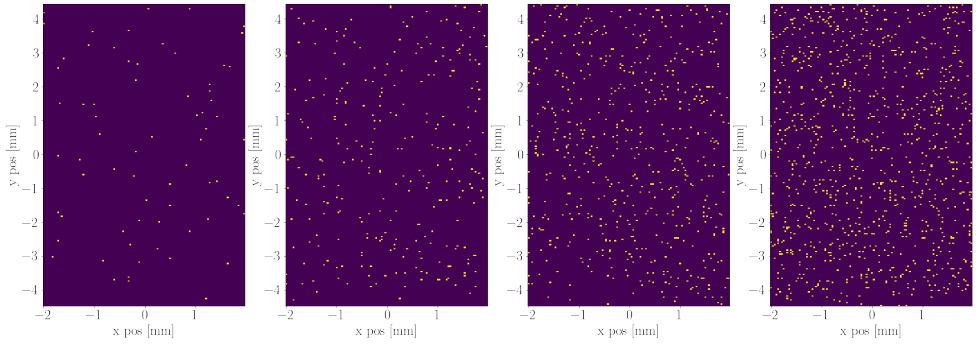

Figure 5.17: 2D cluster map of the TJ-Monopix for intervals of 5 ms from the FC being fully closed (t=0) to fully open (t = 20 ms), from top left to bottom right the intervals are [0,5], [5,10], [10,15] and [15,20] ms. The maps are not accumulative so the hits are not repeated from one map to the next.

5.4 Chapter summary

The TJ-Monopix has been tested with the MC40 cyclotron providing satisfactory performance.

The studies of the performance of the TJ-Monopix at different fluxes with different collimators show good agreement between the expected number of protons and the measured number of protons for fluxes ranging 10^4 up to 10^7 protons per second per cm^2.

The studies also show that the TJ-Monopix saturates at a fluence of 1 M hits/s regardless of the area of the incident beam.

The cluster size is dependent on the flavour structure and thus, a sensor with the RDPW could perform scans with a flux up to 16 % higher than with this mixed structure and up to 33 % than with the FDPW alone.

Several scans have been performed at different currents and the opening times have been computed with two different methods. The results of the methods seem to be in agreement with each other and have been averaged to obtain a final value. The times range between 10 and 20 ms which implies that, if the closing time is similarly fast, the MC40 cyclotron could deliver homogeneous irradiations within a time below 50 ms. This would improve by a factor between 3 and 5 the FLASH radiotherapy dose rates used at the moment. Moreover, the uniform distribution observed in the different intervals while the FC was opening suggests that the use of a shutter placed before the tin foil could still provide a flat beam distribution.

Chapter 6

Tracking MC40 protons with the TJ-Monopix

In this chapter, the methodology, analysis, and conclusions of the studies performed with the first tracker build with TJ-Monopix sensors, at the MC40 cyclotron in Birmingham, are presented. The aims of these studies were to prove the capability of the TJ-Monopix to track low-energy protons and to compare the angular dispersion observed for the ω and θ angles defined in Figure 3.5 with the ones simulated with Geant4 using the same beam profile. The results of this chapter will serve as a base for the use of this tracker with a clinical beam.

6.1 Methodology

Two sets of TJ-Monopix detectors were used for this work as shown in Figure 6.1. The telescope mechanics are explained in Section 6.1.1. The beam profile used was a circular beam with a 2 mm diameter aligned at the center of the sensors to reduce the geometrical inefficiencies. The first sensor was placed 10 cm away from the collimator and the distance between sensors was set to 5 cm. The energy of the protons was set to 28 MeV and the fluence used was of about 0.5 Mp/cm^2/s to ensure single proton events. With this current the percentage of events with more than one proton was negligible. Refer to Figure 5.7 to

see the statistics of multi-proton events for 1 Mp/cm^2/s. This was done to avoid tracking mismatches due to MCS. The effect of MCS is further explained in Section 6.1.3. No external trigger was used for this test beam implying that the TJ-Monopix detectors could not be synchronised. In Section 6.1.2 an algorithm developed to match the events from both sensors is presented. In Section 6.2.1 a Geant4 simulation of the full Birmingham's MC40 beamline is presented in order to compare the angular dispersion of the proton tracks obtained with the TJ-Monopix.

6.1.1 Telescope mechanics and alignment

The mechanical system, seen in Figure 6.1, used for the TJ-Monopix telescope consists of two building blocks: An aluminium frame and a set of "L" shaped sensor holders with two-dimensional micrometers used for precision alignment. The rectangular frame was mounted with precision corners that ensure an angle of 90 degrees between the sides at the bar junctions. The frame bars have a rail that allows up to four other horizontal bars (where the sensor holders are mounted) to move freely in the direction of the proton beam (Z). The bars are screwed with corner shapes, that also ensure perpendicularity, into the desired positions to fix the right distance between sensors. The "L" shaped pieces consist of two aluminium boards, one that holds the three boards of the sensor setup and attaches it to a two-dimensional micrometer, the second mounts the micrometer on the horizontal bar of the frame. The micrometers placed on the detector holder, seen in Figure 6.2, allow for a very high precision alignment with the beam, see the top plots in Figure 6.3. Furthermore, an offline alignment applied during the reconstruction process allows for even finer alignment as seen at the bottom plots of Figure 6.3.

The histograms presented in Figures 6.3 show the X (left) and Y (right) position dispersion for the front and back sensors before (top) and after (right) the fine alignment. The mean of the Gaussian distributions represents the position of the center of the beam. Thus, before the fine alignment, the displacement in the position is of the order of a few

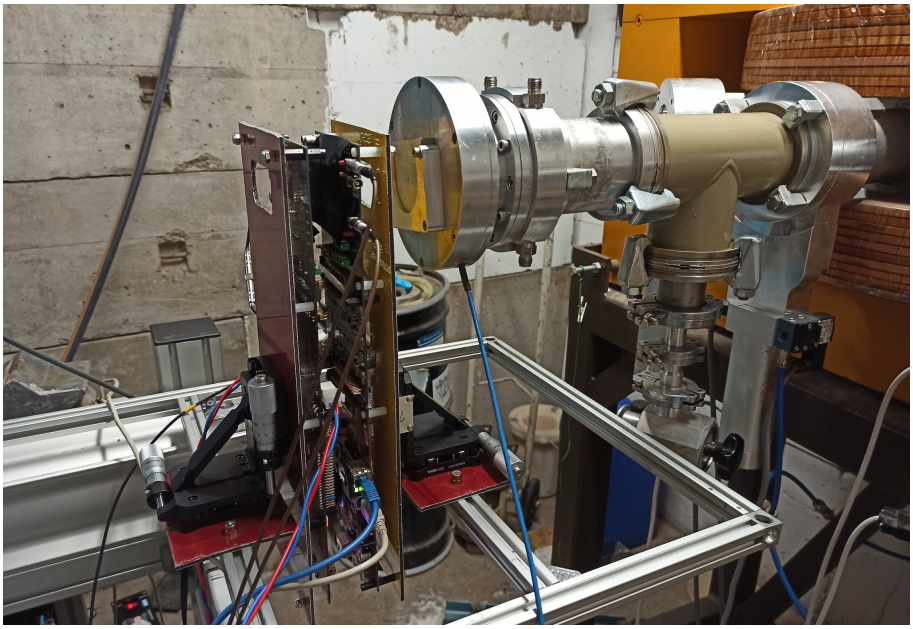

Figure 6.1: Image of the mechanical telescope built at the MC40 Birmingham's beamline.

Figure 6.2: Image of the XY micrometer used for the mechanical system of the TJ-Monopix telescope.

hundred micrometers (up to 10 pixels) as seen in Figure 6.3.

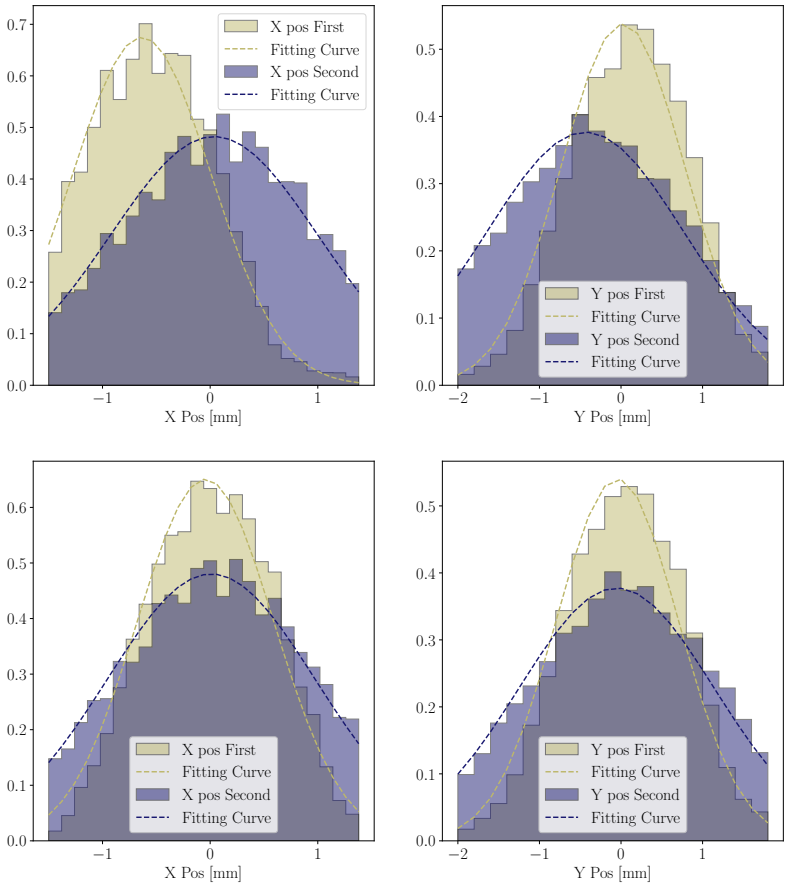

Figure 6.3: X (left) and Y (right) position dispersion for the first (yellow) and second (blue) sensors before (top) and after (bottom) the fine alignment. The μ obtained from the fit represents the deviation from the beam centre.

Beam position before fine alignment:

Front: μ_x = -0.0561 $\pm$ 0.0003 mm μ_y = 0.3165 $\pm$ 0.0008 mm

Back: μ_x = -0.3349 $\pm$ 0.0001 mm μ_y = -0.2176 $\pm$ 0.0001 mm.

The plots presented in Figure 6.3 show an alignment of the order of a few micrometers after the fine alignment translation was applied.

Beam position after fine alignment:

Front: μ_x = -0.0020 ± 0.0003 mm μ_y = 0.0060 ± 0.0008 mm

Back: μ_x = -0.0010 ± 0.0001 mm μ_y = -0.0040 ± 0.0001 mm

The position defined after fine alignment, relative to the beam centre, is going to be used for future sections.

6.1.2 Event matching

As shown in Section 4.1, the TJ-Monopix does not have any internal trigger. Thus, in order to synchronise hits with other sensors a Trigger Logic Unit (TLU) is needed. However, no TLUs were available to be used for this project and an alternative method with an offline event-matching algorithm was proposed. Contrary to the first expectations, matching the first events from both sensors was not enough to define a common t_0 and match the rest of the events according to the time stamp relative to it. The first test beam with two TJ-Monopix sensors at the MC40 cyclotron presented evidence of a delay between sensors' time stamps that could be caused by a difference in the frequencies of the detectors' clocks.

Delay tests

Two independent tests were performed to analyse the delay between the clocks: One testing the time stamps when the beam was turned on and off during a single source scan to be able to use these times as true information; and another, performed after matching the events, comparing the event by event delay defined as the difference between the event's time stamp relative to the one of the first matched event. The left plot in Figure 6.4 shows the integrated number of clusters observed in the front (blue) and back (orange) sensors over time to illustrate the profile of a 45 s test beam scan in which the beam turned on and off every 5 seconds approximately. The lower number of clusters as a function of time for the back sensor was expected due to geometric inefficiencies caused

by the large MCS observed with 28 MeV protons. The geometric efficiency was measured at each data set and consistently found to be 91 %. For this test, the beam was turned on and off at times around t = 7, 12, 17, 22, 27, 32, 36, 40 and 45 s resulting in the flat sections of the plot. As aforementioned, the times in which the beam was switched on, or off, were used as true information to account for differences in the time passed for each sensor. On the right plot, the scattered black crosses show the time delay between the front and back sensors measured at each On-Off point as a function of the scanning time. The black dashed line shows the fit of these points. The red solid line shows the delay between sensors measured at every event relative to the time at the first t_0 after applying the matching algorithm defined below. The good agreement between the On-Off fit and the event-by-event delay measured after matching suggests that the delay is something that indeed grows with time and that can be measured with two independent methods presenting the same result. The gradient of the delay was measured to be around 10 $\mu s/s$ but not consistent enough to perform a permanent correction to the time stamp. Hence, an event-matching algorithm that accounted for this issue needed to be implemented.

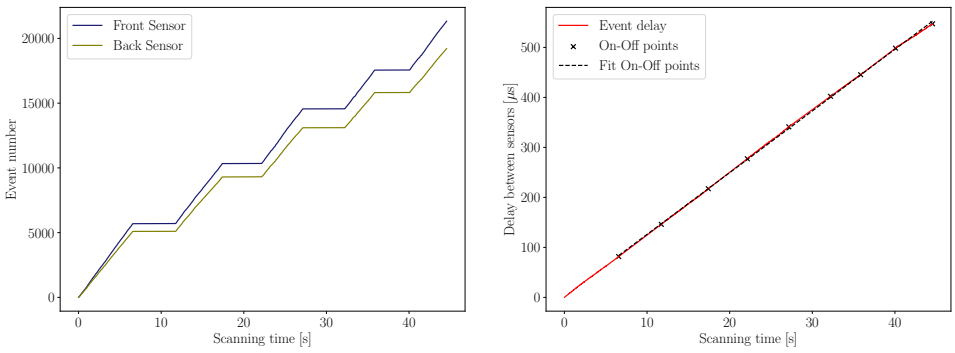

Figure 6.4: The left graph shows a plot of the event number as a function of the scanning time for the front (blue) and back (orange) sensors on a On-Off beam scan. The right plot shows the delay between the front and back sensors as a function of scanning time measured through On-Off points (black crosses and black dashed line) and through the event by event after matching (red line).

Matching algorithm

The algorithm uses sliced sets of **N** events to avoid the accumulated delay impacting the matching. The algorithm works as follows:

- Looking at the time stamp of the first event in the second sensor's list of events and computing the time difference between that event and the **N** following events defining a set of Δt_i, with i growing from 1 to **N**

- Performing the same analysis with the first event in the first sensor and computing the **N** values of $\Delta t'_i$.

- Comparing the Δt_i values to the $\Delta t'_i$:

  If the condition $\|\Delta t_i - \Delta t'_i\| < \delta$, where δ is a free parameter, is fulfilled $\forall i < N$ the events are matched together.

  After that, the algorithm repeats the same procedure starting with the **N**-th hit as the new seed.

- If a match is not found, the algorithm removes the first hit of the first sensor's list and looks for the following N events starting from the 2nd hit on the list.

- The cycle is repeated until reaching the end of the list of hits of the 2nd sensor.

A cut-off condition is applied based on the geometrical efficiency of the system so the seed event in the second sensor is taken away from the pool when: $event\ number_i \geq event\ number_j \times (1-\varepsilon) + K$ where i and j stand for the 1^{st} and 2^{nd} sensor indices respectively, ε is the geometrical efficiency and K is an offset value to prevent errors coming from statistical fluctuations. The values of $\mathbf{N} = 2$, $\delta = 0.2$ μs and $K = 15$ have been found to be the ones that optimise the matching efficiency.

No spatial or angular restrictions have been applied due to the large MCS observed on the low energy protons and the small sensitive area.

Correlation test

The previously observed agreement between the delay observed at the matched events and the *On-Off* points was not proof of the correlation between the matched protons at the front and back sensor. Hence, a new test was performed in order to further study the performance of the matching algorithm dependent on the correlation between the hits in the first and second sensors.

Since the only variable used by the matching algorithm was the time between events, this distribution was fitted and the fit was then used in order to simulate independent data sets from it. Both the real and simulated data are shown on the plot in Figure 6.5.

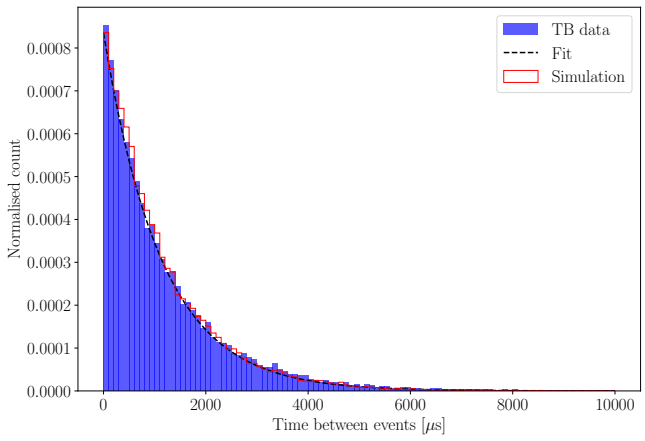

Figure 6.5: Normalised histogram of the time between events. The data measured on a test beam scan is presented in blue, a black dashed line shows the exponential fit and the red line shows the simulation obtained afterward.

Three different tests were performed with these simulations to analyse the performance of the algorithm. For a given test 100000 *time between events* were simulated and each test was repeated 1000 times to ensure good statistics. The first test consisted on using two independent data sets, one for the front and one for the back sensor ensuring no correlation between first and second sensor protons. The second test consisted on using the same data set for the front and back sensors being then completely correlated. For the third, the data sets were simulated for the front sensor, and from these data sets a random 9% of the protons were removed in order to mimic the 91% geometrical efficiency

observed during the TB.

As expected, the algorithm performed with a 100% efficiency when using the same data set for front and back and 0% efficiency when the two data sets were completely independent from one another. The distribution seen in Figure 6.6 follows a Gaussian with a mean at 85.9% efficiency. This result is in good agreement with the 86% efficiency found when applying the algorithm to the TB dataset.

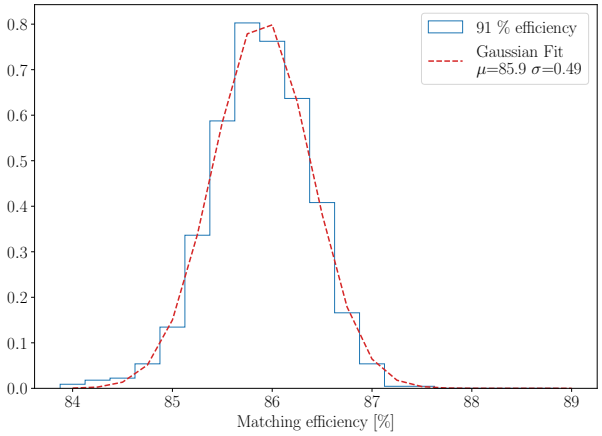

Figure 6.6: Efficiency dispersion of the efficiency of running the matching algorithm for 1000 different data sets of 100000 events each. The mean of the distribution is at 85.9 %
.

Evaluation of the results

With both tests confirming the need for correlation between protons for the algorithm to work, the agreement on the matching efficiency after accounting for the losses due to MCS and the further agreement between the delay observed at the On-and-Off points and the instantaneous delay of the matched events, it was concluded that the algorithm worked efficiently.

6.1.3 Effect of MCS when tracking with two planes

The MCS complicates the tracking and projection of the protons at 28 MeV. A Geant4 simulation of the TJ-Monopix tracker with two sensors separated by 5 cm was performed

using 5000 protons placed in five different positions separated, at least, 0.5 mm each at the (x,y) positions (-0.5,0), (0,0), (0.5,0), (0,0.5),(0,-0.5). This test was performed to illustrate the effect of the MCS.

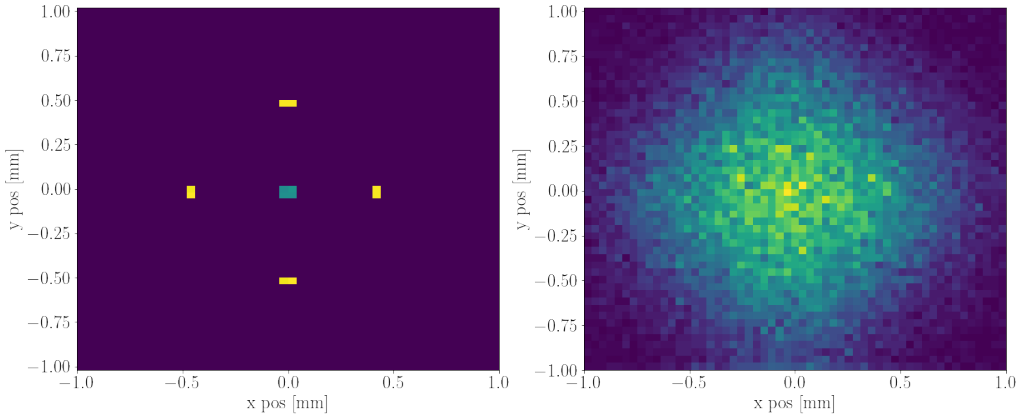

Figure 6.7: 2D histograms of the proton positions at the first (left) and 2nd (right) sensors, 5 cm apart, with a proton beam energy of 28 MeV.

Figure 6.7 shows the hit occupancy scan of the first (left) and second (right) sensors separated by 5 cm. The protons at the first sensor are clearly distributed in the first original positions while the second sensor presents a dispersed cloud of protons occupying the whole region of the sensor. This visualisation shows how the MCS can affect the efficiency when tracking multiple protons found at the same frame (event) due to the MCS allowing them to cross paths.

Figure 6.8 shows a top view of this effect seen on an event with two protons. The orange lines represent the original tracks while the blue lines represent the tracks that would be reconstructed by a common algorithm like the one used in 8.3.1. The protons arrive in a close-to-parallel direction from the beam nozzle and hit the first sensor. If the angular dispersion due to MCS allows the variation in X or Y coordinates between the first and second sensor to be comparable to the mean distance between two protons in the first sensor it is *impossible* to track multiple protons with a high purity. Using the information a scan with the 2 mm diameter collimator and the distance between sensors of 5 cm with single proton events the distributions of the distance due to MCS and

the distance between two protons observed in two consecutive events were studied. The histograms are presented in Figure 6.9. The mean distance between two tracks in the first sensor is 1.19 mm whilst the mean dispersion between the first and second sensor is 0.9 mm. These values are within a 20 % margin and the distributions are clearly overlapping. Thus, tracking multiple protons is not possible at these energies and the currents were reduced to minimise the possibility of multi-proton events. On the same note, projecting the tracks of individual protons with two planes are not accurate. In this section, the aim of the tracking and projection is used only to test the tools used as a base for future test beams at higher energies.

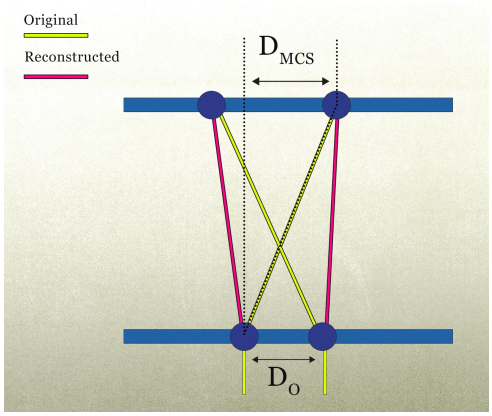

Figure 6.8: Top visualisation of the effect of MCS defining the initial distance between protons (D_0) and the dispersion distance (D_{MCS}) due to the MCS.

6.2 Tracking results at MC40 Cyclotron

Using the matching algorithm described above, the two TJ-Monopix sensors setup was able to track individual protons using small beams at the MC40 cyclotron. As previously mentioned, at this low energy (28 MeV) the MCS is paramount for the dispersion of the beam observed in Figure 6.10. Hence the proton tracking with two layers, while it provides a proof of concept of the capabilities of the sensor, it does not allow to perform a projection of the tracks with a relevant position resolution. The efficiency of the tracker, defined as the ratio of the number of reconstructed tracks over the total number of clusters

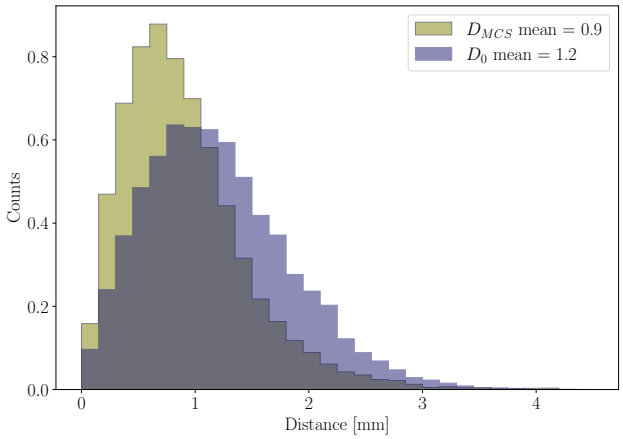

Figure 6.9: Histogram of the distribution of the proton displacement due to MCS (D_{MCS}) in yellow and the initial distance between two consecutive protons (D_0).

measured in the first sensor was 86 %, in agreement with the expected efficiency obtained by the correlation test. The projection back to the collimator of Figure 6.10 shows how, regardless of using true information for the tracks, the back-projection does not recover the collimator shape due to the effect of MCS discussed above.

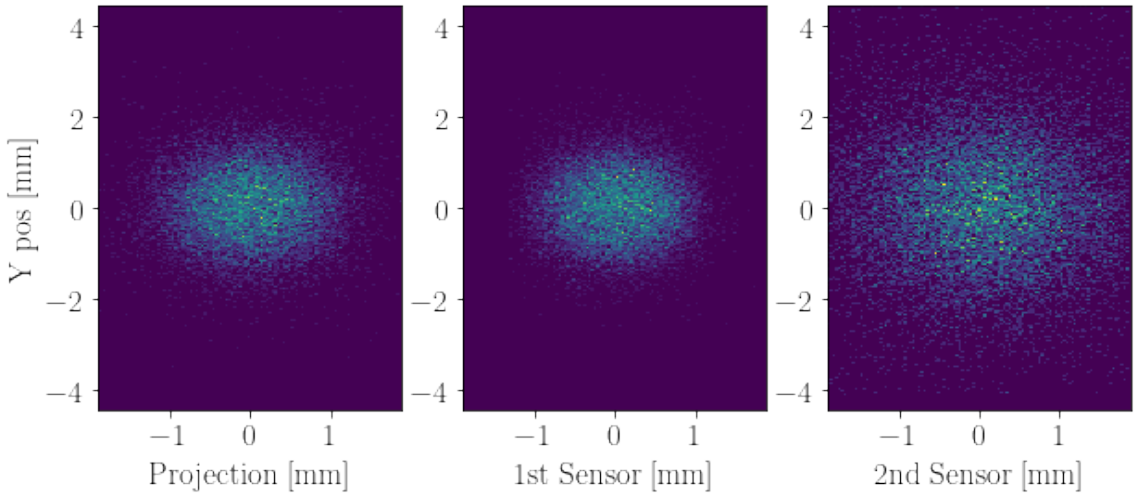

Figure 6.10: 2D hit map of the first (middle) and second (right) sensors and the back projection to the collimator position, of the proton track using a 2 mm circular collimator.

6.2.1 Beam's angular dispersion

The dispersion of the beam observed between the collimator and the first sensor is much smaller than the one observed between the first and second sensors. This suggests that this dispersion is not only intrinsic to the beam profile and is magnified by the effect of the MCS suffered within the 100 μm of silicon in the first sensor plus a layer of tape covering the sensor's back.

The θ and ω angular dispersions of the angles defined in 3.5, together with the position dispersion in X and Y are presented in Figure 6.11. The valley observed in the θ dispersion is expected, as well as the larger variance in the Y position displacement, due to the asymmetry between the sensor's height and width. The ω angle dispersion is an order of magnitude larger than the one expected for clinical protons ($>$ 100 MeV) see Section 7. This dispersion results in a 91 % of geometrical efficiency between planes. This geometrical inefficiency together with the asymmetry between the height and width of the sensors leads to the valley distribution observed in the ω distribution of Figure 6.11. With a lower θ dispersion, as expected for clinical protons, the geometrical efficiency would be close to 100 % and the ω dispersion would become flat since the smaller dispersion would reduce the effect of the asymmetries.

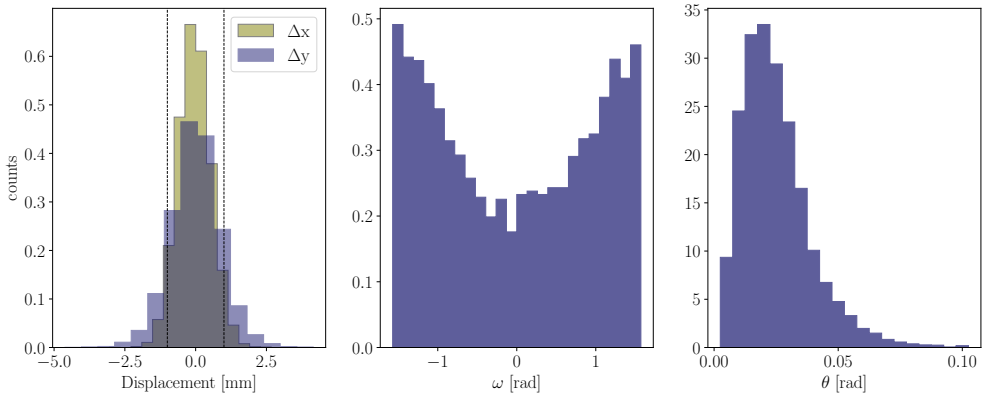

Figure 6.11: Position variation dispersion (left) and angular dispersions for the angles defined in Figure 3.5 middle and right for measured 28 MeV protons from the MC40 cyclotron.

These angular dispersions were compared with Geant4 simulations of the MC40 cy-

clotron beamline using the same collimator shape and obtaining similar results as the ones observed with the TJ-Monpix as seen in Figure 6.12.

Comparison with Geant4 simulations

A Geant4 simulation of the MC40 beamline was performed accounting for the beam leaving the FC1. At the nozzle, a 1 cm thick aluminium collimator with a 2 mm radius whole was placed to mimic the test beams performed for this section's work. Two sensors with the dimensions of the TJ-Monopix, see Section 4.1, were placed 3 and 8 cm away from the collimator similarly to the setup seen in Figure 6.1. The geometrical efficiency between the first and second sensors was observed to be 90.5 % in good agreement with the 91 % observed at the test beams. Figure 6.12 shows the results of the Geant4 simulation of the analog angular dispersions measured with the TJ-Monopix seen in Figure 6.11.

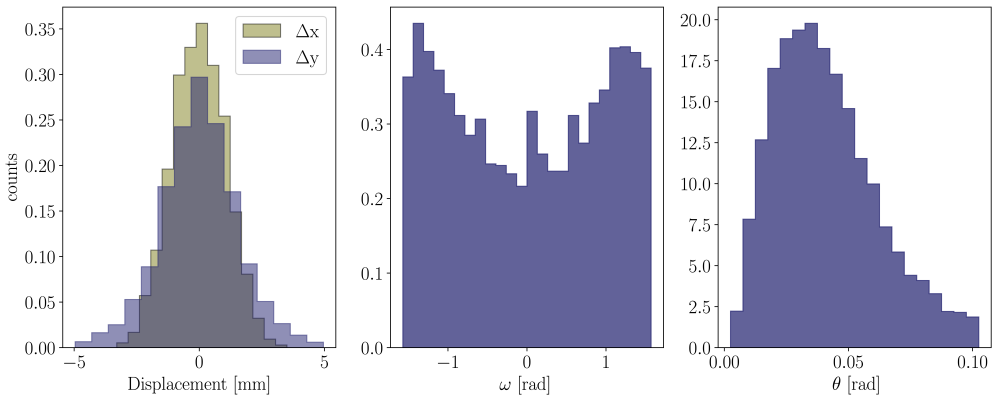

Figure 6.12: Position variation dispersion (left) and angular dispersions for the angles defined in Figure 3.5 middle and right for the simulated 28 MeV protons.

The shapes of the distributions seem to be in good agreement with the original test beam data. However, a larger θ angle results in a wider dispersion in Δ_X and Δ_Y, and some discrepancies in the shape of the ω distribution. A further test using a simple Python simulation with the same θ dispersion measured at the test beam and the same geometry of the sensors showed the same distribution for the ω angle and the position dispersion. Thus, the disagreement could be caused by two different elements: regarding the sensor,

the TJ-Monopix is a test chip, and whilst the pixel pitch is assumed to be $36 \times 40 \mu m^2$ a small variation could accumulate when accounting for tenths or up to two hundred pixels, regarding the sensor as well the thickness is assumed to be 100 μm but it is a factor that was not measured either; regarding the simulations, it could be that there is an element of beam dispersion that has not been properly accounted for.

6.3 Chapter summary

Test beams have been carried out with two sets of TJ-Monopix chips at the MC40 cyclotron. A mechanical frameset, with a micrometer on each sensor, was used to ensure good precision alignment with the larger misalignment being below one millimeter. Using an offline reconstruction algorithm the alignment was achieved was of the order of a few microns.

The first analysis presented evidence of a difference between the frequency of the different chips. In order to resolve this issue, a matching algorithm was developed to match front and back chips by correcting for the timing delay between sensors.

Without being able to test with a telescope that would allow us to have true information, simulations have been carried out to test the reliability of the test with satisfactory results.

Using the suggested algorithm, the two TJ-Monopix system was able to match and track protons from both sensors with an 86 % efficiency given a 91 % geometrically efficiency even with the timing delay.

The angular dispersion observed due to the MCS expected with the low energy protons makes it impossible to project the protons' position in any direction.

Higher energy protons of about 100 MeV, such as the ones used in Section 7, are expected to reduce the azimuthal scattering angle (θ) by two orders of magnitude. This could allow tracking multiple protons per event with high efficiency and purity.

There is promising further work with DMAPS working at clinical energies for pCT

and micro-beam.

Chapter 7

Test beam and simulations of the Curie institute pMBRT line

The clinical proton beam for mini-beam radiotherapy at the Curie Institute is a state-of-the-art facility for cancer treatment. The aim of pMBRT is to take advantage of the beam spread caused by MCS with the use of multiple minibeams to deliver a high dose of radiation to the tumor while minimizing the dose to surrounding healthy tissue. Curie Institute's clinical proton beam for pMBRT includes several key components that ensure the effective and efficient treatment of patients.

A proton cyclotron is the first component of the system. This machine generates the proton beam used for pMBRT treatment. The beam is then directed to the patient using a complex set of magnets used as a beam delivery system, which also includes a collimation system that shapes the beam into multiple microbeams, both for pMBRT and imaging. The collimation system is a crucial component of the pMBRT system, as it ensures the delivery of a high dose of radiation to the tumor while minimizing the dose to surrounding healthy tissue.

To monitor the accuracy and reproducibility of the pMBRT delivery, as well as to measure the dose delivered to the patient, the Curie Institute uses a pixel ionization chamber [87]. This system allows for real-time monitoring of the pMBRT delivery, en-

suring that the correct dose of radiation is delivered to the tumor. The pixel ionization chamber is a crucial component of the pMBRT system, as it helps to minimize the risk of under-dosing or over-dosing the tumor, which can affect the outcome of the treatment.

The beamline at the Curie Institute was selected for these tests for two main reasons. Firstly, as discussed in Section 5, the readout capabilities of the TJ-Monopix do not depend on the number of protons per second to be read, even with high fluences typically used at clinical beamlines. This makes it suitable for the use of a small collimator like the one used in pMBRT at the Curie Institute.

The facility was used for a test beam with two TJ-Monopix chips for tracking purposes. However, at the time of the writing of this thesis, only single sensor data was analysed due to time constraints and the need for a new event-matching algorithm that would work for multiple proton events. Thus, the single sensor measurements were used to improve the simulation and make it more realistic. Later, the simulation and data are used to find the key values to optimise the matching event algorithm such as: the angular dispersion of the beam through the air after leaving the collimator, the geometrical efficiency, the effect of MCS, and angular and position distributions.

The purpose of the study is to showcase the potential of pixel sensors in general, and DMAPS technology based on the TJ-Monopix measurements, and demonstrate how these techniques can be utilized at clinical facilities. The results of this study will help to advance the field of pMBRT and proton imaging, and contribute to the development of new and improved methods for the treatment of cancer. The clinical proton beam for pMBRT and proton imaging at the Curie Institute is a testament to the ongoing commitment to research and development in the field of radiation therapy and the advancement of cancer treatment.

The chapter is divided in three main sections: The first presents a calculation of the number of expected protons hitting the sensor after the mini-beam collimator to test the saturation of the TJ-Monopix; the analysis of the test beam data with a single sensor; and the simulation of the Curie Institute beam line studying the performance of the tracking

system with the two TJ-Monopix chips.

7.1 Expected number of protons at the Curie Institute

A calculation of the expected number of protons per second at the pMBRT line at the Curie Institute [88] was performed in order to understand the capability of the TJ-Monopix to work with clinical currents and optimise the working setup for the test beams. The results of maximum fluence obtained in Section 5.2 were compared with the calculations. The parameters used for the calculations intended to mimic the single slit collimator used for the test beams.

Slit dimensions:

- Width 0.4 mm
- Length[1] 8.96 mm
- Pencil beam with a Gaussian distribution with $\sigma_{x,y} = 8$ mm
- Flux = 10^9 protons/$(min \cdot cm^2)$

Notice that the pencil beam size is much larger than the slits, thus, in order to compute the expected number of protons per second (ε_{exp}) equation 5.2 was used but the integrating the beam profile up to the collimator limits instead of the scanning time.

$$\varepsilon_{exp}(\mu_x, \mu_y) = \int_{-L/S}^{L/2} \int_{-W/2}^{W/2} \frac{e^{\frac{-(\mu_x - x)^2}{2\sigma^2}}}{\sqrt{2\pi}\sigma} \times \frac{e^{\frac{-(\mu_y - y)^2}{2\sigma^2}}}{\sqrt{2\pi}\sigma} \phi \times dxdy \tag{7.1}$$

where $L = 8.96$ mm is the height of the TJ-Monopix and $W = 0.4$ mm is the width of the slit, and (μ_x, μ_y) is the position of the beam centre relative to the centre of the slit.

[1] The Curie Institute single slit length is larger than 8.96 mm but the TJ-Monopix sensor is the limiting factor here.

The Curie Institute mini-beam has a small area allowing for a high proton flux to be read by the TJ-Monopix. The plot seen in Figure 7.1 shows the expected number of protons read at the TJ-Monopix as a function of the position of the beam centre (μ_x, μ_y) relative to the centre of the slit following a diagonal line such that $\Delta(\mu_x, \mu_y) \propto \sqrt{2}$. The blue line represents a beam with $\sigma = 8$ mm as expected before reaching the collimator and the olive line shows the expected number of protons for a beam with $\sigma = 9.5$ as expected after the collimator due to the scattering of the beam through air observed in Section 7.2

The horizontal line drawn in the plot shows an approximation of the expected saturation point. The number of protons expected for saturation was computed by dividing the breaking point of 1 M protons per second by the mean cluster size of the full matrix (averaging FDPW and RDPW) at 100 MeV obtained at the test beam. With 100 MeV protons, the mean cluster size for the whole matrix was measured to be 1.65, see Figure 7.8.

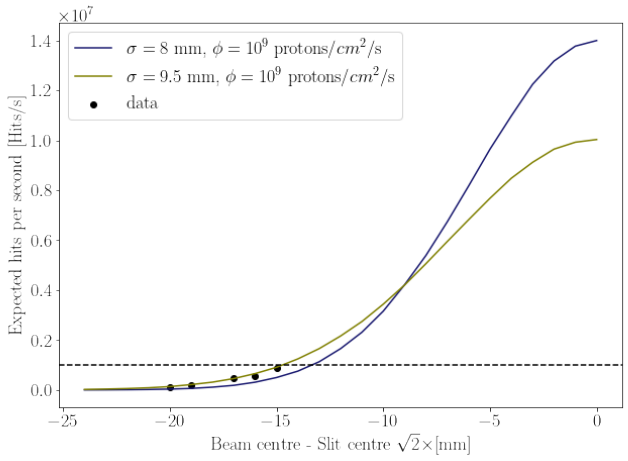

Figure 7.1: Expected number of protons per second at the TJ-Monopix sensitive area for different positions of the Curie pencil beam relative to the center of a single mini beam slit, 400 μm wide and 9 mm long (limited by the sensor height) assuming the $\sigma = 8$ mm (blue) and $\sigma = 9.5$ mm (olive) as expected before and after the collimator.

The black data points of Figure 7.1 represent the number of hits per second obtained by pointing the pencil beam at 5 different distances from the centre of the slit. The last

point at $16\sqrt{2}$ right before the saturation of the TJ-Monopix readout system seems to be in agreement with the expected values shown by the dashed line.

The number of hits expected at the centre of the slit is an order of magnitude higher than the saturation limit. However, standing at a distance $\Delta = 15\sqrt{2}$ mm the TJ-Monopix is expected to be below the threshold of saturation. This implies that the TJ-Monopix was used to track protons at a clinical facility with proton fluence of approximately $3.7 \times 10^7 \mathrm{p/cm^2/s}$.

Furthermore, with a smaller dedicated collimator one could go to the center of the Gaussian beam increasing the fluence.

7.2 Test beam and single sensor analysis

This section shows the test beam methodology and setup with the consequent analysis, and the results obtained for the beam profile; the cluster size dispersion, and the distribution of the number of protons per event.

7.2.1 Methodology

The TJ-Monopix set described in Section 6 was taken to Paris at the Curie Institute and was laid out as shown in Figure 7.2. Despite the image showing the two TJ-Monopix sensors, due to limitations on the experimental day, only data from a single sensor is analysed in this thesis.

The tests were performed with the single slit collimator described above and at 10 cm of the collimator.

The alignment of the sensor with the nozzle was performed by aligning the center of the collimator's slit with the sensor in X and Y directions by rotating the collimator by 90 degrees. Figure 7.3 shows the 2D histograms with the hit occupancy of the scans used for the alignment with a deviation from centre of the slit of 0.06 mm and 0.09 mm in the X and Y axis respectively.

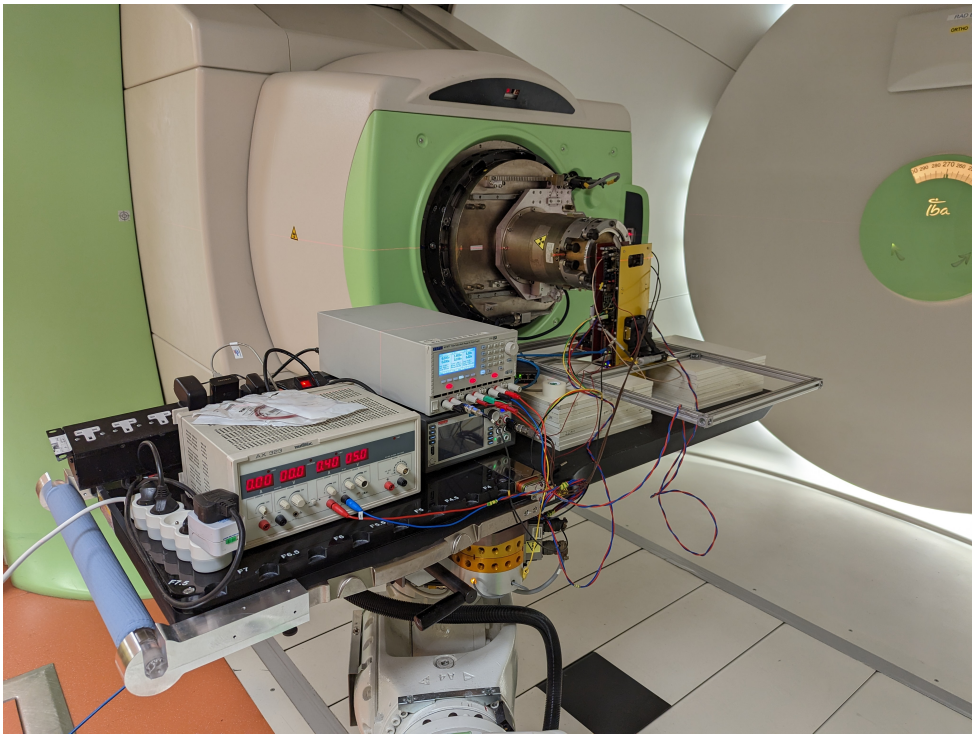

Figure 7.2: Setup for the test beam at the Curie mini beamline with two TJ-Monopix detectors.

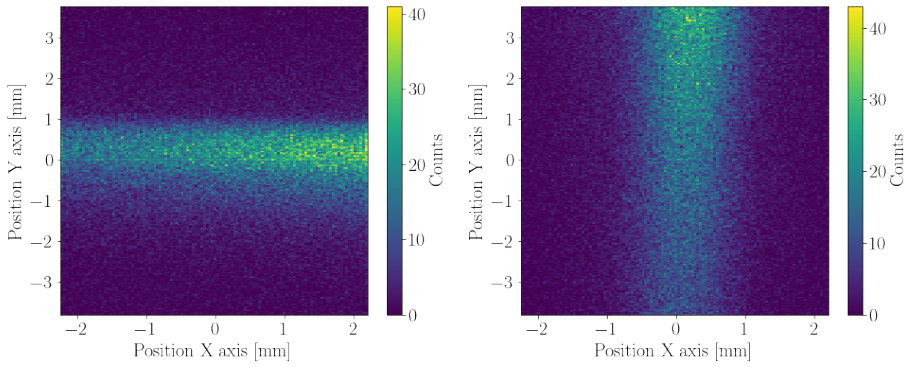

Figure 7.3: Hit occupancy maps of the measurements used for the alignment of the beam with the TJ-Monopix using the slit in a horizontal position (left) and vertical position (right).

An asymmetry is observed when the slit collimator is placed horizontally (left), this is expected due to a known tilt of the slit related to the beam when placed in this position. For this reason, not the mean position of the whole beam but rather a 500 μm section, in the Y direction, in the middle was used to compute the mean position of the beam.

After the alignment, several scans were performed at different distances to the nozzle

within a range of 5 to 15 cm in order to study the beam angular dispersion through air. The data was clustered using the algorithm presented in Section 4.5 and the x position distribution was fitted with a Gaussian using the σ as the parameter to define the dispersion of the proton beam. With the sensor fixed 10 cm away from the nozzle, a different study was also performed by moving the pencil beam in relation to the collimator center, see Figure 7.4, in order to obtain different fluences at the TJ-Monopix and test the limit before the breakdown was obtained at 1 M hits/s. The data points obtained in the fluence study are shown in Figure 7.1.

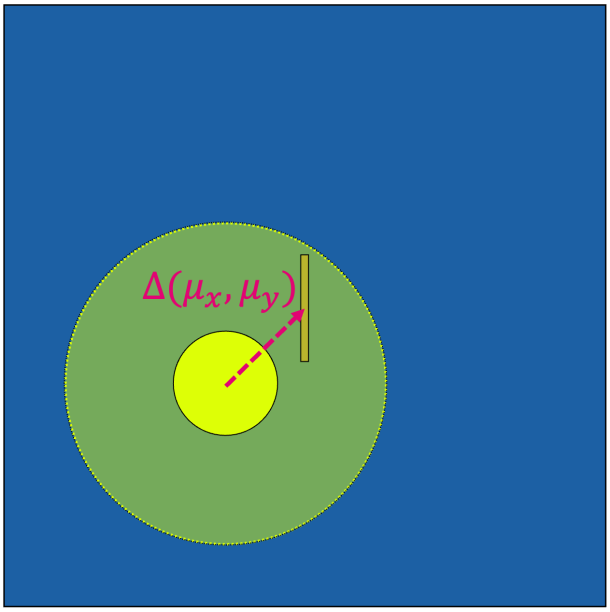

Figure 7.4: Sketch representing the displacement $\Delta(\mu_x, \mu_y)$ between the centre of the slit, represented as an orange box, and the centre of the pencil beam (yellow circle). The proton beam is depicted with the yellow circle and yellow shadow to represent the smaller beam proton density found away from the centre. The red dashed line represents the diagonal along which the beam was moved, where $\mu_x = \mu_y$.

7.2.2 Results

The results of the single-sensor data analysis are presented in this Section.

The left plots in Figure 7.5 show the hit occupancy at the TJ-Monopix when placed, from top to bottom, 55 and 145 mm away from the vertical slit collimator. The plots on the right show projection in the X direction of the same scans in blue and the fitted

Gaussian used to obtain the σ of the distribution (dashed red).

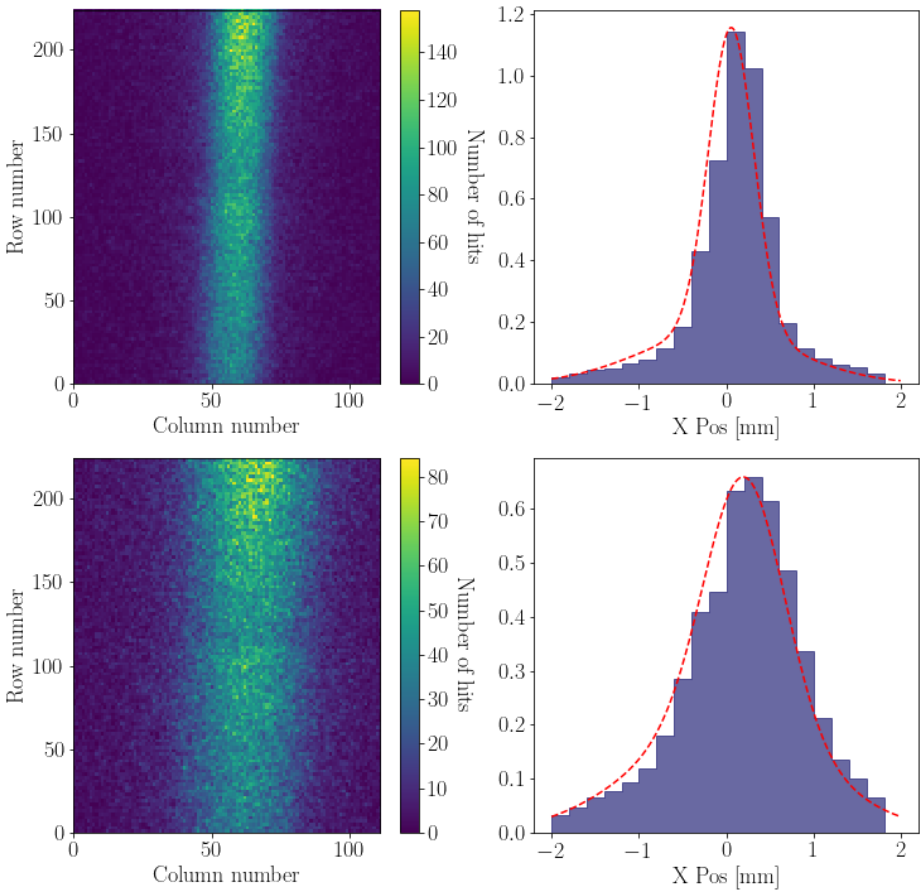

Figure 7.5: Left plots present the hit occupancy scans at 55 (top) and 145 mm (bottom) from the vertical slit collimator. The plots on the right show the X position distribution fitted with a Gaussian to obtain the σ of the distribution.

It can be seen on both left plots in Figure 7.5 that there is a difference in hit density between the top and the bottom of the slit. This is explained by the Gaussian distribution of the beam. Figure 7.6 shows the projection in the Y direction of the right 2D histogram on Figure 7.3 in blue. The dashed red line represents the expected Gaussian seen in the Y direction at 16 mm from the centre with $\sigma = 10.7$ mm and $\mu = 16$ mm. Notice that this plot is not a fit, it is only an illustrative figure to explain the difference in proton densities observed along the slit due to the center of the beam being displaced about two

sigmas away from the centre of the slit.

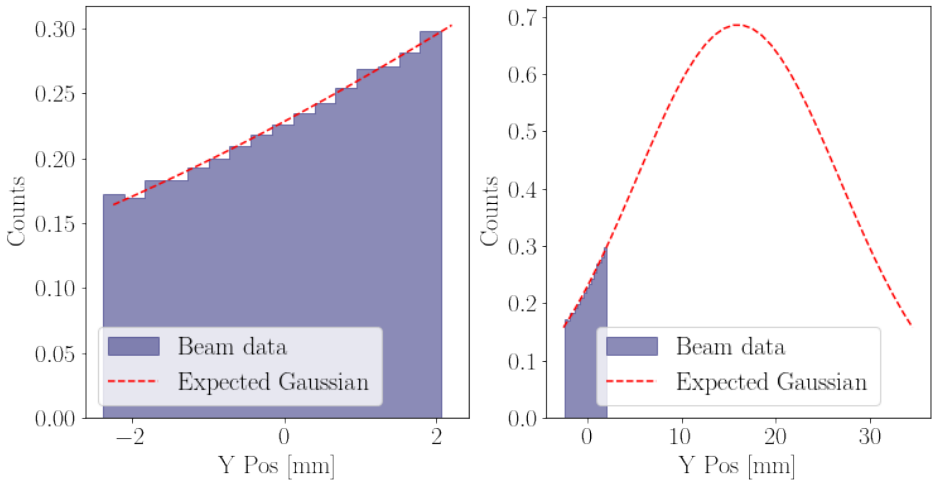

Figure 7.6: Histogram of the hits projection in the Y direction of a scan using the vertical slit at the pMBRT line at the Curie Institute (blue). The red dashed line is a plot of the expected Gaussian seen in the Y direction at 16 mm from the centre with $\sigma = 10.7$mm and $\mu = 16$ mm.

The plot in Figure 7.7 shows the scattered plot of values of the different sigmas obtained as a function of the distance to the collimator (blue dots) and the fitted linear correlation (dashed red).

The linear fit of Figure 7.7 shows a value obtained for the σ at zero distance to be 0.172 mm, which corresponds to a Full Width at Half Maximum (FWHM) of 0.4 mm, equal to the slit width. The gradient of the fit is 0.03 mm/cm. This implies that the sigma increases by a factor of 0.03 mm when moved 1 cm away from the beam nozzle, which is in agreement with the maximum accepted by the geometry of the collimator with a ratio between length and width of 0.08 mm/cm. This gradient also implies that the beam is not entirely parallel when it leaves the collimator and thus it is something to take into account when simulating the beamline since it will play a key role in angular dispersion and geometrical efficiency.

The histogram in Figure 7.8 presents the cluster size measured at the FDPW (olive) and RDPW (blue). The distribution observed at the RDPW follows the expected gradual descent. This might be due to the lower charge generated in the sensor by the 100 MeV

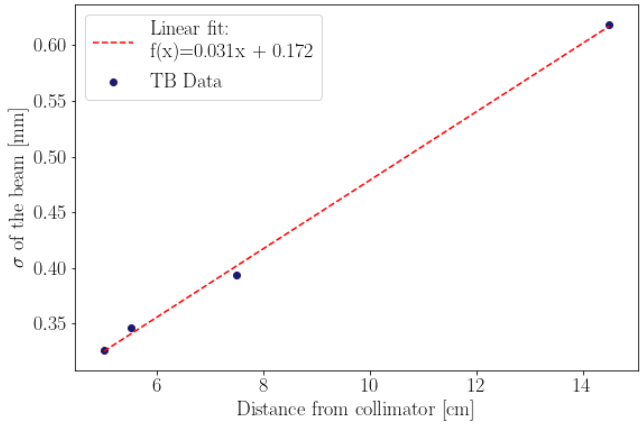

Figure 7.7: Profile of the Curie slit beam opening as a function of distance to the collimator. The blue dots represent the sigma of a Gaussian fitted to the horizontal position dispersion of the protons measured by the TJ-Monopix at the test beam and the dashed red line is the linear fit.

protons compared to the 36 MeV protons of the MC40 cyclotron. As expected, the FDPW shows a distribution with larger cluster sizes due to the weakest electric field at the edges of the pixels.

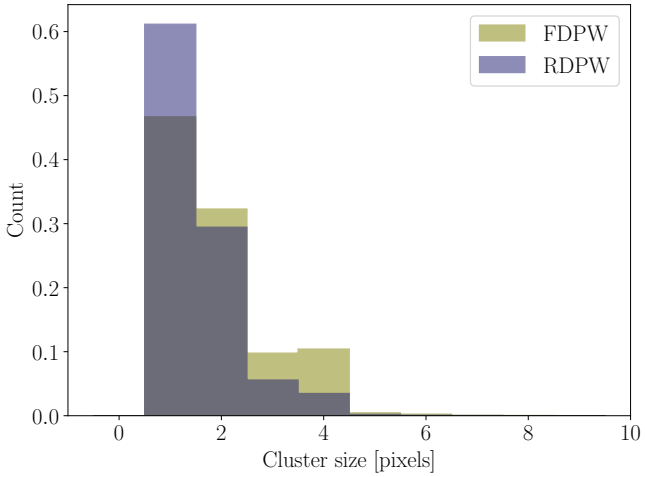

Figure 7.8: Distribution of the cluster size for the FDPW (olive) and the RDPW (blue) from a test beam taken with the 100 MeV protons using the mini-beam line at the Curie institute.

The charge reconstruction after clustering is presented in Figure 7.9. Due to the more common cluster size distribution, the charge reconstruction also shows a much closer

distribution to the expected Landau compared to the one obtained with the 36 MeV at the MC40 cyclotron. A small shoulder is observed at the charge reconstructed for clusters of one pixel. This could be due to secondary particles such as air-scattered electrons or X-rays emitted from the collisions between protons and the collimator. Since secondary particles will mostly be absorbed by only one of the sensors, after the event matching, this could be further studied by comparing the number of hits at the front and back sensors at each event. Secondary particles might affect the tracking efficiency on high occupancy multi-proton events; thus, a higher offline threshold could be also applied to improve to remove these hits. This will be addressed with the simulation of the beam in the future.

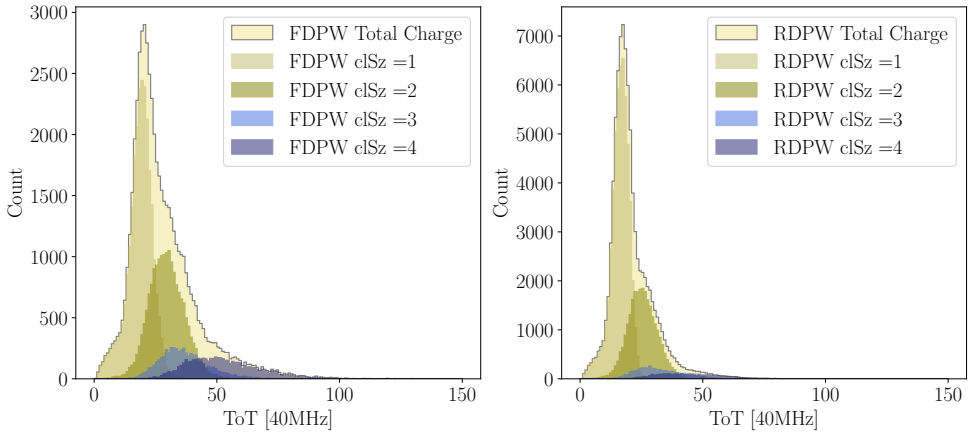

Figure 7.9: Histogram of the reconstructed charge, in ToT, using a vertical slit at the Curie Institute with 100 MeV protons. The histogram shows the summed charge of all clusters (yellow) and the charge separated for different cluster sizes: one (khaki), two (olive), three (royal blue), four (navy blue) for the FDPW (left), and the RDPW (right).

As performed in Section 5.1 the number of total clusters measured as a function of time was fitted in order to obtain the number of protons per second in the detector. This was performed for different distances between the centre of the beam and the slit's centre. As shown in the plot in Figure 7.1 the closest distance before saturating the sensor was at a position of $16\sqrt{2}$ cm.

The plot in Figure 4.16 shows the cluster size distribution for both flavours FDPW (olive) and RDPW (blue).

- Mean cluster size (Cl_{Size}) for the different structures:

  Full Matrix: $Cl_{Size} = 1.68$

  FDPW: $Cl_{Size} = 1.8$

  RDPW: $Cl_{Size} = 1.5$

As expected, the mean of the cluster size distribution of the RDPW is still smaller compared to the FDPW and both are smaller than the ones observed with 36 MeV protons at the MC40 cyclotron.

7.3 Simulation

7.3.1 Methodology

The simulations were performed with Geant4 using the QGSP_BIC physics list. The purpose of this simulation was to set a benchmark for tracking capabilities of the TJ-Monopix at the pMBRT beamline. Due to the geometry of the collimator the dispersion of the beam when traveling through air, observed in Figure 7.7, is not expected to play a limiting role in the tracking. Thus, the simulation consisted of a parallel beam and the equivalent collimator setup defined in [89]. A 5 cm cube of brass, with a small 0.4×20 mm^2 slit, was placed upstream between the proton beam and the sensors. The proton beam was simulated with an energy of 100 MeV and with a 2D Gaussian distribution with an 8 mm sigma before the collimator. The aim of this study was to test the effect in tracking precision of the MCS suffered by clinical protons when passing through the TJ-Monopix chip. Thus, the Gaussian beam has been considered parallel, with no intrinsic angular dispersion[2]. The TJ-Monopix-like sensors used in Section 6.2.1 were also used in this simulation and placed 10 cm away from the brass collimator and 14.5 cm away from each other. Due to the small geometrical efficiency of the collimator, 100 M events were generated to achieve a total number of 3 M protons at the sensitive surface of the

[2]The results of the angular straggle of the beam in air measured in the previous section will be used in future simulations.

sensor. A single proton event simulation was performed first to understand the angular dispersion, the geometrical efficiency of the two-sensor system, and the effect of secondary particles in the tracking. With only two layers the tracking was performed based on the algorithm defined in Section 8.3.1 and using the minimization of the dispersion of the angle θ, defined in Figure 3.5 as the K value.

A thin air layer (5 μm) of Geant4 *sensitive detector* class was placed right at the end of the mini-beam collimator. This was used to define the position of the protons when they leave the collimator and then compared to the position obtained by the back projection obtained with the proton tracking.

7.4 Results

Figure 7.10 shows the angular dispersion of the simulation of the Curie proton beam after going through the 5 cm brass collimator. As expected, the displacement in X and Y directions is much smaller than for the MC40 cyclotron due to the smaller effect of MCS at 100 MeV. The dispersion in X-Y shows that more than 90% of the protons remain within a 0.2 mm radius from the first hit. When computing ω the events with $\Delta_X = 0$ were added as -$\pi/2$ entries to avoid the division by zero.

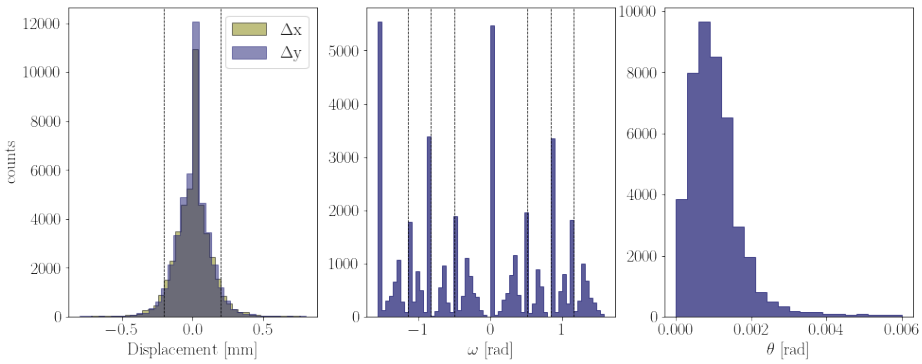

Figure 7.10: From left to right, distributions of the displacement in x (olive) and y (blue) directions, ω and θ dispersion angles

.

The ω distribution is not flat as one could expect. This is due to the fact that the

segmentation of the pixels is of the order of magnitude of the displacement. Thus, a displacement in X or Y equal to zero, or one, is very frequent. With this, the measured distribution shows a peak at 0, which implies there is no displacement in Y, a similar peak at $-\pi/2$ for displacement in X being equal to zero. Then two smaller and symmetric and segmented peaks that correspond to the rest of the combinations with peaks at $\theta = \pm \arctan\left(\frac{Y_p}{X_p}\right)$ where $Y_p = 40\mu m$ and $X_p = 36\mu m$ are the pixel pitches for Y and X respectively. Thus, it is seen that segmentation in this plot correlates to the segmentation of the sensor and thus the quantized possibilities of X and Y displacement.

The distribution of the angle θ shows the small beam dispersion between two sensors. At clinical energies, the thin substrate of the TJ-Monopix results in a very low MCS that could be neglected for most monitoring and imaging processes.

The geometrical efficiency observed for this scenario is 97 % losing only a very small fraction due to the lack of beam dispersion caused by the MCS seen with the 36 MeV protons.

Figure 7.11 shows the 2D hit map for the back projection, the first and second sensors from left to right. The top row shows the full hit occupancy maps for the whole simulation. As expected by the low beam dispersion, the projection of the proton tracks back to the collimator were sharp and well defined without a blurring at the edges as seen with the MC40 cyclotron protons in Section 6. The bottom part shows a set of 5 consecutive protons showing very well-defined and consistent positions along the three planes. This suggests tracking efficiency and resolution for the Curie Institute protons would not be compromised even at high occupancy multi-proton events. However, as it is clear in the projection back projection profile, compared to the original position, the MCS within the 100 μm of silicon is enough to reduce the resolution position of the projection at 100 MeV. The resolution of the proton projection back to the collimator can be seen in Figure 7.14.

Figure 7.12 shows the minimum distance between all the combinations of tracks within an event for the tracks between the first and second layers for all particles (blue) and secondary particles (olive). The number of secondary particles in both layers is around

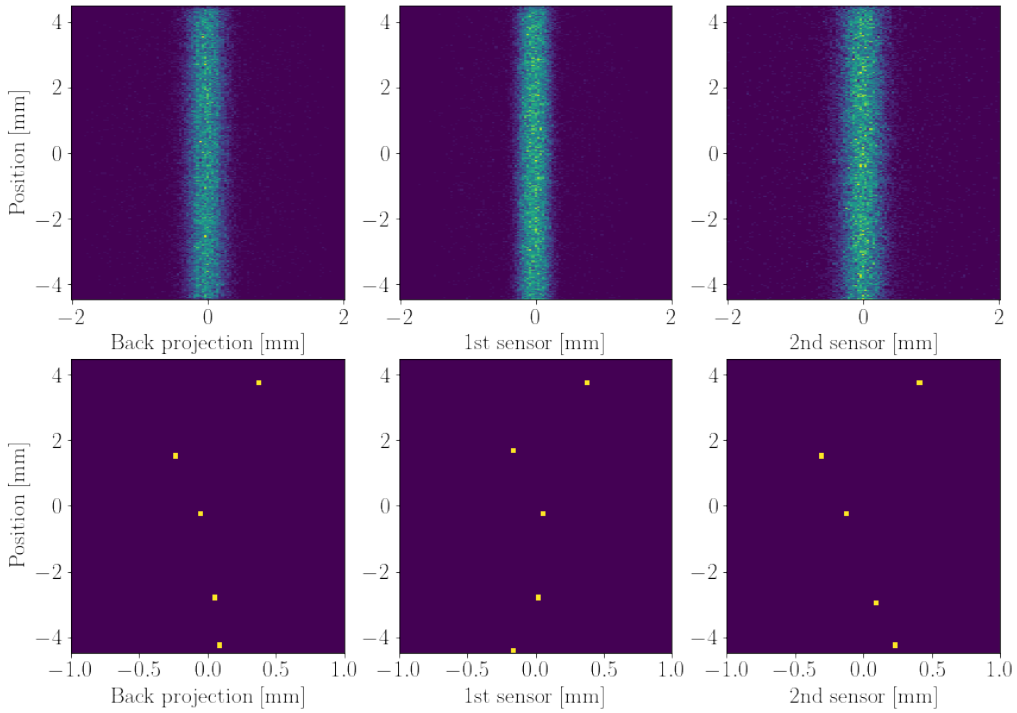

Figure 7.11: Hit occupancy scan of the full 10 M simulated protons (top) and 5 consecutive events (bottom). From left to right; back projection of the tracked protons; and hit map of the first and second sensor.

2 %, thus, for illustrative purposes, both histograms have been normalized. It can be seen that while the minimum distance computed between protons and secondary particles follows a flat distribution within the range between 0 and 1 mm; the proton tracks present a distribution with a steep rise and maximum at 0.1 mm with a hard fall-off after 0.2 mm. Thus, tracking purity was above 99 %; while the effect of secondary particles could play a role in multi-proton events.

A study of the charge collection for each particle has been performed in order to understand if it would be a useful variable for tracking purposes. Figure 7.13 shows the charge collected at the pixel sensors from protons (blue) and secondary particles (olive). This suggests that charge collection could indeed be used to increase the tracking efficiency for multi-proton events, by applying higher thresholds offline after the clustering has been applied and the total charge of the cluster has been reconstructed. Notice that this would

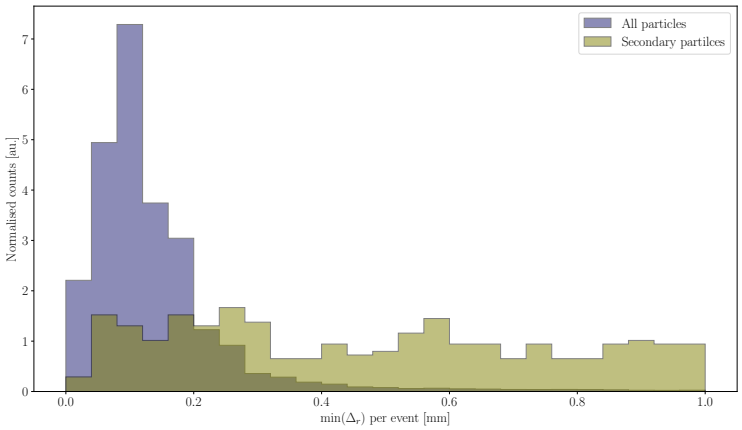

Figure 7.12: Variation in position r between the first and second layer of the pixel tracker for all particles (blue) and secondary particles (olive).

not have the same effect as raising the threshold of the sensor itself due to charge sharing effects. However, this simulation does not include charge-sharing effects nor the low resolution in charge reconstruction of the TJ-Monopix for high threshold distributions. This could be further studied with TCAD data or with the information taken from the test beam.

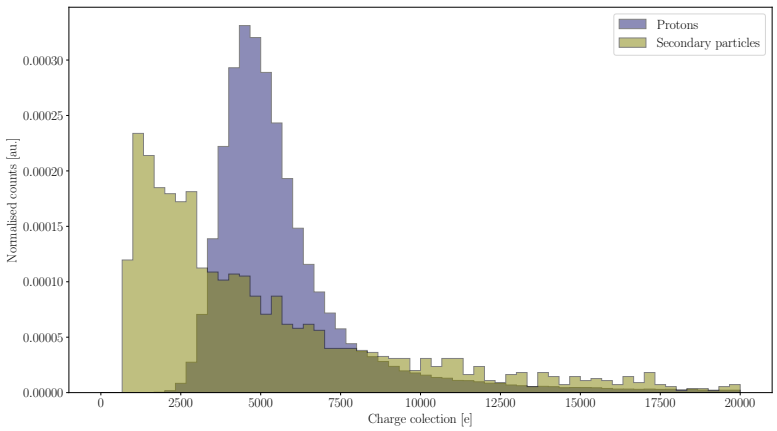

Figure 7.13: Normalised histograms of the charge collected by protons (blue) and secondary particles (olive) at the pixel sensors.

Figure 7.14 shows the spatial resolution of the proton track after being back-projected to the collimator, 10 cm away from the first sensor. The histogram shows both X and Y

dispersions fitted with a Gaussian obtaining both values of resolution around 70 μm.

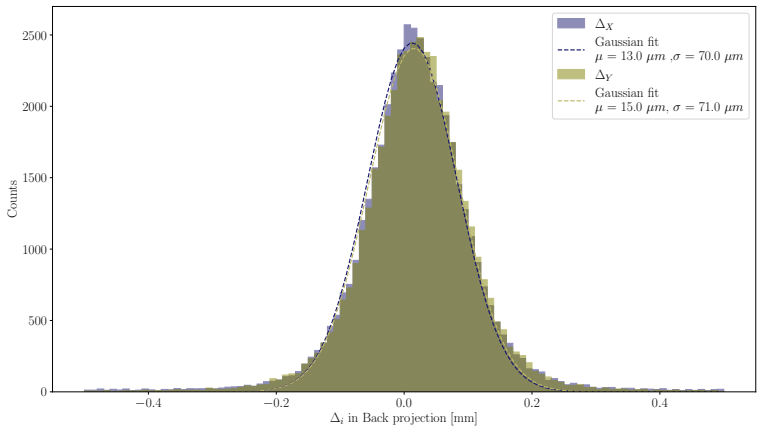

Figure 7.14: Position resolution in X (olive) and Y (blue) of the back projection of the simulated protons with the TJ-Monopix-like sensor with the mini-beam slit.

7.5 Chapter summary

A study of the expected number of protons and hits per second with the single mini-slit setup at the Curie Institute was performed. The number of hits per second suggests that the optimal position where set the slit would be at $R = 15\sqrt{2}$ mm, *i.e.* at ~ 21 mm from the centre.

A new collimator was designed in order to maximize the proton fluence measured by the TJ-Monopix with dimensions of 300 μm and 250 μm wide, per 1 mm high.

A test beam at the Curie Institute was performed and the results of the single sensor analysis were presented here. The results include fine alignment on the X and Y direction with a displacement from the centre of the slit of 0.06 mm and 0.09 mm in the X and Y axis respectively; a profile of the angular beam straggle in air; the confirmation of the saturation point ~ 21 mm away from the centre; and a study of the cluster size and charge reconstruction with the TJ-Monopix.

A setup using the slit collimator of the Curie Institute was simulated with 100 MeV protons and the TJ-Monopix sensor. The proton tracking results show, as expected, a

small angle dispersion due to MCS more than one order of magnitude smaller than for the 36 MeV protons at the MC40 cylcotron. The results suggest that multi-proton tracking and track projections could be performed at these energies with the TJ-Monopix. The effect of secondary particles was measured to be negligible in single proton events tracking when using the algorithm defined in 8.3.1; the use of the charge collection as a variable to improve the efficiency in multi-proton events was suggested; and the resolution of the projection of the proton tracks was measured to be 70 μm when back projecting the protons to the collimator position being 10 cm away from the first sensor.

Chapter 8

Simulation of a full pCT system

8.1 Introduction

With the aim of obtaining a full proton CT image using new HEP technologies a Geant4 simulation of a pCT system was carried out. The system includes four layers DMAPS for tracking purposes and a plastic scintillator range telescope that was designed during the course of this thesis. The results shown in the following sections of this Chapter were obtained using classic algorithms and were already published in the peer-reviewed journal *Physics for Medicine and biology* [1], notice that some paragraphs of the first sections have also been extracted from the paper. In Section 8.4 the potential of performing the data analysis of the A Super Thin RAnte Telescope (ASTRA) system using CNN is presented. The latter was also presented at the 19th International Conference on Calorimetry in Particle Physics (CALOR 2022) being one Selected Papers published in the peer-reviewed journal Instruments from MDPI [90].

8.2 The simulated setup

The setup needed to obtain a pCT image, as explained in 2.3 is based on two key elements: a proton tracker and an energy tagger. The full setup used for these simulations can be seen in Figure 8.1.

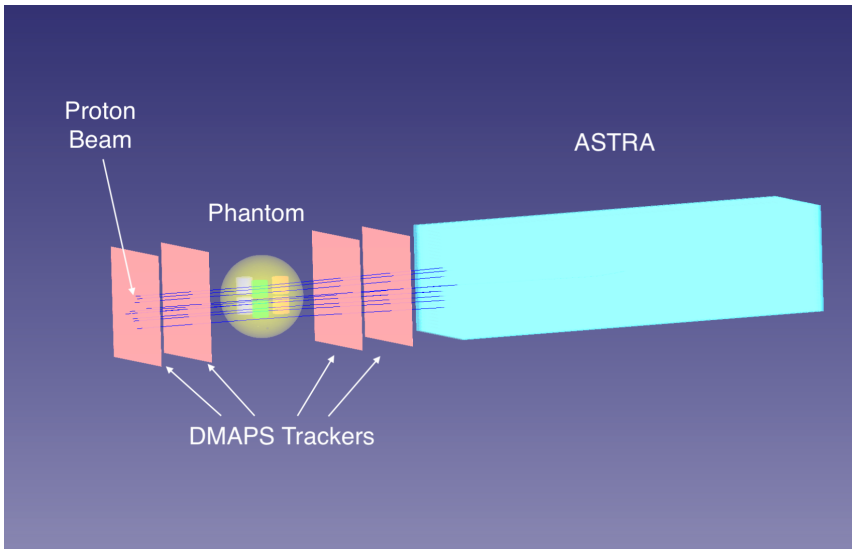

Figure 8.1: 3D visualisation of the pCT system with four DMAPS layers, a spherical phantom with 6 cylindrical inserts in place, and the ASTRA range telescope. In the image, ten protons (dark blue lines) are being measured.

The proton tracker designed for this system consists in two pairs of oversized (10×10 cm^2) pixel DMAPS resembling the geometries and characteristics of the TJ-Monopix. The four pixel sensors are organized in two sub-trackers, front and back, each formed by a pair of DMAPS separated by 50 mm. We consider the gap distance between the front and back trackers to be of 150 mm. For the acquisition of the pCT a spherical phantom with a diameter of 75 mm was placed between the two trackers. Other radiography studies were performed with a squared phantom of dimensions $50\times50\times30$ cm ^{2}.

Variations of the positions of the layers were studied, however, within the realistic dimensions requirements for the system, the impact on the final result was small. Thus, this compact and realistic set of distances was selected.

The characteristics of the sensors were simulated to be similar to these in [91]: 100 μm thick with a 25 μm shallow sensitive layer with a pixel pitch of 40×40 μm^2. Notice that the original pitch size of the TJ-Monopix (36×40 μm^2) was also tested giving equal results and the 40×40 μm was kept for simplicity. Opposite to the small sensitive area of the TJ-Monopix, an array of 2500×2500 pixels covers a total area of 10×10 cm^2. Notice that

such a device does not yet exist but could be produced on a reasonable timescale thanks to the advances of the stitching techniques with MAPS [92], [93] that could also be applied with DMAPS.

For the energy tagging a full plastic scintillator was designed based on the Fine Grained Detector (FGD) of the T2K experiment. The ASTRA detector was designed with 120 layers, each made of 32 bars shaped as $9.6\times9.6\times0.3\text{cm}^3$.

The beam profile used for the simulations was a Gaussian with a σ=10 mm and an energy of 180 MeV.

8.2.1 The design of ASTRA

The ASTRA detector is a novel concept presented first in this article [1]. ASTRA was inspired by the geometry of the existing FGD modules [94] in the ND280 detector of the T2K experiment [95] and by recent R&D in plastic scintillator detectors, such as the time-of-flight panels [96], [97] and the SuperFGD detector [82], [98] developed in the context of the ND280 detector upgrade [98]. Figure 8.2 shows a visualisation of the two concepts, the FGD with the fibers (left) and the ASTRA system with the SiPM attached directly to the edge of bars.

The ASTRA detector is a plastic-scintillator range telescope consisting of layers made up of thin polystyrene bars oriented in an alternate axis, perpendicular to the proton beam. The exact plastic choice could be the EJ-200 plastic scintillator, which has a scintillation rise time of 0.9 ns, a decay time of 2.1 ns, and an attenuation length of 380 cm [99]. As previously mentioned, the Range Telescope (RT) concept consists in bars of $3\times3\times96$ mm^2, arranged in groups of 32 bars per layer. This provides a cross-section of 9.6×9.6 cm^2, well matching the area of the DMAPS tracker. If necessary, the cross-section of ASTRA could be easily scaled up by increasing the length of the bars and the number of bars per layer. The length of ASTRA can be tuned to match the maximum beam energy, optimizing the production costs. Here, we simulated a length of 360 mm (120 layers), enough to stop protons of 240 MeV. Following reference [100] each bar is simulated

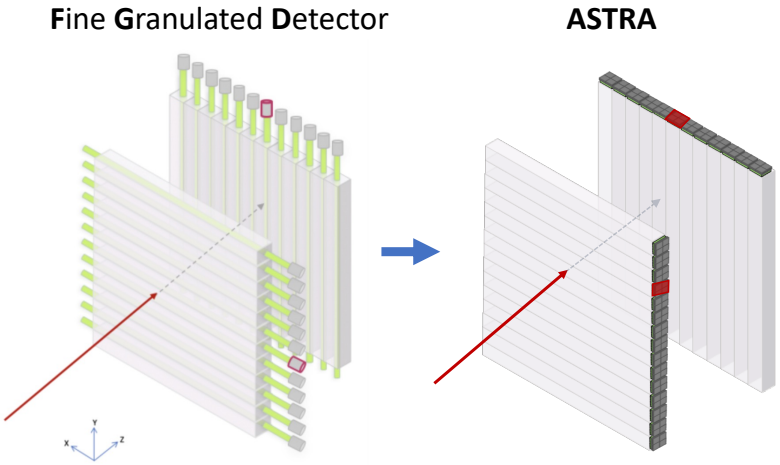

Figure 8.2: Visualisation of two layers of the FGD detector with the 1 cm^2 section bars and the fibers (left) and two layers of the ASTRA detector with the much smaller 3×3 mm^2 section and the SiPM attached directly to the bars. The red and grey arrows show the direction of protons and where the signal is measured.

including an inactive polystyrene layer of 50 μm, necessary to achieve good bar-to-bar optical separation. In practice, the bars will be manufactured by plastic extrusion, and the outer layer produced by etching the bar surface [100]. The bars would be readout by a SiPM directly coupled to the scintillator bulk, as done in [97]. In order to match the fast plastic response of the instrument, the fast output pulse shape from Onsemi's MicroFJ SiPMs [101] could be used, providing a full waveform in the span of a few nanoseconds. Suitable choices for the electronics already exist, such as those used in reference [100], which provide a dead-time free readout at a 0.4 GHz sampling rate. Remarkably, an improved version of the electronics is under development with the goal to achieve 0.8 GHz. Under these specifications, the light of two consecutive protons separated by a time span equal or higher to 10 ns can be realistically expected to be well separated, and accordingly, ASTRA has the potential to reach an event rate equal or higher to 10^8 protons/s (100 MHz). Nonetheless, it must be noted that further reducing the proton's time gap to less than 10 ns with this same system could be possible, e.g. by doing a shape analysis of the waveform, and deserves dedicated attention in the future. As a first step, in Section 8.19, the use of CNN is studied for multi-proton events considering no signal

separation. Concerning ASTRA'a geometry two main motivations drive its design. First, by using bars instead of layers the residual energy can be precisely reconstructed by range even if protons do not follow a perfectly straight trajectory. Second, if the beam has a typical spread comparable to the size of a few of its bars, multiple protons can be tracked simultaneously when the time information is not enough to discriminate their trajectory. This has the advantage of further increasing the already high rate capability and reducing detector inefficiencies when the beam can not be perfectly controlled to deliver a single proton per time frame. Despite that other scintillator-based range telescopes have been proposed and tested in the past, e.g. see references [102]–[105], ASTRA will introduce many significant novelties to this field. On one hand, it has been designed to reach collection rates two orders of magnitude higher than previous technologies. On the other hand, all previous designs were based on layers, instead of bars, limiting the device's intrinsic position resolution. Finally, the novelty of coupling the SiPM directly to the scintillator bulk will eliminate the necessity of introducing dead material inside the sensitive volume of the detector, such as wavelength shifting fibers.

8.3 Geant4 simulations

The system as described in the previous section has been simulated using GEANT4 with the QGSP_BIC physics list. The energy deposit in each of the DMAPS planes has been discretized in a list of fired pixels analogous to the real output. A threshold of 850 electrons, far from the signal's most probable value of $\sim$ 21000 electrons, has been used in agreement with what was observed, in Section 4.1, to have a good response for clinical protons on DMAPS. This threshold value minimizes the noise coming from secondary electrons and is known to have a good performance under clinical conditions, see Section 4.5.1. The energy deposit in ASTRA is discretized in a list of bar hits. In each bar, the energy deposit is converted into a number of SiPM photo-electrons (PE) and randomly accepted accounting for a quantum detection efficiency of 35%. This produces

a light yield of about 50 PE/MeV, with a smearing of about 10%. To account for a realistic detection threshold hits below 3 PE are rejected [100]. As the Bragg peak would be clearly visible even with Birks saturation [100] no quenching corrections have been considered. Neither attenuation nor bar-to-bar optical crosstalk are included in the ASTRA simulation. These assumptions are reasonable as the light yield in optical crosstalk hits is much lower than in the main hits [106] and therefore can be easily identified and removed using simple light yield cuts or machine learning techniques [107]. The attenuation could be corrected following similar prescriptions to those used in SuperFGD [100]. The output of the simulation has a structure that mimics that of the conceptual detector. For a given event a list of DMAPS hits and ASTRA hits is provided.

Regarding the beam, two different beam profiles were used; a pencil beam with with a 2D Gaussian distribution with $\sigma = 10$ mm and a 75×75 mm^2 squared beam with a flat distribution. No initial divergence of the beam was considered and thus, the beam only dispersion is only due to MCS. The size of the beam has been observed to have a big effect on the system's performance. Thus, this was done as a safety-measure assumption to ensure the results were obtained in the hardest conditions.

The simulated materials were defined as combinations of different mass densities of the Geant4 *G4Elements*; with the same definitions used for the PRaVDA [12] and OPTIMA [15] simulations.

8.3.1 Full system analysis with ROOT and classic algoritms

In this section, a preliminary analysis using classic algorithms is shown. The results, already presented in [1] show very promising results with sub 1% energy resolution and sub 0.5 % in the relative error of the RSP for all measured materials[1] for single proton events.

[1] Air does show a 12 % relative error but the absolute error is not relevant for a pCT.

DMAPS Tracking

Custom algorithms were used to associate hits into tracks. The main goal of this algorithm was to provide sufficient performance to evaluate the potential of the simulated pCT system. Although, in principle, further optimizations with superior medical and computational performance might be achieved by improving the reconstruction software, such a dedicated task is out of the scope of these studies, despite it might be addressed in the future as a natural continuation to this work. Accordingly, it is worth noting that the figures presented in the results section, especially regarding multi-proton reconstruction, constitute a lower bound of the potential performance of the system. For a given collection of fired pixels in one event, the DMAPS tracking algorithm finds a set of reconstructed trajectories running the following steps:

Define the number of tracks N as the lowest number of hits on a plane.

- Generate all the possible track combinations that do not share any common point and compute a fitness value (K) for each.
- Select the set of N tracks that maximize the total fitness.

Two different approaches were explored for the K parameter. On one hand, it was defined as the χ^2 of a straight line fit to all four pixel positions. On the other hand, as the minimum line-to-line distance using the two trajectories reconstructed with the two first and the two last planes. The latter was used as it works better for events with several simultaneous protons. Performance results are presented in Figure 8.4. In order to study the performance of the algorithm, two figures of merit were considered, the purity (p) and the efficiency (ε), defined as:

$$p = \frac{N_{well-reco}}{N_{reconstructed}}, \varepsilon = \frac{N_{reconstructed}}{N_{Total}} \tag{8.1}$$

where N_{Total}, $N_{reconstructed}$ and $N_{well-reco}$ stand respectively for the total number of simulated tracks, the total number of reconstructed tracks, and the total number of re-

constructed tracks with all hits belonging to the same true track.

A sketch showing all the possible reconstructed tracks (yellow dots) and the true tracks (yellow lines) can be seen in Figure 8.3. As it can be seen tracks are projected on the plane $Z = 0$ representing the centre of the phantom and the distance between the front and back tracker projections for the *i-th* combination is used as the K_i factor described above.

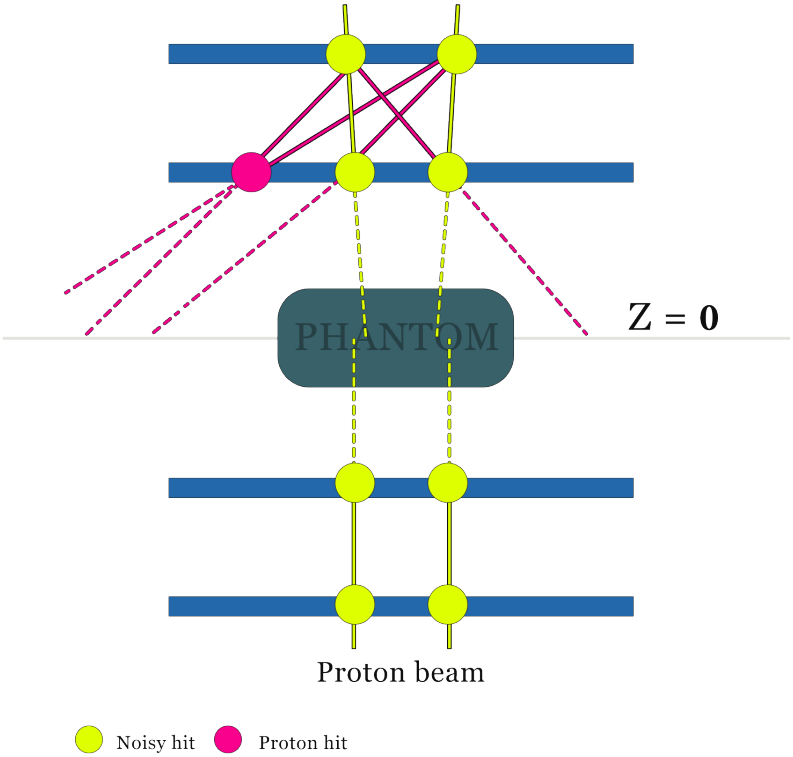

Figure 8.3: Sketch of the tracking algorithm showing the performance with two tracks see from above. Yellow dots represent hits coming from a proton while the red dot represents a noisy hit. The yellow lines represent the true tracks while the red lines represent the tracks discarded. The dashed lines represent the projection of the matched hits onto the $Z = 0$ plane.

Figure 8.4 shows the tracking efficiency times purity ($\varepsilon \times p$) for different thicknesses of a Water Equivalent Material phantom as a function of the number of protons.

Two main factors affect the degradation in $\varepsilon \times p$ observed in 8.4. The first is constant (regarding the number of protons) that varies for each thickness which is the efficiency drop due to the thicker WEPL that results in loss of protons due to strong interactions. The second is a drop in efficiency that increases with the number of protons due to MCS.

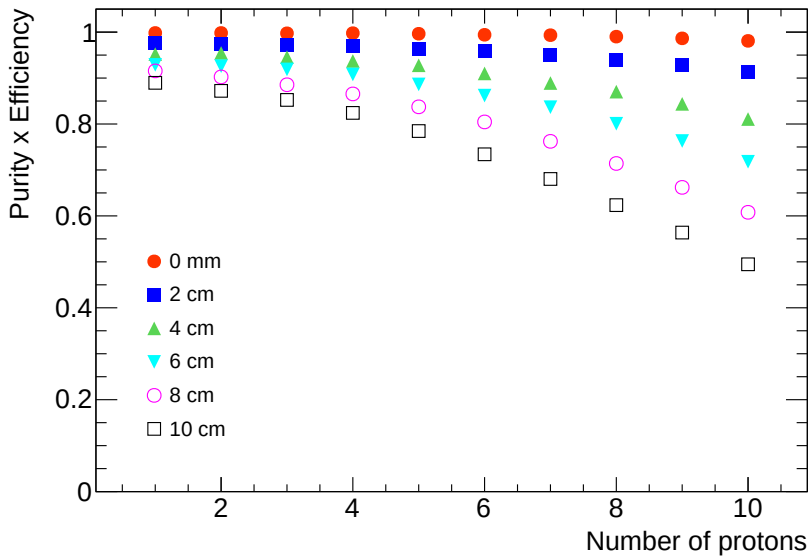

Figure 8.4: Plot of the purity×efficiency of the DMAPS tracker as a function of the number of protons per event for different thicknesses of the phantom in place. The studies are made using a Gaussian beam ($\sigma = 10$ mm) containing 180 MeV protons.

There is a limitation that does not depend on the resolution of the tracker but on the mean distance between protons at the event. If this distance is smaller than the distance that protons can scatter within the phantom then it is impossible to merge the front and back trackers using projections and minimum distances as presented in Figure 6.9.

Tracking within the ASTRA RT

For a given collection of bar hits in one event, the ASTRA tracking algorithm finds a set of reconstructed trajectories running the following steps:

- Make all possible 3D point combinations using the two first ASTRA layers.
- Set as track seeds all 3D points closer than a distance D to the trajectory defined by the last two DMAPS.
- For each seed, it iterates going upstream layer by layer. For each new layer, 3D point candidates are formed from the available hits. All candidates must be closer than a distance D. The closest candidate is added to the track.

- If no new candidates are found a new reconstructed track is formed. The hits used for the track are set as unavailable and the algorithm continues with the next seed until all seeds are processed.

WEPL calibration

To convert the energy loss into WEPL units a Water Tank (WT) test calibration was made. The results, presented in Figure 8.5, show the WT thickness as a function of the energy loss for a monochromatic 180 MeV proton beam.

For this calibration, water phantom slabs were simulated with thicknesses ranging between 1 to 10 cm in steps of 0.5 cm with a 180 MeV proton beam.

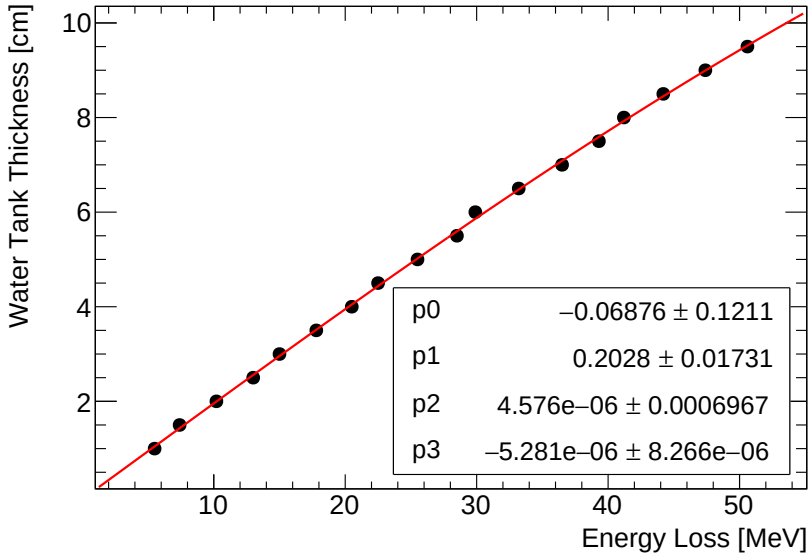

Figure 8.5: Fit of the simulated data of the water tank thickness as a function of the energy loss by a monochromatic proton beam of 180 MeV.

Energy measurements

To study the imaging capabilities of the system, a series of performance tests with phantoms placed between the second and third DMAPS were made. Unless otherwise specified a 180 MeV monoenergetic proton beam with a Gaussian profile (σ = 10 mm) was used well matching the work done in [15]. In order to reconstruct the protons' kinetic energy by range using ASTRA the strategy was to build a map from the reconstructed range in

ASTRA to the true kinetic energy of the proton provided by GEANT4, as presented in Figure 8.6.

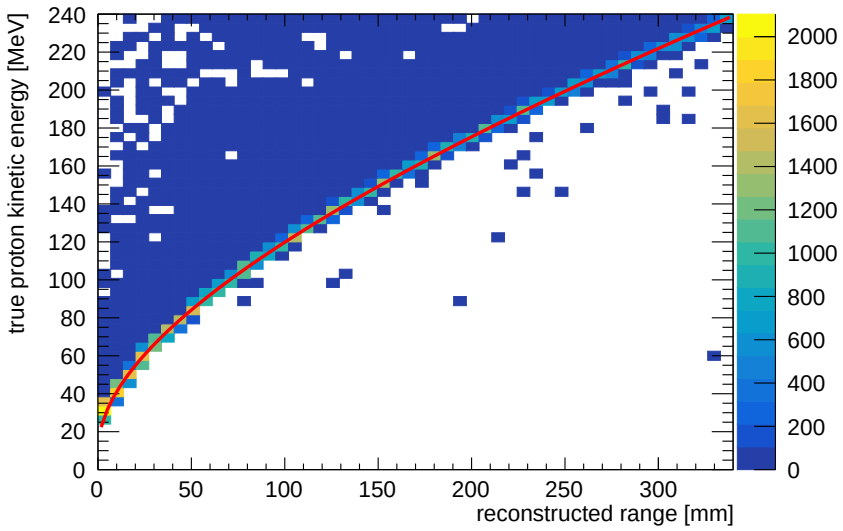

Figure 8.6: Fit of 2D plane of the true energy as a function of the reconstructed range.

The map from the reconstructed range to the reconstructed energy is obtained by fitting the most likely true energy for a given range using the following equation:

$$E_{Reco}(R) = a + bR + c\sqrt{R} \tag{8.2}$$

where R is the reconstructed range of the track and a, b, c are the fitting parameters. To compute the energy resolution, as presented in Figure 8.8, distributions of $1 - \frac{E_{True}}{E_{Reco}}$ were filled for all reconstructed protons. The distributions covered intervals of 20 MeV. Each of the distributions was then fit using a Gaussian function and the sigma of the fit was used as the energy resolution. Examples of two of these distributions and fits are presented in Figure 8.7.

The potential of including calorimetric information from ASTRA, in addition to the range, to reconstruct the energy of the protons was studied. In order to do so, the reconstructed range and the light yield from every hit associated with each reconstructed proton were used to train a Boosted Decision Tree (BDT). In particular, the BDTG method from the TMVA libraries [108] has been used. Half a million reconstructed protons have been

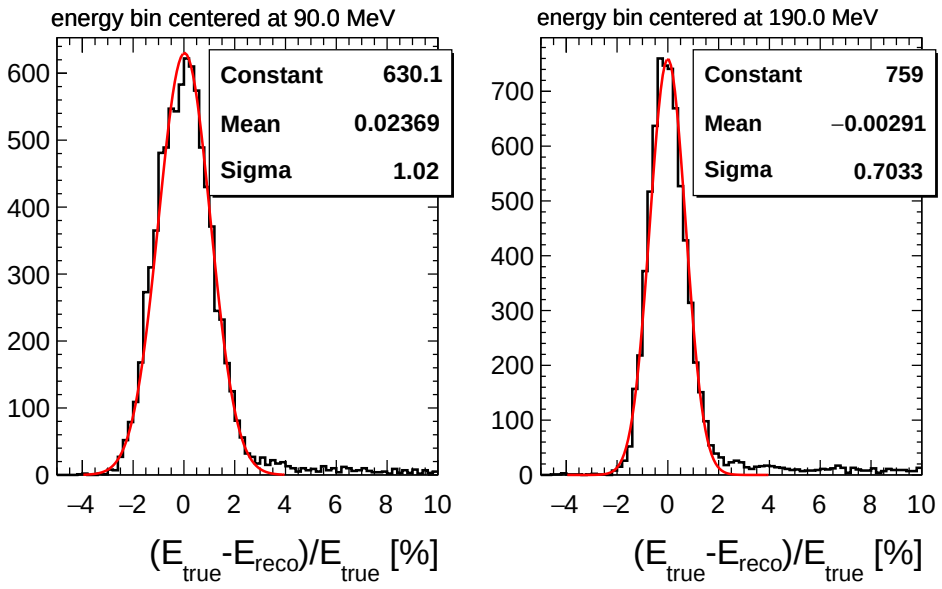

Figure 8.7: Examples of two of the distributions for bars of 3 mm used in Figure 8.8. The left (right) plot corresponds to a resolution of 1.02% (0.70%)

used for training. Later, the trained BDT was used to predict the reconstructed energy with independent data, namely, events not used to train the algorithm. For this study, only the ASTRA calorimetric information was used. An array of the energy deposited per layer with length 120 was passed to the BDT for the training and the true energy was set as the ground truth for the output. When an event had two hits on the same layer due to *e.g.* a tilt in the track, only the higher value of energy deposited was added on the list.

Results

The energy resolution by range in ASTRA, computed following the details described in the previous section, is presented for different bar sizes in Figure 8.8. Overall, the system exhibits a sub-1% energy resolution for the 3 mm configuration for protons with energies above 100 MeV. The energy resolution approaches $\sim$ 0.7% asymptotically. A similar performance is achieved for even coarser segmentations in the high energy limit, opening the possibility to reduce the number of channels of ASTRA and therefore its production costs. Using thick bars has, however, a caveat.

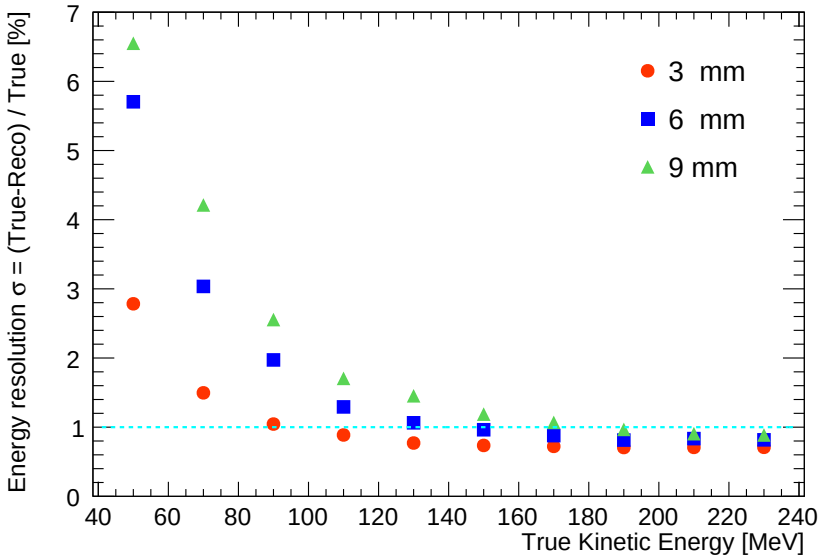

Figure 8.8: Energy resolution of the ASTRA range telescope using range-only information for three different squared-shaped bar sizes of 3, 6, and 9 mm. The dashed line highlights the 1 % threshold.

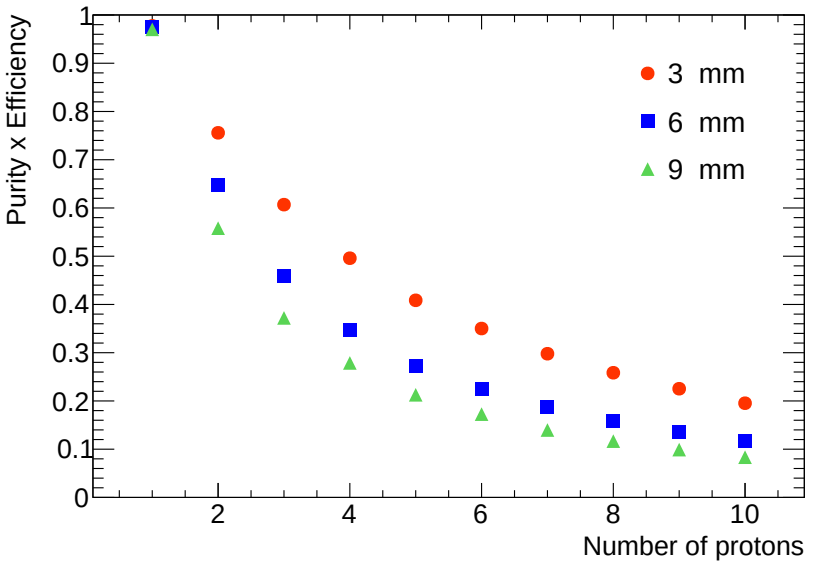

Figure 8.9: Purity×efficiency of reconstructed tracks in the pCT system (DMAPS+ASTRA) for different number of simultaneous protons for the 3 mm, 6 mm and 9 mm squared shaped ASTRA bars configurations.

As presented in Figure 8.9, the multi-proton tracking capacity of the pCT system, in terms of purity and efficiency, is significantly better for the 3 mm configuration. Hence, to explore this possibility, for the rest of the studies we focus on 3 mm bars.

8.3.2 Fully simulated pCT with DMAPS and ASTRA

Imaging tests were performed using the simulated pCT system. Such tests consisted on imaging phantoms, composed of up to seven different materials with densities defined in Table 8.1, placed between the second and third DMAPS planes, see Figures 8.15 and 8.16. Two different types of images were performed. A radiography for the first, using WEPL as the contrast variable for the image, and the full pCT with direct RSP measurements for the second.

Material	Density [g/cm^3]
Water	1.00
Adipose	0.92
PeRSP ex	1.177
Lung	0.30
HC bone	1.84
Rib bone	1.40
Air	1.3×10^{-3}

Table 8.1: Density values of the simulated materials used for imaging.

For the radiography, a proton scan of the phantom was made moving the center of the Gaussian beam in a squared grid over the phantom surface. The image coordinates were reconstructed projecting the reconstructed tracks' trajectory on an imaginary plane, perpendicular to the beam, located at the center of the phantom. A 2D grid of 200×200 image pixels of 400×400 μm^2 was defined on that plane, covering a total area of 8×8 cm^2. For each grid-pixel the protons reconstructed energy spectrum was stored, without correcting for their path-length in the phantom, in a 1D histogram with bins of 1 MeV width, see Figure 8.10. Later, the reconstructed energy was associated for each grid-pixel as the mean from a Gaussian fit to its reconstructed energy spectrum. For the pCT image, 360 radiography images were used, rotating by one degree the phantom for each scan. We accepted as protons Good For Imaging (pGFI) all reconstructed tracks with reconstructed energy in a 2σ range around most probable energy on its corresponding grid-pixel in the associated 2D radiography, as seen in Figure 8.10. The optimisation of an algorithm for image reconstruction was beyond the scope of this project. Thus, a back projection, based

in [109], [110], provided by the PRaVDA [12], was used.

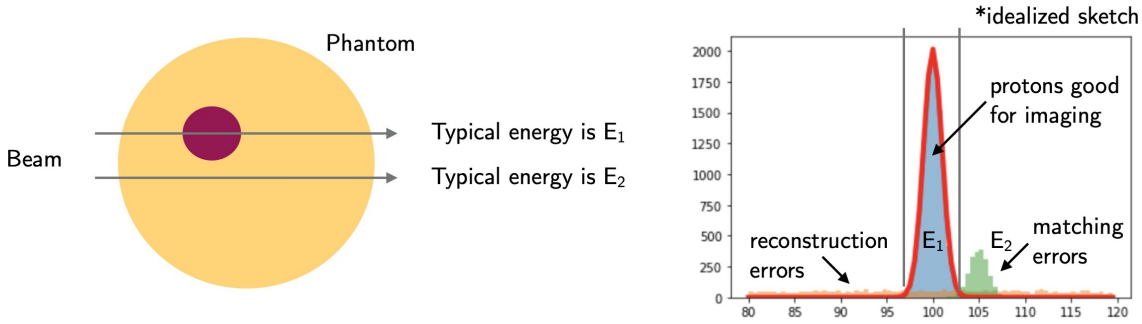

Figure 8.10: Sketch of two protons going through different paths leaving the phantom with different energies E_1 and E_2 (left). When these protons end up in the same pixel for some reconstruction error the energy profile shown on the right appears with the good protons (blue) and mis-reconstructed (green). The Gaussian fit (red line) around the mode is the one used to select the protons good for imaging.

This value was chosen as it accepted most of the protons good for imaging while removing possible tails. The motivations for this are further discussed in the next section. The position and direction of the accepted protons at each plane and the reconstructed energy of each proton were used as inputs to an algorithm developed by the PRaVDA collaboration [111] which outputs 3D RSP tomographic images. For the 2D images, the water tank calibration was only used to convert the energy loss into WEPL. This first set of images was made using energy reconstructed exclusively by range, without considering any calorimetric information.

When reconstructing the energy of protons exclusively by range, some miss-reconstructions are unavoidable. Protons experience inelastic interactions which shorten their expected range contributing to very long tails to the reconstructed energy. In addition, some tracking errors might lead to inaccurate range estimates. Thus, in the reconstructed energy distributions there are two regimes, a Gaussian distributed one arising from the correct reconstruction of elastic protons, and one conformed by long tails produced by tracking errors and inelastic protons. These features can be seen in Figure 8.12 which shows the energy resolution in the reconstructed energy by range. Of course, for events with a single proton tracking errors are expected to be close to zero and the tail contributions to come

mainly from inelastic interactions but for an increasing number of simultaneous protons tracking errors are more common, as the energy of the two trajectories, or some of their hits, might be swapped. Thus, a relevant figure of merit to understand the expected performance of the detector is to quantify how many reconstructed protons are good for imaging. For a pCT system with multi-proton capabilities, this depends significantly on the beam profile: the narrower the beam, the harder to correctly identify the hits associated with each proton.

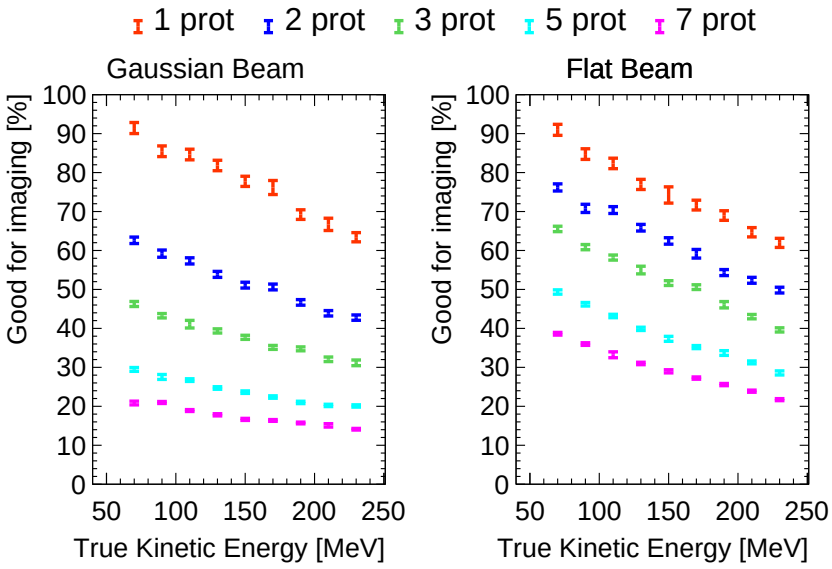

Figure 8.11: Fraction of protons good for imaging as a function of the proton true kinetic energy using a different number of simultaneous protons for a Gaussian beam ($\sigma = 10$ mm) and for a flat 75×75 mm^2 beam.

To illustrate this dependence, we present in Figure 8.11 the fraction of pGFI as a function of the number of simultaneous protons for two different beam profiles. The fraction of pGFI is obtained by fitting each distribution of energy resolutions with a Gaussian and counting the fraction of events within 2σ with respect to the total number of incident protons, such that the pCT system efficiency is considered implicitly. It is important to notice, as earlier presented in Figure 8.9, that the limiting factor for multi-proton tracking for the pCT system under consideration would come from the segmentation in ASTRA, given that the fine pixelisation of the DMAPS tracker allows to efficiently identify multiple protons at the same time with excellent purity. As expected, the results for ASTRA

show that the fraction of pGFI is higher if the simultaneous protons are typically more spaced. With this performance, even for the most challenging of the two beam profiles, which corresponds to a realistic clinical beam, about one proton per bunch can be used for imaging regardless of whether there is one, two, or three simultaneous protons in the bunch.

For the wider beam, even for the bunches with three and five protons about half of them are good for imaging. Finally, notice that, independently of the beam configuration, for higher energies the range is longer and the probability of experiencing an inelastic interaction grows, reducing the fraction of reconstructed protons which are good for imaging. In addition, one might wonder if the width of the sigma defining the Gaussian regime increases with the number of protons. This, however, has a very small effect as presented in Figure 8.12

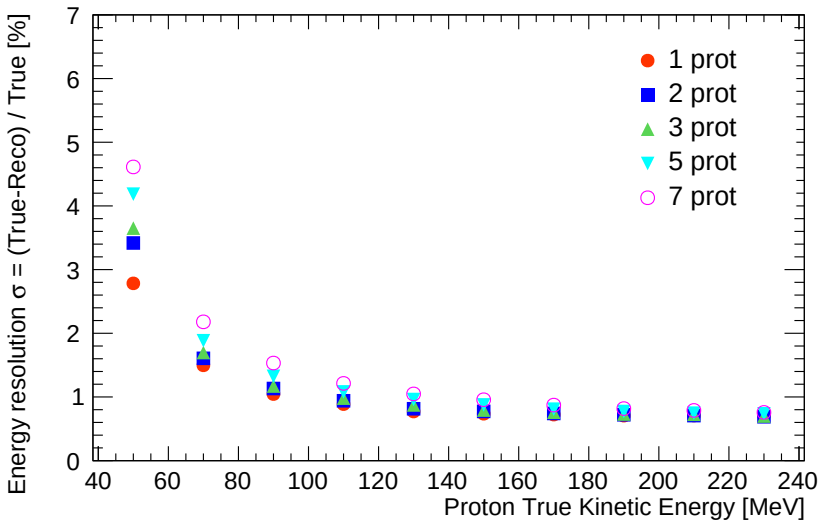

Figure 8.12: Energy resolution for different number of simultaneous protons as a function of the proton initial kinetic energy.

In a real pCT system the true proton energy is not known such that identifying which protons are good for imaging is not straightforward. A common solution is to build a classifier that tries to identify protons bad for imaging, e.g. searching for kinks or a missing Bragg peak in the energy tagger trajectory. The remaining protons are labeled as good. Recently, authors have reported a $\sim 97\%$ accuracy in this task using a CNN [112].

This method, however, is not entirely satisfactory for a multi-proton pCT system as sometimes the correctly reconstructed energy of two simultaneous protons is swapped due to matching errors between the position tracker and the energy tagger. To overcome this, we use the grid method detailed in Section 8.3.2 to determine which protons are good for imaging. Conceptually, the method consists in estimating the true energy in each pixel of the grid as the most probable value in the pixel's distribution and uses the distance between the expected and reconstructed energies to set up the selection criteria.

In order to study the benefits of using calorimetric information in ASTRA, we compare the range-only approach to an energy reconstruction method combining range and calorimetry. Considering the high data rate to produce the pCT, using small data transfers is preferred. Thus, we simulated the light yield as being discretized in 2^N values, to account for the impact of using an N-bits ADC. Two configurations have been considered, one with 4-bits (16 values), and one with 12-bits (4096 values). The difference in the quality of the calorimetric information for each configuration can be seen in Figure 8.13.

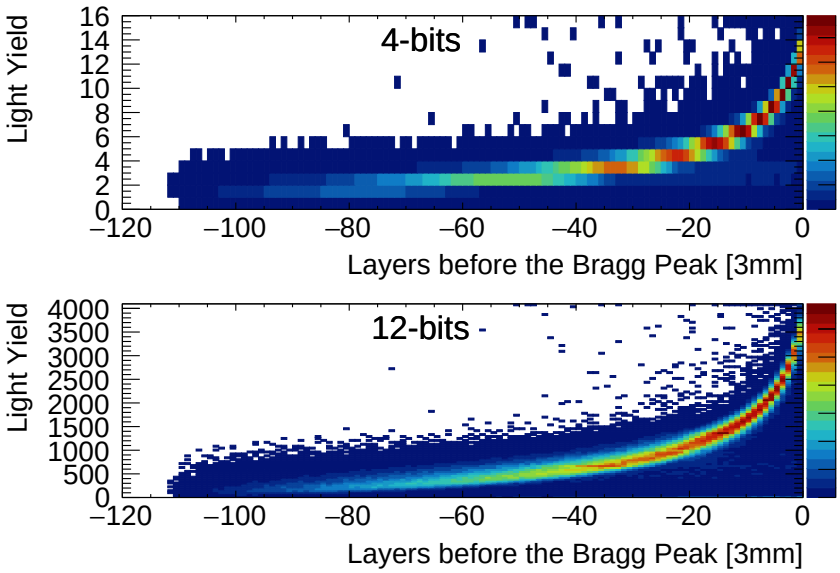

Figure 8.13: Reconstructed protons light yield as a function of the distance to the layer with maximum recorded light yield using the 3 mm bar configuration and two different ranges of values. The initial protons energy is uniform in the range of 40 to 240 MeV.

The associated performance for the energy resolution is presented in Figure 8.14. The results show a significant improvement for low proton kinetic energies. At high energies,

the energy resolution improves from $\sim 0.7\%$ to $\sim 0.5\%$. The results show that using a 12-bit ADC does not provide further performance benefits compared to a 4-bit ADC.

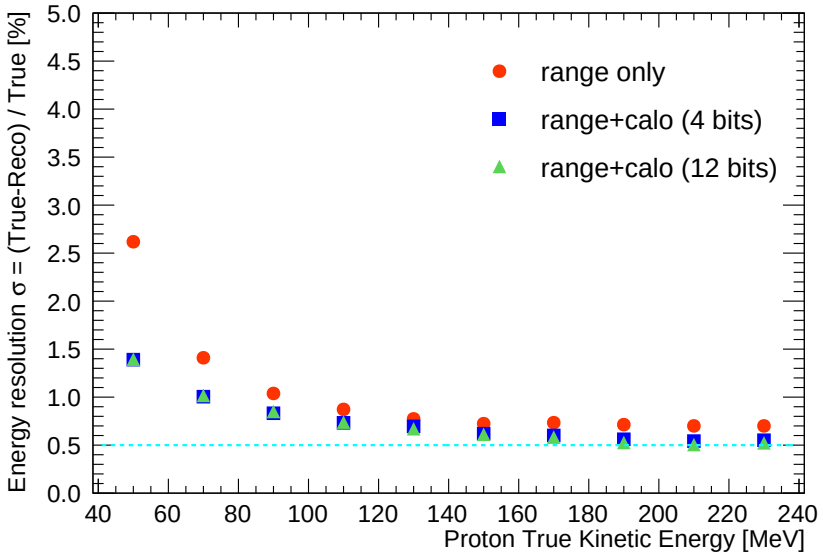

Figure 8.14: Energy resolution for single proton events with and without using calorimetric information. For the latter two configurations are tested, one discretizing the light yield in 16 values (4-bits ADC), and another discretizing the light yield in 4096 values (12-bits ADC). The dashed line highlights the 0.5 % threshold.

Radiography

A radiograph has been performed, using events with a single proton and three simultaneous protons, on a phantom formed by a simulated Water Equivalent Material (WEM) squared frame of 50x50 mm^2 and 30 mm pierced by four columns of cylindrical inserts of 30 mm length. Each column consists of four cylinders of the same material organized in four rows, each with a different radius. From left to right the materials are simulated as equivalent to lung tissue, rib bone, hard cortical bone, and adipose tissue. From the bottom to the top row the radii are 0.5, 1.0, 1.5 and 2 mm. The results are presented in Figure 8.15. For all materials and radii, the insert leaves a clear signature in the image. Notice that the smaller radius is comparable to the image pixel size of 400×400 μm^2. Despite both radiographic images looking equivalent under eye inspection, a quantitative analysis of the fluctuations within a selected 5 cm^2 uniform area of the phantom's frame,

centered at the point $(x, y) = (0, 11)$ between the first and second row of the rib and hard cortical bone inserts, was performed to understand the effects of the noise added by reconstruction impurities due to the multiple protons reconstruction. For the 1 proton (3 protons) radiography, the standard deviation of the Gaussian distributed WEPL fluctuations on pixels placed on top of the 3 cm thick phantom frame are 0.03 cm (0.06 cm), to be compared with a mean measured of 3 cm. Hence, the analysis reveals a significant relative degradation, moving from typical fluctuations of 1% to about 2%.

pCT and RSP measurements

The phantom used for the 3D pCT was a spherical phantom that consists of a 75 mm diameter sphere made of PeRSP ex (PMMA) with six different cylindrical inserts 15 mm high with 15mm diameter. The cylinders are placed in a three-by-three disposition forming two equilateral triangles in two different planes placed 9 mm above and below the center. A sketch of the phantom drawn from above and the front can be seen in Figure 8.16 left and middle respectively on the right, a picture of the real phantom used by the PRaVDA collaboration.

Figure 8.17 shows two sliced sections of a pCT performed using single proton events. Each slice corresponds to the half height of the top (left image) and bottom (right image) sets of inserts. The measured mean values of the RSP for each insert have been computed by selecting the voxel values within half the diameter of each cylinder at six different layers around the center. An equivalent region has been selected to compute the RSP of the perspex frame. The RSP values extracted from Figure 8.17 are presented in Table 8.2. True values have been computed using only true tracks and the true energy of the protons after passing through the phantom in order to provide a reference of the performance. All the reconstructed RSP values, except air, match the reference RSP values within 0.5 %. The air value shows a larger relative discrepancy due to the small RSP of air, comparable to the measurement uncertainty.

The profile in Figure 8.18 shows very stable RSP measurements in the form of smooth

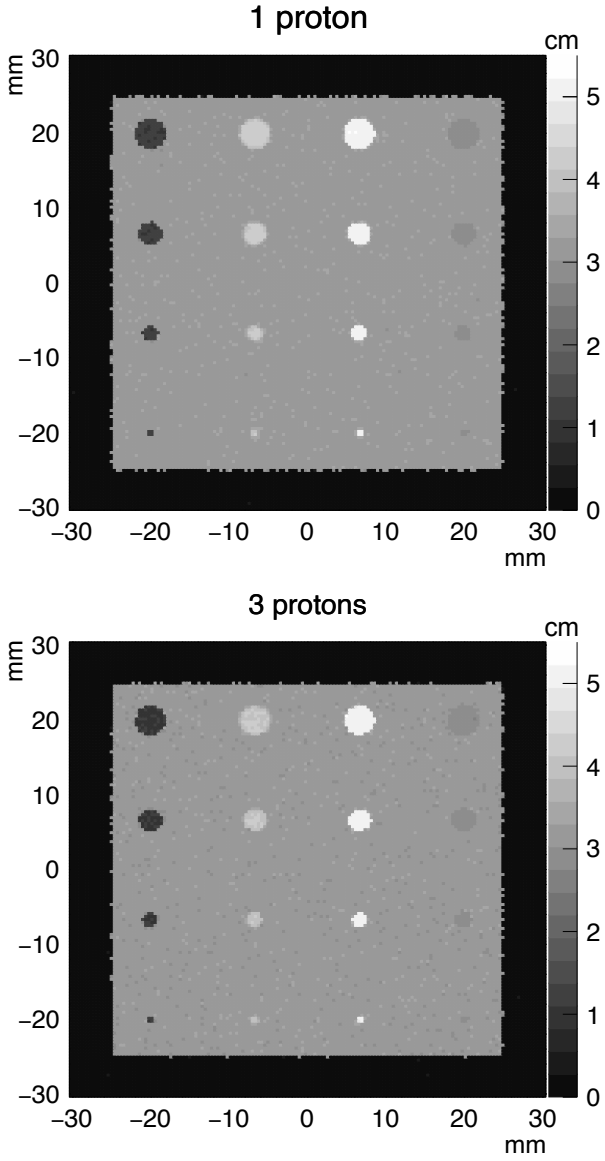

Figure 8.15: Proton radiography of the squared phantom using 1 and 3 protons. From left to right the materials are simulated as equivalent to lung tissue, rib bone, hard cortical bone, and adipose tissue. From the bottom to the top row the radius are 0.5, 1.0, 1.5 and 2 mm. Each image uses $5{\cdot}10^6$ protons. The Z-axis (color) corresponds to WEPL in mm and has been obtained using the energy loss and the data in 8.3.1.

trends and flat plateaus. Interestingly, the profile shows that, despite some circular artifacts that can be seen when carefully looking into Figure 8.17, the absolute values of the fluctuations introduced by such artifacts is relatively small when compared to the RSP variations induced by the presence of inserts. The spatial resolution of the pCT can be characterized by measuring the spread of the transition regions between such plateaus,

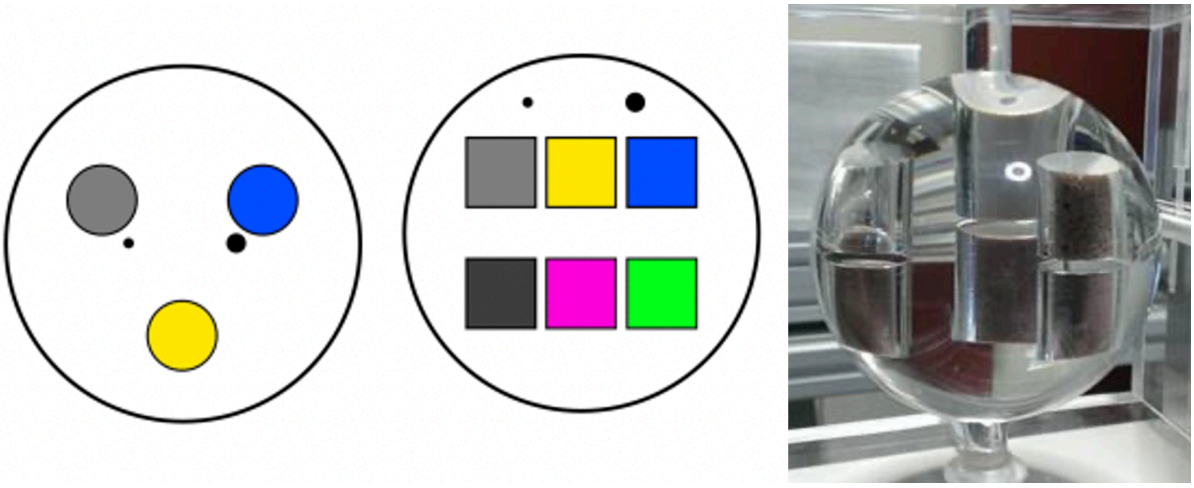

Figure 8.16: Sketch of the PRaVDA phantom used for the pCT measurements seen from above (left) and front (middle) and picture of the real phantom in the lab.

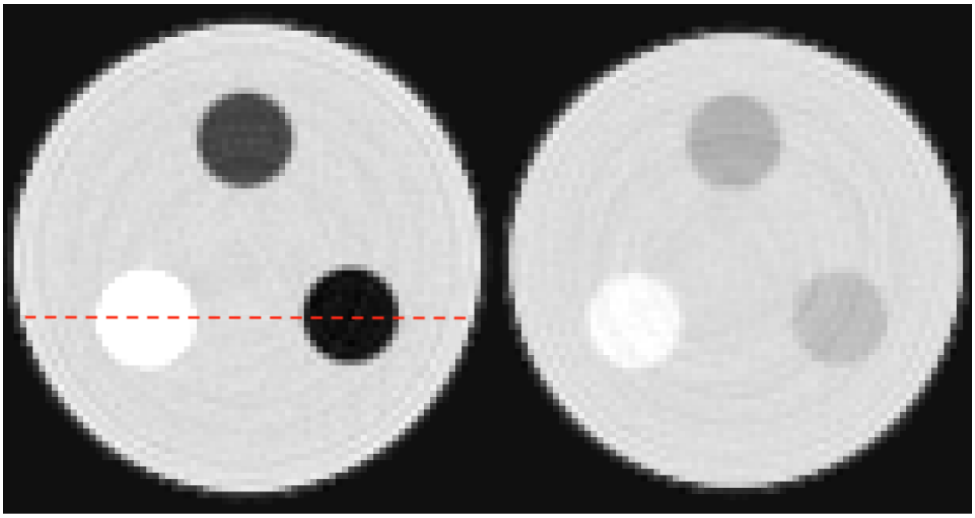

Figure 8.17: Slices of a proton computed tomography using single proton events showing the contrast in RSP for the six inserts. The different insert materials have been simulated to be equivalent to (from left to right): hard cortical bone, lung, and air (left slice) and rib bone, water, and adipose tissue (right slice). The red dashed line highlights the data used in Figure 8.18.

corresponding to moving from outside to inside of an insert (or vice versa). By computing the equivalent Gaussian associated with the error function (sigmoid), the spread has been quantified to be about 1.1 mm.

Finally, the same 3D pCT image has been made using exclusively events with three simultaneous protons. Following a method analogous to that for the single proton events RSP results are presented in Table 8.3.

Material	RSP (Reco)	RSP (True)	%diff
Water	0.992 ± 0.002	0.994 ± 0.002	0.201
Air	0.009 ± 0.002	0.008 ± 0.002	-12.5
Adipose	0.916 ± 0.006	0.917 ± 0.005	0.109
Rib bone	1.325 ± 0.003	1.326 ± 0.001	0.075
HC bone	1.641 ± 0.003	1.646 ± 0.002	0.304
PeRSP ex	1.144 ± 0.004	1.149 ± 0.002	0.455
Lung	0.302 ± 0.003	0.302 ± 0.002	0.000

Table 8.2: Relative Stopping Power (RSP) values for seven different materials extracted from the pCT image of the spherical phantom. The labels *True* and *Reco* stand for the energy used to compute the RSP . To help to compare the values the rightmost column shows the relative difference between the columns on the left.

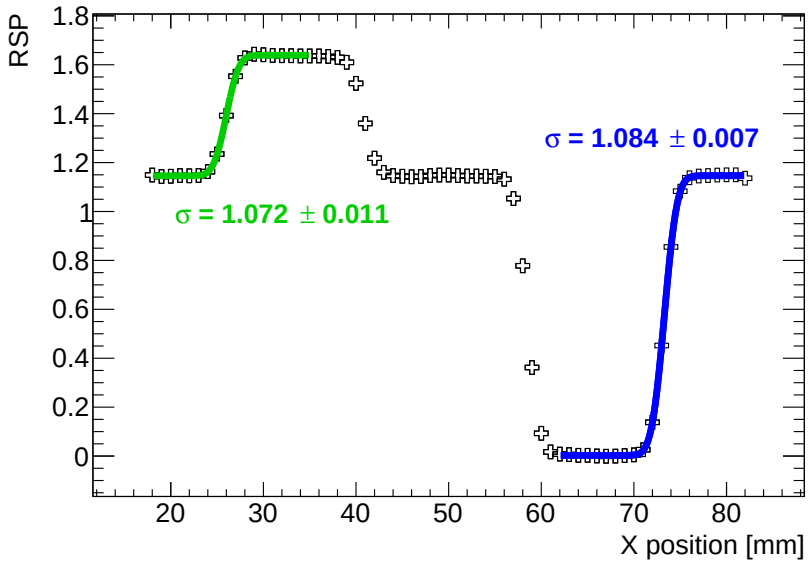

Figure 8.18: Projection of the RSP along the line highlighted in Figure 8.17. The rise in the RSP value has been fitted with an error function for the two inserts, hard cortical bone (green) and air (blue), characterized by a sigma detailed in the image.

Material	RSP (Reco 3p)	%diff (True)	%diff (reco 1p)
Water	1.033 ± 0.002	3.924	4.133
Air	0.076 ± 0.006	850	744
Adipose	0.96 ± 0.02	3.60	3.71
Rib bone	1.34 ± 0.04	1.06	1.13
HC bone	1.66 ± 0.02	0.85	1.16
PeRSP ex	1.14 ± 0.01	-0.78	-0.35
Lung	0.35 ± 0.02	15.89	15.89

Table 8.3: RSP values for the seven different materials of the spherical phantom reconstructed from three proton events compared withe true values and the values reconstructed from single proton events.

Although a significant degradation is observed, especially for the materials with lower RSP , the results are of remarkable quality if one considers the fact that only 3-proton events are used. To put it in context, these lower quality results are already competitive with currently existing technologies using only single proton events [113]. In a real-life situation, the beam settings could be configured to ensure a mode of single-proton events. Multi-proton time frames, often unavoidable due to beam instabilities, would not account for inefficiencies, as in the other existing technologies. Instead, the multi-proton tracking features of ASTRA open the door to developing reconstruction algorithms that associate different weights to each event depending on its reliability, with the goal to deliver a high quality pCT image. If including multi-proton events in the reconstruction chain would be possible an increased usefulness of the dose delivered to the patient could be achieved paired with a potential reduction of the scan times.

8.4 CNN analysis decoupling multi-proton events

The work presented in this section regarding the analysis of the ASTRA data for multi-proton events using Comboluted Neural Networks (CNN) was published by the conference paper by Instruments at [114]. The use of CNN was motivated by two key points: The possibility of performing online analysis of the ASTRA data on GPU farms reducing the data rate by, at least, an order of magnitude, and the potential to improve the multi-proton tracking efficiency. When using classic analysis, each ASTRA event would need to store an array of integers for each bar ID and a float value for the light collected. This would typically result in two arrays of ~ 20 floats and arrays. However, if the ASTRA data was to be analysed in this manner only 2 integers and 3 float numbers need to be stored for each track $(x_0, y_0, \omega, \theta, E)$ where $[x_0, y_0]$ are the horizontal and vertical positions of the proton when it reaches the first ASTRA layer, θ, and ω are the conic angles and E is the reconstructed energy, resulting in a remarkable decrease of the output data. The classic algorithms used to obtain the results of the first section were written using a conservative

approach that avoided using hits that shared a bar with another hit. With this, the drop in efficiency cannot be neglected. The use of CNN aims to use the information of energy deposited in order to reconstruct tracks that share one or more bars.

8.4.1 Methodology

A set of 1M events was simulated with a beam profile with a Gaussian beam with $\sigma = 10$ mm and an energy ranging between 80 and 180 MeV was generated recording the energy deposited on each ASTRA bar. With this data, a U-Net analysis was performed using, first a binary: *hit-no-hit* configuration and later with the energy deposited information. The architecture used an innovative combination of Multi-Label and Signal Segmentation problems. The idea behind this architecture is to provide an output that classifies each pixel in a given category but allows more than one label to be given to a single pixel. For a given two-proton event the labels would be defined as:

- Background = [1,0,0]
- TrackID_1 = [0,1,0]
- TrackID_2 = [0,0,1]
- $\text{Overlap}_{1,2}$ = [0,1,1]

In order to perform this analysis, the output of the ASTRA RT had to be modified in a way that the CNN could read it while the amount of data was not too big. The output included a list of the information of:

- Event number
- Orientation
- Bar ID
- Layer ID

- Energy deposited

These values were first merged into a single image, see Figure 8.19 including both the side (orientation = 0) and the top (orientation = 1) views with the energy deposited as the colour scale. The image was then transformed into a *numpy array* with dimensions [60,64,1] for the input data, with the energy deposited as the third axis; and [60,64,3] for the output data. Notice that the 3rd axis has dimension 3 but it has nothing to do with the RGB but rather the previous definition where the indices 0, 1 and 2 imply background, track ID 1 and 2 respectively. The first dimension (60) stands for the 60 layers for each orientation the 64 stands for the bar ID of each layer resulting into 32 (orientation 0 from 1 to 32) plus 32 (orientation 1 from 33 to 64) as depicted in the sketch in Figure 8.19 and the third dimension stands for the track ID definition from Table 8.4.1.

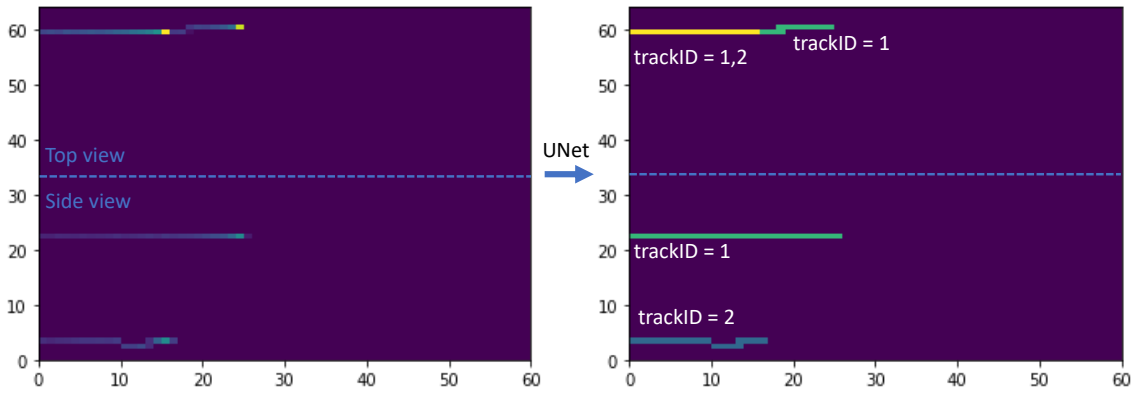

Figure 8.19: Sketch of the U-Net input and output images. On the left the U-Net input presenting the merged top and side views are shown with the energy deposited on each pixel while on the right the output shows the same merged views with the pixels presenting the track ID. The track ID is defined as green for TrackID_1, blue for TrackID_2, and yellow for $\text{Overlap}_{1,2}$. On both left and right images the background is depicted in purple.

Architecture

The architecture used was a symmetric U-Net with 5 layers before and after the bottleneck. The structure of each layer is the following:

(Number of filters, Kernel size, stride) =

[(32, 5, 1),(64, 5, 1),(128, 5, 1),(128, 3, 1),(128, 3, 1)]

The inner structure for each layer is: A convolutional 2D layer, followed by a leaky Rectified Linear Unit(ReLU), another convolutional 2D layer, a max pooling 2D (pool size = 3), a leaky ReLU and batch normalisation. The bottleneck is created by two layers with a structure of (128, 3, 1) with a convolutional 2D layer, a leaky ReLU, and a batch normalisation each. The activation function is a *sigmoid* and the output activation function is a *softmax*. This selection of activation functions was done in order to mimic both the classic multi-label architectures (using *sigmoid*) and the signal segmentation (using *softmax*). The loss function was also a combined defined by:

$$Loss_{comb} = 2.5 \times BFL(y_{true}, y_{predicted}) + CXE(y_{true}, y_{predicted}) \tag{8.3}$$

Where BFL stands for Binary Focal Loss (BFL) and CXE stands for Categorical Cross Entropy (CXE). The optimizer used was ADAM with a learning rate of 0.001 and the batch size was chosen to be 32. The total number of epochs was selected to be 13 by the early stopping call back from *Keras* after not improving the accuracy by 0.0001 in three consecutive epochs.

As seen in Figure 8.19, the U-Net is a machine-learning model that is designed to perform image segmentation. It takes as input an image that represents the combination of the top and side views with the energy deposited as the colour scale and outputs an image with the pixel colour representing the track IDs.

The CXE loss function takes into account the probability of each pixel in the input image belonging to a specific category and uses this information to update the model's parameters. On the other hand, the BFL function focuses on addressing unbalanced

problems, such as the distinction between track IDs 1 and 2 and the background. The combination of these two loss functions allows the U-Net to benefit from the key strengths of both functions and improve its overall performance.

The CNN was trained with 0.5 M multi-proton events with 2 protons on each event. The process was performed in steps, filtering first the data to provide easy tests and adding more complexity to it until protons with hard scattering were included. The last test had a 99.99% of the generated events.

The results of this analysis were then compared for single proton and multi-proton (2) events with the results obtained with classic algorithms by analysing the range resolution, the efficiency as a function of the cut in the relative error, the energy resolution and the efficiency as a function of the cut error in energy reconstructed. The final numbers to compare were the efficiency of the protons good for imaging for the different tracking methods.

8.4.2 Results of the CNN analysis

Disclaimer: In order to analyse the results of the CNN analysis they will be compared with the results obtained with classic algorithms. However one must take into account that the results with classic algorithms use the DMAPS information whilst the ones presented here only use ASTRA information. Furthermore, the benefit of using CNN not only benefits from a potential improvement in tracking efficiency but also in data management and the capability of analysing the tracks with an extra layer allowing the measurement of the energy of the protons that undergo hard scattering processes.

Single proton events

The plot observed in Figure 8.20 shows how close to 96 % of the events have 0 error on the reconstructed range and more than 97 % of the tracks have an absolute relative error below 1 %. The plateau is reached above 97% efficiency. The results are consistent with what was observed with 1 proton in classic algorithms.

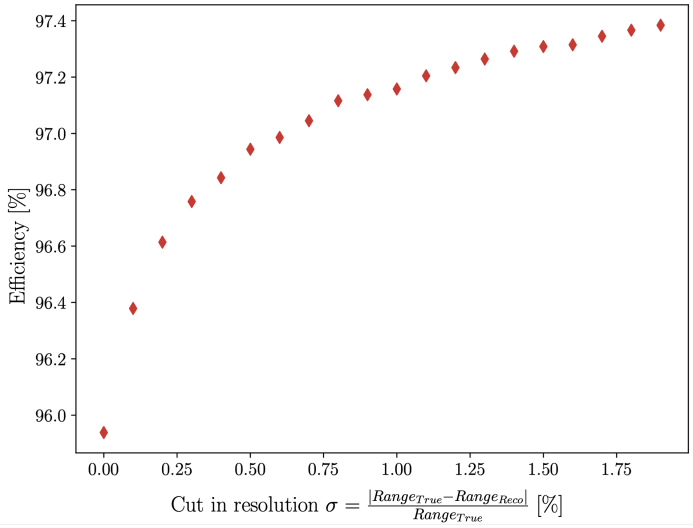

Figure 8.20: Efficiency as a function of the cut in the energy range resolution for a single proton CNN analysis.

Figure 8.21 shows the distribution of the true energy as a function of the reconstructed range for single-proton events with CNN tracking. As expected, and observed with classical algorithms, some events fall over the trend following equation 8.2. As aforementioned this is due to the events that include hard interactions which result in a shorter track for a given energy. About 18 % of the events seem to follow this pattern. Thus, Figure 8.22 shows the resolution of the reconstructed energy. The Gaussian region fitted by the dashed red line has a mean centered at 0.3 which represents the bias of this reconstruction (constant for all energies) and a $\sigma = 0.85$ which represents the resolution of this measurement. The non-Gaussian region on the right side of the plot is due to the hard interacting protons. The vertical lines dashed lines at $\pm$ 1.6 enclose the protons good for imaging for this range of energies between 80 to 180 MeV. As expected, since the protons that interact strongly cannot be reconstructed solely by range the efficiency of protons good for imaging is 80 %, in agreement with the results obtained with classic algorithms presented in Section 8.3.2.

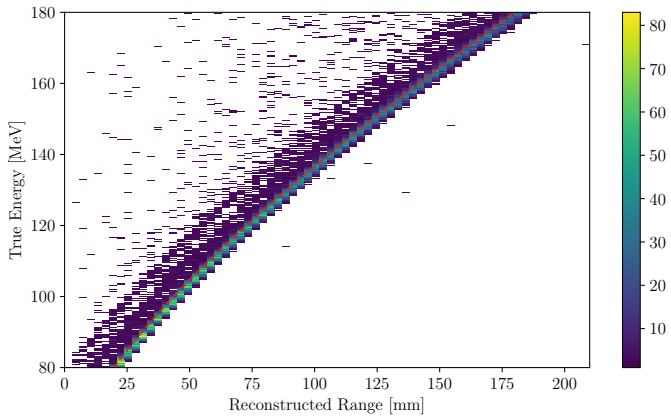

Figure 8.21: 2D histogram of the true energy as a function of the reconstructed range for one proton events with CNN tracking.

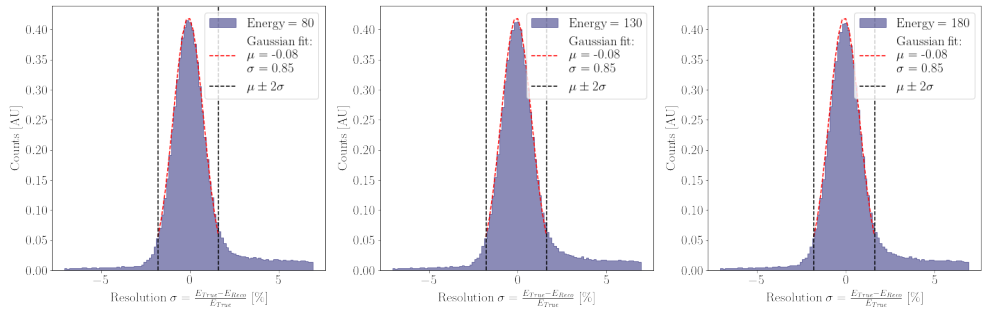

Figure 8.22: Dispersion of the reconstructed energy error for different energies; 80 MeV (left), 130 MeV (middle), and 180 MeV (right) with the range reconstruction done using CNN. The vertical lines at $\pm 2\sigma$ show the range enclosing the protons good for imaging which equals 80 % of the total.

Multi-proton events

The range reconstruction of multi-proton events with a Gaussian beam with a $\sigma = 10$ mm results in a high percentage of tracks with overlap on at least one of the bars. This complicates the tracking inside ASTRA, but with the CNN algorithm, the results recovered are very promising. Figure 8.23 shows a visualisation of the results of the network.

Figure 8.24 shows the acceptance efficiency as a function of the cut in the relative error when computing the track's range with the U-Net. More than 74 % of the protons have a range reconstruction with 0 % error and 82 % of the tracks have an absolute relative error below 1 %. These efficiencies show much better results than the ones obtained by

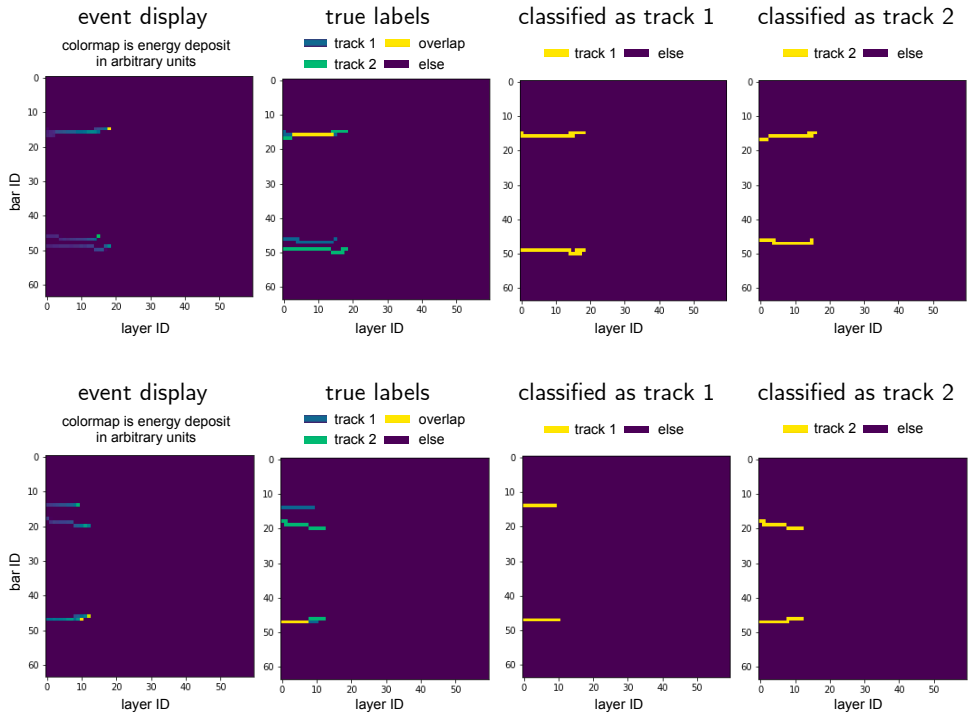

Figure 8.23: Display, from left to right, energy deposited of the track used as input, the true values and the outputs of the U-Net for track ID 1 and track ID 2.

classic algorithms.

The true energy as a function of the reconstructed range is plotted in Figure 8.25. As opposed to what was observed in Figure 8.21, in this case, there are tracks that fall up and down the main trend. This is due to reconstruction errors in which the track has been reconstructed with a range larger than the original. Thus, such a track falls below the trend since it has a reconstructed range larger than expected for its true energy.

Figure 8.26 shows the resolution of the reconstructed energy. The vertical lines at $\mu \pm 1.6$ show the region enclosing the protons that are good for imaging. This range includes 69 % of the data. The tail on the left (negative implying true energy smaller than reconstructed energy) contains 10 % of the data, this is 5 times larger than for the single proton events case and it is due to the errors on the proton tracking. The remaining 20 % of the events are found on the right tail (positive implying reconstructed energy smaller than true energy) which results in a combination of protons that were not properly reconstructed and the larger amount of hard interacting protons reconstructed.

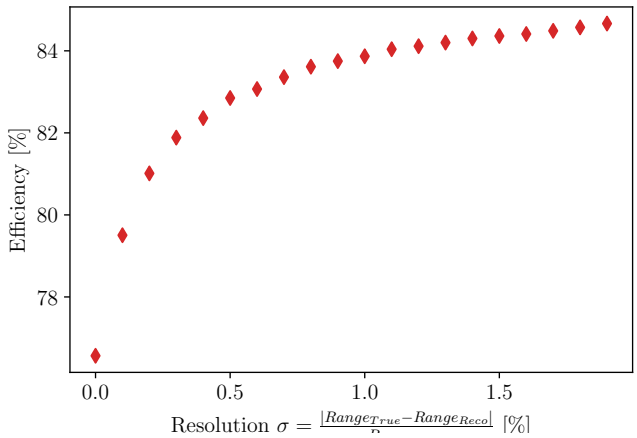

Figure 8.24: Efficiency as a function of the energy range resolution for two proton events with CNN analysis.

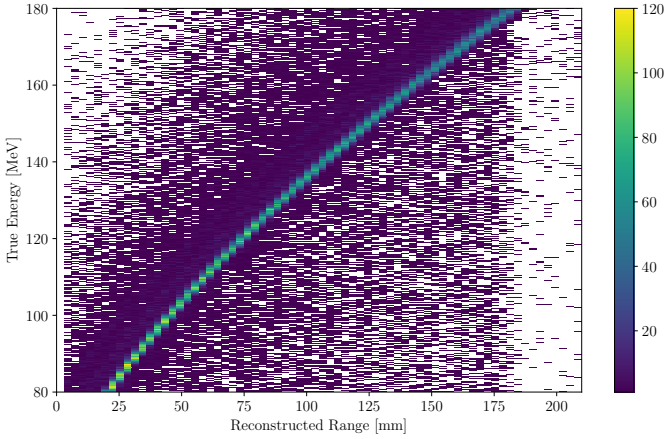

Figure 8.25: 2D histogram of the true energy as a function of the reconstructed range for two proton events with CNN tracking.

8.4.3 Comparing with classic algorithms

Regardless of the intrinsic advantages of using CNN such as being able to use GPU farms to analyse the data online and reduce the amount of data storage per second. The results from the U-Net must be compared with the ones obtained with classic algorithms in order to assess what is the true benefit of using CNN for tracking.

In Table 8.4 there is a comparison between the results obtained with classic algorithms and with the U-Net for single proton and two proton events. The numbers compared are

the percentage of protons that are tracked within a 1 % error in the range and the percentage of pGFI on average for all the energies within the range between 80 and 180 MeV.

The results show that, as expected, for single proton events, the U-Net recreates the results obtained with classic algorithms. However, with two proton events, the range reconstruction and the percentage of protons good for imaging are much better. Furthermore, these results, and the fact that there is a 17 % constant loss in the energy reconstruction, encourage the use of an extra CNN to perform this reconstruction. The protons that interact strongly resulting in kinks in the track cannot be reconstructed by range but with the use of the deviation angle and the energy deposited in the interaction point a CNN could perform a much better energy reconstruction.

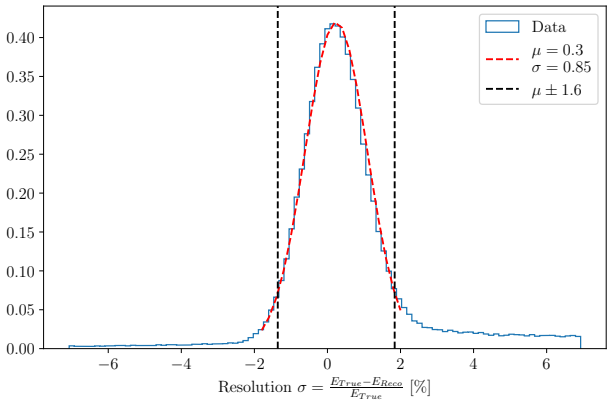

Figure 8.26: Dispersion of the reconstructed energy error on the range between 80 to 180 MeV with multi-proton events (two protons) and with range reconstruction using U-Net. The vertical lines at $\pm\sigma$ show the range enclosing the protons good for imaging which equals to 69 % of the total.

Algorithm	1p (± 1% Range) [%]	pGFI [%]	2p (± 1% Range) [%]	2p pGFI [%]
Classic	97	80	69	55
U-Net	97	80	82	68

Table 8.4: Comparison of the efficiencies between the classic algorithms and the U-Net based tracking for 1 and 2 proton events for within 1 % error in range reconstruction and protons good for imaging.

8.5 Energy measurement with DNN for inelastically scattered protons

As mentioned in the previous section, for both the single and multi-proton events, close to 20 % of the reconstructed tracks are lost due to inelastic scattering when performing the energy reconstruction by range. In this section, an analysis of the energy reconstruction of the ASTRA RT based on the use of DNN for protons that suffer inelastic scattering is presented.

8.5.1 Methodology

In order to train a neural network able to reconstruct properly the energy of the inelastic protons, a pre-selection of events was performed by only accepting the protons falling above the $+\sigma$ Gaussian range. Thus, this selection only contains 17 % of the events which results in a dramatic reduction of the data. An extra simulation of 4 M was performed in order to recover a total number of 524000 events from which 90 % were used for train and test purposes and the remaining 10 % only for validation. Due to the low data and the complexity of the problem the train and test data were re-shuffled after every epoch to avoid overtraining while a validation set was kept intact for the later evaluation of the NN. The architecture used for this network is defined below. The input for this NN is similar to the one used in the previous section, a 60x32 image with the energy deposited in each bar as the pixel value. Notice that only single proton events have been selected. This assumes that after the tracking performed in the previous section, one can use that output combined with the original input in order to recover the full track with the energy deposited. Notice that tracks that fully overlap and which contain the Bragg peak of one track within the other will probably not be reconstructed by this neural network due to the selection of tracks mentioned above. Moreover, MCS within the imaged phantom reduces the probability of tracks in ASTRA being perfectly parallel. Further work would include the test of multi-proton events and the test of different methods of decouplings of

the energy associated with each track.

The design of the architecture and different parameters such as batch size or the optimizer used were optimized by testing different combinations. For simplicity in this Section, only the different results for different batch sizes and the use of different decay parameters for the ADAM optimiser will be presented.

After every ten epochs, the performance of the algorithm was further evaluated by analysing a validation set and computing the efficiency of the pGFI. The shape of the resolution plot presented in 8.29 is significantly different from the one observed for range reconstructed energy. A sum of two Gaussians was fitted to the data. Thus, to preserve the energy resolution of the protons reconstructed by range, the model was directly assumed to have zero efficiency if the energy sigma of the narrower Gaussian was above 1 %. The pGFI were only accepted if within the 2σ range of the narrower Gaussian ensuring that the increase in efficiency does not compromise the energy resolution.

Architecture

The architecture selected for this regression problem consists of a CNN with 5 layers with the following parameters:

(Number of filters, Kernel size, stride) =

[(32, 5, 1),(64, 5, 1),(128, 5, 1),(128, 3, 1),(128, 3, 1)]

The inner structure for each layer is:

A convolutional 2D layer, followed by a leaky ReLU, another convolutional 2D layer, a max pooling 2D (pool size = 3), a leaky ReLU, and batch normalization. Two different architectures were used for the final result. First, an activation and output *linear* layer for the first training. Then a second activation layer of *tanh* was implemented before the

output activation *linear* layer.

The loss function used was the mean absolute error. The optimizer used was ADAM with a learning rate of 0.001. The batch size was chosen to be 16 but tests with 8 and 32 were also performed. The total number of epochs was selected to be 90 after applying the re-shuffle method and thus no early-stopping was used in this case.

The true energy was normalised from 0 to 1 using the following equation:

$$E_N = \frac{E_T - 80}{100} \tag{8.4}$$

Where E_N is the normalised energy and E_T is the true non-normalised value. This is done taking into account that all energies range between 80 and 180.

8.5.2 Results

The plot in Figure 8.27 shows the loss (MAE) as a function of epochs for the training (dashed) and test (solid) data sets for batch sizes of 8 (olive), 16 (blue), and 32 (yellow). Figure 8.27 shows how the error of the test data set oscillates around the value of the training due to the re-shuffling and recasting of the sets after every epoch. Notice that the batch size equal to 8 was early stopped at the fortieth epoch due to the lower performance in both MAE and efficiency compared to the other cases.

The final result was obtained by running an extra training using the already trained weights with 100 epochs of the batch size equal to 16. Figure 8.28 shows the MAE as a function of the epoch for the original train and test samples (blue) and the results after running with the extra *tanh* activation layer using the pre-trained weights (olive).

8.29 presents a histogram of the relative error of the energy reconstructed by the DNN and the true energy when using the validation data set. The red dashed line shows a double Gaussian fit performed to obtain the mean and the dispersion.

The resolution distribution is centered at zero. The sigma of the narrow Gaussian is 0.74 %, and a $2 \pm \sigma$ region is delimited by the black dashed lines. Taking $2 \pm \sigma$ (*i.e.*

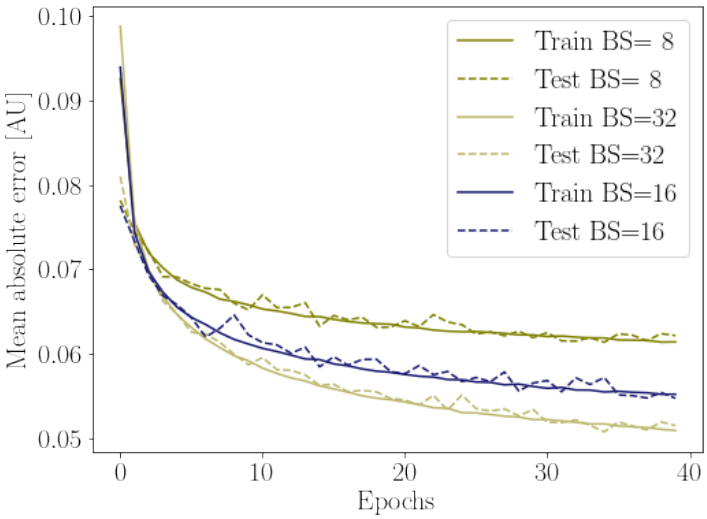

Figure 8.27: Mean absolute error as a function of the epoch for different batch sizes of 8 (olive), 16 (blue)

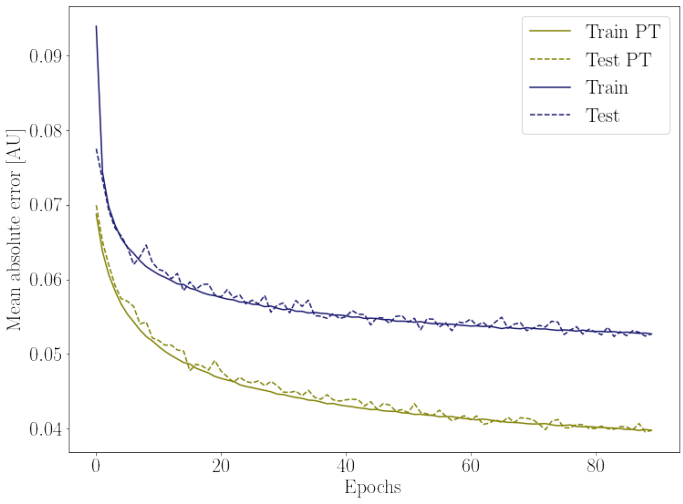

Figure 8.28: Mean absolute error as a function of the epoch for first training with batch size equal to 16 (blue) and for the pre-trained test with batch size equal to 16 and an added extra activation layer of tanh (olive)

the pGFI), 41 % of these formerly rejected tracks are recovered 7 % improve in total efficiency. The results are summarised in Table 8.5.2. The protons recovered are within the pGFI acceptance limit, and thus, this results in an increase of the protons used for imaging without compromising the purity of the reconstruction and the resolution of the

energy reconstructed. It is important to notice that, by looking at the plot in Figure 8.27, one could expect that the best performance was given by the Batch size equal to 32; however, when testing the efficiency of the reconstruction after applying the $\pm\sigma$ cut, the best performance was given by the batch size equal to 16. This presents a disagreement between the minimisation of the loss function and the performance of the problem at hand. Thus, regardless of the results obtained presenting an accpetance of 41 % of the evaluated protons, there is room for improvement on the method by looking for a customised loss function as done in the previous section.

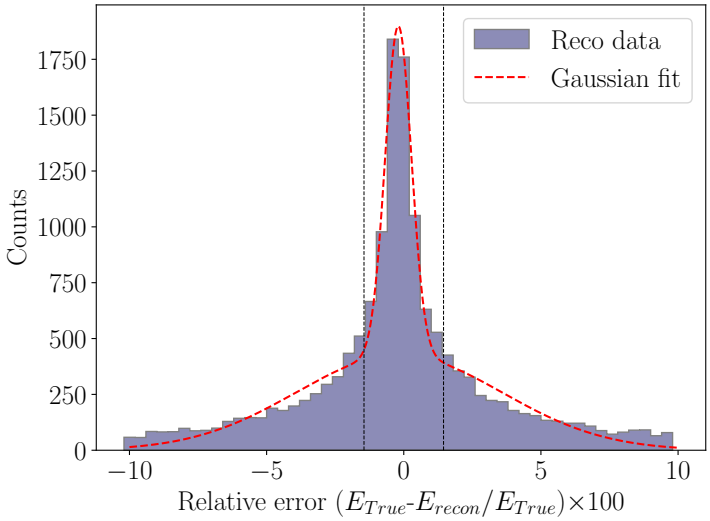

Figure 8.29: Dispersion of the relative error of the energy reconstructed by the CNN.

Algorithm	1p (± 1% Range) [%]	pGFI [%]	2p (± 1% Range) [%]	2p pGFI [%]
Classic	97	80	69	55
U-Net+DNN	97	87	82	75

Table 8.5: Comparison of the efficiencies between the classic algorithms and the U-Net based tracking for 1 and 2 proton events for within 1 % error in range reconstruction and protons good for imaging after using the DNN algorithm to reconstruct the energy of the inelastically scattered protons.

8.6 Summary of the chapter

In this chapter, a novel range telescope concept is presented based on currently existing and well-understood technologies. A full Monte Carlo simulation has been built able to replicate all the relevant features of the proposed system. In its most economic version, with electronics based on single discriminator thresholds, ASTRA would reconstruct the proton's energy exclusively by range, with an expected energy resolution similar to 0.7%. The simulations report that more complex electronic choices could improve this value to about 0.5% by including calorimetric information. Based on the specifications of the proposed components for ASTRA, an unprecedentedly fast deadtime free proton readout able to cope with 10^8 protons/s (100 MHz) is expected.

To study the imaging performance of the system two phantoms have been used to perform respectively a 2D radiography and a 3D proton computed tomography. The radiography results show excellent detail and contrast even for inserts of sizes comparable to a single pixel. The pCT results show very high 3D contrast, quantified studying the RSP values for different materials, and very good spatial resolution similar to 1.1 mm. Additionally, throughout the paper, the additional possibility to use the bar-based ASTRA geometry to reconstruct multi-proton events has been studied. The results highlight the potential of this additional feature which might be exploited in the future to increase the usefulness of the dose delivered to the patient and to reduce the scan times.
Overall, the results report great potential for this novel technology which might pave the way toward the development of high-precision pCT devices capable of working under realistic clinical conditions.

The design of the ASTRA range telescope has been reviewed, and alternatives to its mainstream reconstruction strategy have been presented. A U-Net-based tracking algorithm has been tested as an alternative to enhance the reconstruction of events with piled-up protons. The results are very promising, significantly outperforming those obtained with classical methods by properly reconstructing up to an 82 % of the tracks of two proton events. Additional deep learning methods to reconstruct protons energy were

evaluated to improve reconstruction metrics associated with protons undergoing inelastic interactions resulting in an improvement of a total of 7 % of the total efficiency leading up to an efficiency of 87 % with the potential of further improvements with a dedicated loss function.

Chapter 9

Conclusions

The work performed for this thesis aimed to provide a proof of concept of the potential of pixel chips, such as DMAPS, by testing the TJ-Monopix chip under clinical conditions. For this work, two sets of TJ-Monopix chips were characterised and optimised to work with clinical protons. For the initial tests, the TJ-Monopix was characterised with the use of an ^{55}Fe source.

Later on, tests studying the saturation point of the TJ-Monopix were performed proving that the TJ-Monopix was capable of measuring up to 1 M hits per second, regardless of the area of the irradiated area. With this, measures of up to 10 Mp/cm^2/s. The cluster size was found to be dependent on the flavour structure and thus, a sensor with the RDPW could perform scans with a flux up to 16 % higher than with this mixed structure and up to 33 % than with the FDPW alone.

The TJ-Monopix was also used at the MC40 cyclotron to measure the time it takes for the Faraday cup to fully open the beam. This time was measured to be 15.5 ± 3 ms using two independent methods. It was also measured that during the opening of the Faraday cup, the beam was homogeneous within a 1 cm^2 collimator. This implies that with similar closing times, the Faraday cup system at the MC40 cyclotron allows providing homogeneous irradiations within a time below 50 ms.

Using two TJ-Monopix systems, and a frameset allowing alignment up to few microm-

eters, single proton events, sourced by the MC40 cyclotron at 28 MeV, were tracked using a dedicated matching algorithm.

Tests with simulations have been conducted with good results to assess the reliability of the study. The proposed technique allowed the two TJ-Monopix systems to match and track protons from both sensors with an 86 % efficiency given a 91 % geometrical efficiency even with the timing delay.

As expected for the MC40 cylcotron protons, the MCS suffered within the thin silicon sensor makes it impossible to project the protons' position making the projections unusable due to the low resolution. However, the capability of proton tracking was efficiently tested with such protons.

The pMBRT beamline at the Curie Institute was chosen to perform a second test beam for two main reasons. The single slit collimator allows the TJ-Monopix to work with a very high proton flux of 3.7×10^7 p/cm^2/s and the higher are expected to reduce the azimuthal scattering angle (θ) by two orders of magnitude as shown by the simulations.

A study of the expected number of protons and hits per second with the single mini-slit setup at the Curie Institute was performed. The number of hits per second suggests that the optimal position where set the slit would be at $R = 15\sqrt{2}$ mm, *i.e.* at ~ 21 mm from the centre.

A test beam at the Curie Institute was performed and the results of the single sensor analysis were presented here. The results include fine alignment in the X and Y direction (0.06 mm and 0.09 mm in the X and Y axis respectively); a profile of the angular beam straggle in air; the confirmation of the saturation point ~ 21 mm away from the centre; and a study of the cluster size and charge reconstruction with the TJ-Monopix.

A setup using the slit collimator of the Curie Institute was simulated with 100 MeV protons and the TJ-Monopix sensor. The proton tracking results show, as expected, a small angle dispersion due to MCS more than one order of magnitude smaller than for the 36 MeV protons at the MC40 cyclotron. The results suggest that multi-proton tracking and track projections could be performed at these energies with the TJ-Monopix. The

effect of secondary particles was measured to be negligible in single proton events tracking when using the algorithm defined in 8.3.1; the use of the charge collection as a variable to improve the efficiency in multi-proton events was suggested; and the resolution of the projection of the proton tracks was measured to be 70 μm when back projecting the protons to the collimator position being 10 cm away from the first sensor.

The thesis concludes as a satisfactory work of proving the capabilities of pixel detectors, and more precisely DMAPS, for medical applications in pCT and beam monitoring. The work performed here was also useful in defining the limitations of the TJ-Monopix and providing useful insights on how the future chips would need to be developed and the reasons why they should be improved in the future. Increasing the size of the chips would have a big impact on the usability of the sensors for all medical applications and it could be achieved in the near future thanks to techniques such as stitching [115]. Moreover, there is a need for a dedicated readout electronics architecture for the chip to allow it to measure a higher number of protons per second.

Simulations have been performed showing that, with these two modifications, a dedicated chip would have a great impact on the state-of-the-art tracking techniques used for individual proton tracking for pCT and provide good feedback for beam monitoring at the clinical lines.

In the last chapters, a design for a plastic scintillator-based range telescope was proposed with the name ASTRA. The chapters present the results of the simulations with a $sub-1\%$ energy reconstruction and a $sub-0.5\%$ error in the RSP measurement of six out of the seven different materials tested for single proton events and up to around 1% error for three different materials for three-proton events with two more materials with errors below 4%. These resolutions and the conditions in which they have simulated, imply a big step forward in the field at the time of the publication. Furthermore, the analysis of the data within the ASTRA range telescope was enhanced by the use of CNN algorithms raising the efficiencies of the reconstructions of single protons up to 87 % and up to 75 % for events with two protons. Further tests also showed that this method has the potential

to be further improved with the use of a customised loss function.

Funding has been secured to continue with the work performed for the thesis. A grant has been awarded for a postdoctoral position in order to follow up with the test beams at the Curie Institute, funding a new test beam in order to be able to track protons at the pMBRT line and analyse the data. Moreover, funding has been secured to build a prototype of the ASTRA range telescope and work with the first bar prototypes is already ongoing while the first test beams will be performed during this summer at the MC40 cyclotron.

T2K Tokay to Kamioka 1

IFAE Institut de Física d'Altes Energies 1

BP Bragg peak 2

PSP Proton Stopping Power 2

SECT Single-Energy CT 3

DECT Dual-Energy CT 3

HU Hounsfield Unit 3

RSP Relative Stopping Power xix

pCT proton Computed Tomography xi

CT Computed Tomography 3

MCS Multiple Coulomb Scattering xvi

DMAPS Depleted Monolithic Active Pixel Sensor xii

HL-LHC High-Luminosity Large Hadron Collider 6

pMBRT proton MiniBeam Radiotherapy xi

FC Faraday Cup 6

SiPM Silicon Photo Multiplier xiii

HEP High Energy Physics 5

ROS Reactive Oxygen Species 8

DSB Double Standard Breaks 10

LET Linear Energy Transfer 9

CSDA Continuous Slowing Down Approximation

RBE Relative Biological Effectiveness 16

SOBP spread-out Bragg peak 16

IMPT intensity-modulated proton therapy 17

TCP tumour control probability 17

NTCP normal tissue complication probability 17

PMT Photomultipler Tubes xii

pMBAT proton Mini Beam Arch Therapy 21

CNN Convolutet Neural Network xix

ADAM Adaptive Moment Estimation 58

MSE Mean Squared Error 60

MAE Mean Absolute Error 60

MC Monte Carlo 60

CCE Charge Collection Electrode 51

FE Front End xiii

CSA Charge Sensitive Amplifier 52

ToT Time over Threshold 49

CP Clinical Protons xiii

GPAC General Purpose Analog Card 66

MIO3 Multiple Input/Output 3 66

BILPA Birmingham Instrumentation Lab for Particle physics and Applications

FDPW Full Deep P-Well xiii

RDPW Removed Deep P-Well xiii

ENC Equivalent Noise Charge xiii

MPV Most Provable Value 71

MIP Minimum Ionising Particles 38

RF Radio Frequency 84

IC Ionisation Chamber 85

RT Range Telescope 139

TLU Trigger Logic Unit 107

FWHM Full Width at Half Maximum 127

ASTRA A Super Thin RAnte Telescope 137

FGD Fine Grained Detector 139

PE photo-electrons 141

WEPL Water Equivalent Path Lenght 27

BDT Boosted Decision Tree 147

pGFI protons Good For Imaging 150

WEM Water Equivalent Material 155

WET Water Equivalent Thickness 27

CXE Categorical Cross Entropy 163

BFL Binary Focal Loss 163

Bibliography

[1] M. Granado-González, C. Jesús-Valls, T. Lux, T. Price, and F. Sánchez, "A novel range telescope concept for proton CT," *Physics in Medicine & Biology*, vol. 67, no. 3, p. 035 013, Feb. 2022. DOI: 10.1088/1361-6560/ac4b39. [Online]. Available: https://doi.org/10.1088/1361-6560/ac4b39.

[2] H. Ritchie, F. Spooner, and M. Roser, "Causes of death," *Our World in Data*, 2018, https://ourworldindata.org/causes-of-death.

[3] T. Mitin and A. L. Zietman, "Promise and pitfalls of heavy-particle therapy," *Journal of Clinical Oncology*, vol. 32, no. 26, pp. 2855–2863, 2014, PMID: 25113772. DOI: 10.1200/JCO.2014.55.1945. eprint: https://doi.org/10.1200/JCO.2014.55.1945. [Online]. Available: https://doi.org/10.1200/JCO.2014.55.1945.

[4] P. Gabani *et al.*, "Clinical outcomes and toxicity of proton beam radiation therapy for re-irradiation of locally recurrent breast cancer," *Clinical and Translational Radiation Oncology*, vol. 19, pp. 116–122, 2019, ISSN: 2405-6308. DOI: https://doi.org/10.1016/j.ctro.2019.09.005. [Online]. Available: https://www.sciencedirect.com/science/article/pii/S2405630819300990.

[5] Suneja *et al.*, "Acute toxicity of proton beam radiation for pediatric central nervous system malignancies," *Pediatric blood & cancer*, vol. 60, no. 9, pp. 1431–1436, 2013.

[6] E. Schnell, S. Ahmad, and T. de la Fuente Herman, "Commissioning of a relative stopping power to hounsfield unit calibration curve for a mevion proton radiation treatment unit," in *AIP Conference Proceedings*, AIP Publishing, vol. 1747, 2016.

[7] M. Yang, X. R. Zhu, P. C. Park, *et al.*, "Comprehensive analysis of proton range uncertainties related to patient stopping-power-ratio estimation using the stoichiometric calibration," *Physics in Medicine & Biology*, vol. 57, no. 13, p. 4095, 2012.

[8] B. Li, H. Lee, X. Duan, *et al.*, "Comprehensive analysis of proton range uncertainties related to stopping-power-ratio estimation using dual-energy ct imaging," *Physics in Medicine & Biology*, vol. 62, no. 17, p. 7056, 2017.

[9] D. F. DeJongh, E. A. DeJongh, V. Rykalin, *et al.*, "A comparison of proton stopping power measured with proton ct and x-ray ct in fresh postmortem porcine structures," *Medical Physics*, vol. 48, no. 12, pp. 7998–8009, 2021.

[10] P. Palaniappan, S. Meyer, M. Rädler, *et al.*, "X-ray ct adaptation based on a 2d–3d deformable image registration framework using simulated in-room proton radiographies," *Physics in Medicine & Biology*, vol. 67, no. 4, p. 045 003, 2022.

[11] C. Sarosiek, E. A. DeJongh, G. Coutrakon, *et al.*, "Analysis of characteristics of images acquired with a prototype clinical proton radiography system," *Medical physics*, vol. 48, no. 5, pp. 2271–2278, 2021.

[12] M. Esposito, C. Waltham, J. T. Taylor, *et al.*, "Pravda: The first solid-state system for proton computed tomography," *Physica Medica*, vol. 55, pp. 149–154, 2018.

[13] R. P. Johnson, V. Bashkirov, V. Giacometti, *et al.*, "A fast experimental scanner for proton ct: Technical performance and first experience with phantom scans," *IEEE transactions on nuclear science*, vol. 63, no. 1, pp. 52–60, 2015.

[14] R. P. Johnson, V. Bashkirov, G. Coutrakon, *et al.*, "Results from a prototype proton-ct head scanner," *Physics Procedia*, vol. 90, pp. 209–214, 2017.

[15] A. Winter, A. Aitkenhead, N. Allinson, *et al.*, "Optima: A tracking solution for proton computed tomography in high proton flux environments," *Journal of Instrumentation*, vol. 18, no. 04, P04026, 2023.

[16] I. Caicedo, M. Barbero, P. Barrillon, *et al.*, "The monopix chips: Depleted monolithic active pixel sensors with a column-drain read-out architecture for the atlas inner tracker upgrade," *Journal of Instrumentation*, vol. 14, no. 06, p. C06006, 2019.

[17] e. a. Responsible statistician: Emma Hope. Production team: Jess Fraser. "Chemotherapy, radiotherapy, and surgical tumour resections in england." (2020).

[18] M. Lomax, L. Folkes, and P. O'neill, "Biological consequences of radiation-induced dna damage: Relevance to radiotherapy," *Clinical oncology*, vol. 25, no. 10, pp. 578–585, 2013.

[19] J. TJ, d. CM, and D. P O'Neill, "Induction and rejoining of dna double-strand breaks in v79-4 mammalian cells following γ-and α-irradiation," *International Journal of Radiation Biology*, vol. 64, no. 3, pp. 265–273, 1993.

[20] H. Nikjoo, P. O'neill, M. Terrissol, and D. Goodhead, "Quantitative modelling of dna damage using monte carlo track structure method," *Radiation and environmental biophysics*, vol. 38, no. 1, pp. 31–38, 1999.

[21] H. NIKJOO S. UEHARA WE WILSON M. HOSHI DT GOODHEAD, "Track structure in radiation biology: Theory and applications," *International journal of radiation biology*, vol. 73, no. 4, pp. 355–364, 1998.

[22] D. T. Goodhead, "Initial events in the cellular effects of ionizing radiations: Clustered damage in dna," *International journal of radiation biology*, vol. 65, no. 1, pp. 7–17, 1994.

[23] M. Tepper and I. Gannot, "Monitoring tumor state from thermal images in animal and human models," *Medical Physics*, vol. 42, no. 3, pp. 1297–1306, 2015.

[24] W. D. Newhauser and R. Zhang, "The physics of proton therapy," *Physics in Medicine & Biology*, vol. 60, no. 8, R155, 2015.

[25] W. Newhauser and R. Zhang, "The physics of proton therapy," *Physics in medicine and biology*, vol. 60, R155–R209, Mar. 2015. DOI: 10.1088/0031-9155/60/8/R155.

[26] S. M. MacDonald, T. F. DeLaney, and J. S. Loeffler, "Proton beam radiation therapy," *Cancer investigation*, vol. 24, no. 2, pp. 199–208, 2006.

[27] N. Matsufuji, T. Kanai, N. Kanematsu, *et al.*, "Specification of carbon ion dose at the national institute of radiological sciences (nirs)," *Journal of radiation research*, vol. 48, no. Suppl_A, A81–A86, 2007.

[28] J. Lauritsen and M. E. Bruus, "A comprehensive tool for validated entry and documentation of data," *The EpiData Association, Odense, Denmark*, vol. 2005, 2003.

[29] D. Schulz-Ertner and H. Tsujii, "Particle radiation therapy using proton and heavier ion beams," *Journal of clinical oncology*, vol. 25, no. 8, pp. 953–964, 2007.

[30] M. Brada, M. Pijls-Johannesma, and D. De Ruysscher, "Proton therapy in clinical practice: Current clinical evidence," *Journal of clinical oncology*, vol. 25, no. 8, pp. 965–970, 2007.

[31] M. M. Geenen, M. C. Cardous-Ubbink, L. C. Kremer, *et al.*, "Medical assessment of adverse health outcomes in long-term survivors of childhood cancer," *Jama*, vol. 297, no. 24, pp. 2705–2715, 2007.

[32] E. B. Podgorsak *et al.*, *Radiation oncology physics.* IAEA Vienna, 2005.

[33] T. Schneider, "Technical aspects of proton minibeam radiation therapy: Minibeam generation and delivery," *Physica Medica*, vol. 100, pp. 64–71, 2022.

[34] M. Sammer, S. Girst, and G. Dollinger, "Optimizing proton minibeam radiotherapy by interlacing and heterogeneous tumor dose on the basis of calculated clonogenic cell survival," *Scientific reports*, vol. 11, no. 1, pp. 1–16, 2021.

[35] Y. Prezado, G. Jouvion, A. Patriarca, *et al.*, "Proton minibeam radiation therapy widens the therapeutic index for high-grade gliomas," *Scientific reports*, vol. 8, no. 1, p. 16 479, 2018.

[36] P. Lansonneur, H. Mammar, C. Nauraye, *et al.*, "First proton minibeam radiation therapy treatment plan evaluation," *Scientific reports*, vol. 10, no. 1, p. 7025, 2020.

[37] T. Schneider, L. De Marzi, A. Patriarca, and Y. Prezado, "Advancing proton minibeam radiation therapy: Magnetically focussed proton minibeams at a clinical centre," *Scientific reports*, vol. 10, no. 1, pp. 1–10, 2020.

[38] R. Ortiz, L. De Marzi, and Y. Prezado, "Proton minibeam radiation therapy and arc therapy: Proof of concept of a winning alliance," *Cancers*, vol. 14, no. 1, p. 116, 2022.

[39] J. R. Hughes and J. L. Parsons, "Flash radiotherapy: Current knowledge and future insights using proton-beam therapy," *International journal of molecular sciences*, vol. 21, no. 18, p. 6492, 2020.

[40] A. Beddok, C. Lahaye, V. Calugaru, *et al.*, "A comprehensive analysis of the relationship between dose-rate and biological effects in pre-clinical and clinical studies, from brachytherapy to flattening filter-free radiation therapy and flash irradiation," *International Journal of Radiation Oncology* Biology* Physics*, 2022.

[41] C.-A. C. Fekete, P. Doolan, M. F. Dias, L. Beaulieu, and J. Seco, "Developing a phenomenological model of the proton trajectory within a heterogeneous medium required for proton imaging," *Physics in Medicine & Biology*, vol. 60, no. 13, p. 5071, 2015.

[42] R. Schulte, S. Penfold, J. Tafas, and K. Schubert, "A maximum likelihood proton path formalism for application in proton computed tomography," *Medical physics*, vol. 35, no. 11, pp. 4849–4856, 2008.

[43] Á. Sudár and G. G. Barnaföldi, *Proton computed tomography based on richardson-lucy algorithm*, 2022. DOI: 10.48550/ARXIV.2212.00126. [Online]. Available: https://arxiv.org/abs/2212.00126.

[44] J. Alme, G. G. Barnaföldi, R. Barthel, *et al.*, "A high-granularity digital tracking calorimeter optimized for proton ct," *Frontiers in Physics*, vol. 8, p. 568 243, 2020.

[45] F. Ulrich-Pur, T. Bergauer, A. Burker, *et al.*, "Feasibility study of a proton ct system based on 4d-tracking and residual energy determination via time-of-flight," *Physics in Medicine & Biology*, vol. 67, no. 9, p. 095 005, 2022.

[46] R. Johnson, V. Bashkirov, G. Coutrakon, *et al.*, "Results from a prototype proton-ct head scanner," *Physics Procedia*, vol. 90, Jul. 2017. DOI: 10.1016/j.phpro.2017.09.060.

[47] E. A. DeJongh, D. F. DeJongh, I. Polnyi, *et al.*, "A fast and monolithic prototype clinical proton radiography system optimized for pencil beam scanning," *Medical physics*, vol. 48, no. 3, pp. 1356–1364, 2021.

[48] M. Aehle, J. Alme, G. Barnaföldi, *et al.*, "The bergen proton ct system," *Journal of Instrumentation*, vol. 18, no. 02, p. C02051, 2023.

[49] G. A. Rinella, A. collaboration, *et al.*, "The alpide pixel sensor chip for the upgrade of the alice inner tracking system," *Nuclear Instruments and Methods in Physics Research Section A: Accelerators, Spectrometers, Detectors and Associated Equipment*, vol. 845, pp. 583–587, 2017.

[50] "Https://www.nuclear-power.com/nuclear-power/reactor-physics/atomic-nuclear-physics/radiation rays-roentgen-radiation/x-ray-attenuation/," [Online]. Available: https://www.nuclear-power.com/nuclear-power/reactor-physics/atomic-nuclear-physics/radiation/x-rays-roentgen-radiation/x-ray-attenuation/.

[51] H. Bichsel, "A method to improve tracking and particle identification in tpcs and silicon detectors," *Nuclear Instruments and Methods in Physics Research Section A: Accelerators, Spectrometers, Detectors and Associated Equipment*, vol. 562, no. 1, pp. 154–197, 2006, ISSN: 0168-9002. DOI: https://doi.org/10.1016/j.nima.2006.03.009. [Online]. Available: https://www.sciencedirect.com/science/article/pii/S0168900206005353.

[52] J. Beringer, J. Arguin, R. Barnett, *et al.*, "Review of particle physics," *Physical Review D*, vol. 86, no. 1, 2012.

[53] M. Zarifi, S. Guatelli, D. Bolst, B. Hutton, A. Rosenfeld, and Y. Qi, "Characterization of prompt gamma-ray emission with respect to the bragg peak for proton beam range verification: A monte carlo study," *Physica Medica*, vol. 33, pp. 197–206, 2017.

[54] G. R. Lynch and O. I. Dahl, "Approximations to multiple coulomb scattering," *Nuclear Instruments and Methods in Physics Research Section B: Beam Interactions with Materials and Atoms*, vol. 58, no. 1, pp. 6–10, 1991.

[55] N. Arefyeva, S. Gninenko, D. Gorbunov, and D. Kirpichnikov, "Passage of millicharged particles in the electron beam-dump: Refining constraints from slacmq and estimating sensitivity of na 64 e," *Physical Review D*, vol. 106, no. 3, p. 035 029, 2022.

[56] W. Shockley, "The theory of p-n junctions in semiconductors and p-n junction transistors," *Bell System Technical Journal*, vol. 28, no. 3, pp. 435–489, 1949.

[57] [Online]. Available: https://en.wikipedia.org/wiki/P%E2%80%93n_junction.

[58] W. Riegler, "An application of extensions of the ramo–shockley theorem to signals in silicon sensors," *Nuclear Instruments and Methods in Physics Research Section A: Accelerators, Spectrometers, Detectors and Associated Equipment*, vol. 940, pp. 453–461, 2019.

[59] R. Turchetta, M. French, S. Manolopoulos, *et al.*, "Monolithic active pixel sensors (maps) in a vlsi cmos technology," *Nuclear Instruments and Methods in Physics Research Section A: Accelerators, Spectrometers, Detectors and Associated Equipment*, vol. 501, no. 1, pp. 251–259, 2003.

[60] M. Mager, A. collaboration, *et al.*, "Alpide, the monolithic active pixel sensor for the alice its upgrade," *Nuclear Instruments and Methods in Physics Research Section A: Accelerators, Spectrometers, Detectors and Associated Equipment*, vol. 824, pp. 434–438, 2016.

[61] W. Snoeys, G. A. Rinella, H. Hillemanns, *et al.*, "A process modification for cmos monolithic active pixel sensors for enhanced depletion, timing performance and radiation tolerance," *Nuclear Instruments and Methods in Physics Research Section A: Accelerators, Spectrometers, Detectors and Associated Equipment*, vol. 871, pp. 90–96, 2017.

[62] K. Moustakas *et al.*, "CMOS Monolithic Pixel Sensors based on the Column-Drain Architecture for the HL-LHC Upgrade," *Nucl. Instrum. Meth. A*, vol. 936, G. Batignani, M. Grassi, R. Paoletti, A. Retico, G. Signorelli, and P. Spagnolo, Eds., pp. 604–607, 2019. DOI: 10.1016/j.nima.2018.09.100. arXiv: 1809.03434 [physics.ins-det].

[63] G. Collazuol, "The sipm physics and technology-a review," *LAL Orsay*, 2012.

[64] C. Piemonte and A. Gola, "Overview on the main parameters and technology of modern silicon photomultipliers," *Nuclear Instruments and Methods in Physics Research Section A: Accelerators, Spectrometers, Detectors and Associated Equipment*, vol. 926, pp. 2–15, 2019, Silicon Photomultipliers: Technology, Characterisation and Applications, ISSN: 0168-9002. DOI: https://doi.org/10.1016/j.nima.2018.11.119. [Online]. Available: https://www.sciencedirect.com/science/article/pii/S0168900218317716.

[65] Y. Zou, F. Villa, D. Bronzi, S. Tisa, A. Tosi, and F. Zappa, "Planar cmos analog sipms: Design, modeling, and characterization," *Journal of Modern Optics*, vol. 62, no. 20, pp. 1693–1702, 2015.

[66] P. Lecoq and S. Gundacker, "Sipm applications in positron emission tomography: Toward ultimate pet time-of-flight resolution," *The European Physical Journal Plus*, vol. 136, no. 3, p. 292, 2021.

[67] J. F. Krizmanic *et al.*, "Space-based extensive air shower optical cherenkov and fluorescence measurements using sipm detectors in context of poemma," *Nuclear*

Instruments and Methods in Physics Research Section A: Accelerators, Spectrometers, Detectors and Associated Equipment, vol. 985, p. 164 614, 2021.

[68] Y. G. Kudenko and P. the T2K Collaboration, "The t2k experiment: Status and instrumentation of the 280m near detector," in *Astroparticle, Particle And Space Physics, Detectors And Medical Physics Applications*, World Scientific, 2006, pp. 245–252.

[69] W. Riegler, "Particle physics instrumentation," *arXiv preprint arXiv:1406.7745*, 2014.

[70] J. Birks and F. Black, "Deterioration of anthracene under a particle bombardment," in *Proc. of the Phys. Soc.(Lond.)*, vol. 64, 1951.

[71] A. Krizhevsky, I. Sutskever, and G. E. Hinton, "Imagenet classification with deep convolutional neural networks," *Advances in neural information processing systems*, vol. 25, 2012.

[72] K. Simonyan and A. Zisserman, "Very deep convolutional networks for large-scale image recognition," *arXiv preprint arXiv:1409.1556*, 2014.

[73] O. Ronneberger, P. Fischer, and T. Brox, "U-net: Convolutional networks for biomedical image segmentation," in *Medical Image Computing and Computer-Assisted Intervention–MICCAI 2015: 18th International Conference, Munich, Germany, October 5-9, 2015, Proceedings, Part III 18*, Springer, 2015, pp. 234–241.

[74] X.-X. Yin, L. Sun, Y. Fu, R. Lu, Y. Zhang, *et al.*, "U-net-based medical image segmentation," *Journal of Healthcare Engineering*, vol. 2022, 2022.

[75] D. P. Kingma and J. Ba, "Adam: A method for stochastic optimization," *arXiv preprint arXiv:1412.6980*, 2014.

[76] S. Agostinelli, J. Allison, K. a. Amako, *et al.*, "Geant4—a simulation toolkit," *Nuclear instruments and methods in physics research section A: Accelerators, Spectrometers, Detectors and Associated Equipment*, vol. 506, no. 3, pp. 250–303, 2003.

[77] G. G. Gielen and J. E. Franca, "Cad tools for data converter design: An overview," *IEEE Transactions on Circuits and Systems II: Analog and Digital Signal Processing*, vol. 43, no. 2, pp. 77–89, 1996.

[78] W. Snoeys, G. Aglieri Rinella, H. Hillemanns, *et al.*, "A process modification for cmos monolithic active pixel sensors for enhanced depletion, timing performance and radiation tolerance," *Nuclear Instruments and Methods in Physics Research Section A: Accelerators, Spectrometers, Detectors and Associated Equipment*, vol. 871, pp. 90–96, 2017, ISSN: 0168-9002. DOI: https://doi.org/10.1016/j.nima.2017.07.046. [Online]. Available: https://www.sciencedirect.com/science/article/pii/S016890021730791X.

[79] H. Pernegger *et al.*, "First tests of a novel radiation hard CMOS sensor process for Depleted Monolithic Active Pixel Sensors," *JINST*, vol. 12, no. 06, P06008, 2017. DOI: 10.1088/1748-0221/12/06/P06008.

[80] T. Wang *et al.*, "Development of a Depleted Monolithic CMOS Sensor in a 150 nm CMOS Technology for the ATLAS Inner Tracker Upgrade," *JINST*, vol. 12, no. 01, p. C01039, 2017. DOI: 10.1088/1748-0221/12/01/C01039. arXiv: 1611.01206 [physics.ins-det].

[81] T. Hemperek et al, *Tj-monopix*, https://github.com/SiLab-Bonn/tjmonopix-daq.

[82] A. Blondel *et al.*, "A fully active fine grained detector with three readout views," *JINST*, vol. 13, no. 02, P02006, 2018. DOI: 10.1088/1748-0221/13/02/P02006. arXiv: 1707.01785 [physics.ins-det].

[83] C. Fiorini, M. Bellini, A. Gola, *et al.*, "A monolithic array of 77 silicon drift detectors for x-ray spectroscopy and gamma-ray imaging applications," *Nuclear Science, IEEE Transactions on*, vol. 52, pp. 1165–1170, Sep. 2005. DOI: 10.1109/TNS.2005.852727.

[84] M. Ester, H.-P. Kriegel, J. Sander, X. Xu, *et al.*, "A density-based algorithm for discovering clusters in large spatial databases with noise," in *kdd*, vol. 96, 1996, pp. 226–231.

[85] N. G. Burnet, R. I. Mackay, E. Smith, *et al.*, "Proton beam therapy: Perspectives on the national health service england clinical service and research programme," *The British Journal of Radiology*, vol. 93, no. 1107, p. 20 190 873, 2020.

[86] K. P. Nesteruk and S. Psoroulas, "Flash irradiation with proton beams: Beam characteristics and their implications for beam diagnostics," *Applied Sciences*, vol. 11, no. 5, 2021, ISSN: 2076-3417. DOI: 10.3390/app11052170. [Online]. Available: https://www.mdpi.com/2076-3417/11/5/2170.

[87] A. La Rosa, M. Garella, F. Bourhaleb, *et al.*, "A pixel ionization chamber used as beam monitor at the institut curie—centre de protontherapie de orsay (cpo)," *Nuclear Instruments and Methods in Physics Research Section A: Accelerators, Spectrometers, Detectors and Associated Equipment*, vol. 565, no. 2, pp. 833–840, 2006, ISSN: 0168-9002. DOI: https://doi.org/10.1016/j.nima.2006.06.024. [Online]. Available: https://www.sciencedirect.com/science/article/pii/S0168900206011405.

[88] R. Ortiz, L. De Marzi, and Y. Prezado, "Preclinical dosimetry in proton minibeam radiation therapy: Robustness analysis and guidelines," *Medical Physics*, 2022.

[89] C. Peucelle, C. Nauraye, A. Patriarca, *et al.*, "Proton minibeam radiation therapy: Experimental dosimetry evaluation," *Medical physics*, vol. 42, no. 12, pp. 7108–7113, 2015.

[90] C. Jesús-Valls, M. Granado-González, T. Lux, T. Price, and F. Sánchez, "Enhanced proton tracking with astra using calorimetry and deep learning," *Instruments*, vol. 6, no. 4, p. 58, 2022.

[91] C. Neubüser *et al.*, "Sensor design optimization of innovative low-power, large area MAPS for HEP and applied science," Nov. 2020. arXiv: 2011.09723 [physics.ins-det].

[92] G. Aglieri Rinella, "Developments of stitched monolithic pixel sensors towards the ALICE ITS3," *Nucl. Instrum. Meth. A*, vol. 1049, p. 168 018, 2023. DOI: 10.1016/j.nima.2023.168018.

[93] P. Vicente Leitao *et al.*, "Development of a Stitched Monolithic Pixel Sensor prototype (MOSS chip) towards the ITS3 upgrade of the ALICE Inner Tracking system," *JINST*, vol. 18, no. 01, p. C01044, 2023. DOI: 10.1088/1748-0221/18/01/C01044.

[94] P. A. Amaudruz *et al.*, "The T2K Fine-Grained Detectors," *Nucl. Instrum. Meth. A*, vol. 696, pp. 1–31, 2012. DOI: 10.1016/j.nima.2012.08.020. arXiv: 1204.3666 [physics.ins-det].

[95] K. Abe *et al.*, "The T2K Experiment," *Nucl. Instrum. Meth. A*, vol. 659, pp. 106–135, 2011. DOI: 10.1016/j.nima.2011.06.067. arXiv: 1106.1238 [physics.ins-det].

[96] C. Betancourt *et al.*, "Application of large area SiPMs for the readout of a plastic scintillator based timing detector," *JINST*, vol. 12, no. 11, P11023, 2017. DOI: 10.1088/1748-0221/12/11/P11023. arXiv: 1709.08972 [physics.ins-det].

[97] A. Korzenev *et al.*, "Plastic scintillator detector with the readout based on an array of large-area SiPMs for the ND280/T2K upgrade and SHiP experiments," *JPS Conf. Proc.*, vol. 27, p. 011 005, 2019. DOI: 10.7566/JPSCP.27.011005. arXiv: 1901.07785 [physics.ins-det].

[98] K. Abe *et al.*, "T2K ND280 Upgrade - Technical Design Report," 2019, arXiv:1901.03750. arXiv: 1901.03750 [physics.ins-det].

[99] Eljen Technology, *Plastic scintillator products*, https://eljentechnology.com/products/plastic-scintillators.

[100] A. Blondel *et al.*, "The SuperFGD Prototype Charged Particle Beam Tests," *JINST*, vol. 15, no. 12, P12003, 2020. DOI: 10.1088/1748-0221/15/12/P12003. arXiv: 2008.08861 [physics.ins-det].

[101] Onsemi, *J-series SiPM sensors*, https://www.onsemi.com/pdf/datasheet/microj-series-d.pdf.

[102] H.-W. Sadrozinski *et al.*, "Development of a head scanner for proton ct," *Nuclear Instruments and Methods in Physics Research Section A: Accelerators, Spectrometers, Detectors and Associated Equipment*, vol. 699, pp. 205–210, 2013.

[103] F. Ulrich-Pur *et al.*, "A proton computed tomography demonstrator for stopping power measurements," *arXiv preprint arXiv:2106.12890*, 2021.

[104] S. A. Uzunyan *et al.*, "Development of a proton CT head scanner," in *2015 IEEE Nuclear Science Symposium and Medical Imaging Conference (NSS/MIC)*, 2015, pp. 1–2. DOI: 10.1109/NSSMIC.2015.7582123.

[105] M. Bucciantonio *et al.*, "Development of a fast proton range radiography system for quality assurance in hadrontherapy," *Nuclear Instruments and Methods in Physics Research Section A: Accelerators, Spectrometers, Detectors and Associated Equipment*, vol. 732, pp. 564–567, 2013.

[106] A. Blondel, M. Bogomilov, S. Bordoni, *et al.*, "The superfgd prototype charged particle beam tests," *Journal of Instrumentation*, vol. 15, no. 12, P12003, 2020.

[107] S. Alonso-Monsalve *et al.*, "Graph neural network for 3D classification of ambiguities and optical crosstalk in scintillator-based neutrino detectors," *Phys. Rev. D*, vol. 103, no. 3, p. 032 005, 2021. DOI: 10.1103/PhysRevD.103.032005. arXiv: 2009.00688 [physics.data-an].

[108] J. Therhaag, "TMVA: Toolkit for multivariate data analysis," *AIP Conf. Proc.*, vol. 1504, no. 1, T. E. Simons and G. Maroulis, Eds., pp. 1013–1016, 2012. DOI: 10.1063/1.4771869.

[109] G. Poludniowski, N. Allinson, and P. Evans, "Proton radiography and tomography with application to proton therapy," *The British journal of radiology*, vol. 88, no. 1053, p. 20 150 134, 2015.

[110] J. Taylor, G. Poludniowski, T. Price, *et al.*, "An experimental demonstration of a new type of proton computed tomography using a novel silicon tracking detector," *Medical physics*, vol. 43, no. 11, pp. 6129–6136, 2016.

[111] M. Esposito *et al.*, "Pravda: The first solid-state system for proton computed tomography," *Physica Medica*, vol. 55, pp. 149–154, 2018, ISSN: 1120-1797. DOI: https://doi.org/10.1016/j.ejmp.2018.10.020. [Online]. Available: https://www.sciencedirect.com/science/article/pii/S1120179718313073.

[112] H. E. S. Pettersen *et al.*, "Investigating particle track topology for range telescopes in particle radiography using convolutional neural networks," *Acta Oncologica*, pp. 1–6, 2021.

[113] C. E. Ordoñez *et al.*, "A real-time image reconstruction system for particle treatment planning using proton computed tomography (pct)," *Physics Procedia*, vol. 90, pp. 193–199, 2017, Conference on the Application of Accelerators in Research and Industry, CAARI 2016, 30 October – 4 November 2016, Ft. Worth, TX, USA, ISSN: 1875-3892. DOI: https://doi.org/10.1016/j.phpro.2017.09.058. [Online]. Available: https://www.sciencedirect.com/science/article/pii/S1875389217302171.

[114] C. Jesús-Valls, M. Granado-González, T. Lux, T. Price, and F. Sánchez, "Enhanced proton tracking with astra using calorimetry and deep learning," *Instruments*, vol. 6, no. 4, 2022, ISSN: 2410-390X. DOI: 10.3390/instruments6040058. [Online]. Available: https://www.mdpi.com/2410-390X/6/4/58.

[115] J. Zhu, D. Liu, W. Zhang, *et al.*, "Systematic experimental study on stitching techniques of cmos image sensors," *IEICE Electronics Express*, vol. 13, no. 15, pp. 20 160 441–20 160 441, 2016. DOI: 10.1587/elex.13.20160441.